Lomonosov Moscow State University, Russia
University of Washington, Seattle, USA
Tomsk State University, Tomsk, Russia

Printed as manuscript

Anna Vladimirovna Naumova

Comprehensive Approach to Non-invasive Study of the Heart Using Magnetic Resonance Imaging and Spectroscopy

Specialties: 03.01.02 – «Biophysics», 03.01.08 - «Bioengineering»

DISSERTATION
for a Doctor of Science Degree in Physics and Mathematics

Scientific consultant:
Doctor of Science
in Physics and Mathematics,
Professor,
Yuri Andreevich Pirogov
Lomonosov Moscow State
University

Moscow - 2018

TABLE OF CONTENT

List of abbreviations

ADP - adenosine diphosphate;
AIF – arterial input function;
ANOVA – analysis of variance;
ATP – adenosine triphosphate;
AU - arbitrary units;
AW-CSI - acquisition-weighted CSI;
B_0 - main static magnetic field;
B_1 - magnetic field oscillating at radio frequency;
BIRP - B_1-field independent rotation phase-cycled adiabatic pulses;
bFGF - basic fibroblast growth factor;
b-FFE - Balanced Fast Field Echo;
b-SSFP - Steady State Free Precession;
BMP-4 - bone morphogenetic protein-4;
β-MHC - β-myosin heavy chain;
bp – base pairs (of nucleotides);
bpm – beats per minute;
BrdU - 5-bromodeoxyuridine;
BSA - bovine serum albumin;
C2C12 – mouse skeletal myoblasts;
CDC - cardiosphere-derived cells;
cDNA – complementary DNA;
CEST - chemical exchange saturation transfer;
CHF – congenital heart failure;
CK - creatine kinase;
CLEAR - Constant LEvel AppeaRance;
CNR – contrast-to-noise ratio;
CMV– cytomegalovirus promoter;
CO - cardiac output;
$C_p[n]$ and $C_t[n]$ – contrast concentration in plasma (p) and tissue (t) in the phase n;
CT - computed tomography;
cTnI – cardiac troponin I;
1D-CSI – one dimensional chemical shift imaging;
3D-TRIPS – 3-Dimentional True Polarity Recovery with Independent Phase Estimation Using Multi-layer Stacks Based Region-Growing;
DAB - 3,3'-diaminobenzidine;
DCE – dynamic contrast enhancement;
DEMRI - delayed-enhancement MRI;
DIR - double inversion-recovery;
DMEM – modified basal medium eagle;
DMD - Duchenne muscular dystrophy;
DNA – deoxyribonucleic acid;
DS-1 – canine bone marrow fibroblasts;
DTI - diffusion-tensor imaging;
E - early wave velocity of the mitral inflow;
echo – resulted MRI signal;
ECG, EKG – electrocardiogram;
ECV - extracellular volume fraction;
EDTA - ethylenediaminetetraacetic acid;
EDV - end-diastolic volume;
eGFP – enhanced green fluorescent protein;
ESV - end-systolic volume;
EE – extraction efficacy;
E/e' - early diastolic velocity;
FA – flip angle;
FAST - four-angle saturation transfer;
FBS – fetal bovine serum;
FDG - ^{18}F-fluorodeoxyglucose;
FID – free induction decay;
^{18}FHBG - ^{18}F-9-(4-[^{18}F]fluoro-3-hydroxy-methylbutyl);
FLASH - fast low angle shot;
FOV – field of view;
Ft_{mt} - mitochondrial ferritin;
Gd-DTPA – gadolinium diethylenetriamine penta-acetic acid;
GE - General Electric;
GLS - global LV peak systolic longitudinal strain;

GRE – gradient echo;
G° - the standard free-energy change;
ΔG_{ATP} - ATP hydrolysis free-energy change;
^{1}H – protons;
H-ferritin – ferritin heavy chain;
HCP-1 - heme carrier protein-1;
HRG-1 - heme response gene-1;
iPSCs - induced pluripotent stem cells;
IR – inversion recovery;
HA - influenza hemagglutinin;
H&E - hematoxylin and eosin;
hESC - human embryonic stem cells;
hESC-CM – human embryonic stem cell-derived cardiomyocytes;
HR - heart rate;
HRP – horse radish protein;
HSV1-tk - herpes simplex virus thymidine kinase type 1;
iMSDE - improved motion sensitized driven equilibrium;
i.e. - that is (Latin);
i.v. - intravenous;
i.p. - intra-peritoneal;
IR - inversion-recovery;
kDA – kilo Dalton;
KFRS - Kalman filtering, registration, and smoothing;
k_{ep} - transfer rate constant;
k_{for} - forward rate constant;
K^{trans} - contrast transfer constant;
LAD - left anterior descending coronary artery;
LAVi - left atrial volume index;
LGE – late gadolinium enhancement;
LL – Look-Locker;
LRP - lysine-rich protein;
LV – left ventricle;
LVEDD - left ventricular end diastolic dimension;
LVEDV – left ventricle end-diastolic volume;
LVESD - left ventricular end systolic dimension;
LVESV – left ventricle end-systolic volume;
LVEF – left ventricle ejection fraction;
LVmass – left ventricle myocardial mass;
MBF - myocardial blood flow;
MEF-CM - mouse embryonic fibroblast conditioned medium;
MEMRI - Mn^{2+}-enhanced MRI;
MI – myocardial infarction;
MOLLI - modified Look-Locker inversion;
MPI - magnetic particle imaging;
MRI – magnetic resonance imaging;
MSCs - mesenchymal stem cells;
MSDE - motion-sensitized driven equilibrium;
n – number of observations;
na – number of signal averages;
NHPs – non-human primates;
NIS - sodium iodide symporter;
NS – (statistically) not significant;
p – statistical significance level;
PBS – phosphate buffer solution;
PCr – phosphocreatine;
PCR – polymerase chain reaction;
PD TSE BB – proton-density weighted turbo spin echo black blood;
PEEP - positive end-expiratory pressure;
^{31}P *MRS* – phosphorus magnetic resonance spectroscopy;
PE – phase encoding;
PET – positron-emission tomography;
Pi - inorganic phosphate;
PPA - phenyl-phosphonic acid;
ppm – parts per million;
PSC – pro-survival cocktail;
PSIR – phase-sensitive inversion recovery;
PTCA - percutaneous transluminal coronary angioplasty;
R – contrast retention coefficient;

r – correlation coefficient;
RF - radio frequency;
RO – read-out,
ROI – region of interest;
RPMI - Roswell Park Memorial Institute cell medium;
Scara5 - scavenge receptor family class A member 5;
SD – standard deviation;
SENSE - SENSitivity Encoding
SFM – serum-free medium;
ShMOLLI - shortened MOLLI;
SIR – signal intensity ratio;
sMHC - sarcomeric myosin heavy chain;
SNR – signal-to-nose ratio;
SPIO – superparamagnetic iron oxide nanoparticles;
SPECT - single photon emission computed tomography;
SS – slice selection gradient;
SV - stroke volume;
T - Tesla;
T_1 - longitudinal relaxation time;
T_2 - transverse relaxation time;
TDI - tissue Doppler imaging;
TE – echo time;
Timd2 or Tim-2 - T-cell immunoglobulin and mucin-domain containing protein-2;
TfR - transferrin receptor;
TI – inversion time;
TR – repetition time;
TSE – turbo-spin echo;
TTC - tetrazolium chloride;
U – contrast uptake coefficient;
US – ultrasound;
UTE-CSI - ultra-short echo time chemical shift imaging;
VCG - vector cardiogram;
WT – wild type cells;
XO – xanthine oxidase;
XOI – xanthine oxidase inhibitors;
λ - partition coefficient.

1. INTRODUCTION

1.1. Significance

One of the most important direction in the experimental biophysics is development of the complex systematic approaches and methods enabling novel bioengineering solutions of medical problems. The heart is one of the least regenerative organs in the human body, and mortality from cardiovascular diseases is highest among all causes of death. Considerable progress has been made in recent years in the development of new therapeutic approaches to recover the failed heart and to replace the scar tissue with viable cardiomyocytes. Despite of considerable break-troughs in cell transplantation, many questions remain unanswered regarding survival, engraftment of the transplanted cells and the functional outcome. *Ex vivo* histological or immunohistochemical methods provide the most detailed picture of the tissue with high spatial resolution, but they lack functional and dynamic information and require the sacrifice of large numbers of animals in order to complete longitudinal studies. *In vivo* imaging technology is irreplaceable for guiding cell therapy by visualization of biological processes on the cellular and subcellular levels, enabling the longitudinal, non-invasive monitoring of the fate and function of transplanted cells. Non-invasive assessment of heart structure and function is necessary for evaluation of the therapeutic intervention efficacy.

Various imaging modalities such as radionuclide, optical, magnetic resonance imaging (MRI), computed tomography (CT), and ultrasound can be used for anatomic and functional assessment of organs and for *in vivo* cell tracking. Specific research questions determine the choice of imaging modality. Several constructive reviews have been published in recent years outlining the uses of each imaging modality for cell tracking, achievable image resolution and scan time [1-4]. Superior soft-tissue contrast, large availability of imaging techniques, variety of contrast mechanisms, multinuclear capability, absence of ionizing radiation (safety), as well as capability for monitoring functional, anatomical and metabolic information enable MRI to stand out. MRI contrast weighting techniques can detect areas of pathology (scar, inflammation) [5], volume loss [6], complex tissue architecture [7, 8], chemical exchange within the macromolecular environment [9, 10], cellular death and inflammation [11], metabolite concentration [12, 13], tissue perfusion [14, 15], and vascularity [16-18]. Recent advances in MRI reporter gene techniques have enabled *in vivo* imaging of specific cell populations of interest regarding cell survival, proliferation, migration, and differentiation [19, 20], which makes MRI a valuable technology among other molecular imaging modalities.

The current work is using magnetic resonance imaging (MRI) and magnetic resonance spectroscopy (MRS) to study heart structure, contractile function, perfusion and metabolism on small and large laboratory animals. Animal studies are very important in pre-clinical evaluations of new therapeutic agents. Different transgenic mouse species are available for scientists to study the etiology of cardiovascular diseases. Large animals are used as surgical models that emulate human disease and to study transplanted cells. Noninvasive accurate measurements of cardiovascular indices (e.g., ventricular volumes, mass, ejection fraction) are very important for phenotyping of these animals and for quantitative evaluation of the therapeutic efficacy. Cardiac MRI studies on animals are challenging, because clinical scan protocols are not immediately transferable due to small heart size and rapid heart rates (average heart rate of 300-400 beats/min in rats and 500-600 beats/min in mice). Cardiac MRI studies in rodents have mostly been done using the non-clinical high field MR magnets (4.7 Tesla and higher) to provide adequate signal. However, many institutions do not have this capability. Therefore, development of the technology enabling cardiac MRI studies on animal using clinical scanners is very important.

Important part of the current work is devoted to the specific hardware design and development of the advanced cardiac MRI techniques for non-invasive studies on animal species: from rodents to non-human primates. This dissertation describes the methods to perform a cardiac MRI exam in laboratory animals on a high field and clinical-grade scanners, the equipment needed to perform the imaging study and monitor the animal, and the tools needed for accurate analysis of the cardiac function. Important technical developments of this work include construction of the specialized radiofrequency coils, pulse sequence development for assessment of heart structure and function, infarct and viable tissue visualization, for imaging of transplanted cells, kinetic modeling of the contrast agent dynamics for myocardial perfusion quantitation.

Phosphorus magnetic resonance spectroscopy (^{31}P MRS) is the only non-invasive technology for assessment of energy metabolism in different tissues. Non-localized ^{31}P MRS is widely used in the isolated Langendorff-perfused heart studies [21]. Combination of ^{31}P MRS with proton (^{1}H) MRI allows spatial localization of the spectra and obtaining metabolic information from the specific location [22]. Spatially-localized ^{31}P MRS has been used in this work for assessment of myocardial energetics in normal mice after adrenergic stimulation and in the infarcted mice after pharmacological correction of the myocardial damage.

This is a multidisciplinary work that combines advanced biomedical imaging, biophysics, cell biology, genetic engineering and molecular imaging methods. The feasibility of MRI detection and quantification of the cardiac grafts by overexpressing MRI gene-reporter ferritin has been shown as well as advantage of gene-reporter vs. the standard nanoparticle-based cell labeling methods for longitudinal tracking of transplanted cells in the infarcted heart. Non-invasive imaging can provide quantitative and qualitative assessment of transplanted cell dynamics that would lead to personalized patient care.

The *significance* of this work can be summarized in the following statements:

1. Development of non-invasive imaging technologies to study the heart is very important for pre-clinical and clinical evaluation of therapeutic interventions to cure cardiovascular diseases, which are number one cause of death in the world.
2. Magnetic resonance imaging plays a key role in evaluation of the myocardial structure and function, in treatment planning as well as in the assessment treatment outcome.
3. Pre-clinical studies of cardiovascular diseases are very important for evaluations of new therapeutic interventions. Cardiac MRI studies on animals are challenging; clinical scan protocols are not readily transferable to imaging of animals due to small heart size and rapid heart rates. Design of the specific hardware and development of the advanced cardiac MRI techniques are required for non-invasive studies on large and small animals.
4. Development of the novel imaging probes and methods for longitudinal tracking of the transplanted cell survival and functional benefits are very important for progress in regenerative therapy and personalized patient care.

1.2. Specific aims

The main **purpose** of this work is development of the advanced biophysical approaches and technological solutions for non-invasive evaluation of the heart structure, contractile function and metabolism in the laboratory animals, visualization of transplanted cells and regeneration of myocardium. To achieve this purpose the following **Specific Aims** were formulated:

1. To create a technological infrastructure, based on the novel approaches in physics and biophysics, for non-invasive studies of heart in small and large laboratory animals using magnetic resonance imaging and spectroscopy.

2. Using ^{1}H MRI, to evaluate the extend of structural and functional restoration of the heart in small and large laboratory animals after infarction and cell transplantation.

3. Using spatially-localized ^{31}P MRS, to evaluate changes in myocardial energetics of the mouse heart during stress as well as following myocardial infarction and pharmacological interventions.

4. To develop non-invasive physiologically meaningful method of myocardial perfusion quantitation using kinetic modeling of the contrast agent dynamics in tissues.

5. To explore the possibility of using the new processing method of the post-contrast MRI, 3D-TRIPS, for infarct visualization.

6. To explore the feasibility of visualization and quantification of the cardiac grafts by overexpressing MRI gene-reporter ferritin.

7. To compare the standard nanoparticle-based cell labeling methods with expression of MRI gene reporters for longitudinal tracking of transplanted cells in the infarcted heart.

1.3. Innovation

1. The biophysical technology and MRI pulse sequences developed in this work for non-invasive studies of the heart in laboratory animals are unique.

2. MRI methods developed during course of this work were applied for the first time for evaluation of structure and function of the infarcted heart in rats and non-human primates after transplantation of human cardiomyocytes. Visualization of the human transplant in the heart of laboratory animals and improvement of the infarcted heart structure and contractile function has been shown for the first time. Results of this work form the basis for future clinical studies of human embryonic stem cell derived cardiomyocytes.

2. For the first time, spatially localized ^{31}P MRS has been used to assess changes in myocardial energy metabolism in stress and after myocardial infarction in mouse models; the possibility of pharmacological correction of energy metabolism has been shown.

3. New analytical approach for automatic extraction of the myocardium perfusion parameters from dynamic contrast enhanced MR images has been developed. Efficacy of this method for quantitation of myocardial perfusion has been demonstrated on different models of heart failure.

4. For the first time, the new processing method for MRI sequence «inversion-recovery», 3D-TRIPS, has been applied for visualization of the myocardial infarction in laboratory animals. Advantage of the new method over the standard approaches has been demonstrated.

5. Possibility of using MRI gene-reporter ferritin for imaging of cardiac grafts has been shown for the first time in the infarcted mouse heart *in vivo*.

6. New MRI pulse sequences were developed for visualization of cardiac transplants over-expressing gene-reporter ferritin; high correlation of the graft size measurements between MRI and histology has been demonstrated.

7. Advantage of cell labeling with the gene-reporter ferritin over the standard techniques with superparamagnetic iron oxide nanoparticles has been shown for longitudinal tracking of live transplanted cells in the heart.

1.4. Theoretical and practical importance

Physical and technological developments of this work in cardiac magnetic resonance imaging and spectroscopy played key role in non-invasive assessment of myocardial structure, function, energy metabolism and visualization of transplanted cells in the hearts of small and large laboratory animals. Novel data on the infarcted heart regeneration after human cardiomyocyte transplantation could not be obtained without the background work on developments of non-invasive cardiac MRI methods applicable for studies on large and small laboratory animals. Fundamental and practical knowledge obtained during the performance of this work will be used for future translational studies of human cardiomyocyte transplantation to patients that are planned for the nearest years, therefore, this work in timely and important. Developed methods of quantitative evaluation of myocardial perfusion and metabolism enable longitudinal non-invasive studies of heart on animals and potentially on humans. New method of post-contrast MRI processing, 3D-TRIPS, allows scan time shortening and obtaining high-contrast images of myocardial scar. This method has a potential to become a primary MRI technique for visualization of the infarct zone. Genetic modification of the cells for over-expression of the natural endogenous protein ferritin enables *in vivo* visualization of transgenic cells, evaluation of graft size and viability.

1.5. Methodology

Methods of non-invasive studies of the heart included echocardiography (GE Vivid 7, 10S, 10 MHz), magnetic resonance imaging (3 Tesla (3T) Achieva Philips clinical scanner; 4,7T Varian and 14T Bruker BioSpec spectrometers), multinuclear magnetic resonance spectroscopy (4,7T Bruker BioSpec spectrometer), catheter-based electrophysiology (CARTO III mapping system), and EKG-telemetry (Vmed Vetcheck Technology).

Different human and animal cell lines were used in this work, such as mouse skeletal myoblasts (C2C12), human embryonic stem cell (hESC) lines H7 and RUES2, canine bone marrow fibroblasts (DS-1). For cell nucleofection were used commercially available reagents such as Lanza Human Stem Cell Nucleofector kit 1 and FuGENE6. Methods of molecular biology and cloning were used for creation of expression vectors. The following laboratory animals were used for modeling myocardial infarction and cell transplantation: mouse lines C57B1 and C3H, immunodeficient Sprague Dawley rats (*rh rnu-rnu)*, mongrel dogs and dogs with the symptoms of the Duchenne muscular dystrophy (DMD), and non-human primates *Macaca nemestrina.* Methods of fluorescent and light microscopy, histology and immunohistochemistry were used to study cells and tissues.

MRI data analysis was conducted using the standard software Philips IntelliSpace Portal (software version v7.0.1.20482, Philips, Best, Netherlands), and free software ImageJ 1.34u (National Institute of Health, Bethesda, MD, USA). For automatic extraction of the myocardial perfusion parameters from the dynamic contrast enhanced MRI the discrete kinetic model was implemented into a custom quantitative perfusion analysis package programmed in Matlab (The Mathworks, Natick, MA, USA). Reconstruction of the 3D inversion-recovery late gadolinium enhanced MR images was done with the custom-written algorithm 3D-TRIPS implemented at the software Matlab (The Mathworks, Natick, MA, USA).

Statistical data analysis was done using the software packages Office Excel (Microsoft Inc, Redmond, WA, USA) and SPSS 12.0 (SPSS Inc, Chicago, IL, USA). Student's T-test (two-sample assuming unequal variances) and ANOVA were used for comparison of groups at any single time point. For analysis of time course changes in cardiac contractility a paired T-test analysis of means was used. All data were analyzed in a blinded manner, with the breaking of the identifier code only after the data were acquired. Values are expressed as means ± standard deviation (SD) of the mean, unless otherwise stated. The differences were considered statistically significant with the threshold for significance level set at $p < 0.05$.

1.6. Thesis submitted for defense

1. Magnetic resonance imaging (MRI) methods developed at this work allows quantitative evaluation of the heart contractile function and regeneration after myocardial infarction and transplantation of human embryonic stem cell-derived cardiomyocytes (hESC-CM).

2. Spatially localized phosphorus magnetic resonance spectroscopy (^{31}P MRS) enables non-invasive evaluation of the energy metabolism changes in mouse heart after myocardial infarction and pharmacological correction.

3. Developed method of modeling kinetics of the contrast agent dynamics enables automatic extraction of the myocardial perfusion parameters *in vivo* in different models of heart injury.

4. New image reconstruction method 3D-TRIPS over-performs the standard method for infarct visualization in image quality and scan time.

5. Genetic modification of cells leaded to overexpression of the endogenous iron storage protein ferritin enables detection of cardiac grafts with MRI and assessment of graft size *in vivo.*

6. MRI gene reporter ferritin is better suitable for longitudinal imaging of live transplanted cells, while MRI signal from the superparamagnetic iron nanoparticles do not reflect the graft viability.

1.7. Reliability and robustness of results

To ensure robust and unbiased results all MRI acquisitions (data collection), image and histology analysis were performed in a blinded manner where animal numbers did not reflect time point or study group name. Scan-rescan reproducibility has been assessed in the same animals within 2-3 days interval. Multiple independent measurements of the region of interest (ROI) in adjacent slices were used to assess quantitative values on MRI maps as well as in histological slices. To consider biological variables animals both sexes were used. Variability in the infarct and graft sizes is natural; therefore, each animal was scanned in multiple time points serving its own control. Assignment to treatment groups (control animals, cell-treated) was randomized with multiple treatments per cage where possible to eliminate cage effects. All antibodies used for immunohistochemical staining are commercially available and have been used extensively by us and others previously.

1.8. Approbation of the dissertation work

Approbation of this doctorate work was taking place at the Lomonosov Moscow State University Department of Physics on May 25, 2018. Main results were presented at the 28 International scientific conferences and 17 international invitational lectures as listed below.

Presentations at the scientific conferences:

1. **Naumova AV**, Chacko VP, Weiss RG. MRS/MRI Assessment Of In Vivo Murine Cardiac High-Energy Phosphates During Dobutamine Stress. ISMRM Eleventh Scientific Meetings & Exhibition. Program number 1548. Toronto, ON, Canada. July 10-16, 2003.

2. **Naumova AV**, Chacko VP, Ouwerkerk R, Stull L, Marbán E, Weiss R.G. Xanthine Oxidase Inhibitors Improve Energetics and Function In The Post-Infarction Remodeled Mouse Heart. ISMRM 13th Scientific Meeting and Exhibition. Session: Global and Regional Cardiac Function. Program number 281. Miami Beach, Florida. May 7-13, 2005.

3. **Naumova A**, Yarnykh V, Wilson G, Yuan C. Rodent Cardiac MRI on 3T clinical scanner: comparison with 4.7T. ISMRM-ESMRM Joint Annual Scientific Meeting and Exhibition. Session: Cardiac Perfusion & Mouse Cardiac Imaging. Program number 3634. Berlin, Germany. May 19-25, 2007.

4. **Naumova A**, Chen K, Laflamme M, Muskheli V, Gold J, Hassanipour M, Yuan C, Murry C. 1H MRI assessment of cardiac function following transplantation of human embryonic stem cell-derived cardiomyocytes for cardiac repair. ISMRM-ESMRM Joint Annual Scientific Meeting and Exhibition Session: Cardiac Function Imaging in Animal Models. Program number 701. Berlin, Germany. May 19-25, 2007.

5. **Naumova A**, Reinecke H, Yuan C, Murry C. Molecular MRI of Stem Cell Based Cardiac Repair. Conference on Cardiovascular Cell and Gene Therapy IV. New York, NY, USA. April 11-13, 2008.

6. **Naumova A**, Fernandes S, Yarnykh V, Muskheli V, Yuan C, Murry C. Functional Effects of Human Embryonic Stem Cell-Derived Cardiomyocyte Transplantation on Chronic Myocardial Infarction in Rats. ISMRM 16th Scientific Meeting and Exhibition. Session: Animal Cardiac Imaging. Program number 1027. Toronto, Canada. May 3-9, 2008.

7. **Naumova A**, Reinecke H, Yarnykh V, Yuan C, Murry CE. Molecular MRI of Gene Reporter Ferritin for Stem Cell Based Cardiac Repair. 2008 World Molecular Imaging Congress (WMIC 2008). Program Number: 1382. Nice, France. September 10-13, 2008.

8. **Naumova A**, Reinecke H, Yarnykh V, Yuan C, Murry CE. Ferritin Overexpression for Molecular Imaging of Transplanted Cells. ISMRM 17th Scientific Meeting and Exhibition. Session: MR Tracking of Capsules & Cells. Program number 3072. Honolulu, HI. April 18-24, 2009.

9. **Naumova A**, Stevens K, Deem J, Reinecke H, Yarnykh V, Yuan C, Murry CE. Ferritin overexpression as a tool for detection of live cells transplanted into infarcted heart. ISMRM 17th Scientific Meeting and Exhibition Session: MR Probes II. Program number 5797. Honolulu, HI. April 18-24, 2009.

7. Fernandes S, **Naumova AV**, Dupras SK, Muskheli V, Fugate JA, Gold J, Murry CE. Human Embryonic stem cell-derived cardiomyocytes do not alter cardiac remodeling in a rat model of chronic myocardial infarction. NHLBI Symposium for Cardiovascular Regenerative Medicine. Bethesda, MD. October 14-15, 2009.

8. **Naumova AV**, Yarnykh V, Reinecke H, Murry CE, Yuan C. In vivo MRI Signal Features of Transgenic Grafts Overexpressing Ferritin in the Murine Myocardial Infarction Model. ISMRM 19th Scientific Meeting and Exhibition. Montreal, Canada. May 7-13, 2011.

9. **Naumova AV**, Balu N, Yarnykh VL, Reinecke H, Murry CE, Yuan C. MRI Tracking of Graft Survival in the Infarcted Heart: Iron Oxide Particles vs. Ferritin Overexpression Approach. ISMRM Workshop. Miami Beach, FL. January 29 – February 1, 2012.

10. **Naumova AV**, Yarnykh VL, Balu N, Reinecke H, Murry CE, Yuan C. Improved Identification of Ferritin-Tagged Grafts in Mouse Heart at Higher Magnetic Field Strength. ISMRM 20th Scientific Meeting and Exhibition. Melbourne, Australia. May 5-11, 2012.

11. Nan X, **Naumova AV**, Wei J, Wan Q, Gao L, Liu X, Qiu B. In vivo Molecular MRI of GFP/Ferritin Dual Gene Expression. ISMRM 20th Scientific Meeting and Exhibition. Melbourne, Australia. May 5-11, 2012.

12. Balu N, Wang J, **Naumova A**, LeBoeuf RC., Yuan C. MRI quantification of changes in fat distribution due to feeding a high fat diet in C57BL/6 mice. ISMRM 20th Scientific Meeting and Exhibition. Melbourne, Australia. May 5-11, 2012.

13. **Naumova AV**, Margineantu DH, Kreutziger KL, Palpant NJ, Fugate J, Murry CE. Metabolic Changes of Human Embryonic Stem Cells During Cardiomyocyte Differentiation. ISMRM 20th Scientific Meeting and Exhibition. Melbourne, Australia. May 5-11, 2012.

14. **Naumova AV**, Palpant NJ, Balu N, Shen X, Yuan C, Murry CE. MRI Tracking of Transplanted Cell Viability and Function Using a Multimodal Quadruple Fusion Gene

Reporter. ISMRM-ESMRMB Joined Annual Scientific Meeting and Exhibition. Milan, Italy. May 10-16, 2014.

15. **Naumova AV**. State-of-the-art MRI methods for transplanted cell tracking. First International Conference Translational Magnetic Resonance Imaging and Young Scientist School, Tomsk State University, Russia. December 5-7, 2014.

16. **Naumova AV**. Cardiac magnetic resonance imaging and spectroscopy in preclinical studies. First International Conference Translational Magnetic Resonance Imaging and Young Scientist School. Tomsk State University, Russia. December 5-7, 2014.

17. **Naumova AV**. Magnetic Resonance Imaging of the Labeled Cells in Central Neural System. 11th International Multidisciplinary Congress Neuroscience for Medicine and Psychology. Sudak, Russia. June 6-12, 2015.

18. **Naumova AV**, Palpant NJ, Yarnykh V, Murry CE. Multimodality Imaging for Characterization of Transplanted Cell Survival and Function. 6th NHLBI Symposium on Cardiovascular Regenerative Medicine. National Institutes of Health, Bethesda, MD. September 29−30, 2015.

19. **Naumova AV.** Magnetic Resonance Imaging of Brain Regeneration. 2nd International Conference and Young Scientist School "Magnetic Resonance Imaging in Biomedical Research". Tomsk, Russia. September 7-9, 2015.

20. **Naumova AV**, Liu YW, Kerwin W S, Murry CE. Changes in myocardial perfusion and contractility after human cardiomyocyte transplantation in non-human primates. International scientific conference "New technologies for restoration of cardiac function in experiment and in clinic" devoted to 150th anniversary of A.A. Kulyabko. Tomsk State University, Tomsk, Russia. April 21-22, 2016.

21. **Naumova AV**, Wilson GJ, Maki JH, Tuck SA, Chen B, Thies RS, Liu Y-W, Murry CE. Magnetic Resonance Imaging of Primate Heart Regeneration after Stem Cell Transplantation. International Congress for Clinical and Translational Neurovisualization. Novosibirsk State University, Russia. November 24-26, 2016.

22. **Naumova AV.** Non-invasive Imaging of Transplanted Cell Fate and Function. University of Washington Symposium "International Collaborations in Imaging: Vascular & Beyond". Seattle, WA, USA. May 1st, 2017.

23. **Naumova AV**, Wilson GJ, Maki JH, Tuck SA, Chen B, Thies RS, Liu Y-W, Murry CE. Assessment of Myocardial Contractility, Perfusion and Infarct Size in a Preclinical Heart Failure Model: Non-human Primates. ISMRM Workshop on Magnetic Resonance Imaging of Cardiac Function. New York, NY. August 17-20, 2017.

24. **Naumova AV**, Liu Y-W, Chen B, Wilson GJ, Maki JH, Tuck SA, Thies RS, Murry CE. Magnetic Resonance Imaging of Heart Failure and Regeneration in Non-Human Primates. 7th NHLBI Cardiovascular Regenerative Medicine Symposium. Bethesda, MD. September 27−28, 2017.

25. **Naumova AV,** Liu Y-W, Chen B, Yang X, Kerwin WS, Wilson JG, Maki JH, Tuck SA, Thies RS, Murry CE. Magnetic Resonance Imaging (MRI) of myocardial infarction and heart regeneration in non-human primates after human cardiomyocyte transplantation. 4th International Conference "Magnetic Resonance Imaging in Biomedical Research" with elements of the youth scientific school. National Research Tomsk State University, Tomsk, Russia. October 27-29, 2017.

26. **Naumova AV**, Vande Velde G. Genetically encoded iron-associated proteins as MRI reporters for molecular and cellular imaging. International Scientific-Practical Conference "Molecules and Systems for Diagnosis and Targeted Therapy (MSDT2017)". Siberian State Medical University, Tomsk, Russia. November 1–3, 2017.

27. **Naumova AV**. Non-invasive visualization of the primate's heart regeneration with human cardiomyocyte transplantation. XVI Russian school-seminar «Waves-2018». Lomonosov Moscow State University, Moscow, Russia. May 27 - June 1, 2018.

28. **Naumova AV**, Balu N, Wilson G, Liu H, Tsuchida H, Thies R, Murry CE, Yuan C. Fast imaging of primate myocardial infarction with novel phase sensitive late gadolinium enhancement MRI. World Molecular Imaging Congress. Seattle, Washington, USA. September 12-15, 2018.

International invitational lectures:

1. Invited presentation for the educational session at the ISMRM-ESMRMB Joint Annual Meeting. Lecture title: "Preclinical Models for Cardiovascular Structure and Function: Applications". Berlin, Germany. May 19, 2007.

2. Invited presentation at the Cardiovascular Breakfast Club. Presentation title: Magnetic Resonance Imaging of Gene Expression. University of Washington, Seattle, WA, USA. June 24, 2008.

3. Invited presentation at the South Lake Union 14T MRI Mini-Symposium. Presentation title: “In vivo Cardiac MRI and Spatially Localized 31P Spectroscopy”. University of Washington, Seattle, WA, USA. December 16, 2010.

4. Invited presentation at the University of Washington Radiology Imaging Science Research Series. Lecture title: Ferritin Overexpression for Molecular Imaging of Transplanted Cells. March 2, 2010.

5. Invited lecture “Molecular Basis of Disease: Atherosclerosis and Myocardial Infarction” for the shared course Path 515: Mechanisms of Cardiovascular Disease. University of Washington, Seattle, WA, USA. April 30, 2010 and June 1, 2012.

6. Invited presentation at the BioMolecular Imaging Center Symposium: “Ferritin Overexpression for Molecular Imaging of Transplanted Cells. University of Washington, Seattle, WA, WA, USA. June 22, 2012.

7. Invited presentation at the Institute for Stem Cell and Regenerative Medicine: “Novel Quadruple Fusion Reporter Gene for Multimodality Imaging of Transplanted Cells”. Seattle, WA, USA. November 12, 2013.

8. Invited presentation at the Radiology Imaging Sciences Research Series: “Novel Quadruple Fusion Reporter Gene for Multimodality Imaging of Transplanted Cells”. University of Washington, Seattle, WA, USA. September 3, 2013.

9. Invited lecture “Cardiovascular Magnetic Resonance Imaging” for the shared course Path 515: Mechanisms of Cardiovascular Disease. University of Washington, Seattle, WA, USA. May 20, 2014.

10. Invited presentation at the Department of Human and Animal Physiology, Tomsk State University, Russia. Lecture title: Heart regeneration with stem cells. December 23, 2014.

11. Invited presentation at the Vasculata Workshop, University of Washington: “Cardiac MRI and Stem Cell Tracking. Seattle, WA, USA. July 15, 2014.

12. Invited presentation at the Center for Biomedical Imaging Research Tsinghua University: “Magnetic Resonance Imaging of Heart Regeneration”. Beijing, China. June 23, 2016.

13. Invited presentation at the University of Science and Technology of China:

“Magnetic Resonance Imaging of the Stem Cells Transplantation”. Hefei, Anhui, China. June 20, 2016.

14. Invited presentation at the 25th International Multidisciplinary School “Waves-2016” Lomonosov Moscow State University: “State-of-the-arts MRI Methods for Visualization of Transplanted Cells”. Moscow, Russia. June 9, 2016.

15. Invited presentation at the Department of Human and Animal Physiology Tomsk State University: “Primate Heart Regeneration after Stem Cell Transplantation”. Tomsk, Russia. December 1, 2016.

16. Invited presentation at the Skolkovo Institute of Science and Technology: “Magnetic Resonance Imaging of Myocardial Infarction and Heart Regeneration in Non-Human Primates after human cardiomyocyte transplantation”. Moscow, Russia. November 8, 2017.

17. Invited presentation at the University of Leuven, Belgium: “Changes of the primate’s heart contractility, perfusion and infarct size after human cardiomyocyte transplantation”. Department of Imaging and Pathology, Biomedical MR Unit/MoSAIC, KU Leuven, Belgium. June 27, 2018.

1.9. Author’s input

The author of the current dissertation was personally involved into all studies presented at this work. The author has established an infrastructure at the University of Washington (Seattle, WA, USA) enabling non-invasive studies of the heart on small and large laboratory animals using magnetic resonance imaging and spectroscopy, visualization of transplanted cells and myocardium regeneration. These types of studies have not been conducted at the University of Washington previously. Majority of results presented at this work were obtained by the author herself or with her direct involvement and leadership. Author of the current work is one of the main collaborators of the Dr. Charles E. Murry (University of Washington, Seattle, WA, USA) in the heart regeneration studies using human cardiomyocyte transplantation. Author thanks Drs. Vasily L. Yarnykh and William S. Kerwin (University of Washington, Seattle, WA, USA) for their help in development of the MRI pulse sequences. Name of co-authors are shown in the related publications.

2. LITERATURE OVERVIEW

Literature overview presents the critical analysis of the published data on visualization methods in biomedical research, advanced magnetic resonance imaging and spectroscopy methods for noninvasive assessment of cardiac structure, function and energy metabolism, the importance of using animal models to study human heart disease and technological challenges in non-invasive studies on animals. The information about the unique structure and metabolism of the heart, the main types of stem cells used in cardiac regeneration studies and methods of the transplanted cell labeling for *in vivo* visualization are also discussed.

2.1. Role of biomedical imaging in regenerative medicine

Imaging is used routinely in pre-clinical research and clinical practice both to provide secondary endpoints that complement primary health outcomes and to investigate the mechanisms of therapeutic successes and failures. The main biomedical imaging modalities in use today are magnetic resonance imaging (MRI), computerized tomography (CT), positron emission tomography (PET), single photon emission tomography (SPECT), ultrasound (US) and multimodality imaging that combines techniques (PET/CT, SPECT/CT and MRI/PET) to provide co-registration of images and extract morphological and functional information from the patient (**Box 1**). These technologies have improved considerably in recent years and now provide sophisticated multimodality imaging and computational data processing, shorter acquisition times and lower radiation doses. The latest generation of scanners offers new opportunities in regenerative medicine for assessing the tissue composition of various organs, detecting transplanted cells and evaluating changes in micro- and macro-environments and tissue function. They are beginning to be applied to non-invasively assess the survival, migration, biodistribution, and differentiation of transplanted cells and the underlying mechanisms of stem cell biology [23]. However, human imaging is inherently more constrained than animal studies due to limits on radiation and, more importantly, limits on the use of genetically modified cells for long term reporting. These limitations translate into reduced sensitivity, specificity and temporal resolution.

Box 1. Overview of the imaging modalities.

Magnetic resonance imaging (MRI) uses magnets (from 0.5 up to 7T clinical magnetic field strength and up to 21T in animal research) to polarize the hydrogen nuclei in water molecules in human tissues. MRI scanner use pulse sequences that transmits a radio frequency (RF) pulse to excite hydrogen nuclei

and time-varying gradient magnetic fields, for spatial encoding thus providing the spatial distribution of signals emitted from excited proton that can be processed and displayed as high-resolution multidimensional images with image contrast depending on pulse sequences that are used to produce the images. MRI does not use ionizing radiation and can be performed serially over time. MRI is the most versatile with improved sensitivity to morphology, pathology and function from the body.

X-ray computed tomography (CT) uses computer processed X-rays to produce tomographic images. The disadvantage of CT technology is presence of ionizing radiation in the form of X-rays that directly or indirectly damage DNA. There are two new approaches under development rely on more exotic forms of radiation: proton beams and synchrotron radiation. Proton CT records the position, direction and energy loss from a proton beam as it traverses a patient's body. Proton CT provides a more detailed image of the body's density, because protons release their energy at predictable depths in the body, allowing reduction in radiation exposure. CT images based on synchrotron X-rays are produced when charged particles are accelerated around a curved path and have much higher photon energies than conventionally generated X-rays.

Positron emission tomography (PET) is a nuclear medical imaging technique that produces multidimensional image of functional processes in the body. A biologically active positron-emitting radio-tracer such as ^{18}Fluorine attached to a small molecule has to be introduced to the body (injected into the blood circulation), included into the metabolic processes and detected by PET. Images of tracer concentration within the body that are undergo computer analysis. Short life-time of radioligands requires fast image acquisition at the same day of tracer synthesis. Sensitivity of PET for detection of radio-labeled probes is very high and there is no limitation in tissue penetration depth, therefore PET is used for tracking cells that have reporter genes inserted into the cell genome. PET scans are usually co-registered with MRI or CT images.

Single Photon Emission Tomography (SPECT) is a nuclear medicine tomographic imaging technique using gamma rays to detect radioactive probes (radioisotopes), such as Technetium-99m (^{99m}Tc) and Indium-111 (^{111}In) injected into the bloodstream. Sensitivity of SPECT for detection of radio-labeled probes is very high; there is no limitation in tissue penetration depth, there is only one FDA approved SPECT agent (^{111}In oxine) that is used for cell tracking in clinic. SPECT can report whole body biodistribution of the injected radiolabeled cells but does not provide high-resolution anatomical information that would allow a precise delineation of cellular location. Main limitation of this method is decay in signal radioactivity, therefore injected labels cannot be tracked longitudinally over weeks, the signal will diminish over time as cells divide and the radio-labeled components get metabolized. Ionizing radiation can cause DNA damage, therefore radioactive dosage should be monitored closely and repetitive studies on the same patients are not routinely performed.

Ultrasound (US) is an oscillating sound pressure wave with a frequency greater than the upper limit of the human hearing range. Sonograms (US images) are made by sending a pulse of ultrasound into tissue using an US transducer (probe). The sound reflects and echoes off parts of the tissue; this echo is recorded and displayed as an image. Compared to other medical imaging methods, ultrasonography has several advantages. It provides images in real-time (no processing delay after an acquisition), it is portable and can be brought to a sick patient's bedside, it is substantially lower in cost, and it does not use harmful ionizing radiation. Ultrasound is widely used in clinic and research for evaluation organ's structure, function and blood flow. Sufficient image resolution for cell tracking by US requires high frequencies; however, depth penetration of high frequency US waves is limited, therefore tracking of transplanted cells by US is not a widely used method in research and in clinical studies.

Multimodality imaging became widely used in recent years for co-registration of images obtained from different scanners. Advantage is a combination of highly sensitive/quantitative but low-resolution methods, such as PET and SPECT, with high resolution anatomical images acquired with MRI or CT scanners. Examples of multimodality scanners: MRI/PET, PET/CT, SPECT/CT. Examples include registration of brain CT/MRI images or whole body PET/CT images for tumor localization, registration of contrast-enhanced CT images against non-contrast-enhanced CT images for segmentation of specific parts of the anatomy, and registration of ultrasound and CT images for prostate localization in radiotherapy.

Magnetic resonance imaging is a macroscopic technology and has limitations when applied to the detection of transplanted cells. The detection depends on the concentration of the labeling agent in the cells, the number of injected cells per voxel, the signal-to-noise ratio of the detection method and the scanner technology. Uptake or expression of labels and their retention over time varies for different cell types and labels. Imaging contrast can be lost or diluted with cell division. Transplanted labeled cells, or free label released by dying cells, can be engulfed by macrophages—a process that can begin as soon as minutes to hours after transplantation and continue for months depending on the lifespan of the transplanted cells within host —confounding interpretation of the imaging signal. Single cell imaging has been reported in high field MRI scanners, for example, single hepatocytes in mouse liver at the 7T MRI scanner [24] and in rodent's embryos at 11.7T magnet [25]. Labeling with two contrast agents—superparamagnetic iron oxide (SPIO) nanoparticles and indium ^{111}In-oxine—and imaging with a clinical 3T MRI and SPECT scanner allowed detection of ~2000 dendritic cells injected into a lymph node [26]. The sensitivity of MRI to SPIO-labeled cells can be increased

in several ways. Quantitative mapping of T_2 decay can improve the calculated detection limit to ~600 labeled cells/voxel using a 3T clinical scanner [27]. Higher intracellular iron content, up to ~2+/-1pg iron/cell, allowed for the detection of ~2-5 $x10^3$ labeled cells could be detected in the brain using a clinical 3T MRI scanner [28, 29]. Techniques with low background noise, such as perfluorocarbon nanoparticles, have enabled detection of ~6,000-10,000 cells using an experimental 11.7T scanner and of ~10^5 cells at the clinical 1.5T magnetic field strength [30]. However, perfluorcarbon labeling is less sensitive than proton imaging [31] and requires specialized equipment that is not available on all commercial scanners.

2.2. Unique structure and metabolism of the heart

Heart is one of the most fascinating and complicated organs in the human body; it starts beating at three weeks old embryo and keeps working during all our life. The unique myocardial structure and metabolism enable its efficient function. The microstructure of the heart was histologically described more than 40 years ago in landmark studies by Streeter [32]. The architecture of a healthy heart is made up of three layers of crossing spiral myofibers. The subendocardium fiber orientation is a right-handed helix, while the subepicardium is a left-handed helix, and fibers in the mid-myocardium are circumferential [32]. This structure allows for maximal contractile force to ensure effective blood pumping. Many cardiomyocytes exhibit binucleation and, in some instances, extensive polyploidy [33]. At birth, few cardiomyocytes are binucleated, but within 2 weeks after birth, number of binucleated cardiomyocytes reach the adult level (~75% in rodents) [34]. Young cardiomyocytes have high proliferative capability, however, only 11 cardiomyocytes out of 1 million are still proliferate in the adult human heart [35]. The shape of the cardiomyocytes also has important functional implications including excitation-contraction coupling. Adult cardiomyocytes have organized sarcomeric structure to facilitate force-generating process [36, 37] that includes sarcomeric proteins such as cardiac troponin T, cardiac troponin I, alpha actinin and beta-myosin heavy chain [38, 39]. It is well-known that in the rodents there is a switch from beta-myosin heavy chain (MHC) before birth to alpha-MHC after birth, which correlates with a postnatal heart rate increase. In the adult human heart, there is more beta-MHC than alpha-MHC, while in the fetal human heart, there is more alpha- than beta-MHC [40]. The prevalence of beta-MHC in human adult hearts correlates with a decrease in heart rate.

T-tubules are the membrane invaginations along the Z-line regions, with regular spacing (~2 μm) along the longitudinal axis of adult mammalian ventricular myocytes. T-tubules make

possible for an adult cardiomyocyte to have rapid electric excitation, initiation, and synchronous triggering of sarcoplasmic reticulum calcium release and coordinated contraction. Alterations in T-tubule composition and structure have been associated with various cardiac pathologies [41]. Cardiomyocytes have a unique capability for autonomous generation of the action potential, with several ionic channels involved into the process. Electro-mechanically coupling of cardiomyocytes enables synchronous contraction. The adult human left ventricle myocardium has a conduction velocity of 0.3-1.0 meters/sec. The gap junction protein connexin-43 and the adherens junction protein N-cadherin are concentrated into intercalated disks at the ends of the cells and accelerate conduction velocity [42].

Myocardial energy demand and energy production are the highest per gram of any organ in the body and this fuels mechanical function [43]. During increased contractile demand, such as during exercise or adrenergic stimulation, myocardial metabolic rates increase to supply the energetic needs [44]. The prime myocardial high energy phosphates are ATP and phosphocreatine (PCr); these are reversibly converted by the creatine kinase (CK) reaction [45]. Mitochondria occupy ~20-40% of the adult myocyte volume and are distributed throughout the cell in a crystal-like lattice pattern [46]. During cardiac development, corresponding with the structural changes from an immature to a mature state, the oxidative capacity of the mitochondria increases, as reflected in a metabolic substrate switch [47]. During early cardiac development, glycolysis is a major source (80%) of energy for proliferating cardiomyocytes. As cardiomyocytes mature and become terminally differentiated, mitochondrial oxidative capacity increases, with fatty acid β-oxidation (80%) becoming a major source of energy for the heart. Although high-energy phosphate levels can be determined by conventional biochemical techniques on digested tissue samples, ^{31}P magnetic resonance spectroscopy (MRS) is the only non-invasive means for quantifying high-energy phosphates in the beating heart [12, 48, 49].

2.3. Myocardial infarction and mechanisms of heart failure

Heart disease caused by the loss or dysfunction of cardiomyocytes is the leading cause of death worldwide [50, 51]. The neonatal mammalian heart can regenerate following injury [52]. During neonatal life, there is a transition from hyperplastic (typical for fetal heart) to hypertrophic growth of cardiomyocytes; thus, further increases in myocardial mass are achieved principally by increases in cardiomyocyte size [34]. The regeneration capacity of adult hearts is limited. A genetic lineage tracing in the adult heart showed that progenitor cells

do not contribute new cardiomyocytes during normal aging, but after myocardial infarction or aortic banding, approximately 5% of the cardiomyocytes in the heart appear to have been progenitor-derived. The integration of ^{14}C, generated by nuclear bomb tests during the Cold War, into DNA was used at the unique study to establish the age of cardiomyocytes in humans [53]. It was shown that cardiomyocytes renew, with a gradual decrease from 1% turning over annually at the age of 20 to 0.3% at the age of 75, therefore less than 50% of cardiomyocytes are exchanged during a normal lifespan [53]. The low rate of cardiomyocyte regeneration in the adult human heart suggests that the development of therapeutic strategies aiming to stimulate regeneration process might be important in cardiac pathologies.

Myocardial infarction (MI) is usually caused by the blockage of an artery in the coronary circulation. Obstructions of coronary arteries lead to regional undersupply of oxygen and nutrients (ischemia). Any injury associated with large-scale loss of myocardium, such as by infarction, causes myocardial replacement by collagen-rich scar, which does not contract [54]. The common clinical scenario of the heart failure is characterized by a loss of roughly one billion cardiomyocytes after acute myocardial infarction (MI), leading to a rapid initial functional loss followed by a slower decline as the ventricle undergoes adverse structural remodeling [33]. The term “remodeling” was used for the first time in 1982 to characterize the replacement of infarcted tissue with scar tissue [55]. Multiple factors contribute to the development and progression of cardiac remodeling and LV dysfunction. The early phase of myocardial remodeling involves migration of macrophages, monocytes, and neutrophils to the infarct zone initiating a local inflammatory response. Inflammation is sustained through the upregulation of cytokine release, leading to fibroblast proliferation and metalloproteinases activation [56, 57]. Furthermore, oxidative stress and alteration in energy metabolism trigger the hypertrophic and profibrotic signaling cascades, resulting global remodeling, dilation, hypertrophy, contractile dysfunction, impaired energy metabolism, cardiomyocyte loss and scar formation [58, 59]. This remodeling process aims to normalize the wall stress and to preserve cardiac output. Depending on the initial size of the infarcted area, the replacement of cardiomyocytes by non-contracting collagen scar tissue can lead to progressive dilation which often ends with heart failure and death [60].

Myocardial remodeling and impaired energy metabolism lead to heart failure. The term “heart failure” usually refers to the inability of the heart to maintain the blood flow necessary to satisfy the metabolic requirements of the body [61]. Dysregulation of excitation-contraction

coupling is a common feature of several pathophysiological cellular alterations in cardiac remodeling. In a failing cardiomyocyte, there is impaired calcium uptake [58]. Calcium dysregulation causes systolic dysfunction, arrhythmias and can interfere with hypertrophic growth, energy metabolism, mitochondrial function, and cell survival [62]. These alterations change heart geometry from an elliptical to a spherical shape, which in turn contributes to impair the contractile function of the heart. Furthermore, cardiac remodeling is characterized by increased left ventricular (LV) mass with a reduction in LV ejection fraction [63, 64]. Cardiac hypertrophy is a compensatory adaptive response to mechanical and physiological stress impairing cardiac output. However, chronic hypertrophy is also associated with interstitial fibrosis and cellular apoptosis. A precise balance of muscle growth, inflammation, and angiogenesis is necessary to ensure adaptive hypertrophic remodeling; alterations to this equilibrium result in deterioration of cardiac structure and function. During maladaptive cardiac remodeling cardiomyocyte force production gradually decreases leading to contractile dysfunction, ventricular dilation, and arrhythmias [65]. Schematic overview of the main events that contribute to cardiac remodeling and leading to heart failure are shown in the Figure 1.

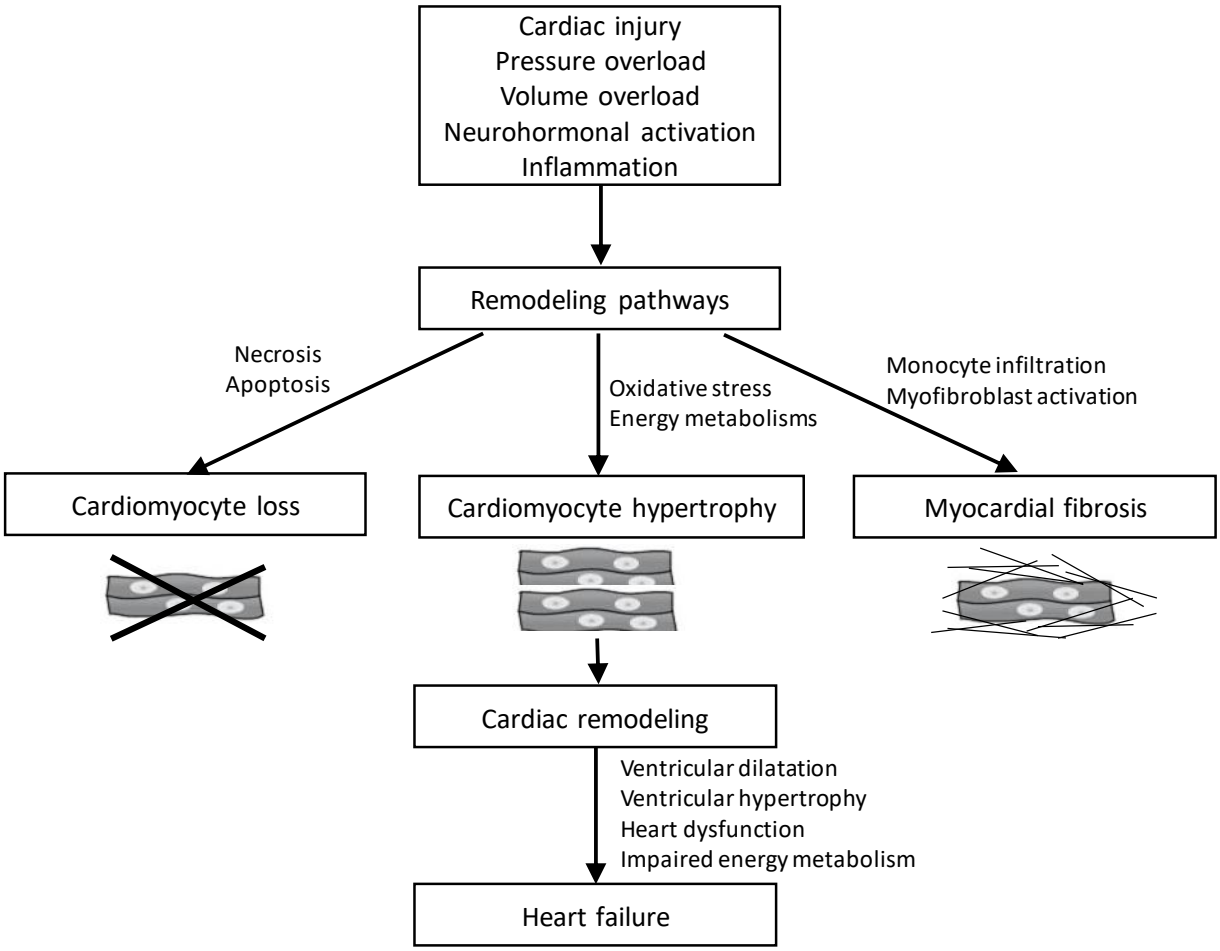

Figure 1. Schematic overview of the main events that contribute to cardiac remodeling.

2.4. Cardiac magnetic resonance imaging

Magnetic resonance imaging (MRI) is a preferred imaging modality to study cardiovascular anatomy, myocardial function, viability, and perfusion. Important advances in cardiac MRI in recent years are the introduction of prospective and retrospective ECG-triggered scanning using the vector cardiogram (VCG), the development of respiratory navigators for free-breathing scanning, the use of surface receiver coils to improve signal-to-noise ratio and/or allow parallel imaging (SENSitivity Encoding - SENSE), the introduction of stronger gradient systems allowing fast scanning protocols, and the incorporation of inhomogeneity correction into the scanning process (Constant LEvel AppeaRance - CLEAR). MRI is now able to image morphology, contractile function (left ventricle wall motion), perfusion, viability and the vasculature around the heart, as well as to quantify blood flow. For these reasons, MRI is often considered as the comprehensive imaging modality, capable of acquiring most of the required information during a single scanning session of less than one hour. MRI is an extremely flexible technique and has a large number of user-defined examination parameters which, for example, allow the image contrast to be adapted to specific needs. This ability to fine-tune acquisitions typically results in a different type of scan for each specific imaging question. A typical characteristic of all MRI scans is that the scan time depends on the spatial and temporal resolution, as well as on the volume coverage; the higher the spatial and/or temporal resolution, and the larger the volume coverage (field of view or volume thickness), the longer the scan time will be.

2.4.1. Heart function assessment

The main goal of functional analysis is the visualization and quantification of the contractile function of the heart at various stress levels. Global parameters for left ventricular functioning are the stroke volume (volume of the ejected blood per heart beat), the ejection fraction (percentage of the left ventricular blood volume ejected per heart beat) and cardiac output (volume of blood pumped out of the heart per unit of time). More local information about ventricular functioning can be obtained by quantifying the local wall motion, thickness and thickening. A decrease in wall motion with increasing stress may be an indication of ischemia, whereas a total absence of motion at all stress levels may indicate infarction. Several MRI techniques can be used to image heart in different phases of cardiac cycle. Cardiac MR imaging has evolved over the years through traditional spin-echo sequences [67, 68] to breath-hold fast gradient-echo sequences with FLASH (fast low angle shot) imaging [69-71]. Several

technical advances have occurred during this time. Prospective or retrospective cardiac gating [68, 72] offset the effects of cardiac motion, which permits multiphase MR imaging of cardiac contraction. With k-space segmentation [73, 74], spatial resolution is traded for temporal resolution, and high-spatial resolution CINE MR imaging is allowed in a single breath hold. ECG-gated single-phase spin-echo and multi-phase (CINE) gradient echo pulse sequences been shown to be very accurate for quantifying left ventricle (LV) contractile function and mass. Cine MRI is often performed using a bright-blood multi-phase spoiled gradient echo technique [75]. With improved gradient performance, the TR and acquisition time can be reduced substantially. With short TR, however, inflow enhancement and blood-myocardial contrast might be compromised.

The differences in the relaxation rates between blood and myocardium can be exploited by recycling transverse magnetization. This goal can be achieved with the balanced Steady-State Free Precession (b-SSFP) technique [76, 77]. B-SSFP sequences are typically bright blood and usually are better known by their vendor-specific nomenclature: TrueFISP (Siemens), FIESTA (GE), or b-FFE (Philips). The steady-state signal is dependent on the T_2/T_1 ratio, which is relatively high for blood. SSFP-based bright-blood images of the beating heart are essential for displaying cardiac function and are part of nearly every cardiac MRI examination. The motion of the ventricular walls during systole and diastole can be assessed both qualitatively and quantitatively. Additional information about valve function is also possible. The pulse sequence diagram for the b-SSFP is shown in the figure 2.

CINE images can be obtained by repeatedly imaging the heart at a single slice location throughout the cardiac cycle. Between 16 and 32 cardiac phases are usually sampled and displayed in a movie loop. Data is acquired over multiple cardiac cycles using retrospective ECG-gating and breath-hold.

A black blood gradient echo imaging technique that can be used to create images with improved definition of the endocardial border across the entire heart cycle in mice was implemented as an alternative to SSFP (figure 3). Dark ("black") blood sequences are utilize Inversion recovery (IR) pre-pulses to null the signal from blood alone (double IR), or from both blood and fat (triple IR). The double inversion-recovery technique, black-blood cine imaging can provide more accurate measurements of LV mass and volumes throughout the entire cardiac cycle [79].

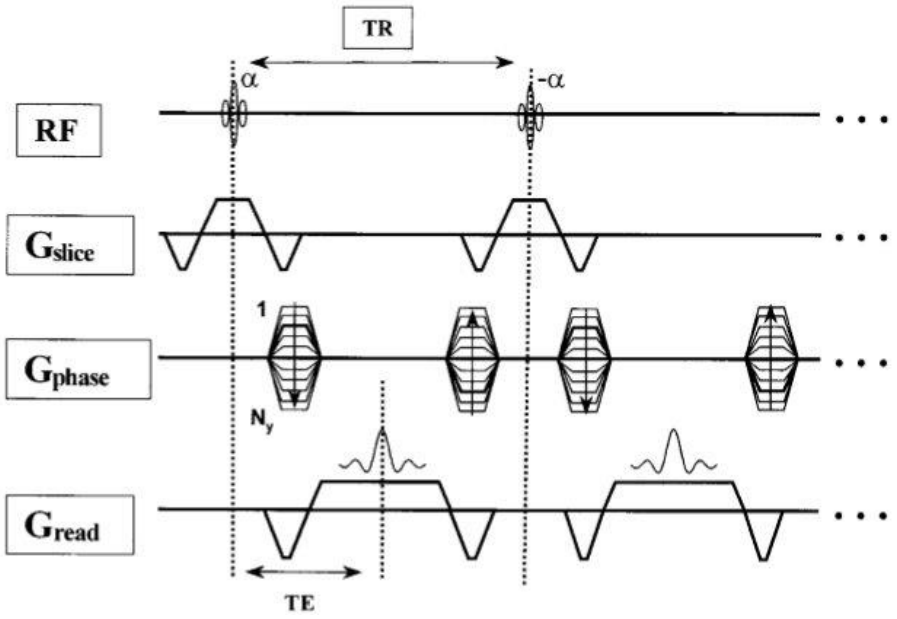

Figure 2. Timing diagram for the balanced Steady-State Free Precession (b-SSFP) pulse sequence. Transverse magnetization is maintained in the steady state from one TR to the next by rewinding the gradient (G) waveforms on all axes. The gradients are perfectly balanced, and the total gradient area is zero at each a radio-frequency (RF) pulse. A 180° phase alternation is applied to every α radio-frequency excitation pulse. N_y - number of phase-encoding steps, TE - echo time. Figure from [78].

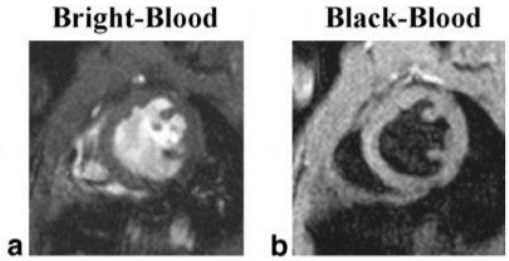

Figure 3. Bright-blood (a) and black blood (b) MR images from the same mid-ventricular slice in the same mouse in end-diastole. Due to the fast heart rate of mice, the double inversion recovery pulses can be applied approximately every 200 – 300 msec. Figure from [79].

To assess the heart anatomy and to measure the cardiac functional parameters imaging planes should be done carefully. The main planes of the heart are shown in the figure 4. The standard clinical planning of the cardiac MRI exam is shown in the Figure 5: 1) 4-chamber (horizontal long-axis) view, 2) left ventricular 2-chamber (vertical long-axis) view, 3) left ventricular 3-chamber view including the mitral valve inflow and left ventricular outflow tracts, 4) right ventricular 3-chamber (right anterior oblique) view including tricuspid valve inflow and right ventricular outflow, and 5) a stack of two-dimensional contiguous slices from the base to the apex in short-axis orientation of the heart which completely encompass both ventricles (Figure 6). Thus, analysis of myocardial mass and function by cine-MRI does not rely on geometric assumptions.

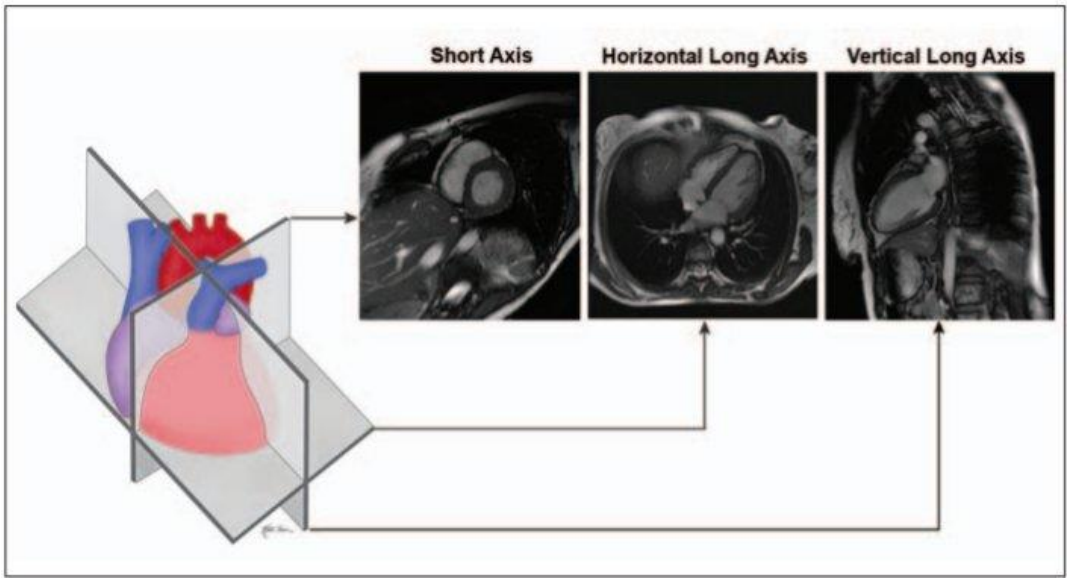

Figure 4. Scheme of the major cardiac planes orientation and their appearance on the bright blood sequences. Figure from [80].

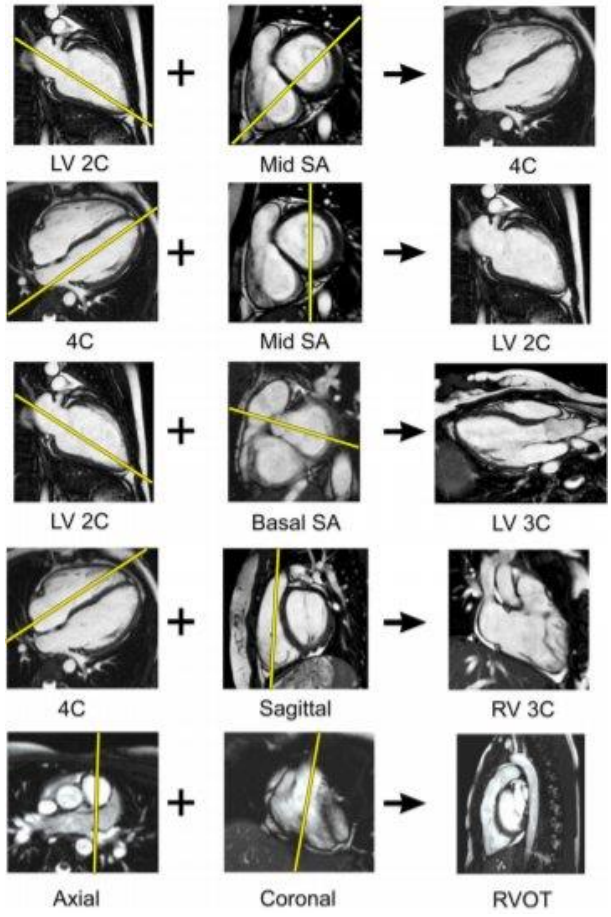

Figure 5. The diagram illustrates one approach to planning standard ventricular views (right column) based on adjusting the slice location on two other views (left and middle columns). Note that for the 4C, LV 2C, and LV 3C, the imaging plane is carefully positioned to pass through the apex of the LV and bisect the mitral valve plane. LV, left ventricle; RV, right ventricle; RVOT, right ventricular outflow tract; SA, short-axis; 2C, 2-chamber; 3C, 3-chamber; 4C, 4-chamber.

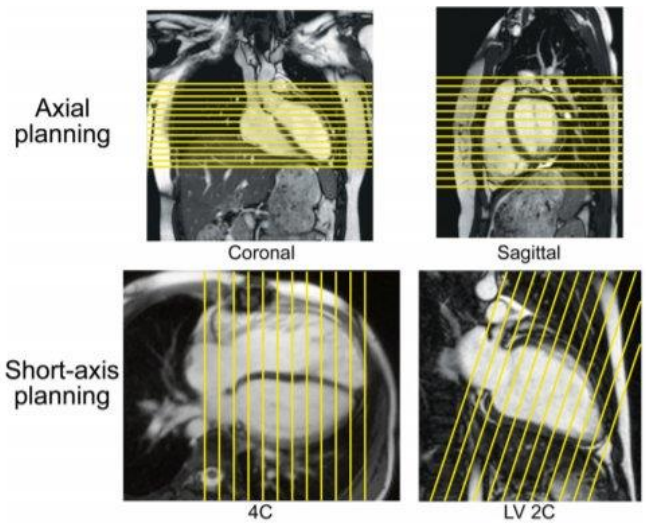

Figure 6. An axial stack of CINE images is planned by adjusting the slice locations on both coronal and sagittal images (top row). A short-axis stack of CINE images is planned by adjusting the slice locations on 4-chamber (4C) and left ventricular 2-chamber (LV 2C) images in diastole (bottom row). In this short-axis example, the slices are oriented perpendicular to the ventricular septum on the 4C view, and care is taken to ensure that coverage includes the anterior portion of the dilated right ventricle which extends above the tricuspid valve plane.

The main image-processing issue in functional analysis is the segmentation of the epicardial and endocardial boundaries of the myocardium of the left ventricle in each of the acquired images (Figure 7). These contours are required for the calculation of the global and regional contractile function parameters. Several software packages for cardiac MR analysis are commercially available for semi-automatic contour segmentation of short-axis images. The user has to draw an initial epicardial and endocardial contour on one of the images (i.e. one phase of a selected slice). These contours are then automatically propagated to all remaining slices and phases.

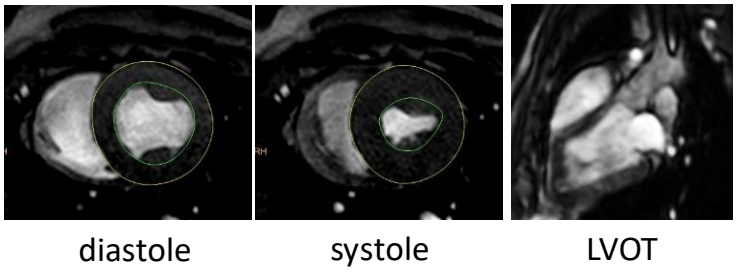

Figure 7. Short-axis functional MR images of the pig heart at end-diastole and end-systole with manually drawn endocardial and epicardial contours and the long axis image (left ventricle outflow tract, LVOT). Author's image of the pig heart (3T Philips scanner, Seattle, USA).

The iterative repositioning of the contours per image is driven by external forces (image features, such as bright-to-dark transitions) and internal features (restrictions on the shape of

the contours). This approach generally works well in areas with clear image features, e.g. clear transitions (edges) from the bright left ventricular blood pool to the darker myocardium, but manual correction is usually required for positioning the contours in areas where features are weak or lacking, such as on parts of the epicardial contour (e.g. adjacent to lungs) and in locations where the papillary muscles touch the endocardial contour. Other proposed segmentation approaches include matching with models which provide a statistical description of the local shape (geometry) and the appearance (brightness) [81], and the non-rigid registration of the myocardium in adjacent phases followed by contour propagation from phase to phase using the derived non-rigid transformation [82]. The standard measurements taken from the CINE images:

Stroke volume: $SV = EDV_{lumen} - ESV_{lumen.}$, where EDV is end-diastolic volume, ESV is end-systolic volume.

Cardiac output: CO = SV × heart rate.

Ejection fraction: $EF = (SV/EDV_{lumen}) \times 100\%$.

LV myocardial mass is calculated as $LVmass = (ESV_{ventricle} - ESV_{lumen}) \times D$, where D is the density of the myocardium (1.05 g/mL) [83].

2.4.2. Myocardial tissue composition

T_1 mapping

Cardiac MRI techniques can provide detailed tissue characterization, which is the key to aid diagnosis, prognosis, and treatment decisions. Different weighting techniques allow earlier detection of potentially reversible conditions such as diffuse fibrosis, edema, etc. The most studied technique for assessment of diffuse myocardial fibrosis is assessment of T_1 relaxation times of tissue, termed T_1 mapping. A T_1 map is a two-dimensional (2D) slice image where each voxel of the image displays the T_1 relaxation time as signal intensity using a color scheme for easier visual assessment. High T_1 relaxation times are observed in diffuse fibrosis, protein deposition, and water in edema. Low T_1 values are seen in iron or lipid deposition [84]. The multipoint approach to T_1 sampling first described by Look and Locker (LL) in the 1970s involved continuous sampling of the T_1 relaxation curve at multiple time points after an initial preparation pulse [85], however, cardiac motion prevented the acquisition of a voxel-by-voxel T_1 map and limited spatial resolution. Subsequently, the development of the modified Look-Locker inversion (MOLLI) recovery sequence in 2004 allowed acquisition during a single breath-hold [86] by selectively acquiring data at a given time point in the cardiac and merging

multiple LL sequences with varying inversion times into a single dataset (figure 8). However, the T_1 values are consistently underestimated in MOLLI at high T_1 values (>800 ms) and higher heart rates, although newer MOLLI sequences have shown much less heart rate dependence. In addition, the relatively long breath-hold may be challenging in some patients, particularly in the elderly or those with pulmonary disease or bradycardia. The shortened MOLLI (ShMOLLI) recovery sequence was developed to address these limitations. Full recovery of longitudinal magnetization is not achieved in ShMOLLI [87], but an algorithm allows conditional interpretation of T_1 values to obtain precise measurements with a consistent underestimation of T_1 values, which can be corrected. This results in a halving of breath-hold times to approximately 7-9 seconds. Furthermore, the sequence is independent of heart rate, easier to post-process, and is accurate and reproducible over a wider range of T_1 values [88].

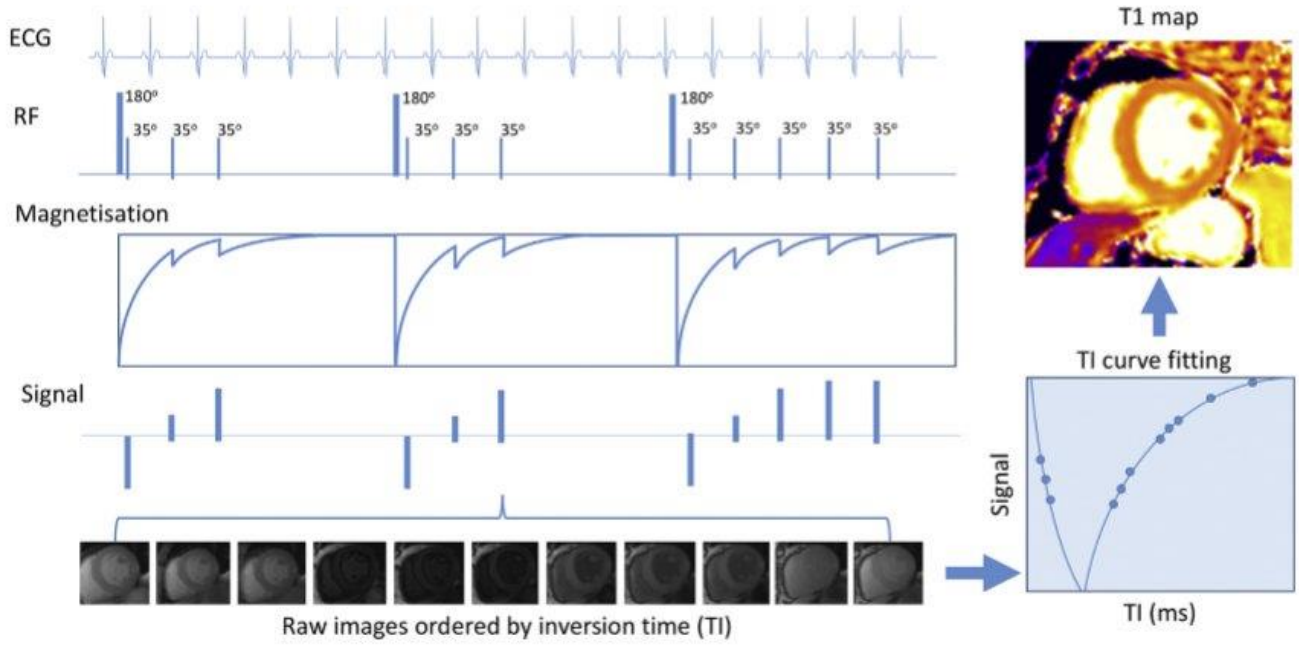

Figure 8. Use of MOLLI recovery sequence to calculate an estimate of T_1 time. Three inversion recovery experiments are performed with three, three, and five images acquired. The resulting raw images are then ordered by TI and signal values used to plot a T_1 recovery curve, which is used to derive the T_1 value. T_1 values are then used to create a two-dimensional voxel map. Figure from [89].

Myocardial fibrosis causes the accumulation of excess type I collagen, which results in expansion of the extracellular interstitial space in relation to the total myocardial volume. Expansion of myocardial extracellular interstitial space is also seen with protein deposition in amyloidosis and acute myocardial edema in MI, myocarditis, and Takotsubo cardiomyopathy. T_1 mapping technique does not directly measures the extracellular matrix. The extracellular volume fraction (ECV) measures the extracellular space occupied by the extracellular matrix,

and therefore, is assumed to reflect diffuse myocardial fibrosis in the absence of protein deposition or edema. ECV is different in different diseases as shown in the figure 9. A head-to-head comparison of the several T_1 mapping sequences had shown that the different sequences yield different ECV values; however, all sequences have similar reproducibility for ECV quantification [90].

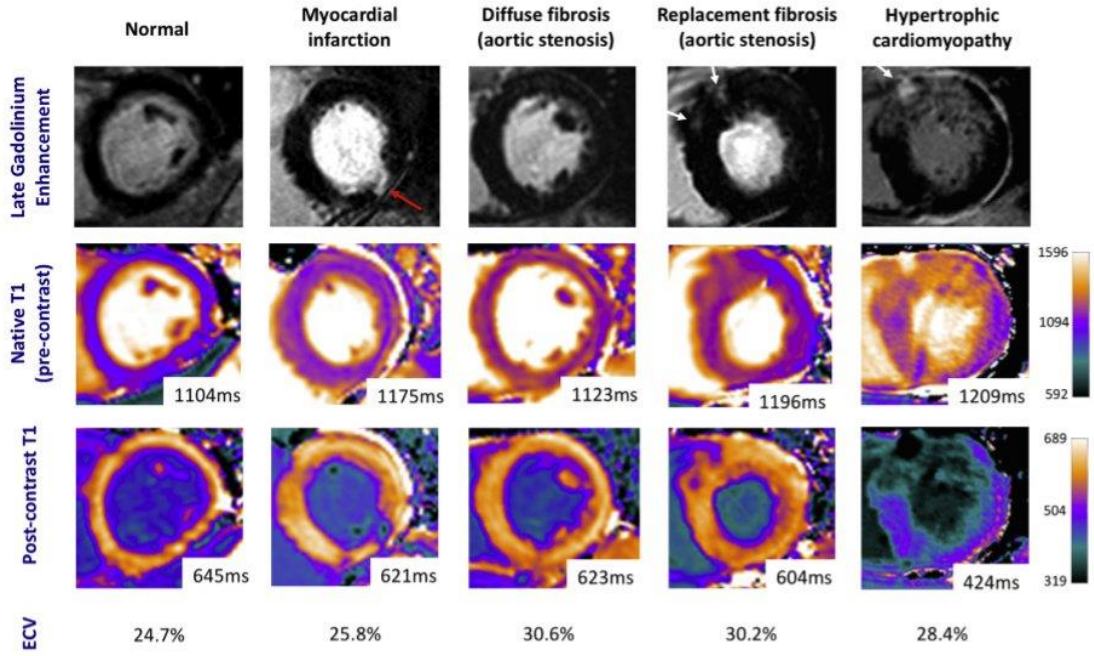

Figure 9. Short axis images with LGE and T_1 mapping in different cardiac conditions. Areas of subendocardial (myocardial infarction, red arrow) and mid wall (white arrows) late gadolinium enhancement are also identified visually with pre and post-contrast T_1 maps. There is an increase in diffuse fibrosis in the aortic stenosis patients as represented by higher ECV values. There is significant overlap between native T_1 values in healthy controls and disease states. Figure from [89].

T_1 mapping can also be performed after administration of gadolinium-based contrast medium administration, which shortens T_1 relaxation times. Although providing increased signal, these post-contrast T_1 values need to be corrected for a range of factors including individual variation in gadolinium kinetics and time from contrast medium administration to imaging. Gadolinium concentration has a strong non-linear relationship with the R_1 relaxation rate ($1/T_1$) and measuring the change in T_1 in both the myocardium and blood pool following contrast medium administration allows estimation of the concentration of gadolinium in these compartments. The ratio of myocardial contrast medium concentration to blood concentration is termed the partition coefficient and corrects for many of the above confounders. At contrast equilibrium, the gadolinium concentration will be equal in the myocardium and blood pool. Knowing the blood volume of distribution (haematocrit) allows the myocardial volume of

distribution to be calculated as a surrogate for the extracellular space - the ECV. The ECV is an index generated by native and postcontrast T_1 mapping, measures the cellular and extracellular interstitial matrix compartments. The ECV in the myocardium may be estimated from the concentration of extracellular contrast agent in the myocardium relative to the blood in a dynamic steady state. The change in relaxation rate ΔR_1 (where $R_1 = 1/T_1$) between pre- and post-contrast is directly proportional to the Gd-DTPA concentration: $\Delta R_1 = \gamma$ [GdDTPA] ($\gamma = 4.5$ L mmol^{-1} s^{-1}). A dynamic steady state exists for tissues that have a contrast exchange rate with the blood which is faster than the net clearance of contrast from the blood. A dynamic steady state between the myocardial and blood contrast agent may be achieved by slow intravenous infusion. The ECV is calculated based on the formula [91].

$$\mathrm{ECV} = (1 - \mathrm{hematocrit})\frac{(1/\mathrm{T1\ myopost} - \mathrm{T1\ myopre})}{(1/\mathrm{T1\ bloodpost} - \mathrm{T1\ bloodpre})}.$$

T_2 mapping

T_2-weighted cardiac MRI has been successfully applied to detect myocardial edema, which may be related to chest pain, fever, ECG abnormalities, and acute myocardial diseases. T_2-weighted cardiac MRI of edema is acquired by combining acceleration techniques with motion suppression and pre-pulse techniques. These MRI techniques freeze the cardiac and respiratory motion effectively with giving high contrast between the blood, fat, normal myocardium, and myocardial edema. Turbo spin-echo imaging with multiple refocusing pulses has replaced spin-echo imaging in T_2-weighted cardiac MRI to reduce the scan time by a factor of 10–12 [92]. A parallel imaging technique is also used to reduce the scan time [93]. The black-blood prepulse technique, consisting of two inversion-recovery pulses combined with ECG-gating, is applied to T_2-weighted cardiac MRI [94]. By using slice nonselective and selective 180° pulses, the static tissues experience net zero rotation, whereas the blood signal is nullified at the imaging slice. The black-blood prepulse technique suppresses the blood signal in the cardiac chamber, thereby improving the visualization of cardiac structures and myocardial edema. Fat-suppression technique using inversion-recovery or spectrally selective pulse highlights myocardial edema by reducing the signal of the adipose tissue close to the myocardium [92].

Myocardial edema is quantified with T_2-prepared or multi echo acquisition [95]. The measurement of the signal ratio between the myocardium and skeletal muscle is useful for detection of myocardial edema related to the irreversible myocardial injuries in acute

myocarditis. T_2 mapping generated from the T_2-value measurement of the ventricular myocardium can allow for both visual and quantitative analysis of the myocardial edema. T_2 mapping is generally performed by pixel-wise fitting for a T_2 decay curve of a series of T_2 weighted images. These source images can be acquired by a turbo-spin echo (TSE) sequence with varying echo time [96], a bSSFP or spoiled gradient echo (GRE) sequence with an initial T_2 preparation module [95, 97], or a sequence scheme that combines spin echo excitation with gradient echo readout (GraSE) [98]. In these T_2 mapping sequences, images are acquired with different echo times and are used to estimate the T_2 values using a two-parameter or three-parameter fit model [99]. The scheme of T_2 mapping sequence based on the bSSFP acquisition with an initial T_2 preparation module is shown in the figure 10. The sequence design incorporates non-selective composite pulses for insensitivity to motion and B_0 and B_1 inhomogeneities. The SSFP readout module was applied immediately after the T_2 preparation to sample the magnetization prior to reaching the SSFP steady state.

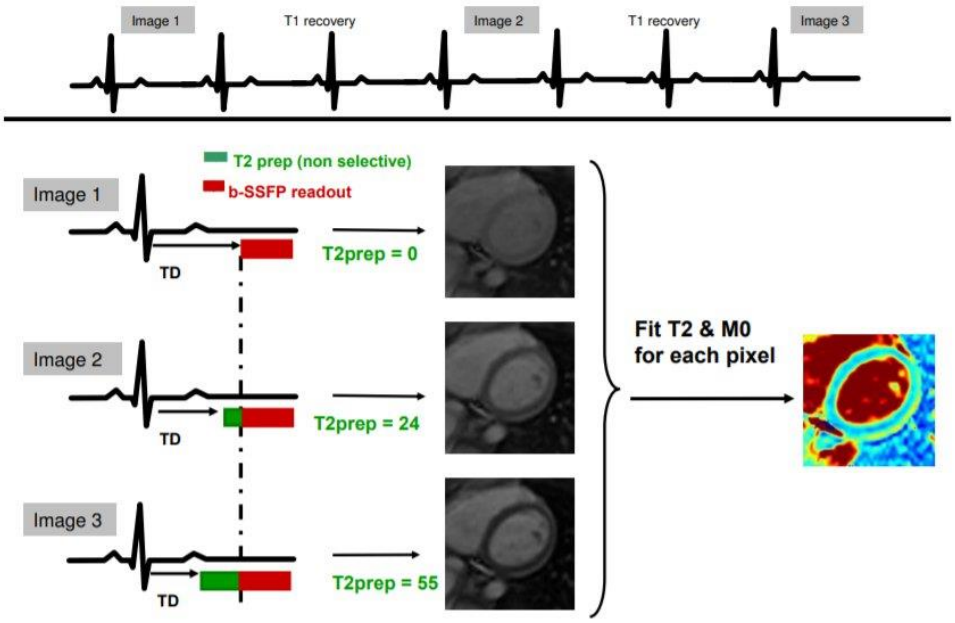

Figure 10. T_2 mapping scheme. Three images were acquired with different T_2 preparation times with a gap of 2 RR intervals to allow for sufficient T_1 recovery. Seven heartbeats were required for image acquisition performed during breath-hold. Trigger delay (TD) was adjusted for each of the three images to ensure that the readout was always in the same phase of cardiac cycle. The three acquired images were processed to fit the T_2 decay curve at each pixel to yield a T_2 map. Figure from [95].

T_2 maps are generated by fitting the following two parameter equation to corresponding pixels from each of the three images: $S(x,y) = M_0(x,y)exp(-TE_{T2P} / T2(x,y))$, where S(x,y) is signal intensity, M_0(x,y) includes the equilibrium magnetization and local receiver coil gain,

and TE_{T2P} is the T_2 preparation time [95]. A linear 2-parameter model was used to fit the equation after its logarithmic transformation. The TE_{T2P} times (0 ms, 24 ms, and 55 ms) were chosen based on the expected range of T_2 values in the myocardium. T_2 for normal myocardium is approximately 55 ms; accordingly, the longest TE_{T2P} was chosen to be 55 ms because longer TE_{T2P} would cause significant signal loss. The myocardial T_2 estimation is improved by including an image without T_2 preparation (TE_{T2P} = 0 ms). TE_{T2P} = 24 ms was the minimum time permitted by the preparation scheme and was chosen as an intermediate point on the curve to support a least-squares fit.

The advantage of T_2 mapping over T_2 weighted imaging is that it is a quantitative method and can detect global or diffuse changes in myocardium as may be expected to occur in myocarditis [92] or cardiac allograft rejection [100]. Additionally, T_2 mapping will enable accurate monitoring of the treatment and/or progression of disease.

In conclusion, native and post-contrast T_1 mapping, T_2 mapping, and ECV provide important knowledge about myocardial tissue composition and disease processes affecting the myocardium that can otherwise be difficult to detect.

2.4.3. Myocardial perfusion

The measurement of contrast enhancement during the first pass of a contrast agent bolus through the cardiac chambers and the myocardium is currently the most widely used technique to assess myocardial perfusion. It is often referred to as first-pass imaging. The purpose of first-pass myocardial perfusion analysis is the visualization and quantification of the regional inflow of blood into the myocardium. This type of study is usually performed with dynamic contrast enhanced (DCE) MRI sequence. To track the first pass of a contrast agent bolus through the LV chambers and myocardium, the DCE technique allows image acquisition during a fraction of a heartbeat, which is repeated every heartbeat during the first pass (Figure 11).

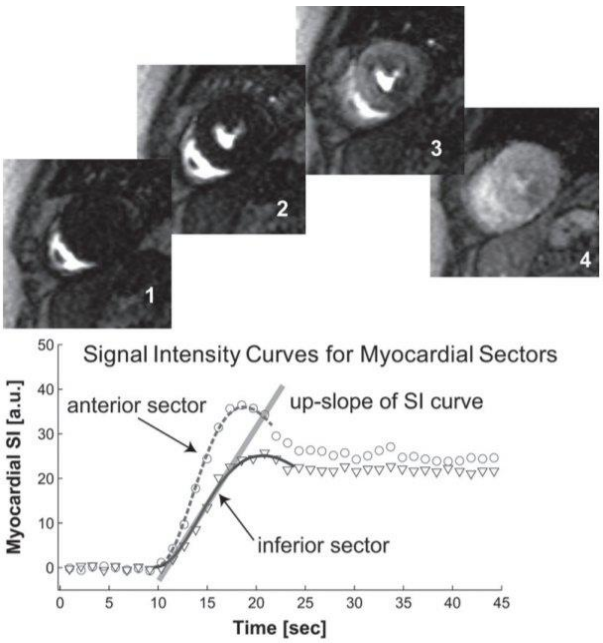

Figure 11: Scheme of the dynamic contrast imaging for myocardial perfusion assessment. Frames 1–4 acquired with a saturation-recovery-prepared gradient-echo sequence covering four sections during each heartbeat. The graph shows signal intensity (SI) changes in anterior and inferior myocardial sectors, with the latter showing reduced myocardial enhancement. The linear rate of contrast enhancement (up-slope) is a parameter sensitive to myocardial blood flow differences. a.u. = arbitrary units. Figure from [101].

In a myocardial perfusion study in patients, the images are acquired during approximately 60 heart beats to cover a pre-contrast phase, the first pass of the contrast agent after its injection, and the recirculation of contrast agent. The total acquisition time is too long for a single breath hold, although patients are typically asked to hold their breath for the initial phase of the study and resume breathing when necessary. DCE images typically have magnetization preparation for T_1 weighting followed by image readout (figure 12). The magnetization preparation can be a saturation preparation [102], which nulls the bulk longitudinal and dephases the transverse magnetization components, or an inversion preparation. The image readout, mostly in the form of sequential two-dimensional acquisitions for multiple sections, follows magnetization preparation, with a possible delay that controls the T_1 weighting of the measured signal. For the image readout, the primary concerns are the time it takes to read out the image, the SNR, motion artifacts, susceptibility artifacts, and a need to preserve the T_1 weighting introduced by the magnetization preparation that precedes the image readout. Motion artifacts can be reduced already by fast image readout and using short echo time.

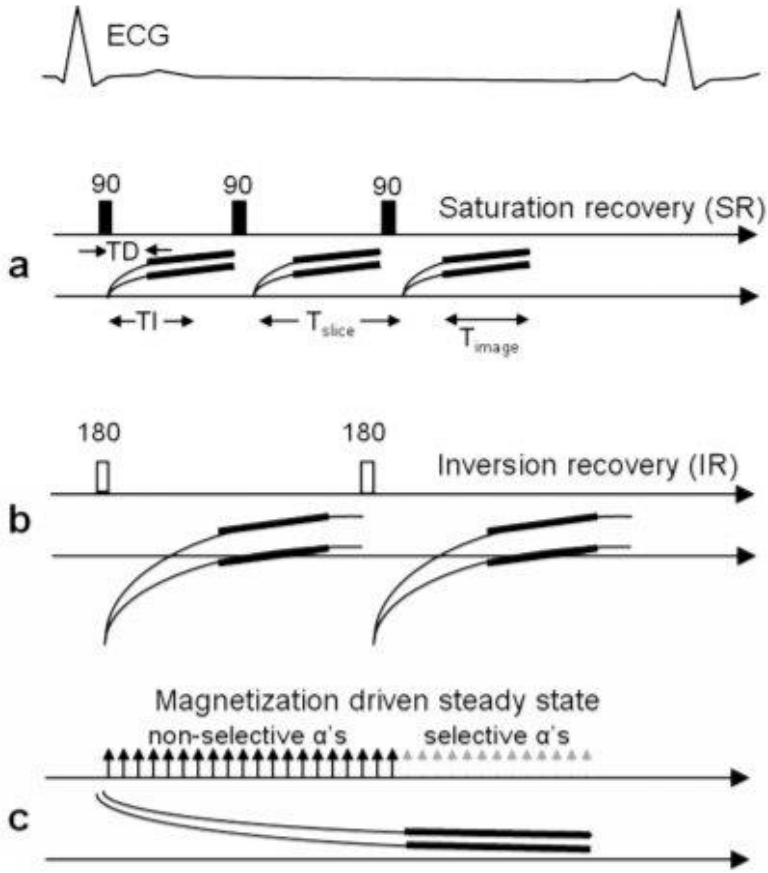

Figure 12. Magnetization preparation schemes for T_1-weighted myocardial perfusion imaging. (a) saturation recovery (SR), (b) inversion recovery (IR), (c) magnetization driven steady state. Figure from [103].

An alternative approach is based on labeling blood as an endogenous tracer by applying a spatially selective inversion preparation and tracking the signal changes that result from the flow of the inverted spins in or out of an adjacent region [104]. This method has given rise to arterial spin labeling techniques, but their use in the heart remains limited and almost absent in clinical settings because of confounding effects of cardiac motion and the relative modest signal changes achievable with spin labeling [105, 106].

The clinically preferable method of interpretion myocardial perfusion studies is based on the visual assessment of myocardial contrast enhancement when the perfusion images are displayed in CINE mode. Regions with perfusion defects are characterized by a reduced rate of contrast enhancement. During early myocardial contrast enhancement such regions can be identified in CINE frames by appearing hypointense. Playing the images in CINE mode is essential for differentiating between image artifacts, such as dark-rim artifacts at the endocardial border and true perfusion defects [107]. A key distinguishing feature between dark-rim artifacts and true perfusion defects is the number of frames during which the signal

hypointensity can be observed, with artifacts typically only appearing in a couple of frames during peak contrast enhancement in the blood pool and before peak contrast enhancement in the myocardial tissue.

A quantitative analysis of the myocardial perfusion is based on deriving parameter values from a time series of regional signal intensity values. The regions for such an analysis can be based on the definition of myocardial sectors (such as standardized American Heart Association 17-segment model [108]) or represent myocardial pixels to derive maps of myocardial perfusion with a spatial resolution equivalent to the underlying spatial resolution of the images [109]. Both the sector- and pixel-based analyses require that the endo- and epicardial borders of the left ventricular wall be detected or traced for each image frame of a perfusion study, a task that still relies, to a large degree, on user intervention and represents the most time-consuming step of a quantitative analysis. The subsequent analysis algorithms can be derived mostly without any further user intervention, parameters that relate to the rate of contrast enhancement, or the relative or absolute myocardial blood flow.

For any quantitative analysis of myocardial perfusion, special consideration must be given to the contrast enhancement in the blood pool since the arterial input is used as reference. Any systematic underestimate of arterial contrast enhancement results in an overestimate of myocardial perfusion. The contrast enhancement of the blood should be in approximately linear relation to the concentration of a contrast agent in the blood. To address this requirement, the “dual bolus” [110] and “dual contrast” were introduced [111]. The dual bolus approach involves giving a low dosage contrast bolus to characterize the arterial input of contrast, followed by a higher dosage bolus to image the myocardial contrast enhancement. The two bolus dosages are in a pre-determined ratio (for example, 1:10) that is then used to scale the arterial input function (AIF) from the low-dosage bolus to analyze the myocardial contrast enhancement with the rescaled and time-shifted AIF.

Semi-quantitative perfusion measures are the basis of perfusion reserve indices. The maximum upslope of the local myocardial time/intensity profiles in MR first-pass perfusion image series is considered to be a good indicator of myocardial perfusion [112]. For normally perfused myocardial tissue, the ratio of the maximum upslopes under stress and at rest should exceed a certain threshold. Myocardial segments with a value below the threshold may be ischemic. The stress/rest maximum upslope ratio is usually described as the myocardial perfusion reserve index (MPRI). Determination of the MPRI is not simple, because of the

properties of first-pass perfusion series, such as respiratory motion. Without motion compensation, the myocardial contours must be individually repositioned for each image in the series. The analysis should be performed both at rest and after pharmacological stress; then the stress/rest upslope ratio is calculated. Another measure of myocardial perfusion is perfusion reserve, which is defined as the area under the myocardial signal curve, up to the time where the first pass peak is observed in the blood. The coronary flow reserve can be measured with cardiac MRI by direct visualization of the lumen of the proximal coronary artery and with quantification of blood flow velocity by using the phase-contrast technique [113].

In summary, cardiac magnetic resonance can be used to quantify myocardial blood flow with high spatial and temporal resolution. Standardization of the quantitative analysis is not finalized yet, therefore, this remains a field of active investigation. Despite its evolving status, quantitative MRI perfusion imaging is important in studies of cardiac diseases.

2.4.4. Myocardial viability

Delayed contrast-enhanced MRI of the heart using T_1-weighted imaging and gadolinium–diethylenetriamine penta-acetic acid (Gd-DTPA) has become the gold standard technique for detecting the presence and size of myocardial infarction (MI) in human patients [114, 115] and animals [5, 116, 117]. Specifically, by using either a high flip-angle gradient-echo sequence or an inversion-recovery gradient-echo sequence applied 10–20 min after intraperitoneal infusion of 0.1–0.2 mmol/kg Gd-DTPA, images clearly depicting the region of infarction. An example demonstrating this technique is shown in Figure 13, where contrast-enhanced regions of the heart highlight the non-viable infarcted zones, and dark regions in the heart represent viable myocardium. Breath hold imaging is preferred though multiple signal average imaging, respiratory navigator gating, or single-shot imaging can be used with free-breathing. Imaging planes and slice thickness should match those used for CINE imaging of the ventricles to facilitate comparison. In order to improve the image contrast between normal myocardium and regions of increased gadolinium concentration, an inversion pulse is incorporated into the pulse sequence. The time between the inversion pulse and image acquisition, known as the inversion time (TI), should be set to null normal myocardium (Figure 13). Selecting the appropriate inversion time may be facilitated by imaging iteratively with different TIs, or by the use of a TI-scout or Look-Locker sequence. Because the gadolinium concentration in normal myocardium decreases with time, the optimal TI will become longer as time elapses.

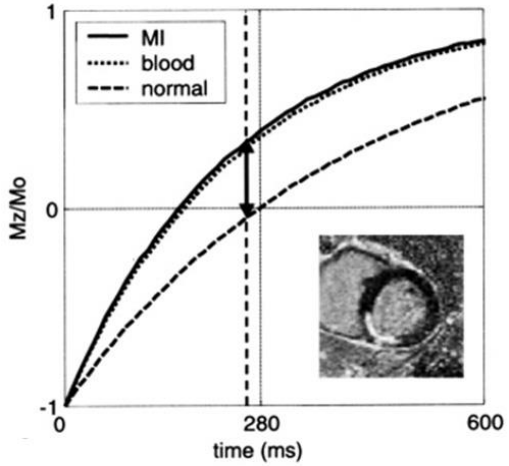

Figure 13. Plots of signal intensity vs. TI for phase-sensitive detection for MI (solid), blood (dotted), and normal myocardium (dashed), using nominal values of T_1 at 15 min following a double dose of contrast agent. Example images correspond to acquiring images earlier than the null time for normal myocardium. The solid lines with double arrows depict the contrast between the MI and the normal myocardium. Figure from [118].

An error in selecting the optimum null time leads to a reduced infarct to myocardium contrast. Phase-sensitive detection has been used to improve infarct to myocardium contrast by preserving the sign of the desired magnetization during IR and reduce the dependence on prescribing at exact TI time. Phase-sensitive inversion recovery (PSIR) is now the standard MRI method for scar imaging [118]. The PSIR pulse sequence is shown in the Figure 14.

Phase-sensitive detection can be used to remove the background phase while preserving the sign of the desired magnetization during IR. In this context, the term “background phase” includes effects due to off-resonance, surface coils, and receivers. Phase-sensitive detection achieves consistently good contrast during multislice imaging by decreasing the sensitivity to changes in the value of tissue T_1 with increasing delay from contrast agent injection. Phase-sensitive detection has the additional benefit of background noise reduction, which leads to an improved contrast-to-noise ratio (CNR) between areas of high signal intensity, such as blood and infarcted myocardium, and regions of low signal intensity, such as nulled myocardium. It is possible to acquire the reference image during alternate heartbeats without increasing the breath-hold duration. This type of acquisition provides a reference image with the full spatial resolution and eliminates mis-registration errors due to motion.

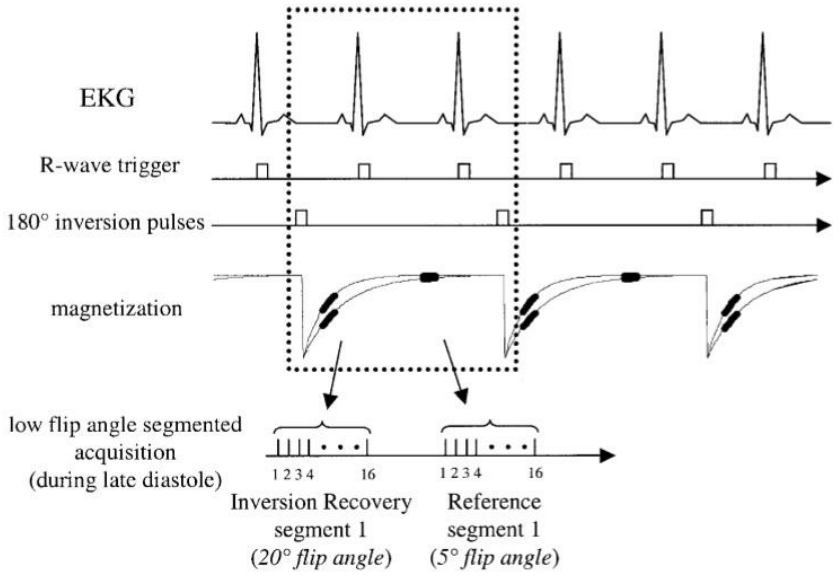

Figure 14. Time diagram of the pulse sequence phase sensitive inversion recovery (PSIR). Figure from [118].

The reference image is used to estimate both the background phase and surface coil field maps. For each slice, imaging is performed in mid-diastole using a prospectively gated segmented acquisition of k-space over several heartbeats during a single breath-hold. IR pulses are applied every other heartbeat to permit full recovery of magnetization in the presence of Gd-DTPA. This minimizes any disruption of the steady state due to heart rate variability. A reference phase map is acquired during the same breath-hold and cardiac phase in alternate heartbeats using a reduced flip angle readout. Both the IR and reference image are spatially registered, avoiding errors due to respiratory and cardiac motion. A fast gradient-recalled echo pulse sequence is used with interleaved phase-encode ordering. The inversion is performed via a nonselective, adiabatic pulse. The T_1-weighted IR image is acquired using multiple 20° flip angle pulses, while the reference used 5° flip angle pulses. The reference image is acquired after the magnetization had virtually recovered. The use of a 5° flip angle for the reference image reduces the T_1 contrast of this image and minimizes relaxation effects on the primary T_1-weighted IR image. Using this method three images are produced for each breath-hold acquisition: the conventional magnitude image, the phase-sensitive and reference images.

The main image-processing steps include the segmentation of myocardial boundaries, the discrimination between normal and infarcted tissue, the quantification of volume of the infarcted tissue, and the comprehensive visualization of the results from the processed slices. The myocardial contours should to be manually delineated, then automatic histogram-based thresholding is performed to detect infarcted tissue, and the results are visualized in a bull's-

eye plot (figure 15). Typical thresholding methods for detection of myocardial scar are full-width-half-max (FWHM) and mean signal intensity plus 5 standard deviations (SD). Infarct size usually is measured as percent of the scar to the LV area.

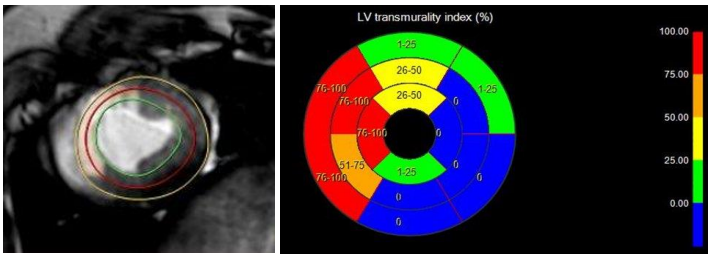

Figure 15. Gd-enhanced MRI (PSIR) of the pig heart shown in one short axis slice through mid-ventricle. Scar and blood are bright, viable myocardium is dark. LV transmurality index is showing the scar extend. Image collected and analyzed by Naumova AV. University of Washington, Seattle, WA, USA. 3T Philips scanner and Philips IntelliSpace Portal software.

Gd-DTPA is a T_1-shortening agent that has an extracellular distribution volume leading to enhancement of non-viable myocardium. Contrast-enhanced MRI accurately measures scarred and viable myocardium after infarction and represents a useful tool for assessing dynamic changes in the infarct. There is a high correlation in the infarct size measurements between MRI and histology (figure 16).

Manganese (Mn^{2+}) is another T_1-shortening agent that is actively pumped into viable myocytes through the voltage-gated L-type Ca^{2+} channels. Mn^{2+}-enhanced MRI (MEMRI) can be used to image viable myocardium [5]. Dynamic MEMRI showed the ability to measure relative Ca^{2+} channel activity: the rate of change in signal intensity in MEMRI increased during infusion of dobutamine (a Ca^{2+} channel agonist) and decreased during infusion of diltiazem (a Ca^{2+} channel antagonist). These results were obtained by dynamic T_1-weighted imaging during and after a 20 min infusion of $MnCl_2$ and quantification of the rate of signal enhancement [120]. In a different study, T_1-weighted imaging in post-infarct mice applied 20–26 min after injection of $MnCl_2$ showed signal enhancement of 128% in non-infarcted regions, only 58% in infarcted regions, and, subsequently, an excellent correlation ($r = 0.96$) of infarct volume determined by MEMRI with histology [121].

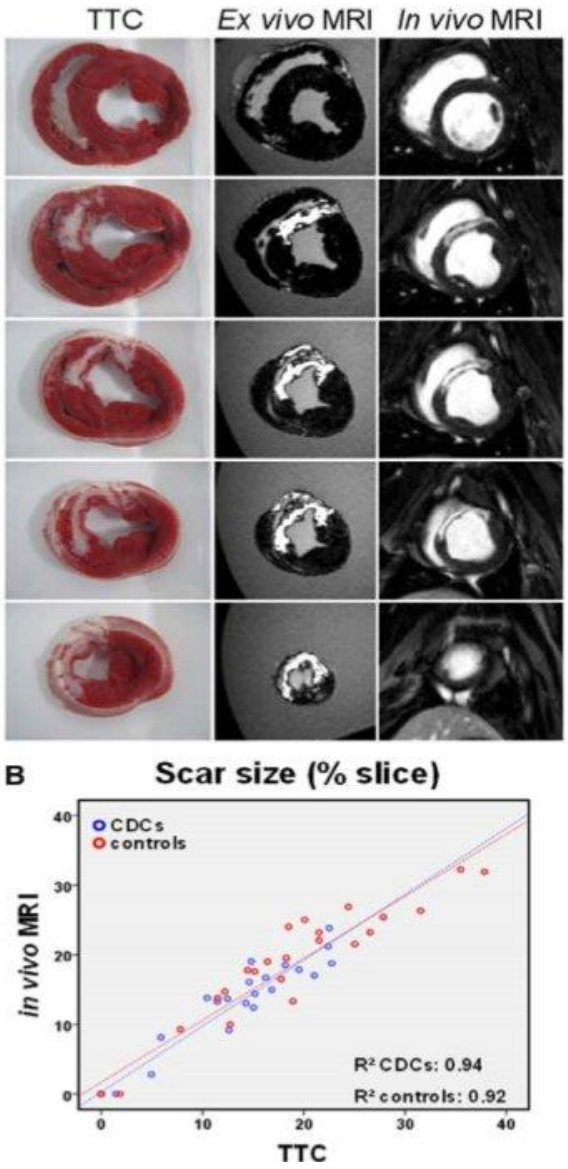

Figure 16. Comparison of cardiac MRI with histology for assessment of scarred and viable myocardium in pigs after cell therapy. TTC - 2% 2,3,5-triphenyltetrazolium chloride stained cardiac slices matched with their corresponding delayed contrast-enhanced MRI images (from both the *in vivo* and *ex vivo* MRI datasets). Areas of hyperenhancement in cardiac MRIs correspond excellently to regions of scarred myocardium in histological slices. CDC - cardiosphere-derived cell–treated minipigs. Figure from [119].

The dual-contrast MRI is enabling assessment of the infarct border zone in myocardium *in vivo* in a porcine ischemia-reperfusion model. Gadolinium (Gd)-based delayed-enhancement MRI (DEMRI) identifies nonviable myocardium but is nonspecific and may overestimate nonviable territory. Manganese (Mn^{2+})-enhanced MRI (MEMRI) denotes specific Mn^{2+} uptake into viable cardiomyocytes. The examples of the MR images of the myocardial scar and viable border zone in the infarcted pig heart are shown in the figure 17.

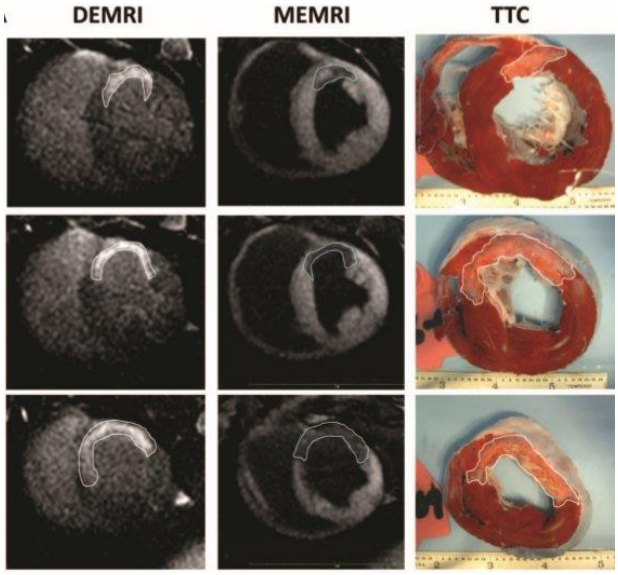

Figure 17. DEMRI versus MEMRI versus TTC histology staining. Representative slice progressing from the base to the apex of the heart (top row to bottom row), showing short axis *in vivo* MRI images and matching TTC sections from an explanted swine heart at 21 days after ischemia-reperfusion. Figure from [5].

In conclusion, late Gd enhancement MRI is accurately measures scarred and viable myocardium after cell therapy, supporting the utility of contrast-enhanced MRI for assessing dynamic changes in the infarct and monitoring therapeutic regenerative efficacy.

2.5. Phosphorus magnetic resonance spectroscopy

Myocardial energy production is the highest per gram of any organ in the body and this fuels mechanical function [43]. During increased contractile demand, such as during exercise or adrenergic stimulation, myocardial metabolic rates increase to supply the energetic needs [44]. The prime myocardial high-energy phosphates are adenosine triphosphate (ATP) and phosphocreatine (PCr); these are reversibly converted by the creatine kinase (CK) reaction: PCr + ADP + H^+ $\Leftrightarrow$ ATP + Creatine. The CK reaction serves as an intracellular spatial energy shuttle, facilitating the transfer of high-energy phosphates from the mitochondria (where ATP is produced) to the cytosol (where ATP is used) and facilitating the return of products to the mitochondria for re-phosphorylation [122, 123]. Relatively large rates of ATP synthesis are required to sustain normal systolic and diastolic function. The ‘‘energy starvation’’ hypothesis of heart failure suggests that inadequate ATP supply underlies the contractile dysfunction present in heart failure [124, 125].

Although high-energy phosphate levels can be determined by conventional biochemical techniques on digested tissue samples, ^{31}P magnetic resonance spectroscopy (MRS) is the only

non-invasive means for quantifying high-energy phosphates in the beating heart. ^{31}P MRS has been used in isolated, perfused hearts [21] and has been combined with spatial localization techniques and ^{1}H MR imaging in intact large animals and humans [126-130]. The sensitivity of the naturally abundant ^{31}P nucleus is relatively high (one-fifteenth that of ^{1}H), and the chemical shift range is fairly wide (about 30 parts per million for biological phosphates). Application of ^{31}P MRS in cardiovascular research has generally involved measurement of the concentration ratio of PCr to ATP, which is a sensitive indicator of the energetic state of the heart. Alterations in cardiac high-energy phosphate metabolism have been found in patients with a variety of diseases, such as coronary artery disease [131, 131], type 2 diabetes [133, 134], hypertrophic cardiomyopathy [135], heart failure [136-138], and valve disease [139]. ^{31}P MRS provides a potential tool for the evaluation of therapeutic interventions [140].

Cardiac ^{31}P MR spectra might be obtained in open-chest preparations where a radio frequency (RF) surface ^{31}P coil is placed in direct contact with the exposed LV surface [130, 141]. One of the pioneered work in the non-invasive image localized cardiac ^{31}P MRS was published by Dr. Ugurbil [142]. In this study the technique incorporates both Fourier series windows and selective Fourier transform methods utilizing all three orthogonal gradients for 3D phase encoding. The number of data acquisitions for each phase-encoding step was weighted according to the Fourier coefficients to define cylindrical voxels. Spatially localized ^{31}P spectra was generated for voxels of desired location within the field of view as a postprocessing step. Figure 18 shows spectra originated from the different locations in the chest of the anesthetized dog [142]. The animals were placed in the prone position on a coil cradle with the heart directly over the 7-cm diameter single-loop ^{31}P coil. Study was performed at the 31-cm horizontal bore 9.4T magnet (Magnex) interfaced to a Unity console (Varian).

3D B_0 spatially localized ^{31}P NMR spectroscopy at 9.4T can generate minimally contaminated transmural cardiac spectra from subepicardium and subendocardium with excellent SNR. 3D spatial localization was achieved by using three orthogonal gradient-weighted k-space acquisitions for enhanced SNR [142]. Postprocessing of the acquired FIDs enabled accurate placement of an arbitrarily shaped voxel in a desired location within the FOV. The use of a quadrature RF coil improved the B_1 penetration and sensitivity compared with a similar size linear coil. The high magnetic field strength of 9.4T contributed to increasing the SNR of the spectra.

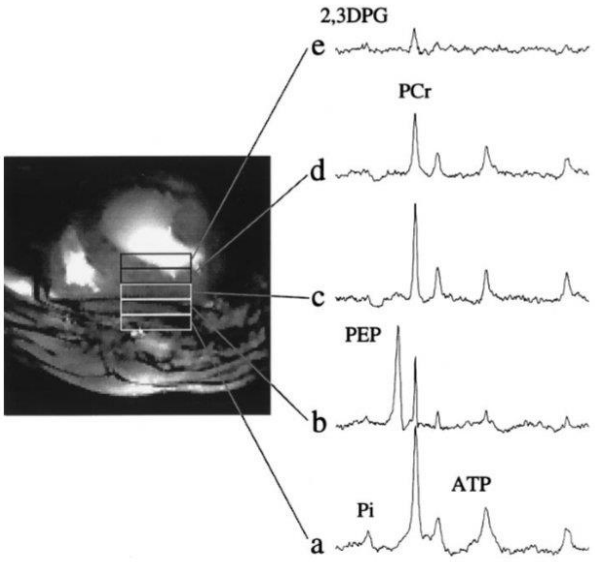

Figure 18. Set of spatially localized spectra obtained from the dog chest with an implanted 2-phosophoenolpyruvate (PEP) phantom between the anterior left ventricular (LV) wall and the chest wall. MRI of the dog chest obtained with the turboFLASH and spectrum (**a**) originated from chest wall skeletal muscle as indicated by a Pi resonance and a high PCr/ATP ratio. Spectrum **b** is from the voxel containing the implanted PEP phantom located between the chest wall and the anterior LV wall; this spectrum shows the PEP resonance located at ~3 ppm upfield of PCr. Spectrum c is mostly from the voxel containing sub-epicardium; spectrum **d** is mostly from the voxel containing sub-endocardium mixed with LV cavity blood, which contributes to the decreased signal-to-noise ratio in spectrum **d** compared with spectrum **c**, and spectrum **e** is from a voxel containing mostly blood in the LV chamber with some interventricular septal tissue as indicated by the resonances of 2,3-diphosphoglycerate (2,3-DPG) and small high-energy phosphate resonances. Figure from [142].

A multi-voxel chemical shift imaging (CSI) [143] acquisition protocol can be used to produce spectra of high quality with high specificity to the myocardium within a clinically feasible scan time [141]. ^{31}P MRS data from the human heart might be acquired with a 3D acquisition-weighted CSI sequence (AW-CSI) [145]: acquisition matrix size 16×16×8 and the FOV 240×240×200 mm, which, with 10 averages at the center of k-space, led to 1690 total acquisitions and a nominal voxel size of 5.6 mL (figure 19). Prospective ECG gating was used with an acquisition trigger delay of 400 msec, with data acquisition occurring during diastole. The TR was set to one R–R interval leading to an acquisition time of 31±5 min. The CSI acquisition utilized the ultra-short echo time CSI (UTE-CSI) [146] technique to reduce the interval between excitation pulse and signal acquisition to a minimum (TE 0.3 ms) to maximize the acquired signal and to reduce the first order phase effects that contribute to baseline artifacts in the acquired spectra. An optimized RF pulse (length 2.4 ms), centered between the γ- and α-ATP resonance frequencies was used to ensure uniform excitation of all

spectral peaks. This pulse produced an excitation flip angle of 32±3° at the inter-ventricular septum averaged over all subjects scanned.

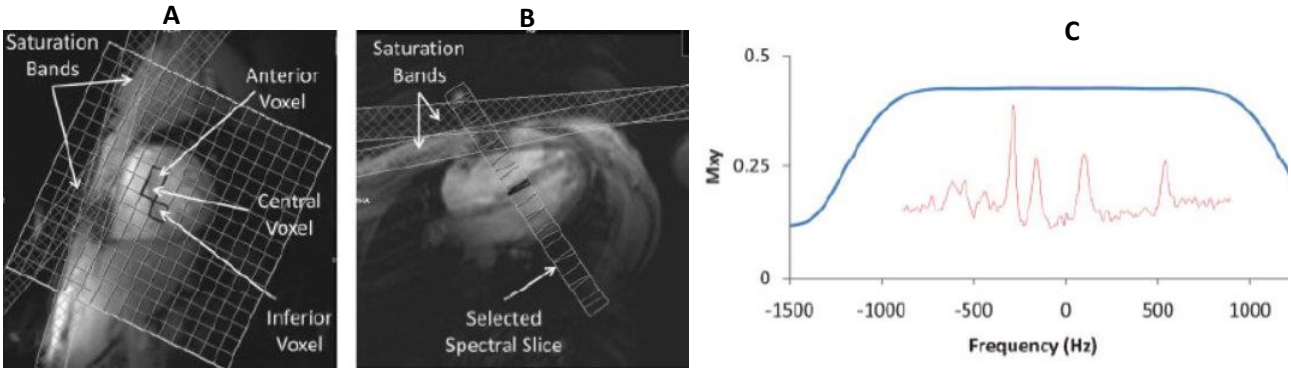

Figure 19. Orientation of the CSI matrix shown (A) in the two-chamber cardiac short axis view and (B) in the four-chamber cardiac horizontal long axis view, showing the rotation of the grid to position the three voxels so as to maximize inclusion of the septal myocardium in the short axis plane and the position of the volume of interest along the long axis of the septum. The position of the two saturation bands was adjusted to cover the chest wall, thus minimizing skeletal muscle contamination. Profile of the optimized RF pulse providing uniform excitation of the measured peaks and an example ^{31}P spectrum is overlaid on the plot to demonstrate the location of the spectral peaks within the excitation profile (C). Figure from [144].

The feasibility of analyzing the murine cardiac energy state with high spatial resolution in vivo by acquisition-weighted 2D ^{31}P CSI at a field strength of 9.4T has been explored [147]. A double-tuned ^{1}H/^{31}P birdcage resonator to record anatomical ^{1}H MR images and the corresponding 2D ^{31}P CSI data set (figure 20). The 2D ^{31}P CSI data set was recorded using a sine-bell acquisition weighted sequence to improve the spatial response function [145], with FA 45°; TR 250 ms; FOV 30×30 mm^2; data points in the spectral domain 1024; spectral width 6510 Hz; and slice selection with a 500-µs sinc3 pulse. The numbers of acquisitions in the middle row of the symmetrical acquisition matrix were 0, 256, 768, 1024, 1024, 768, 256, and 0 (for a total of 18432 acquisitions within 75 min). An exponential filter of 20 Hz was applied in the spectroscopic direction, and zero-filling by a factor of 2 was applied in each spatial dimension, resulting in a 16×16 matrix with are solution of 1.875 mm in the x and y directions. The slice thickness depended on the heart size (usually 6–8 mm, yielding a voxel size of 21–28 µL). In this study the spatially localized spectra were acquired simultaneously from the posterior, lateral, anterior, and septal walls of the mouse heart. This permits the noninvasive, repetitive analysis of transgenic mouse models regarding cardiac anatomy and function together with the regional energy state in one experimental session.

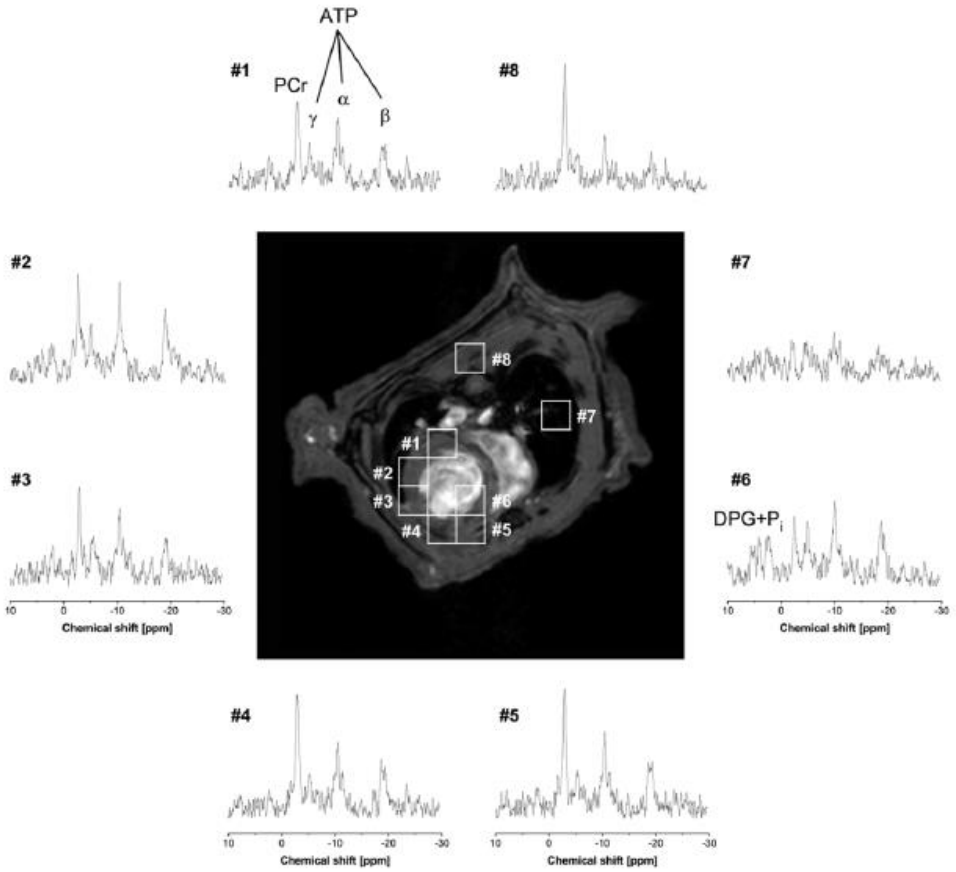

Figure 20. Representative ^{31}P MR spectra from selected voxels of the mouse thorax superimposed with the anatomical ^{1}H MR image (FOV 30 x 30 mm^2). Spectra were recorded using an acquisition-weighted 2D ^{31}P CSI sequence with a resolution of 1.875 x 1.875 x 6.5 mm^3 (22.8 µL). Spatially localized spectra of the posterior (#1), lateral (#2 and #3), and anterior (#4 and #5) walls, and the septum (#6) of the heart are displayed. Spectra from the lungs (#7) and the skeletal muscle of the animal's back (#8) are shown. Figure from [147].

The metabolite pool sizes do not directly index flux or energy turnover. Dynamic measures of energy metabolite turnover have been possible with saturation transfer MRS in animals [148, 149], but flux measurements in the human heart have been unobtainable because of the complexity, sensitivity, and inefficiency of standard methods. A four-angle saturation transfer (FAST) method has been developed for rapidly measuring CK flux rate by using ^{31}P MRS [150]. Also, noninvasive methods for quantifying myocardial metabolite concentrations was developed by the same group of authors [151]. An absolute quantification of the high-energy phosphate metabolites is technically more challenging than a measurement of PCr/ATP, but it alone can detect changes in the ATP pool size. In addition, the size of the PCr pool is used in the calculation of ATP flux through the CK reaction in magnetization transfer studies, and this flux is critically altered in experimental and human heart failure. The study of ATP flux in human patients was performed on a clinical 1.5-T General Electric Signa MRI scanner [152]. A one-dimensional (1D) chemical-shift imaging sequence was applied (1-cm resolution)

with B_1-field independent rotation phase-cycled (BIRP) adiabatic pulses [153] to provide exact flip angles of 15° or 60°. Square pulses at 2% of the BIRP power level were applied to selectively saturate the γ-phosphate of ATP (γ-ATP) at -2.7 ppm and to provide a control irradiation at +2.7 ppm relative to the PCr resonance. FAST measurements consisted of two pairs of measurements of the PCr signal with flip angles of 15° and 60°: one pair with γ-ATP saturated and the other pair with control irradiation (total scan time 38 min; TR 1 sec). The forward CK rate constant k_{for} was derived from the classic relationship $k_{for}\ T'_1 = 1 - M'_o/\ M_o$ corrected for spillover irradiation, where T'_1 is the spin-lattice relaxation time in the presence of saturating irradiation and $M'_o/\ M_o$ is the fully relaxed fractional reduction in PCr. After the examination, the patient was replaced by a large, phosphate-containing phantom, and fully relaxed ^{31}P and ^{1}H MR spectra were acquired to calibrate concentration measurements [151]. PCr and ATP concentrations were determined by both the water- and phosphate-reference methods [48, 131, 151]. Metabolite measurements were saturation-corrected, and ATP concentration was corrected for blood contamination. The resulted spectra are shown in the figure 21.

CK flux can be calculated from the classic relationship: $CK_{flux} = k_{for} \times [PCr]$, where k_{for} is the pseudo-first-order rate constant measured by saturation transfer techniques. In addition, CK flux = $k_2 \times [PCr] \times [ADP]$, where [PCr] and [ADP] are the respective concentrations of the metabolites, and k_2 is the second-order CK rate constant [154, 155]. Intracellular free ADP concentration can be calculated from the CK equilibrium reaction: [ADP] = ([ATP][free Cr])/([PCr][H^+] K_{eq}), where K_{eq} is 1.66×10^9 liters/mol for a Mg^{2+} concentration of 1.0 mmol/liter, the cytosolic volume is taken as 0.725 ml/g of wet weight [156], and intracellular pH is taken as 7.05. The free-energy change of ATP hydrolysis [$-\Delta G_{ATP}$ (kJ/mol)] is determined as $\Delta G_{ATP} = \Delta G° + RT \log ([ADP][P_i]/[ATP])$; where G° is the standard free-energy change, R is the universal gas constant, and T is the absolute temperature [157]. This study demonstrated that the forward cardiac CK flux is reduced in chronic heart failure (figure 22).

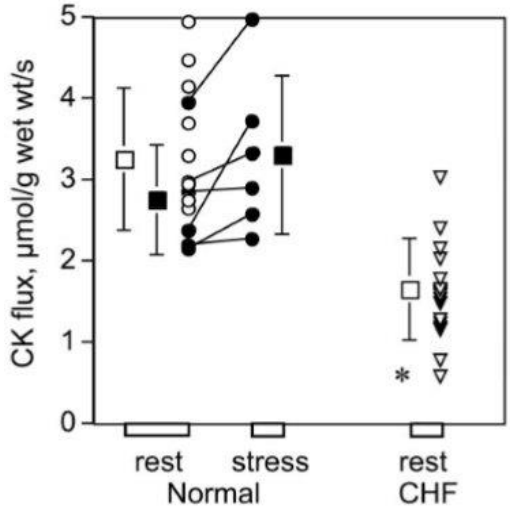

Figure 21. MRI/MRS detection of CK energy flux in the human heart. Shown are cardiac MRI and ^{31}P spectra of a normal subject acquired at rest (a and b) and during dobutamine stress (c), and of a 37-year-old patient with NYHA class III heart failure at rest (d and e). Horizontal white lines in images denote the source of the spectra in the anterior myocardium. The white box shows the detector coil location. Arrows on the spectra identify the frequency of the saturating irradiation tuned to the γ-ATP resonance (spectra on right) and in a symmetric control location, relative to PCr (spectra on left). With γ-ATP saturated, the PCr resonance decreases (oblique lines) in direct proportion to the forward CK flux because the saturated γ-ATP signal is unable to contribute to the PCr signal by the reverse reaction: the greater the flux the greater the decrease. The spectral scale is chemical shift in ppm. Figure from [152].

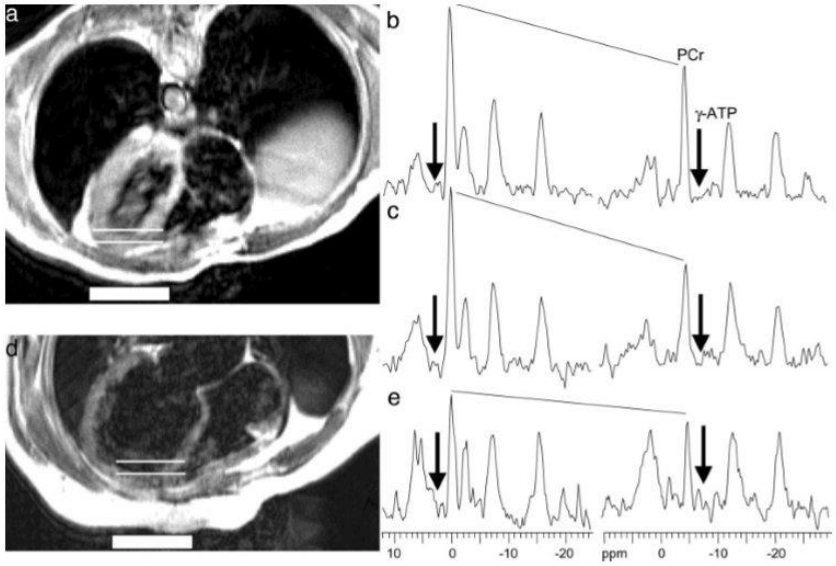

Figure 22. Forward myocardial CK flux is measured in normal subjects at rest (at left), during dobutamine stress (in the center, filled symbols), and in patients with NY HA class I–IV CHF (at right). Square symbols with vertical error bars denote means ± SD. *, $p<0.0005$ vs. normal subjects at rest. Figure from [152].

The direct measures of ATP synthesis through CK in the human heart demonstrate a deficit in energy supply in clinical heart failure. This reduction in ATP synthesis through CK is

cardiac-specific and occurs in mild-to-moderate heart failure before a significant reduction in ATP can be detected. This study has shown that the failing human heart has a deficit in energy supply. The reduction in ATP turnover through CK is cardiac-specific and out of proportion to the reduction in metabolite ratios and pool sizes. We find that reduced ATP supplied by the CK reaction, rather than an increase in ADP concentration, may contribute to dysfunction. The results support the use of heart failure treatment strategies that reduce metabolic demand as opposed to those that stimulate contractility and deplete energy reserves.

In summary, although the concentration of high energy phosphate metabolites can be measured by enzymatic methods on processed cardiac tissue, ^{31}P MRS is the only noninvasive technique for measuring high-energy phosphates under *in vivo* conditions. Spatially localized ^{31}P NMR spectroscopy technique offers the potential for improved characterization of human heart as well as animal models of human diseases. Abnormalities in myocardial high energy phosphates content and reduced ATP production through CK would have an adverse affect on myocardial function and progression of human heart failure.

2.6. Stem cell types used in cardiac repair studies

Stem-cell biology and regenerative medicine are the fastest moving areas of biomedical research. Regenerative medicine aims to achieve functional recovery of damaged tissues by providing specific cell populations, with or without biomaterial scaffolds that enhance the body's intrinsic healing capacity [158]. Stem cells offer the possibility of repairing damaged organs. A number of different cell types have been considered for such therapies, including skeletal myoblasts [159-164], smooth muscle cells [165], adipose-derived cells [166-168], bone marrow-derived stromal cells [169, 170], hematopoetic stem cells [171-173], mesenchymal stem cells [174-177], resident cardiac progenitor cells [178-181], embryonic stem cells [40, 182-185] and induced pluripotent stem cells [185-187]. Here we focus on the stem cell types closest to clinical trials and those for which there are the most reliable data. We will touch briefly on major cell types that have been explored and present our rationale for focusing this proposal on human embryonic stem cells.

2.6.1. Adult stem cells

Adult stem cells include many cell types that exist in different tissues of the adult organism. Experimental cell therapy approached for cardiac repair began with the use of *skeletal myoblasts* derived from skeletal muscle satellite cells [159-162]. Besides their non-cardiac origin, skeletal myoblasts have almost all the properties of ideal donor cell type.

Although it was originally hoped that skeletal myoblasts would transdifferentiate into cardiomyocytes, current data suggests that these cells improve function either through angiogenesis or prevention of ventricular dilation, with no generation of new cardiomyocytes [161, 188, 189].

Another well-studied type of adult stem cell type used in pre-clinical and clinical cardiac repair studies is *bone-marrow-derived mesenchymal stem cells (MSCs)* (Figure 23). Human MSCs, that represent a mesoderm derived population of progenitors, are easily expanded in culture [190]. They are capable to differentiate into osteoblasts, chondrocytes, and adipocytes and exhibit the potential to repair or regenerate damaged tissues. Considerable interest in for cardiac repair was prompted by reports of haematopoietic stem cells transdifferentiating into cardiomyocytes [171] but are now thought to exert their main actions in a paracrine manner through the release of cytokines [172]. Recent studies of bone marrow-derived stem cells showed that they continue to differentiate along haemotopoetic lineage [172, 182] and the observed functional improvement is caused by indirect mechanisms, such as stimulation of angiogenesis, decreasing myocyte apoptosis and collagen disposition, but not related to trans-differentiation into the cardiac tissue [183]. One possible advantage of MSC is their ability to be delivered either in autologous procedures or using an allogeneic strategy as some reports suggest that they may be relatively immune-privileged [184]. These apparent attractive capabilities of the cells have recently led investigators to begin clinical trials, however, initial benefits of intracoronary bone marrow cells delivery to patients with MI were reported, but no differences were observed after 18 months [195].

Other adult cell types such as *fibroblasts* and *smooth muscle cells*, which clearly cannot contract like cardiomyocytes, also were reported to enhance function of the injured heart [197, 198]. These studies suggested that noncontractile effects, such as “paracrine effect” might be at play, whereby transplanted cells are proposed to produce growth factors, cytokines, and other local signaling molecules that are beneficial for the infarct repair. Taken together, the current facts indicate that bone marrow cells and other adult stem cells do not differente into new cardiomyocytes. Instead, these cells have release signals that control the healing response of cells native to the myocardium.

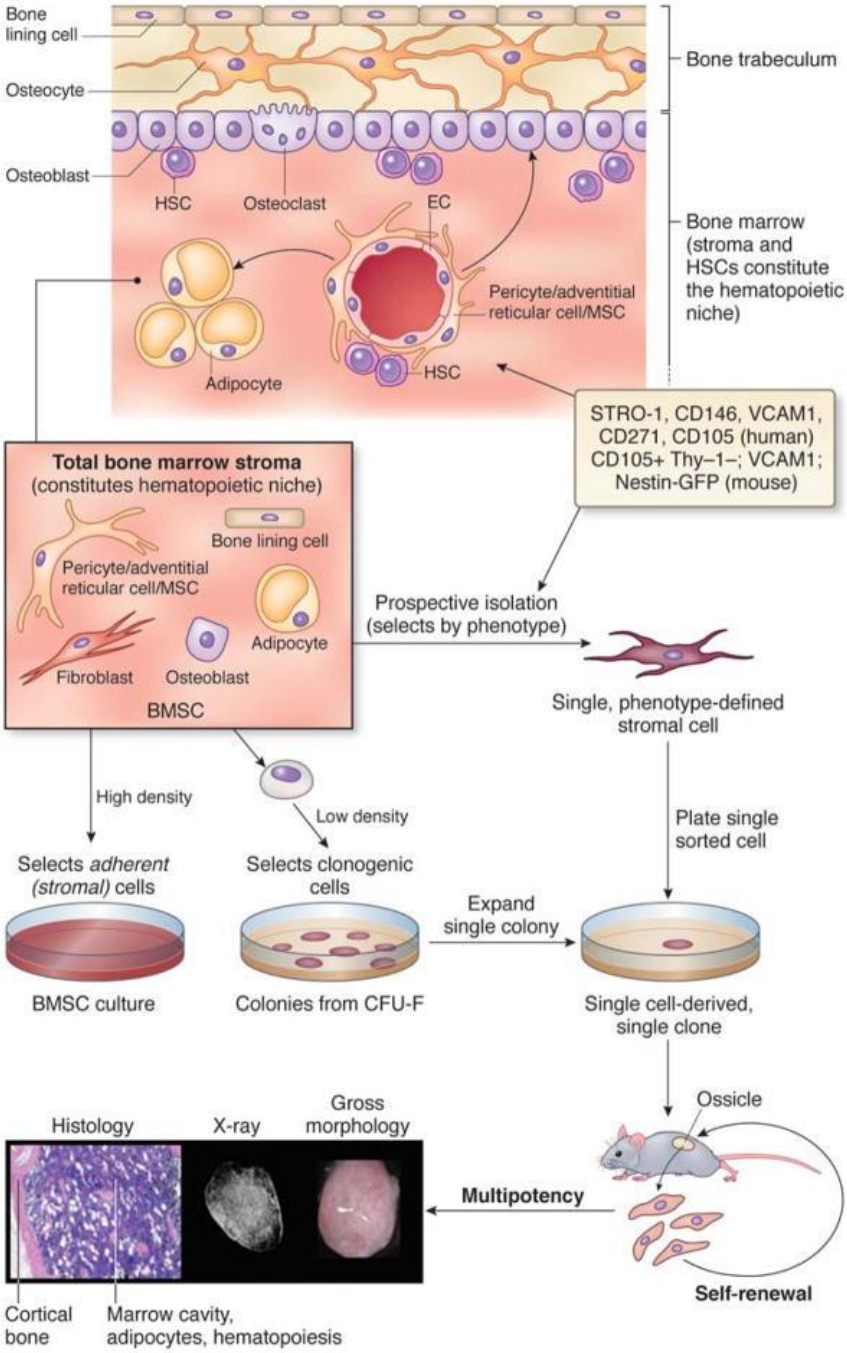

Figure 23. Bone marrow stem cells. In the postnatal bone marrow, mesenchymal stem cells (MSCs) reside around sinusoids, maintain a niche for hematopoietic cells, support hematopoiesis and replenish the differentiated compartment of osteoblasts and adipocytes during tissue growth and turnover; they also generate cartilage under specific conditions such as trauma. Total populations of MSCs are established when total bone marrow cell suspensions are plated in culture at high density. Adherence to plastic separates the stromal cells from nonadherent hematopoietic cells. If cell suspensions are plated at low density, only cells capable of density-insensitive growth are selected. These cells initiate the growth of clonal colonies. Figure from [196].

It has been reported that adult myocardium itself contains resident populations of *cardiac progenitor cells (CPCs)* capable of giving rise to new cardiomyocytes [178, 179, 181]. The role of the intrinsic progenitor cells in tissue maintenance and possible therapeutic

applications is an exciting area of investigation. Another CPC population in clinical trials is cardiosphere-forming cells. Isolation of these cells is based of their ability to migrate out of cultured cardiac tissue fragments and form spheroids in the suspension cultures [180, 199, 200]. CPCs have been reported to give rise to cardiomyocytes *in vitro* and *in vivo* after transplantation, and to enhance cardiac function after infarction [199]. The 'stemness' of CPCs has recently been questioned, and it has been suggested that these cells are principally cardiac fibroblasts [201]. Thus, although the study of CPCs is an exciting, new area of cardiac research, it is also one of the most controversial.

The described above stem cells types are present in the mature somatic tissues and their called adult stem cells. Although adult stem cells have been found to be more versatile than originally believed, they typically can differentiate to a relatively limited number of cell types, but do not yield functional cardiomyocytes sufficient for cardiac repair.

2.6.2. Pluripotent stem cells

Embryonic stem cells (ESCs) and induced pluripotent stem cells (iPSCs) have two main properties specific to truly pluripotent cells: both ESCs and iPSCs can be propagated indefinitely, while still retaining the capacity to differentiate into almost all cell types including beating cardiomyocytes.

Embryonic stem cells (ESCs) are derived from the inner cellular mass of 4-5 days old embryo, a blastocyst stage of embryonic development (Figure 24). ESCs have a number of potential advantages for cardiac repair: first, the protocols for isolation and maintenance of ESCs are well-defined, and ESCs have a tremendous capability for expansion *in vitro*, which make them scalable for human applications [202]. Second, ESCs have an unquestioned ability to differentiate into functional cardiomyocytes *in vitro* [40, 182-184].

Human ESC-derived cardiomyocytes (hESC-CMs) possess the cellular elements required for electromechanical coupling with host myocardium [183, 184]; therefore, these cells could potentially electrically integrate and contribute to heart systolic function. hESC-CMs express early cardiac transcription factors such as NKX2.5, as well as the expected sarcomeric proteins, ion channels, connexins and calcium-handling proteins. Gepstein and co-authors had demonstrated that hESC-CMs were able to survive, function and integrate in the *in vivo* heart and to be efficient as a 'biological pacemaker' [203]. Laflamme and co-authors demonstrated that grafted hESC-CMs are able to survive and proliferate in the noninfarcted rat

heart [204] or immunosuppressed pigs [203]. hESC-derived cardiomyocytes can also form pacemakers when the native one is dysfunctional [205].

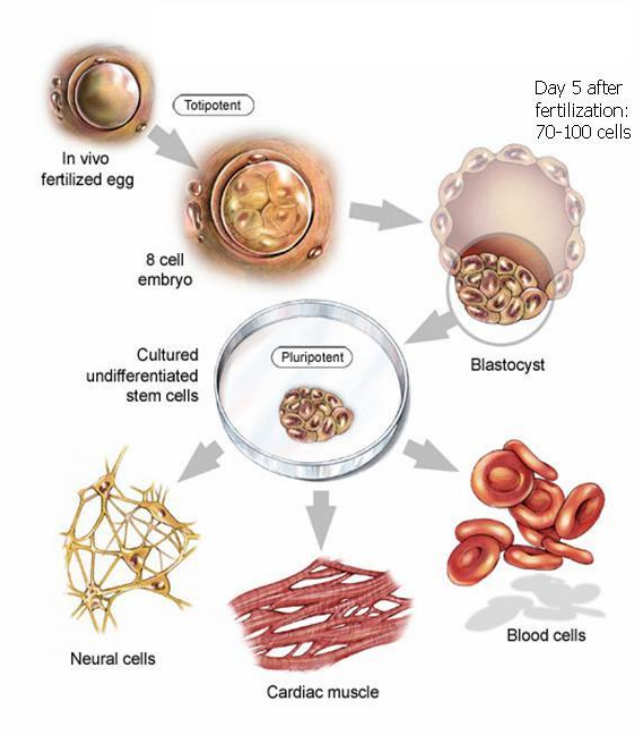

Figure 24. Human embryonic stem cells (hESC) (figure from internet). hESC are derived from 4-5 days old embryo (blastocyst stage of embryonic development) and have unlimited differential potential.

No studies have explored the suitability of hESCs to repair the heart in the setting of myocardial infarction. Therefore, the unique properties of hESC-CM and their enormous potential make them the most promising cell type for regeneration of diseased myocardium. This stem cell type has been used in the current work for the regeneration of the infarcted heart in small and large laboratory animals.

Induced pluripotent stem (iPS) cells were first established in 2006 by Takahashi and Yamanaka [186] by the reprogramming of adult somatic cells such as dermal fibroblasts using the retrovirus-mediated transduction of 4 transcription factors (c-Myc, Oct3/4, SOX2, and Klf4). Human iPS cells were established in 2007 [187, 206] by the transduction of either the same set of transcriptional factors (c-Myc, Oct3/4, SOX2, Klf4) or another set of transcriptional factors (Oct3/4, SOX2, Nanog, Lin28) into human fibroblasts. iPS cells have similar to embryonic stem cells characteristics, such as the capacity of self-renewal and differentiation into many types of cells, including cardiomyocytes (Figure 25). A lot of efforts have been made to improve the reprogramming efficiency and to establish iPS cells with either substantially fewer or no genetic alterations.

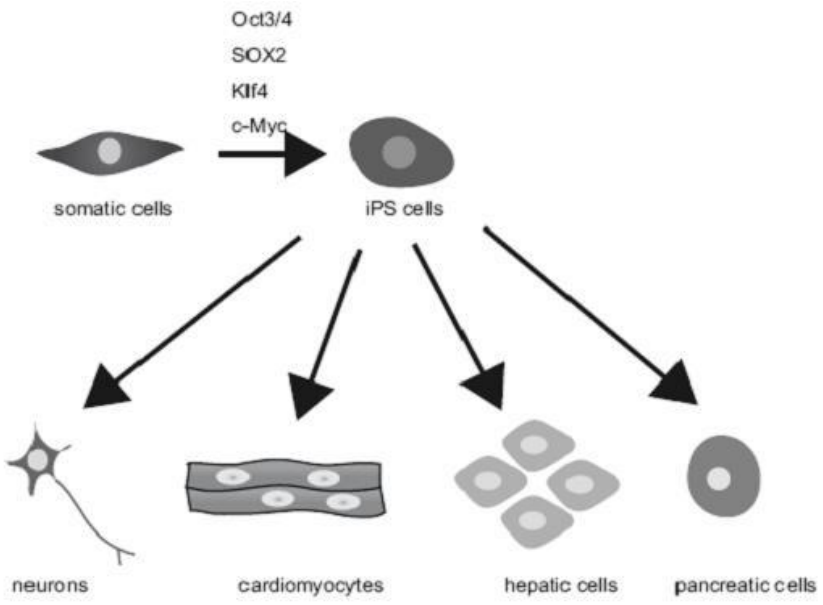

Figure 25. Induced pluripotent stem cells (iPSC). iPS cells are derived from somatic cells by introducing defined reprogramming factors, and they have the ability to differentiate into various types of somatic cells. Figure from [207].

iPS cells have been derived from various tissues, including embryonic fibroblasts [208], adult tail-tip fibroblasts [209], hepatocytes [210], gastric epithelial cells [210], pancreatic cells [211], neural stem cells [212, 213], B-lymphocytes [214], keratinocytes [215], peripheral blood cells [216] and even urinary cells [216]. It is unclear whether iPS cells derived from various tissues have the same characteristics. Application of iPSC into clinic does not raise ethical concerns since their derivation does not involve the destruction of embryos. iPS cells can be used as autologous cell transplants. iPS cells had shown the potential in several types of disease models, including sickle cell anemia [218], Parkinson disease [219], and hemophilia A [220]. The intramyocardial delivery of iPS cells derived from mouse embryonic fibroblasts was reported to successfully restore post-ischemic cardiac function while achieving the *in situ* regeneration of cardiac, smooth muscle, and endothelial tissue [221].

2.7. Cell labeling strategies

In molecular and cellular imaging, imaging probes are required to label cells or to target the biological processes of interest. The imaging probe usually consists of a carrier (such as nanoparticle, microbubble, liposome, etc.) and a signal element or contrast agent that is recognized by the corresponding imaging system. An imaging probe may or may not contain a targeting element so that the contrast agents either bind to specific cell surface proteins or are transported into the target cell by diffusion, endocytosis, or active transport (e.g., radiolabeled indium oxine and iron oxide nanoparticles) [4, 222].

Another way to label cells is integration of reporter genes into cellular DNA. Transgene then will be transcribed into messenger RNA and translated into proteins that are detectable by an imaging modality or interact with a molecular probe for imaging signal generation. Examples of MRI gene reporters are ferritin [223-225], transferrin [226-228], bivalent metal transporters DMT1 [229] and Timd2 [230-232], CEST reporters [9, 223], reporters based on gas vesicles [234], etc. Each cell labeling method has its strengths and weaknesses. Unmet needs in stem cell transplantation studies include: non-invasive detection of transplanted cells survival and measurement of graft size; evaluation of graft viability and proliferation; assessment of structural and functional integration of graft with host tissue; and discrimination of immediate vs. long term benefits of cell transplantation to determine the necessity for long term graft persistence. Currently, no single imaging modality can evaluate all these endpoints. Development of new technology for longitudinal tracking of the transplanted cell survival and functional benefits are needed. The ideal cell labeling agent would be safe, non-toxic, would be retained by target cells over sufficiently long period of time at high concentration, would correlate stoichiometrically with cell number and would be cleared rapidly after cell death. Unfortunately, none of the available labeling agents satisfy all these criteria.

2.7.1. Direct labeling

The most common contrast agents used for direct labeling are nanoparticles or radionuclides [235-237]. Nanoparticles suitable for MRI include superparamagnetic iron oxide (SPIO) nanoparticles (ferumoxides, ferucarbotran-1, ferumoxytol), gadolinium-filled microcapsules and liposomes, perfluorocarbon nanoparticles [238, 239] and manganese-based particles [240] (Table 1). Advantages of nanoparticle-based MRI cell tracking are a strong signal, allowing high-resolution visualization of the migration and homing of injected cells, as well as relative ease of cell labeling. SPIO nanoparticles also can be detected by ultrasound [241, 242].

Table 1. Cell labels in different imaging modalities.

Modality	Applications	Labels (exogenous, endogenous reporter gene)	Main characteristics	Depth of penetration	Sensitivity	Image resolution (voxel size)	Acquisition time	Injected reagents	Clearance of label after cell death	Disadvantages
MRI	Anatomy Pathology Metabolism Chemical exchange Physiology Function Intervention Cellular Molecular	Iron oxide particles Gd chelates Microcapsules with fluorine sodium carbon Ferritin Lysine-rich protein protamine	Versatile High soft tissue contrast Metabolite concentrations Perfusion Characterization of the microenvironment Short- and medium-term cell tracking Graft size	No limit	Moderate	~<1–3 mm^3	Microseconds to minutes	Stable Commercially available	Slow	Not compatible for patients with implants Acoustic noise Specialized coils (^{19}F ^{23}Na, ^{13}C)
PET	Metabolism Physiology Function Cellular Molecular	^{18}FDG $^{18}FHBG$ $^{18}FDOPA$	Graft proliferation Tissue viability Inducible cell death Longitudinal serial imaging Differentiation possibilities	No limit	High	~3–5 mm^3	Minutes to hours	Labile Commercially available, Custom synthesized	Rapid Depends on $T_{1/2}$ Isotope	Ionizing radiation Biohazardous labels
SPECT	Metabolism Physiology Cellular Molecular	Radioisotopes: Tc-99m In-111 NIS Dopamine receptor	Distribution of injected cells	No limit	High	~5 mm^3	Minutes to hours	Labile Commercially available Custom synthesized	Rapid	Ionizing radiation Limited short-term cell tracking
X-ray, CT	Anatomy Pathology Intervention Vascular delivery Biopsy	Microcapsules Barium Gold nanoparticles	Multimodal pairing with PET, SPECT Bone, lung	No limit	High	<1 mm^3	Seconds	Stable Commercially available	Slow	Ionizing radiation Not suitable for soft tissue imaging
Ultrasound	Anatomy Pathology Intervention Vascular delivery Biopsy	Microbubbles Microcapsules Liposomes	Real-time fast imaging	Tradeoff with spatial resolution	Moderate	1 mm	Seconds to minutes	Stable Commercially available	Rapid	Tradeoff between depth of penetration and spatial resolution Limited field of view

SPIO-based cell labeling approaches are used in clinical trials to track transplanted cells in the brain [243]. Labeling cells with perfluorocarbon nanoparticles is presently undergoing clinical trials [238]. Direct cell labeling with radionuclides for SPECT and PET imaging has a major advantage over MRI, CT, and US techniques because of the inherent lack of background signal. However, limited spatial resolution of clinical PET and SPECT requires image co-localization with CT or MRI. Radionuclide labeling is readily quantitated and can offer greater sensitivity than MRI, but it has the disadvantage of relatively short half-lives and considerably poorer spatial resolution than MRI. Concerns regarding radiation exposure limit the ability to repeatedly use these approaches to tracking cells [244]. Direct cell labeling with radioisotopes, such as ^{111}In-oxine or ^{99m}Tc chelates, is the most common method in SPECT imaging of inflammation [245]. The relatively long half-life (67 hours) and high *in vivo* stability of ^{111}In-oxine provides the option to acquire images after 24 hours or more, whereas ^{99m}Tc chelated agents have relatively short half-life (6 hours). ^{18}F-fluorodeoxyglucose (FDG) also can be

taken up and metabolically trapped by the cells and subsequently tracked *in vivo* [246, 247]. However, the short half-life of radiolabeled fluorine-18 (110 min) precludes its applications in long-term cell monitoring.

It is possible to combine noninvasive high-resolution MRI techniques with use of the specific targeted MR contrast agents to localize molecular targets, for example, to report on the expression of cell surface receptors [248]. Targeted contrast agents can bind to the specific surface molecules, such as integrins [249], surface phospholipids of apoptotic cells [250], vascular adhesion molecules [251] and macrophage receptors [252]. Gd-DTPA chelates can be conjugated with monoclonal antibodies to target cell surface proteins.

Delivery of the contrast agent to the target site is one of the most important issues in the development of molecular markers for MRI. If the molecular targets have intravascular locations, such as selectins [253] or $\alpha\nu\beta3$ integrin receptors [249, 254], they are highly accessible for targeted contrast agents; therefore, large blood pool nano-complexes, such as paramagnetic polymerized liposomes [255] or Gd-perfluorocarbon nanoparticles [256, 257], can be used. Delivery of the targeting molecules outside the vascular compartment is much more challenging. There were only few successful examples, such as the targeting of inflammation sites with human polyclonal IgG attached to MION particles [258, 259]. Efficient delivery of the contrast agents in this case can be explained by significantly increased vascular permeability in inflammation sites or in treated tumors. Delivery of targeted contrast agents to transplanted cells has never been successfully performed.

Although direct labeling gives strong signals in the first days after cell transplantation, it has several drawbacks for long-term imaging. First, it cannot distinguish live and dead cells [260, 261]. Nanoparticles released from dead cells are phagocytosed by macrophages [262, 263], which produce imaging signals identical to those of labeled cells. Second, contrast agents are diluted as cells divide, resulting in a gradual disappearance of the contrast [28]. Third, imaging signals can be difficult to distinguish from background. For example, SPIO nanoparticles are detectable in MRI as areas of decreased signal intensity, and similar signal voids can be caused by iron depositions in the form of hemosiderin from old hemorrhage [264]. Finally, all labeling approaches raise concerns of cellular toxicity, particularly when contrast agents are used in high concentrations. High doses of SPIOs have been shown to inhibit mesenchymal stem cell migration, colony formation ability [265] and chondrogenesis [266], although these results are controversial [267]. Therefore, it is important to assess cell viability,

cell proliferation and contrast-agent retention. In summary, the direct labels are best suited to study events in the immediate peri-transplant period (days to weeks) and are not useful to monitor longer-term (months to years) graft dynamics. A potentially important application of direct labels is real-time MRI guidance of cell delivery via vascular routes or direct implantation.

2.7.2. Indirect labeling

In indirect labeling, cells are genetically modified to express reporter genes encoding proteins that generate imaging signals. For some reporter genes a molecular probe or substrate is required that will be taken up by cells (Figure 26). Reporter genes incorporated into the genome are propagated by daughter cells, and the imaging signal is stoichiometrically related to live cell mass.

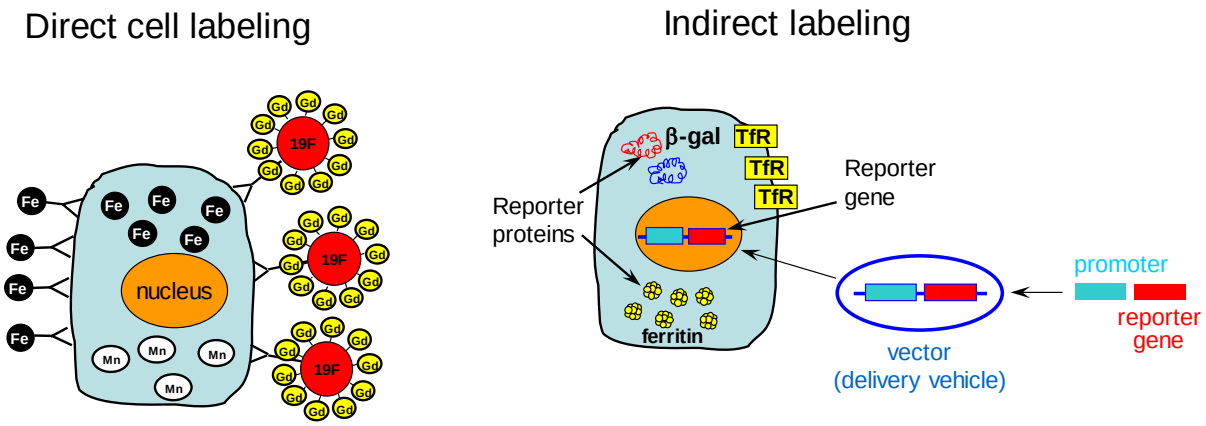

Figure 26. Cell labeling methods. Direct labeling is based on cell loading with exogenous particles containing paramagnetic or superparamagnetic contrast agents detectable by MRI. Exogenous labels can be accumulated inside the cells or attached to the cell surface using an antibody-targeted approach (iron-oxide based particles, manganese-based particles, perfluorocarbon nanoparticles, gadolinium loaded liposomes for MRI; ^{18}F-FDG radiolabeled glucose analog for PET; ^{111}In-oxine and ^{99}mTc for SPECT). Indirect labeling is based on genetic modification of cells with reporter gene construct(s) to express specific enzymes/proteins or receptors detectable by imaging (ferritin, β-galactosidase and lysine-rich protein for MRI; HSV1-tk for PET; luciferase for bioluminescent imaging; sodium iodide symporter for SPECT).

Multiple reporter proteins have been developed for different imaging modalities. Firefly luciferase, detectable by bioluminescence imaging, is often used in small-animal research; however, absorption of the emitted light precludes its use in the large animals and humans. There are several potential options for large animal and clinical applications. The natural endogenous iron-storage protein ferritin is detectable by MRI as voxels with reduced signal intensity [268]. Because ferritin is ubiquitously found in most organisms produced by naïve cells it has the potential to translate to the clinic. Herpes simplex virus thymidine kinase type 1 (HSV1-tk) is frequently used for PET imaging in large animals [269, 270] and has been

incorporated into sensitized cytolytic T-cells to image metastasis in a patient with recurrent spreading glioblastoma using a gancyclovir analog ^{18}F-9-(4-[^{18}F]fluoro-3-hydroxymethylbutyl) guanine (^{18}FHBG) [271]. The high-affinity HSV1-tk substrate, ^{18}FHBG, is phosphorylated by HSV1-tk and trapped within cells. Mammalian thymidine kinases have low affinity for this reagent making it possible to distinguish transplanted HSV1-tk cells from surrounding tissues by PET [269-273]. Another approach is genetically modifying cells to express biotinylated peptides on the plasma membrane; a contrast agent conjugated to streptavidin binds tightly to the biotinylated cells [274, 275]. Expression of a transgene expressing sodium-iodide symporter (NIS) causes cells to take up ^{123}Iodine [276]. Imaging of transplanted cells carrying a NIS reporter gene was used to follow survival and distribution in pigs by hybrid SPECT/CT imaging. This approach is promising for clinical applications because it uses a human protein that should not be immunogenic.

Chemical exchange saturation transfer (CEST) technique is a method that uses radiofrequency saturation pulses to detect molecules containing protons that exchange rapidly with water. With CEST-based approaches, the exchanging intracellular protons have a unique offset resonance that distinguishes them from extracellular water protons in the microenvironment. Exchange rate and CEST contrast depend strongly on the pH [9, 233, 277]. Because cell death and inflammation are associated with extracellular acidification, CEST probes can be used as sensors of cell viability [11]. Unique CEST-detectable amino acids and proteins (e.g., L-arginine, lysine-rich protein, protamine) can be genetically encoded and used to identify the location of transplanted cells by MRI [278]. The threshold for detecting CEST protein tagged cells by clinical MRI field strengths may range from 10^4-10^6 cells/voxels [238]. Recently, a novel reporter probe, 5-methyl-5,6-dihydrothymidine, was described for detection of HSV1-tk expression with CEST imaging [278]; this opens up the possibility of using MRI for HSV1-tk imaging. The main limitation of CEST imaging is difficulty in distinguishing the reporter signal from that of intrinsic macromolecules.

Reporter-gene imaging is widely used in animal research, but clinical applications are limited. The two main concerns are related to the safety of genomic integration and potential immune response to some of the foreign reporter proteins. Insertion of reporter genes into the genome theoretically can alter cell potency, immunogenicity [279], differentiation potential and can increase tumorigenicity [280]. Targeted integration into ‘safe harbor’ loci could address many of these concerns.

2.8. Iron and MRI contrast

MRI contrast is dependent on tissue relaxation properties in a magnetic field following a radio frequency (RF) excitation pulse. The spin-lattice (T_1) relaxation time characterizes the return of nuclear spins to the equilibrium state along the direction of the static magnetic field (B_0). The spin-spin (T_2) relaxation time characterizes the loss of spin coherence and net magnetization in the transverse plane. A relaxation mechanism of coherent transverse magnetization, called T_2* decay, combines effects of B_0-inhomogeneities, susceptibility artifacts, and chemical shifts that affect MRI contrast generation. Positive (bright) contrast is typically generated with contrast agents shortening T_1 relaxation, such as gadolinium (Gd^{3+}) or manganese (Mn^{2+}). Iron accumulation in cells and tissues affects the transverse (T_2) magnetic relaxation and T_2*-weighted MR images based on magnetic susceptibility effects. It creates dark areas of signal hypointensity, also referred to as negative contrast.

Superparamagnetic iron-oxide (SPIO) nanoparticles are the most popular agents for cell labeling. Cells may be easily labeled with SPIOs by adding these nanoparticles to cell media with or without transfection reagents. High intracellular concentrations of the SPIOs provide strong image contrast as signal void areas on T_2* weighted images (decrease in signal intensity in areas of particle accumulation up to 80-90%) or as areas of reduced T_2- relaxation on calculated T_2-maps [242, 243]. SPIO-tagged cells can also be directly imaged by Magnetic Particle Imaging (MPI) [281-283]. This recently introduced technique directly detects the intense magnetization of synthetic iron-oxide tracers using low-frequency magnetic fields which enables monitoring of cellular grafts with high contrast, sensitivity, and provides highly quantitative "hot spot" imaging [282-284]. MRI contrast can also be enhanced by manipulation of the iron content in cells using iron-associated proteins as contrast agents. Iron-associated gene reporters exhibit changes in MRI contrast and transverse relaxation in T_2- and T_2*-weighted sequences. However, iron-associated reporters exhibit weaker MRI contrast properties in comparison with nanopartiecles, which is determined by the structure of the ferrihydrite mineral core, that contains fewer iron atoms [285] as well as alignment of the iron magnetic spin moments causing smaller net magnetization [286].

2.9. Iron homeostasis

Iron is one of the essential elements for life because of its ability to donate and accept electrons with relative ease. Many proteins and enzymes have iron as an integral cofactor critical for many biological functions, such as oxygen binding and transport (hemoglobins), oxygen metabolism (catalases, peroxidases), cellular respiration, electron transport (cytochromes) and fundamental cellular processes such as DNA synthesis, cell proliferation and differentiation (ribonucleotide reductase), gene regulation, drug metabolism, and steroid synthesis [287]. Iron deficiencies as well as iron overload lead to diverse pathological changes. Iron deficiency results from defects in acquisition or distribution of the metal and causes anemia. In opposite, high concentrations of iron are toxic for cells, because free iron catalyzes radical formation in oxygenated tissues (Fenton's reaction) leading to cell damage [288, 289]. Iron homeostasis is therefore tightly regulated in the organism for maintaining the balance between iron storage and utilization by controlling intestinal absorption of the metal from the diet along with the expression of iron transport and storage proteins such as transferrin, transferrin receptor, hepcidin, and ferritin.

The human body contains ~3–5 g of iron present as heme in hemoglobin of erythrocytes (>2 g), myoglobin of muscles (~0.3 g), in macrophages of spleen, liver and bone marrow (~0.6 g). Excess of the metal is stored in the liver parenchyma within ferritin (~1 g) [290]. All other cellular iron containing proteins and enzymes bind an estimated total of ~0.008 g of iron. Iron is delivered to erythroblasts and to most tissues via circulating transferrin, which carries ~0.003 g of the metal at steady-state. In humans, normally about 30% of plasma transferrin is saturated with iron. A transferrin saturation of 45% is a sign of iron overload. When the saturation exceeds 60%, non-transferrin-bound iron begins to accumulate in the circulation and to damage parenchymal cells [291].

Most mammalian cells acquire iron from circulating transferrin upon binding of the transferrin-iron complex to the transferrin receptor (TfR). The TfR is a homodimer transmembrane glycoprotein with an overall molecular weight of approximately 180 kDa, located at the cell surface. It is ubiquitously expressed in almost all cells [292], with higher levels of expression in highly proliferating cells and those that have a functional need for iron [287]. Transferrin receptors are therefore naturally present in large numbers in erythrocyte precursors, placenta, and liver [293-296]. The main function of transferrin is mediation of iron internalization through receptor-mediated endocytosis. Most eukaryotic cells use receptor-

mediated endocytosis almost exclusively for Fe(III)-TfR uptake [297]. Iron is released from the transferrin receptor complex by a pH-change in the endosomal compartment, caused by proton-pump ATPase-activity [298]. The TfR tightly controls cellular iron homeostasis by regulating cellular uptake of holo-transferrin [299]. Mutations in the transferrin gene cause severe anemia [291]. Targeted deletion of the mouse transferrin gene causes embryonic lethality at day E11.5 due to severe anemia, indicating that transferrin-mediated iron delivery is indeed critical for hematopoietic cells [300].

Cytosolic iron is transported to intracellular sites either for local use or for storage in ferritin. Ferritin is found in most cell types of humans, animals, vertebrates, invertebrates, higher plants, fungi, and bacteria, but the concentration of the protein among different cell types can vary 1000-fold. The iron storage protein ferritin consists of a spherical polypeptide shell (apoferritin) surrounding a 6-nanometer inorganic core of the hydrated iron oxide ferrihydrite [$Fe_5O_3(OH)9$] [301]. The mammalian apoferritin is a hollow sphere composed of 24 heavy (H; 21 kDA) and light (L; 19 kDA) folded chains. The apoferritin shell can accommodate up to 4500 iron atoms attached to the inner wall of the shell [302-304]. Iron load in ferritin is dependent of the H_2O_2 detoxification reaction and can be at low, intermediate, and high iron level [305, 306]. Ferritin stores iron in soluble form, available for use by enzymes and for DNA synthesis. Both ferritin subunits are ubiquitously expressed, but their expression ratios vary depending on the cell type and in response to stimuli such as inflammation or infection. Ferritin H-chain has the ferroxidase activity that is necessary for iron deposition into the nanocage, while ferritin L-chain facilitates iron nucleation and increases the turnover of the ferroxidase site. Ferritin provides cells with a means to lock up excess iron in a redox-inactive form to prevent iron-mediated cell and tissue damage [289, 307, 308]. There are three variations in ferritin function in different cell types: a) the storage of iron for other cells (e.g. recycling iron in macrophages, short- and long-term iron storage in red blood cells of embryos or in hepatocytes of adults); b) the storage of iron for intracellular use (providing reserve of iron for cytochromes, nitrogenase, ribonucleotide reductase, hemoglobin, myoglobin); and (c) detoxification in iron excess [309, 310]. Expression of ferritin is essential for life which is proved by the early embryonic lethality of ferritin H-chain knockout mice [311].

Mammalian cells can obtain iron via multiple routes based on the specific biochemical requirements. Additionally to a transferrin-mediated endocytosis, cells can acquire iron complexed with proteins or small molecules. For example, internalization of ferritin via

ferritin-specific receptors such as T-cell immunoglobulin and mucin-domain containing protein-2 (TIM-2) [230] or Scavenge receptor family class A, member 5 facilitates iron import [312]. Cells can internalize iron indirectly via a heme carrier protein-1, HCP-1 [313]. Iron can also be transported from lysosomes to the cytosol by the heme response gene-1, HRG-1 [314].

Cells also express mitochondrial ferritin (Ft_{mt}) that, similarly to H-ferritin, possesses ferroxidase activity [315]. In contrast to cytosolic ferritin, the expression of Ft_{mt} is restricted to few tissues and is not iron-regulated [316]. Ft_{mt} serves as a molecular sink to prevent accumulation of unshielded iron in mitochondria, which protects the organelle against iron's toxicity. The iron storage capacity of Ft_{mt} is similar to the ubiquitous ferritin, however Ft_{mt} has greater avidity for iron [317] and higher iron load when Ft_{mt} is expressed as a transgene in a cell line [318].

The presence of ferritin is not limited to the intracellular compartment. It is also found in body fluids, such as serum, cerebral-spinal fluid and synovial fluids. The origin of the extracellular ferritin may originate from cell damage or from active and regulated ferritin secretion. Assessing the concentration of serum ferritin is a clinically useful index of body iron status. Low serum ferritin levels indicate depleted stores and iron deficient anaemias, whereas increased levels may indicate iron overload. Serum ferritin concentration increases also in inflammation, infection, liver diseases, cancer and in response to oxidative stress [291, 319]. At high iron loading, ferritin aggregates in the lysosomes to form hemosiderin [320, 321]. Hemosiderin is a mixture of ferritin, lipids and iron [322, 323] that is often formed during pathological processes and neurodegenerative diseases associated with altered brain iron metabolism such as Alzheimer's and Parkinson's diseases, and multiple sclerosis [324-327]. Iron deposition in the brain also increases as a result of the normal aging process, and these changes are detectable by MRI [328].

2.10. Endogenous iron associated proteins as MRI reporters

The properties of endogenous proteins involved to regulation of the cellular iron content allowed to study those as potential imaging reporters capable in MRI contrast modulation. Examples of genetically encoded iron-associated proteins employed to image of distinct cell populations are shown below.

2.10.1. Transferrin receptor (TfR)

The TfR was the first MRI reporter gene proposed by Koretsky et al in 1996 [226], based on its function of facilitating metal transport across membranes by internalizing the

transferrin-iron complex through receptor-mediated endocytosis [329]. It raises the level of labile iron in the cells, therefore can be used as one potential way to generate MRI contrast. The transferrin receptor has a fast rate of turnover ($2x10^4$ transferrin molecules internalized per minute), which results in the quick uptake of large amounts of iron [330]. The synthesis of the endogenous receptor is tightly controlled through an iron-dependent negative feedback in cells; this provides an adequate supply of the essential metal in function of the iron need, while guarding against toxic excess of iron [299, 331, 332]. Genetic modification of cells to express a TfR lacking mRNA destabilization motifs leads to constitutively overexpressed high levels of transferrin receptor with subsequently increased accumulation of iron in cells, resulting in higher MR contrast [227].

The TfR is a receptor that can be (over-)expressed in very high numbers (several million copies per cell) on the cell membrane. Fibroblasts overexpressing TfR exhibited an approximately threefold increase in iron content yielding significant MRI contrast in T_2-weighted sequences [226]. In the absence of iron, the binding sites of transferrin can accommodate a number of other metals including gallium, copper, chromium, cobalt, manganese, vanadium, aluminum, terbium, plutonium, europium, indium, and platinum [330]. The feasibility of manganese labeling of murine hepatocytes via the transferrin-receptor-dependent and/or independent metal-transport pathways has been documented [333]. This method of cell labeling is based on the chemical similarities between manganese and iron (e.g., similar ionic radii; similar valence states (II) and (III) – under physiological conditions; and similar binding affinities for transferrin). The results of these studies demonstrate that Mn(III)-transferrin is an effective MRI contrast agent for labeling murine hepatocytes.

2.10.2. Ferritin, iron storage protein

The intracellular level of ferritin can be genetically altered. The higher number of ferritin complexes per cell causes higher iron accumulation, thus directly affecting MRI contrast. The possibility of using ferritin in biomedical imaging and cell labeling was shown in 1992 by Meldrum [301]. In 2005 ferritin and eGFP expression under tetracycline control was used to visualize C6 glioma cells transplanted to the mouse [223]. At the same time use of ferritin as an MRI reporter gene was demonstrated by injecting an adenoviral vector for transient overexpression of human ferritin into the brain parenchyma of mice, resulting in significant loss of signal at the site of vector injection [224]. During the last decade, ferritin overexpression has been extensively explored for a variety of applications, such as imaging of

transgenic tumors [223, 334, 335]. Ferritin overexpression has been detected *in vivo* in the mouse brain [224, 225], *in utero* in transgenic mice [336] and in liver hepatocytes [337]. A ferritin shell was used in material science as a precursor for making nano-composite particles as an effective MRI contrast agent for macrophage tracking [338] and for non-invasive imaging of atherosclerosis [339]. Replacing the native iron core in ferritin with a synthetic paramagnetic core [340] has proven to result in effective T_2/T_2*contrast both *in vitro* [340] and *in vivo* [341]. Additionally to cell labeling, it was shown that a ferritin expression vector can also be used to monitor *in vivo* gene expression [334]. GL261 mouse glioma cells expressing ferritin–DsRed fusion protein under b-actin promoter showed reduced T_2-weighted signal intensity for *in vitro* and *in vivo* MRI studies as well as DsRed fluorescence in optical imaging. First application of mitochondrial ferritin (Ft_{mt}) as an MRI reporter has been proposed by Iordanova [342]. In that study, mitochondrial ferritin was modified to localize within the cell cytoplasm for efficient iron load and MRI tracking on olfactory sensory neurons [342]. Ferritin expression has not been used as MRI reporter for non-invasive imaging of cardiac grafts until the present study.

It is important to emphasize that no exogenous iron supplementation is required for MRI contrast generation by overexpressed ferritin. The fact that ferritin-tagged grafts cause strong signal intensity can be explained only by redistribution of endogenous iron and its accumulation from the host tissue in the overexpressed ferritin complexes [223]. However, external iron supplementation can enhance MRI contrast based on ferritin overexpression [343].

To date, several molecular biology approaches and different vectors have been used to overexpress ferritin: adenoviral [224], retroviral [223], lentiviral [335, 344-346] and adeno-associated virus gene delivery [346]; different plasmid vectors have also been used [228, 334, 347]. The technique chosen for reporter gene expression is crucial as its properties will determine whether contrast generation will be transient or stable, constitutive, inducible or tissue-specific. Continuous expression is best suited for tracking the survival and the migration of labeled cells. Therefore, several studies investigating MRI reporter genes for long-term tracking of transplanted cells have focused on methods to introduce reporter genes stably into the cells of interest, such as lentiviral (LV) and adeno-associated viral (AAV) vectors for reporter gene expression. By introducing a genetic switch, ferritin expression can be turned on or off and changes in the imaging signal can be detected within several days thereafter [223,

337]. Being able to control overexpression is important in avoiding potential toxicity issues associated with constitutive overexpression of ferritin, even though overexpression of ferritin results in suppression of the damaging Fenton reaction and thus can protect cells from oxidative damage enhancing the survival of the administered cells. These results suggest that ferritin holds significant promise as translational MRI reporter gene for *in vivo* imaging of live transplanted cells.

2.10.3. Bacterial magnetosome-associated MRI reporters (magA and mms6)

Iron-associated biomolecules were found not only in mammalian cells, but also in bacteria, and explored as potentially interesting MRI reporter genes. Formation of iron biominerals is a naturally occurring phenomenon among magnetotactic bacteria which produce magnetite (Fe_3O_4) in a subcellular compartment termed the magnetosome. There are two main components to the magnetosome: the biomineral and the lipid bilayer that surrounds it. Magnetotactic bacteria naturally synthesize these intracellular magnetic structures which help to direct motility of the bacteria based on the earth's magnetic field [348, 349]. The magnetosome-associated proteins are important for vesicle formation, cytoskeletal attachment, iron transport, and crystallization [350]. Expression of magnetosome genes in non-bacterial cells provides new opportunities for development of reporter gene-based contrast for MRI.

Based on the involvement of *magA* in the synthesis of magnetosomes in *Magnetospirillum* bacterial species [351-353], the use of this gene has been explored as an inducer of MRI-detectable contrast. It has been shown that *magA* can be expressed in mammalian cells and its expression leads to the formation of magnetic nanoparticles that strongly affect the MRI signal [354]. However, it is not yet known if *magA* expression leads to the formation of the same iron oxide crystals seen in magnetotatic bacteria. MRI detection of *magA* expression has been shown in mouse neuroblastoma (N2A) cells [355] and in the human 293FT cell line [351]. The iron-based MRI reporter *magA* resulted in larger increase in R_2 relaxation: cell pellets expressing *magA* consistently showed an increase in R_2 of approximately three- to four-fold [354], comparing to an increase in R_2 of approximately 2.5-fold for ferritin expression [224]. It was shown that expression of both magnetotactic bacterial gene *magA* and mammalian iron storage protein ferritin in MDA-MB-435 tumor cells sequestered iron within a membrane-enclosed vesicle and permitted iron biomineralization with simultaneous regulation of mammalian iron homeostasis [356]. These results highlight the potential of magnetotactic bacterial gene expression for improving MR contrast. However,

magA's status as a putative MR reporter gene is controversial as its implication in magnetosome formation has been contested [353].

Another bacterial gene, magnetosome-associated mms6, has been proposed as a reporter gene for MRI of mammalian cells [357]. In vitro experiments show that mms6-expressing cells form clusters of nanoparticles within and outside membrane-enclosed structures and produce changes in MR contrast, most likely by increasing iron uptake of intracellular iron. In vivo MRI experiments demonstrate that mms6-expressing tumors can be distinguished from parental tumors not expressing mms6, even in the absence of exogenous iron supplementation. Whether mms6 is an efficient genetic MR reporter, remains to be established, and potential toxicity issues should be clarified. Mms6 protein fused to the C-terminal of murine h-ferritin has been proposed as a novel chimeric magneto-ferritin reporter gene, ferritin-M6A, enabling magnetite biomineralisation of ferritin and enhancing R2 relaxivity of ferritin-M6A-expressing C6-glioma cells [358].

2.10.4. Timd2, mediator of ferritin endocytosis

T-cell immunoglobulin and mucin domain containing protein receptor (Timd2 or Tim-2) is expressed primarily on immune cells, where it plays a role in signaling and mediates ferritin endocytosis [230, 231, 359]. Timd2 expression elsewhere is limited, but is also found in both liver and kidney, where it functions primarily as a ferritin receptor to remove ferritin from the blood [230], as well as on oligodendrocytes, where it is upregulated during myelination to meet increased iron demands [231]. It has been shown that cells expressing Timd2 and incubated with ferritin or manganese-loaded apoferritin showed large increases in R_2 and R_1, respectively. Cells expressing Timd2 implanted as xenografts in mice also showed changes in R_2 following intravenous injection of ferritin, although these changes in contrast were more modest than those observed *in vitro* [232]. Therefore, Timd2 represents another potential MRI-based gene reporter.

2.11. Imaging of myocardial regeneration

Medical imaging is essential in the evaluation of cardiac repair by regenerative therapy. End points that can be measured include heart contractile function, morphology, vascularity, inflammation, infarct size, tissue viability, and metabolism. Infarction causes significant loss of cardiomyocytes (often 25% of the left ventricle), which cannot be restored by current pharmaceutical therapies. Stem cells offer the possibility of rebuilding the damaged heart from its component parts. Functional outcome after cell transplantation is dependent on several

aspects, including engraftment success, graft survival, structural and functional integration within the host tissue. Non-invasive imaging can help to define the optimal cell type, delivery method and time, changes in host microenvironment as well as provide information about off-target behavior and oncogenic events. The following three conditions must be achieved to prove true myocardial regeneration: 1) an increase in the volume of viable myocardium within the infarct zone; 2) structural integration of the new myocardium with the host tissue, including restoration of myocardial fiber architecture; and 3) functional integration of the new myocardium with host myocardium without conduction delay or arrhythmias. Medical imaging is essential in the evaluation of cardiac repair by regenerative therapy. End points that can be measured include heart contractile function, morphology, vascularity, inflammation, infarct size, tissue viability, and metabolism.

Imaging studies have shown that cell therapy in the heart to date is hampered by low retention of transplanted cells. For example, PET scans showed that retention of stem cells in the ischemic myocardium was dependent on the delivery method and cell type. Intravenous injection of adipose-derived stem cells resulted in relatively few cells (1.2%) being retained in the infarcted rat heart [360]. Similarly, low retention (1.5%) of ^{18}F-FDG-labeled peripheral hematopoietic stem cells was observed at 2 hours after intracoronary administration to patients with myocardial infarction [361]. ^{111}In-labeled peripheral blood-derived progenitor cells delivered by intracoronary routes to acute infarct patients were retained at 6.9%, and lower retention (~2.5%) was found in a subgroup of patients with chronic myocardial infarction [362]. Low viability of the infarcted myocardium and reduced coronary flow reserve were significant predictors of pro-angiogenic progenitor cell homing [362]. Direct injection into the myocardium has been shown to be the most effective delivery method for cell transplantation to the heart. Cell retention was systematically studied in acutely infarcted rats using MRI and PET, and direct injection afforded 14% retention, significantly greater than rates with injection into the LV cavity (3.5%) or intravenous delivery (1.2%) [360]. Biodistribution studies demonstrated that a substantial number of bone marrow mononuclear cells injected into the rodent heart migrated to the bone marrow, liver, and spleen [363]. Low retention of transplanted cells may explain some of the poor clinical results. Retention of cells in the heart can be increased by injecting them in a hydrogel made of either natural or synthetic materials. PET/CT imaging was used to detect human MSCs expressing HSV1-tk implanted with Matrigel in uninjured porcine myocardium [270]. Surprisingly, myocardial radiotracer

(^{18}FHBG) uptake was not elevated when $200x10^6$ human MSCs were directly injected in PBS, despite the grafts being readily detected by histology. When the same number of cells was injected in Matrigel, SNR increased to 1.87, and increased further to 8.02 when $600x10^6$ cells were administered. The relatively low sensitivity for PET detection in this study may relate to timing: imaging was done the same day as cell transplantation, so delivery of radiotracer required its diffusion into a vascular cell clumps. Presumably, a graft that is vascularized would be more easily detected.

Once cells are successfully retained in the heart, the next challenge is the wave of cell death that is initiated by ischemia, loss of survival signals due to matrix detachment, and the toxicity of reactive oxygen species and cytokines [364]. Long-term survival of transplanted cells in the heart can be monitored using the sodium-iodide symporter and SPECT imaging, where viable human iPSC derivatives were visualized for up to 15 weeks in the infarcted pig heart [276]. It was also reported that ^{111}Indium-labeled endothelial progenitor cells were cleared more quickly by SPECT from reperfused canine infarcts than from infarcts with permanent coronary occlusions [362, 365].

Quantitative imaging, such as diffusion-tensor imaging (DTI), can be used for assessment of the fiber architecture in remodeled myocardium in animals and humans *in vivo* [8, 366, 367]. Myocardial fibers have complicated helical structure that is critical for efficient contractile and conductive function of the heart. DTI tractography has shown a smooth transition in fiber orientation from epicardium to endocardium in the healthy heart and severe disruption of myofiber architecture after infarction [367]. Transplantation of bone marrow mononuclear cells [8] was associated with preserved myofiber architecture a small subset of hearts in a murine infarct model based on DTI, indicating that this technique has potential for assessing structural integration and adequate alignment of the transplanted cells with host myocardium in humans.

Finally, imaging is useful for evaluating functional integration of transplanted cells with host myocardium. It is important to determine whether the graft is electrically connected with the host tissue whether transplanted cells create areas of arrhythmia. Recently, a genetically encoded Ca^{2+}-indicator fused with green fluorescent protein was used to demonstrate that human ESC-derived cardiomyocyte grafts are electrically coupled with host myocardium of the guinea pig [368] and of a non-human primate [369], indicating that this cell type meets physiological criteria for true heart regeneration.

In summary, imaging has played an important role in advancing cell-based cardiac repair, providing key information on transplanted cell retention, viability, proliferation, graft size, integration with the host tissue and restoration of myofiber architecture, in addition to providing evidence for enhanced cardiac structure and function. Future approaches should include development of novel exogenous imaging probes capable of detecting dynamic changes in grafted cells (i.e., labeling live transplanted cells and that quickly disappear after cell death) and development of techniques for genetically labeling cells for their long-term tracking in humans and animals.

2.12. Animal models to study human heart disease

Animal models are an important in research to study a variety of cardiac diseases and therapeutic approaches. Large animals are often used for pre-clinical testing of new pharmacologic agents, cell-based regenerative therapies in infarction or heart failure models, interventional and surgical approaches in treatment. Disadvantage of the large animals is the high cost of housing, veterinary care and maintenance. Small animals, especially mice, are increasingly popular in research because large number of genetically modified rodents are available to study mechanisms of diseases. Small animals are much less expensive than large animals, easier to handle, therefore, more popular in research. The choice of animal model is dependent of the study aims, primary hypothesis and on the available resources and facilities.

A number of large animal models have been developed for cardiovascular research because of the naturally occurring heart failure or induced heart failure by specific interventions [370]. Non-human primates are the closest animal species to humans with similar physiology, therefore primates are the preferable animal species in pre-clinical research. However, high cost of these animals is prohibiting its wide use. Swine as a cardiovascular disease model are widely used for studying treatment effects, developing new devices, and developing interventional MRI techniques. The collateralization in swine is relatively non-existent and less than seen in humans. Farm pigs or Yucatan mini-pigs are used as modes of cardiovascular diseases and in testing of new treatments and interventions. Myocardial damage models of heart failure include induced ischemia, caused by coronary occlusion or intracoronary microembolism, toxic cardiomyopathy from adriamycin, doxorubicin or catecholamines. Overload models of heart failure may be induced by high pressure from aortic constriction, aortic regurgitation, renal artery constriction, pulmonary stenosis or aortocaval shunts, or by induction of mitral regurgitation from chordae or leaflet damage. Large animals

are also used to study myocardial complications of the genetic diseases, for example, dogs with Duchenne muscular dystrophy [371].

While all mammals have 4-chamber heart, there are some other differences in cardiovascular anatomy and physiology in different laboratory animals. The differences include heart size, heart rate, development of collateral vessels, while the blood pressure remains relatively constant across various laboratory animals and humans (Table 2). The closed-chest, ischemia-reperfusion models were originally developed in dogs, ethical issues and the extensive collateralization in the canine heart has limited their use. Hearts of smaller species contract and relax more rapidly than larger species in order to maintain cardiac output. This difference in cardiac contractile kinetics vary between species due to differences in excitation, calcium handling, myofilament protein isoforms, etc. (figure 27).

Table 2. Comparison of cardiovascular parameters of human and animal models. Table from [372].

Species	Body Weight (kg)	Heart Rate (bpm)	Systolic Pressure (mmHg)	Diastolic Pressure (mmHg)
Mouse	0.02–0.063	310–840	113–160	81–110
Rat	0.225–0.52	250–493	84–184	58–145
Rabbit	1–6	130–300	90–130	60–90
Canine	7–16	70–160	95–136	43–66
Sheep	20–160	60–120	91–116	102
Pig	200–300	50–116	135–150	-
Human	50–86	72	120	80

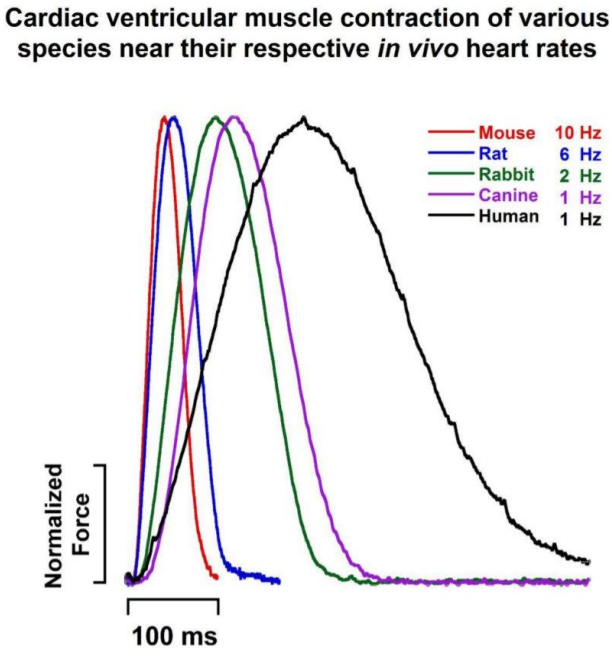

Figure 27. Right ventricle muscles stimulated *ex vivo* near the species' resting heart rates at 37°C. Figure from [373].

Small rodents are easier to handle, and they have lower maintenance cost than larger animals. These characteristics make rodent models the most used model for cardiac physiology and disease, genetics, pharmacology, and long-term survival studies. Many different genetic models of the human diseases are available in mice. Mouse models of the genetic diseases can be developed in a shorter period of time due to their short gestation age of ~18–21 days [372]. However, even if the genetic mouse models recapitulate some of the characteristics of the human cardiac phenotype of a disease, but findings in mice cannot be directly translated to the humans. Due to the extremally fast heart rate in rodents, the kinetics of contraction and relaxation are considerably accelerated in small rodents (Figure 27). The action potential properties and myosin heavy chain isoforms are responsible for faster contractile and relaxation kinetics in small rodents. This shows the limitations of using small rodents for studying cardiac kinetics; larger animal species generally are better suitable for translational studies to humans.

Large and small animals are handled differently during MRI examination. While MRI protocols and pulse sequences developed for human patients can easily be modified and implemented for large animal studies, the small animals are much harder to image, especially the fast beating rodent heart. While the breath hold can be used in cardiac MRI on large animals, this technique is not available for imaging of rodents. A special equipment for ECG and respiratory gating should be used in rodent studies. Measurements of LV mass, wall thicknesses, and internal dimension of the LV chamber in end-systole and end-diastole are possible even in the smallest mammals used in the pre-clinical studies [79, 117, 374, 375]. The necessity in development of MRI technology for small animal imaging is based on a growing interest in transgenic animal models, mostly mouse models.

The degree of myocardial damage after infarction is varying in different animals. This depends of the animal physiology, development of collateral vessels in the heart, development of fibrosis and revascularization. Examples of the infarcted heart MR images of different animal species are shown in the figure 28. Similar imaging approach can be used in different animal species to visualize infarction (inversion recovery pulse sequence at 10-20 minutes after injection of gadolinium). In summary, the choice of the animal model to study cardiovascular diseases is very important and should be relevant to the disease in humans. The experimental outcomes are depending of the chosen animal model; this should be accounted

especially in the translational studies, whether findings of the study can be reasonably translated to humans.

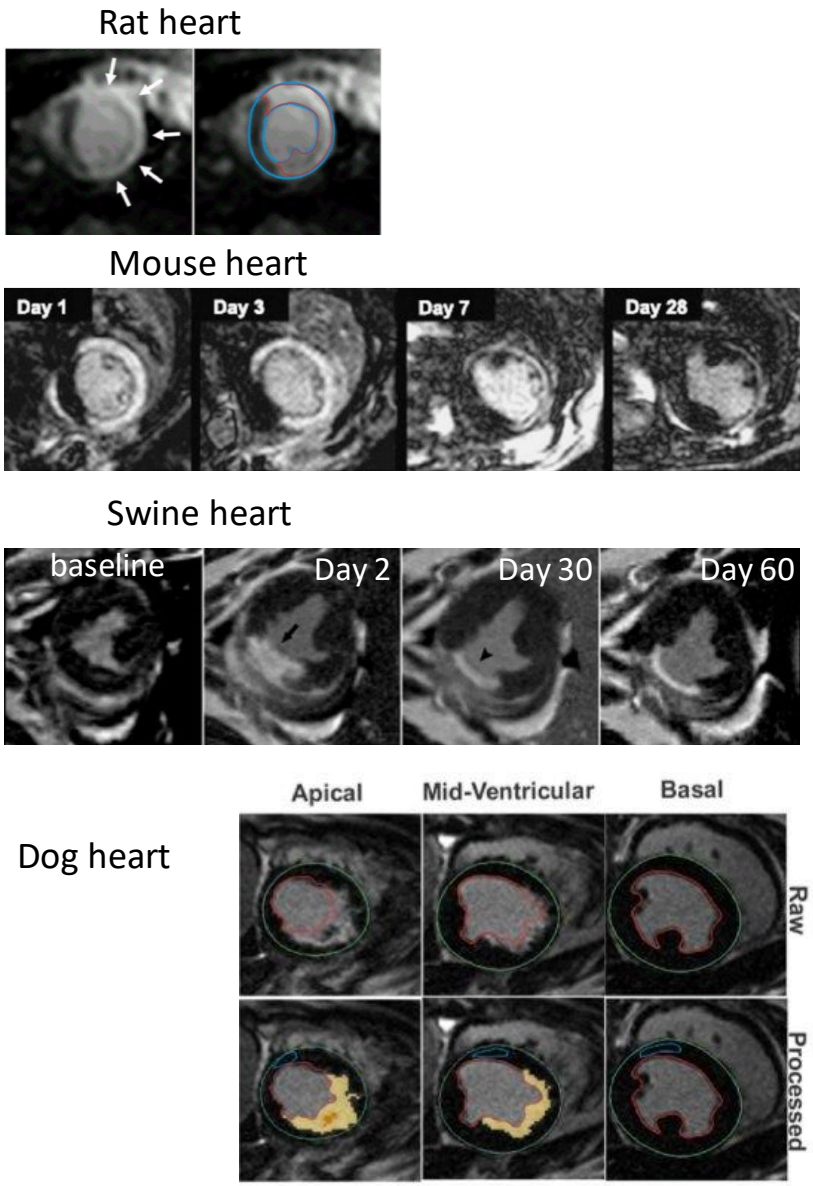

Figure 28. Examples of the late Gd-enhanced (LGE) MRI of the infarcted heart in different animal species. Inversion recovery pulse sequence was used.

1. Rat heart at 1.5T. The bright hyper-enhanced region (white arrows) corresponds to non-viable infarcted myocardium. Following planimetry (right) of the epicardial and endocardial border (blue lines), the hyper-enhanced region (red) can be segmented using full-width half-maximum criteria (Gilson and Kraitchman, 2007).

2. **Mouse heart.** Gd-enhanced MRI in mice can be used to assess the temporal evolution of scar during the course of post-infarct LV remodeling: infarct expansion, wall thinning, and scar development (French et al, 2005).

3. **Yucatan mini-pigs at 1.5T**. Time-course of the ventricular remodeling was studied in up to day 60 after infarction. There is increased wall thickness at the infarct region (arrows) followed by wall thinning (arrow heads) at later time points. (Lopez et al, 2017).

4. **Dog heart at 3T**. LGE images of basal, midventricular, and apical slices acquired at 7 days after myocardial infarction in a dog. Infarcted myocardium was identified on LGE images using the mean+5SD criterion with respect to the reference region of interest drawn in remote myocardium (Kali et al, 2014).

3. MATERIALS AND METHODS

3.1. Echocardiography

Small animals. Two days following the ischemia-reperfusion infarction and two days prior to engraftment, the rats were anesthetized with inhaled isoflurane (Novaplus, Lake Forest, IL) and scanned by transthoracic echocardiography (GE Vivid 7, Milwaukee, WI) with a 10S (10 MHz) pediatric probe to record physiological data and to stratify the rats by left ventricular systolic function. Specifically, the left ventricular end diastolic dimension (LVEDD), the left ventricular end systolic dimension (LVESD) and heart rate (HR) were measured and recorded. Fractional shortening, an index of LV systolic function, was calculated by this equation: FS = 100 × (LVEDD – LVESD)/LVEDD. HR is expressed in beats per minute (bpm).

Large animals. All the echocardiographic images in dogs and non-human primates were acquired using an ultrasound system with a 7 MHz probe (Vivid-7, GE Healthcare, Horten, Norway) at the following time points: prior to MI, 14 days after MI (prior to intravenous cell infusion), and prior to euthanasia. The animals were sedated with the combination of drugs, including butorphanol 0.1 mg/kg i.v., acepromazine 0.025 mg/kg i.v., glycopyrrolate 0.011 mg/kg i.v.; or diazepam alone (0.275-0.55 mg/kg i.v.; or diazepam with acepromazine. The animals were then examined in the prone position to acquire 2-dimensional gray-scale images in 3 standard apical views (i.e. apical 4-chamber, apical 2-chamber, and apical long-axis) for 4 cardiac cycles. Based on the recommendation of the American Society of Echocardiography [376], left atrial volume index (LAVi) and the ratio of early transmitral velocity to tissue Doppler imaging (TDI) annular early diastolic velocity (E/e′) were used to assess LV diastolic function. Pulsed-wave Doppler was acquired to measure the peak early wave velocity (E) of the mitral inflow and the TDI early diastolic velocities (e') at the septal mitral annulus. E and e' were measured at 3 end-expiratory beats and averaged for further analysis. Off-line analysis was performed using automated function imaging software (EchoPAC work station, BT09, GE Healthcare, Israel) by 2 independent cardiologists blinded to experimental conditions. Peak systolic longitudinal strain was automatically obtained from the 3 standard apical views. The average peak systolic longitudinal strain value from the 3 apical views is defined as GLS [344].

3.2. Magnetic resonance imaging (^{1}H MRI) and spectroscopy (^{31}P MRS)

Cardiac MRI and ^{31}P NMR spectroscopy on mice

Experiments were performed using a GE Omega NMR spectrometer and Bruker Medical BioSpec Spectrometer (Bruker BioSpin Corp) equipped with a 4.7T / 40 cm Oxford

magnet and a 15 cm (ID) actively shielded AccustarTM gradient set. Mice were anesthetized with 1% isoflurane in oxygen (1 liter/min) delivered through a nose cone and placed in a custom-constructed ^{1}H coil with the heart centered over the ^{31}P coil on a flat Plexiglas platform with temperature control (37±1°C). The mice were rotated to the left so that the un-involved septum was centered over the surface coil thus minimizing contributions from the infarcted lateral wall. Single-lead ECG was recorded from platinum electrodes attached to each animal's extremities and was used to trigger the MRI acquisitions using commercial software ("Small Animal Monitoring and Gating System" SA Instrument Inc., Stony Brook, NY).

High-resolution spin-echo transverse ^{1}H MR images (echo time 11 msec, recycle time 500 msec, slice thickness 2 mm, field of view 32 mm, acquisition time 2 min) were obtained to define the regions of metabolic interest, as well as to confirm the position of the left ventricle over the center of the ^{31}P MRS surface coil (OD 11 mm), and to quantify left ventricular function. A set of multi-slice short-axis images (slice thickness 1.2 mm without gap between slices) for end systole and another for end diastole were acquired. Each slice was acquired exactly at the same time during R-R interval in cardiac cycle. Epicardial and endocardial borders were manually delineated for determination of left ventricular volumes at end systole and end diastole (ESV, EDV) and left ventricular mass (LV mass) using the software package NIH Image version 1.52 (Bethesda, MD) for a Macintosh computer. Total LV volumes were calculated as the sum of all slice volumes. Stroke volume (SV) was calculated as EDV minus ESV and cardiac output (CO) as SV multiplied by heart rate (HR). The left ventricular ejection fraction (EF) was calculated from the relative difference in end-diastolic and end-systolic cavity volumes. Myocardial infarct size was determined from short-axis systolic images. The circumference of the left ventricle that was thinned due to infarction (systolic wall thickness <0.5 mm) was compared with that of viable tissue and a score was assigned as a percent of overall ventricular circumference [375]. For each heart, the mean score was determined from all of the image slices.

Spatially localized ^{31}P MR spectra were acquired after optimization of the magnetic field homogeneity using the 1H coil to shim on a thick slice containing the heart. A one-dimensional chemical shift imaging sequence (1D-CSI) was used with 32 phase encode steps in the direction perpendicular to the plane of the coil. The time of the phase encode gradient was 0.5 msec, the field of view 32 mm, the recycle delay 1s, and 64 averages were obtained per phase encode step. Adiabatic pulses with a flip angle of 45° were used for uniform

excitation. Total acquisition time was ~34 min. In a prior study these non-invasive image-guided ^{31}P MRS techniques gave identical results to those obtained from invasive measures, indicating minimal contamination from surrounding structures with this approach [129]. All mice awoke within ~1 min after completing the MRI/MRS examination.

^{31}P spectra were analyzed with a combination of custom [49] and proprietary (NIH Image, Bethesda, MD) software. The PCr/ATP ratio was determined from the integrated peak areas of the creatine phosphate and [β-P]ATP resonances from voxels centered on skeletal muscle in the anterior chest or on cardiac muscle identified from the high-resolution ^{1}H MR images, as described previously [12]. Voxel shifting was performed when necessary to optimize slice alignment with cardiac structures and minimize skeletal muscle contamination of cardiac spectra [48]. The PCr/ATP ratios were corrected for partial saturation effects using a factor determined in separate studies that included fully relaxed acquisitions [12, 128, 129, 377].

Non-invasive MR imaging of myocardial grafts in mice

The clinical 3T Achieva Philips scanner with 42 cm horizontal bore and gradient strength 80 mT/m has been used. A single-channel solenoid mouse coil (Philips Research Laboratories, Hamburg, Germany) was used with a built-in heating system maintaining physiological body temperature. Animal sedation was induced by the inhalation agent isoflurane (3% in oxygen) in an induction chamber; anesthesia was maintained during imaging session by 1% isoflurane in oxygen (flow rate 1 liter/min) delivered through a nose cone. The Small Animal Monitoring and Gating System (SA Instrument Inc., Stony Brook, NY) was used for physiological monitoring of heart rate, respiration and body temperature. The electrocardiogram (ECG) of the mouse heart was recorded using needle electrodes attached to the animals' extremities subcutaneously. MRI acquisitions were triggered by R-peaks of ECG. The imaging protocol included three ECG-gated sequences applied in the short-axis plane with 1 mm slice thickness providing whole-heart coverage. To obtain high resolution *in vivo* MR images of the mouse heart, we used ECG-gated proton-density weighted black-blood double inversion-recovery turbo spin echo (PD TSE BB) multislice sequence (TE 10 ms; TR ~ 1100-1200 ms dependent of the heart rate, matrix 248×245; flip angle 90°; field of view 50×50 mm; 4 signal averages, image resolution 202×204 μm). The PD TSE BB sequence allowed clear delineation of the left ventricle borders in the mouse heart and excellent blood suppression.

To detect iron accumulated in the overexpressed ferritin complexes bright- and black-blood T_2*-weighted sequences were tested. Bright-blood imaging was performed using used T_2* weighted cine gradient echo (GRE) multislice sequence (TR/TE = 14/9 ms; slice thickness 1mm; flip angle 15°; echo train length 1; field of view 50×50 mm, matrix 200×198; 6 signal averages, image resolution 250×250 μm). For black-blood imaging of transgenic grafts a recently introduced (Wang et al, 2010) improved motion sensitized driven equilibrium (iMSDE) preparative sequence was executed prior to the GRE imaging sequence. iMSDE preparation parameters: gradient amplitude 12 mT/m, first gradient moment 500 mT.ms^2/m and slew rate 100 mT/(m.ms). The imaging parameters were as follows: TR/TE=16/8ms; flip angle 13°; slice thickness 1 mm, field of view 50×50 mm, 8 signal averages, image resolution 298×303 μm.

The following formulas were used to quantify MRI signal intensity changes in the transgenic grafts. Graft-to-myocardium signal intensity ratio (SIR) was calculated as the ratio of signal intensities (SI) from in vivo MRI using regions of interest centered in the middle of the graft and in the non-infarcted area of the left ventricle (LV). $SIR = SI_{graft} / SI_{LV}$

Signal-to-noise ratio (SNR) was calculated as the ratio of SI of the region of interest centered in the left ventricle wall (SI_{LV}) of the mouse heart, or at the area of graft (SI_{graft}), and a standard deviation of noise in background air.

$$SNR_{graft} = SI_{graft} / SD_{noise}$$

$$SNR_{LV} = SI_{LV} / SD_{noise}$$

Contrast-to-noise ratio (CNR) was calculated as the difference between SNR of the non-infarcted area of the left ventricle and SNR of the graft area.

$$CNR = SNR_{LV} - SNR_{graft}$$

The area of signal hypointensity was manually delineated in each MR image at the short-axis plane of the heart using the image analysis software NIH ImageJ 1.43u. Graft size was expressed as a ratio of graft area to the total left ventricle (LV) area in each slice of the mouse heart.

$$\text{Graft size} = \frac{\text{graft area}}{\text{total LV area}} \times 100\%$$

Cardiac MRI studies of the infarcted rats

4.7T Varian NMR spectrometer (horizontal bore) has been used. Rats were anesthetized with 1.5% isoflurane in oxygen (1 liter/min) delivered through a nose cone and

placed in a custom-constructed ^{1}H transmit-receive volume coil on a flat Plexiglas platform. Needle electrodes were attached to the animal's extremities for ECG monitoring and to trigger the MRI acquisitions using commercially available software ("Small Animal Monitoring and Gating System" SA Instrument Inc., Stony Brook, NY). High-resolution spin-echo transverse ^{1}H MR images were obtained to quantify left ventricular function (field of view: 50 mm^2; 2D matrix: 256×128; TR: 400ms; TE: 13ms; flip angle: 90°, two signal averages). A set of multi-slice short-axis images (slice thickness 1.5 mm without gap between slices) for end-systole and another for end-diastole were acquired. Each slice was acquired at exactly the same time of R-R interval during cardiac cycle. Epicardial and endocardial borders were manually traced for calculation of left ventricle volumes at end-systole and end-diastole (ESV, EDV) and left ventricular mass (LVmass) using the software package NIH ImageJ version 1.34s. Total LV volumes were calculated as the sum of all slice volumes. The left ventricular ejection fraction (EF) was calculated by the equation (EDV-ESV)/EDV×100%. Left ventricle wall thickening was measured in the central infarcted region and in the non-infarcted mid-septal wall, using averages obtained from the four apical-most slices for each heart. Wall thickening was then calculated as the relative difference in LV wall thickness in end-systole and end-diastole and expressed as a percentage of end-diastolic thickness.

For the rat cardiac imaging at the 3T Achieva Philips whole body scanner a custom-constructed 2-turn solenoid receive-only coil was used. Single-lead ECG was recorded from subcutaneous needle electrodes attached to animal's extremities and was used to trigger the MRI acquisitions using commercial software (Small Animal Monitoring and Gating System, SA Instrument Inc., Stony Brook, NY). Due to the heart rate limitations of the 3T human scanner (250 bpm) and high heart rate in rats (about 400 bpm) we triggered MR acquisitions on every 2-3 heart beats using SA Instrument software tools. A prospectively triggered, cartesian turbo-gradient echo cine (TFE CINE) sequence through the short-axis slices of the heart was used with a slice thickness of 1.5 mm without gap between slices, TR/TE 8.3/3.8 ms, field of view 70×49 mm, flip angle 30°, 2D acquisition matrix 232×163, two signal averages, phase interval 8.3 ms.

Cardiac MRI studies on dogs

Cardiac MR protocol included CINE imaging for assessment for the LV systolic function; dynamic contrast enhanced MRI (DCE) and late gadolinium enhancement (LGE) imaging. For scanning, the animals were sedated with acepromazine 0.025 mg/kg; 0.04

mg/kg/atropine; and butorphanol 0.1-0.2 mg/kg, iv. All studies were conducted on a 3T MRI system (Philips Achieva, Best, Netherlands). CINE images were acquired with a turbo field echo (TFE) sequence that generated 30 cardiac phases for 8 to 10 short axis slices spanning the left ventricle. Acquisition parameters included repetition time (TR) / echo time (TE) of 4.7/2.3 msec, 15 degree flip angle, 4 mm slice thickness with 2 mm gaps and in-plane resolution of 2 mm × 1.67 mm. The dynamic perfusion sequence was a mid-ventricle, single-slice, single-shot saturation recovery TFE acquisition with TR/TE of 3.0/1.4 msec, 20° flip angle, 5 mm slice thickness and in-plane resolution of 1.99 mm × 1.96 mm. During the acquisition, 0.1 mmol/kg Gd-DTPA (Magnevist, Bayer Schering Health Care Limited, UK) was manually injected, followed by a saline flush. At 10 minutes after injection, three-dimensional delayed-enhancement images were acquired with an inversion-recovery TFE sequence. Acquisition parameters were TR/TE of 4/1.27 msec, 15° flip angle, resolution of 1.48 mm × 1.76 mm × 10 mm, TFE factor 24 and SENSE factor 1.5. LV endocardial boundaries were interactively traced at end-diastole and end-systole using standard cardiac analysis software (Philips, Best, Netherlands) to obtain end-systolic volume, end-diastolic volume, and EF. Papillary muscles were excluded from the volume calculations.

Cardiac MRI studies on non-human primates

In vivo imaging studies were conducted on a 3T Achieva clinical scanner (Philips, Best, Netherlands). Depending on the animal size, two overlapped Flex-M and Flex-L coils (dual-element, approximately 15 and 20 cm diameter, respectively) or an 8-element knee coil was used. Pediatric ECG leads were used for gating of MRI acquisitions. ECG, respiration rate, arterial oxygen saturation and body temperature were monitored continuously. Cardiac MRI protocol included CINE imaging for assessment for the LV geometry, global LV contractile function, regional systolic LV wall thickening and delayed gadolinium enhanced imaging for assessment of the infarct size. CINE images were acquired with a RF-spoiled turbo field echo (T_1-TFE) sequence that generated 25-30 cardiac phases for 10-12 short axis slices spanning the left ventricle. Acquisition parameters included a repetition time (TR) 3.9 msec, echo time (TE) 1.9 msec, a 15° flip angle (FA), 4 mm slice thickness (no gap), field of view (FOV) 120×120 mm^2, 1 mm^2 voxel size, 6-8 signal averages, retrospective ECG gating without breath hold.

Animals subsequently received an intravenous bolus injection of gadolinium-based contrast agent ProHance (Bracco Diagnostics Inc., Princeton, NJ) 0.2 mmol/kg, followed by a saline flush. During the contrast agent injection the dynamic perfusion images were acquired

through a mid-ventricle single-slice using a single-shot saturation recovery TFE acquisition with TR/TE of 3.0/1.4 msec, 20 degree flip angle, 5 mm slice thickness and in-plane resolution of 1.99 mm × 1.96 mm. At 8 minutes after injection, TI-scout images were acquired for determination of inversion time (TI) to null signal from non-infarcted myocardium. At nine minutes post-injection of contrast agent, phase-sensitive inversion recovery (PSIR) multislice images were acquired at the LV short axis to visualize infarct: TR/TE 7.3/3.5 msec, FA 25°, voxel size 1.3 mm^2, FOV 150×150 mm^2, slice thickness 4 mm without gap, four averages. This was repeated in the long axis plane. Inversion time range 280-350 msec, adjusted by the operator based on TI-scout values. Signal intensity threshold to differentiate normal myocardium from scar was set as "Full Width Half Max".

Global LV contractile function and regional wall thickness data were computed from the short-axis cine images. LV endocardial boundaries were interactively traced at end-diastole and end-systole using standard cardiac analysis software (Intellispace Portal, Philips, Best, Netherlands) to obtain end-systolic, end-diastolic volume, LV myocardial mass (LVmass), stroke volume (difference between end-diastolic and end-systolic volumes), cardiac output (CO) and LV ejection fraction (LVEF). LVEF was calculated as the ratio of stroke volume to end-diastolic volume. Papillary muscles were excluded from the volume calculations. Left ventricle wall thickening (LVTh) was calculated as relative difference in LV wall thickness in end-systole and end-diastole. LVTh was evaluated at the infarcted and non-infarcted areas of each slice of the heart. Infarct size was calculated from delayed Gd enhanced images and presented as the ratio of scar area to total LV area.

3.3. Cells

The following cell lines were used in this work.

- Mouse myoblasts (C2C12) cells originally derived from the C3H mouse [378] were maintained on gelatin-coated plates in DMEM media supplemented with 20% FBS.
- H7 human ESC line [379] was maintained in the undifferentiated state on matrigel-coated plates with mouse embryonic fibroblast conditioned medium (MEF-CM) [380] supplemented with 4 ng/ml human bFGF.
- RUES2 ESC line was obtained from Rockefeller University; it was maintained same as H7 hES cells.
- WTC11 (obtained from www.allenCell.org) human induced pluripotent cell line (iPSC) was maintained on laminin-coated dishes in E8 media.

- DS-1 cells, clonal marrow fibroblasts derived from a primary culture of canine bone marrow stromal cells. DS-1 cells were cultured in DMEM medium, supplemented with 10% fetal bovine serum, L-glutamine (0.4 mg/mL), sodium pyruvate (0.1 mmol/L), penicillin (100 U/mL), and streptomycin sulfate (100 pg/mL).

Stem cell differentiation into cardiomyocytes

hESC-derived cardiomyocytes were generated from H7 and RUES2 embryonic stem cell lines using directed cardiac differentiation protocol since it was reported protocol as more efficient for cardiogenesis than a "standard" embryoid body culture protocol [381]. The protocol for directed differentiation uses sequential treatment of the high-density undifferentiated hESC monolayer with recombinant human activin A, bone morphogenetic protein-4 (BMP-4) as well as small molecules agonists or inhibitors of the Wnt pathway [382, 383]. In brief, undifferentiated hESCs were detached by 10-minute incubation with 0.5 mM EDTA or 200 U/ml collagenase IV and seeded onto matrigel-coated plates at a density of 100,000 cells/cm^2. Cells were re-fed daily with MEF-CM plus 4 ng/mL bFGF for 6 days. One day before inducing differentiation (day -1) Wnt agonist Chiron (CHIR99021, 1 uM) was added to the CCM media. To induce cardiac differentiation, MEF-CM was replaced with RPMI-B27 medium supplemented with 100 ng/ml human recombinant activin A in 1x matrigel for 12-18 hours (day 0). Day 1 media change: RPMI supplemented with B27 (no insulin), 5ng/ml BMP4 and 1uM Chiron 99021. On day 3: Wnt/β-catenin-inhibitor WNT-939 (1 uM) was added to the media. On day 5: the medium was exchanged for RPMI-B27 (without insulin) without supplementary cytokines. Media was changed on day 7 to RPMI-B27 (plus insulin), then cells were re-fed every 2 days for 2-3 additional weeks. Widespread spontaneous beating activity was typically observed by day 10-12 after addition of activin A. For control experiments involving "non-cardiac" preparations, hESCs were differentiated under otherwise identical culture conditions, but activin A and BMP-4 were omitted.

For monolayer directed cardiac differentiation of iPSC WTC11 stem cell line, undifferentiated pluripotent WTC11 cells were plated on rhLaminin-521 coated plates (2 µg/cm^2) in the density 150,000 cells per well in 12-well dish in E8 media with addition of 10 µM Rock inhibitor. After 24 hours, media was changed to 2 ml E8 with Chiron 99021 (day -1) and incubated obernight at 37°C. One day 0, cells were washed with PBS, media was changed to RPMI supplemented with BSA (500 µg/ml), ascorbic acid (213 µg/ml) and 4 µl Chiron 99021. Cells were incubated for 2 days at 37°C. On day 2, cells were washed with PBS, media

was changed to RPMI supplemented with BSA (500 µg/ml), ascorbic acid (213 µg/ml) and 2 µl Wnt/β-catenin-inhibitor WNT C-59. On day 4, cells were washed with PBS, media was changed to RPMI supplemented with BSA (500 µg/ml) and ascorbic acid (213 µg/ml). On day 6, cells were washed with PBS, media was changed to RPMI supplemented with B-27 (plus insulin) and then media is replaced every other day. Initial beating is usually observed between days 8-10 of the differentiation start.

To ensure comparable cardiac purity amongst preparations, a small subset of the cells to be implanted were routinely plated-out (50,000 cells/cm^2) on gelatin-coated substrates and cultured for 48 hours prior to fixation and immunostaining for β-myosin heavy chain. This analysis revealed the Percoll-enriched cells to be 82.6±6.6% cardiomyocytes (range 71-95%). Equivalently prepared cells have been exhaustively examined for the presence of skeletal muscle cells. Control "non-cardiac" preparations contained a mean of only 0.8% cardiomyocytes.

Nucleofection

Mouse C2C12 skeletal myoblasts were nucleofected with pcDNA3-HA-ferritin cDNA using FuGENE6 reagent and cells were cultured on gelatin-coated tissue culture dishes in growth medium (DMEM, Invitrogen) supplemented with 20% fetal bovine serum (HyClone, Logan, UT), 2 mM L-glutamine (Invitrogen) and penicillin/streptomycin. Neomycin (G418) was added to the cell culture media at 1.2mg/mL to select for stably transduced cells.

Nucleofection of the undifferentiated hES cells on Matrigel: rock inhibitor was added to cells one hour before passaging. Cells were washed with dPBS, then incubated with warm Versene 7-10 minutes at 37°C. Checking cells on microscope: cells should become separated from each other in colonies, but colonies should be still attached to plate. Making a nucleofection solution: 30 µg of the transgenic DNA, add 5µg of "AAVS1 R&L ZFN Reverse" (70 ng/µl; take 71.43 µl for reaction) and 5µg of "AAV57 L&R Reverse" (708 ng/µl; take 7.1 µl for reaction), mix all plasmids and evaporate to final volume 10 µl. Add 81.9 µl of Solution-1 and 12.2 µl of Supplement (Lanza Human Stem Cell Nucleofector kit 1). Aspirate Versene from cells and add hES media, pipet up and down to take cells off plate, count cells. Take at about 1 million cells, spin to make a pellet. Take prepared nucleofection solution, add to cell pellet and resuspend pellet in it. Add mixture to the nucleofection cuvette. Electroporation is done for 1 sec. Cells were removed from a cuvette by small plastic pipette and put to eppiendorf tube. 400 µl of cells were added to one MEF-coated plate and 600 µl to another

plate. Transfected cells were fed every day with hES media + Rock inhibitor. Re-plated colonies were fed with Conditioned Media+bFGF+Rock inhibitor. G418 (neomyocin) was added for 2-3 days for cell selection (75 μg/ml).

Preparation of stem cell derived cardiomyocytes for transplantation

Transplantation to the rat heart. Cells were subjected to transient heat-shock (with a 30 min exposure to 43°C medium), followed by a return to either control medium or, for to pro-survival cocktail (PSC), medium supplemented with IGF-1 (100 ng/ml) and cyclosporine A (0.2 μM). Twenty-four hours later, cells were enzymatically dispersed for implantation using Blendzyme IV (Roche, prepared at 0.56 U/ml in phosphate-buffered saline) and DNAse (Invitrogen, 60 U/ml) for 30 minutes at 37°C and enriched for cardiomyocytes by separation over a discontinuous Percoll gradient. The resultant cardiomyocyte-enriched fractions, the denser fractions III and IV were used for transplantation studies. Cells to be implanted were then suspended in a 70 μl volume per rat of either serum-free medium ("SFM" group, using RPMI medium without B27), Matrigel ("MGel only" group, using 50% (v/v) Matrigel:cells+RPMI medium), or the full pro-survival cocktail including Matrigel ("PSC"). The full PSC cocktail consisted of 50% (v/v) growth factor reduced Matrigel, supplemented with 100 μM ZVAD [384, 385], 50 nM Bcl-XL BH4 [386], 200 nM cyclosporine A [387-389], 100 ng/ml IGF-1 [390, 391], and 50 uM pinacidil [392-394].

Cell transplantation to the heart of non-human primates. On the day 21 of differentiation, cardiomyocyte aggregates were dissociated by treatment with Liberase TH followed by TrypLE. Dissociated CMs were cryopreserved with CryoStor CS10 with 10μM Y-27632 in liquid nitrogen. Approximately 3 hours before transplantation, the cardiomyocytes were thawed in a 37°C H_2O bath (~2 minutes), after which RPMI+B27(w/insulin) supplemented w/ ≥200 Kunitz Units/ml DNase I, was added to the cell suspension to dilute the cryoprotectant. Subsequent wash steps were done in RPMI-1640 with no supplementation and in progressively smaller volumes in order to concentrate the cell suspension. After the final centrifugation step, the cells were resuspended in a defined volume of the final component of the cell injectate - a 5-factor Pro-Survival Cocktail (PSC) consisting of the basal media, RPMI-1640 and supplemented with 1) ZVAD-FMK/Caspase Inhibitor (Calbiochem/EMD-Millipore, 10μM final), 2) TAT-BH4 / BCL-XL (Calbiochem/EMD-Millipore, 50nM final), 3) Cyclosporine A (Sandimmune/Novartis, 200nM final), 4) Pinacidil (Sigma, 50μM final), and finally, 5) IGF-1 (Peprotech, 100ng/ml final). After the cells were resuspended in PSC, an

aliquot was removed for counting and the sample pelleted one final time. Concomitantly, a calculation based on this final cell count is made in order to determine the volume of PSC supernatant to be removed in order to achieve the target cell-suspension density used for grafting (goal ~6.5 x 10^8 – 1 x 10^9 cells in ~1.5 ml PSC).

3.4. Animals

All studies were approved by the University of Washington Animal Care and Use Committee and were conducted in accordance with federal guidelines. The following laboratory animal species were used in the study:

1) C57B1 and C3H mice (20-30 g). C57B1 mice were used for non-invasive studies of heart contractility and energetics after myocardial infarction. C3H mice were used in C2C12 cell transplantation studies. The C2C12 myoblast line was originally derived from the C3H mice [378] and, therefore, we chose this mouse strain as recipient to minimize immunological rejection of engrafted cells.

2) Athymic Sprague Dawley rats (*rh rnu-rnu*, 240-300g, Harlan, Indianapolis) were used as a host for human cardiomyocyte transplantation studies because of its well-established history in xenotransplantation and the comparative ease and reliability of physiologic studies in the rat.

3) Mongrel dogs (13-18 kg) and dogs with developed Duchenne muscular dystrophy (DMD).

4) Non-human primates: *Macaca nemestrina* (5-14 kg) was used in pre-clinical studies of human cardiomyocyte transplantation.

3.5. Modeling myocardial infarction in animals and cell transplantation

Mouse model of myocardial infarction

In the first series of experiments anesthesia was induced in adult mice by inhalation of methoxyflurane and maintained with intraperitoneal injection of Etomidate (20 mg/kg) and with subcutaneous Buprenorphine (0.24 mg/kg). Additional doses of Etomidate were administered as needed. Mice were intubated and ventilated with a custom-made ventilator and the body temperature was maintained constant as monitored with a rectal probe. A left thoracotomy and percardiotomy were performed and the left main coronary artery was completely ligated with suture. After verification that coronary occlusion had occurred by blanching of the tissue distal to the suture, the ribs were closed with suture and the mice

recovered. Additional doses of Buprenorphine (0.96 mg/kg) were administered to limit discomfort.

For cell transplantation studied mice were anesthetized by intraperitoneal injection of 2.5% Avertin (Phoenix Pharmaceuticals; 0.02-0.026 ml/g), intubated and mechanically ventilated with supplemental oxygen and 3 cm H_2O of positive end-expiratory pressure. The heart was exposed via an open thoracotomy and subjected to myocardial injury by permanent ligation of the left anterior descending artery by 8-0 Prolene suture. After verification that coronary occlusion had occurred (blanching of the tissue distal to the suture), C2C12 cells suspended in 7µl of serum/antibiotics-free medium were directly injected into the border of infarcted region of the left ventricle using a 30-gauge needle. 150,000 or 500,000 cells were injected per animal in two injection sites (3.5µl per site). Six C3H mice received 150,000 cells ferritin-tagged cells, 6 animals received 500,000 ferritin-tagged cells, and 4 mice received WT C2C12. The chest was then closed aseptically, and animal recovery from surgery was monitored in a heated chamber.

Rat model of myocardial infarction

Athymic male Sprague Dawley rats were anesthetized with an intraperitoneal injection of 70-100 mg/kg ketamine (Phoenix Pharmaceuticals, St Joseph's MO) and 7-10 mg/kg xylazine (Phoenix Pharmaceuticals), intubated and mechanically ventilated with room air supplemented with oxygen. The heart was exposed via an open thoracotomy and subjected to 60 minutes of ischemia-reperfusion injury by temporary ligation of the left anterior descending artery by 7-0 Prolene suture. Two days after recovery from this procedure, animals underwent echocardiographic evaluation. Animals meeting the echocardiographic inclusion criterion (fractional shortening <40%) were stratified to one of three groups: those receiving intra-cardiac injections of human embryonic stem cell-derived cardiomyocytes suspended in PSC, PSC-only, or serum-free media (SFM) only. These implantations were performed four days after the initial ischemia-reperfusion infarct (two days following echocardiography). On the day of engraftment, the rats were again anesthetized with ketamine/xylazine, mechanically ventilated, and subjected to a second thoracotomy followed by direct injection of 70 µL of agent (hESC-derived cardiomyocytes in PSC vs. PSC-only vs. SFM-only) using a Hamilton syringe (Hamilton Company, Reno, NV) and a 30 gauge needle. To better ensure exposure of implanted cells to therapeutic levels of cyclosporine A throughout the period in which graft cell death would be expected to be maximal, all cell-treated and PSC-only control rats received

daily subcutaneous injections of cyclosporine A (0.75 mg/day, Wako Pure Chemicals, Osaka, Japan), starting one day prior to engraftment and continuing for seven days after engraftment.

Dog model of myocardial infarction

Myocardial infarction in mongrel dogs was created as ischemia-reperfusion injury using percutaneous transluminal coronary artery catheterization techniques. A specialized shape guiding catheter was used to engage the left coronary artery and then inflated a percutaneous transluminal coronary angioplasty (PTCA) balloon catheter (2.5mm/8mm, Apex^{TM} monorail balloon catheter, Boston Scientific) with 6-10 atm for 90 minutes to occlude all flow distal to the first diagonal branch of the left anterior descending coronary artery (LAD). MI was confirmed by ECG and subsequent post-MI 24-hour serum cardiac troponin I (cTnI) assay (Phoenix Central Laboratories, Everett, WA). Pre-emptive and post-MI analgesia was provided through a 50 microgram/hour Fentanyl patch applied to the dog's shaved tail from Day -1 through Day 1. After MI surgery, the dogs were recovered to consciousness in the surgical suite, then monitored for 6 hours post-recovery within the clinic and evaluated at least twice daily thereafter.

Non-human primate (NHP) model of myocardial infarction

Macaca nemestrina monkeys of either sex, weighing 5.2–12.6 kg, ages 11±2 years, were obtained from the Washington National Primate Center. Macaques first underwent a 2-4 week period of acclimation and training to wear a mesh jacket with an exteriorized line that attached to tether system to prevent removal of intravenous (i.v.) catheter and ECG electrodes. For all major surgeries and procedures, macaques were sedated with ketamine and propofol, intubated and ventilated using sevoflurane to maintain anesthesia. Buprenorphine was administered to provide perioperative and postoperative pain relief. Before myocardial infarction creation, an i.v. lidocaine bolus of 1 mg/kg and an infusion of 20 μg/kg/min were used to prevent ventricular arrhythmias. Heparin was delivered i.v. to maintain activated clotting times of 250–350 s to prevent thrombus formation. Under fluoroscopic guidance (OEC 9800 Plus, GE Medical Systems), a 5F coronary catheter was used to engage the left main coronary artery (LAD). A coronary guide wire and angioplasty balloon catheter were passed into the mid-left anterior descending artery. The balloon was inflated until occlusion (as demonstrated by fluoroscopy) and left inflated for 180 min. Myocardial infarction was confirmed by ST-segment elevation on ECG and by subsequent serum assays for cardiac troponin. For telemetric monitoring, tunneled subcutaneous ECG electrodes were implanted (2

in the chest wall and 1 in the abdomen; lead II equivalent) and connected to wireless Vetcheck modules (Vmed Technology) through the jacket/tether system. Dual lumen venous catheters were implanted and tunneled to allow peripheral blood sampling and intravenous drug administration with minimal distress to the animals. Immune suppression was achieved with three drugs. Methylprednisolone was given i.v. 30 mg/kg on the day before hESC-CM delivery, followed by maintenance doses of 6 mg/kg for two days, and then 3mg/kg thereafter until monkeys were euthanized. Cyclosporine A was given i.v. to maintain serum trough levels of 200-250 μg/L from 5 days before hESC-CM delivery until macaques were euthanized. Finally, Abatacept (CTLA4-Ig) 12.5 mg/kg on the day before hESC-CM and every 2 weeks thereafter. Ceftazidime, cefazolin, vancomycin, gentamycin, fluconazole, and acyclovir were administered for prophylaxis of opportunistic infections.

On day 14 after myocardial infarction, macaques were anaesthetized and underwent left-sided thoracotomy. The heart was exposed and a pericardial cradle created. The infarct region was directly visualized. Cell injection was done under direct surgical visualization with a needle and syringe targeting the central infarct and border zones via 15 injections each of 100 μl volume. Needle tips were placed within a preformed mattress suture, and three injections were delivered via the same epicardial puncture, changing the trajectory of the needle for each. Before withdrawal of the needle, the mattress suture was cinched around the needle tip to facilitate cell retention. For control macaques, an equal volume of PSC-RPMI vehicle was injected in the same manner as for hESC-CM delivery. Euthanasia was induced by i.v. injection of saturated KCl. Control and cell-treatment groups were allocated in an un-blinded and non-randomized manner.

Post-surgery care. Post-infarct animals were monitored daily with particular attention paid to signs of distress, which may indicate post-procedure pain or symptoms of heart failure. If necessary, furosemide was injected to relieve pulmonary congestion or limb edema. Signs of distress, such as increased respiratory rate and crackles on auscultation of the chest were used to assess signs of pulmonary congestion. Surgical wounds were carefully examined for signs of infection. In the event of possible infection, wound swabs were obtained and sent for microbiology with the commencement of empirical antibiotics in consultation with veterinary staff. If there were any severe complications noted in the animal, we consulted the veterinarian staffs and treated as clinically appropriate. If the clinical or attending veterinarian diagnosed an

untreatable complication, the animal was euthanized. All animals had full necropsies performed by an experienced primate pathologist.

Telemetric ECG. ECG recordings were acquired from conscious, freely mobile animals using a Vmed Vetcheck telemetry system. Animals had tunneled subcutaneous ECG wires implanted, providing lead II tracings. Continuous telemetry was sent wirelessly to a dedicated laptop for all macaques with myocardial infarction with or without hESC-CM delivery. All ECG traces were evaluated manually by a cardiologist using ECG Reviewer (Vmed) and determined the total number and duration of ventricular arrhythmias. Premature ventricular complexes (PVC's) were defined as QRS complexes greater than 60ms. Ventricular tachycardia (VT) was defined as a run of four or PVC's with ventricular rate of more than 180 beats per minute. Accelerated idioventricular rhythm (AIVR) was defined as four or more PVC's with a rate of less than 180 beats per minutes. VT or AIVR were considered sustained if the duration was greater than 30 seconds.

3.6. Histology, immunocytochemistry, *in situ* hybridization

Histology in rats

Rats were euthanized with Beuthanasia (1.5-2 ml intraperitoneal injection, Schering-Plough, Union NJ). One hour prior to euthanasia, rats received an intraperitoneal pulse of 5-bromodeoxyuridine (BrdU, 1.0 ml of a 10 mg/ml solution, prepared in phosphate-buffered saline) to mark cells synthesizing DNA. The heart and various organs were harvested, fixed in methyl Carnoy's solution and processed for histological analysis. To ensure equivalent sampling, all hearts were fixed and vibratome-sectioned to 1 mm thickness, and the resultant uniform transverse sections were routinely processed and paraffin-embedded for histology. Five-micron sections were then stained with hematoxylin-eosin and picrosirius red/fast-green (to determine infarct area), as well as subjected to *in situ* hybridization and immunohistochemistry. Immunostaining was performed with antibodies directed against the muscle antigens sarcomeric myosin heavy chain (clone MF-20, Developmental Studies Hybridoma Bank), the β-myosin heavy chain isoform (clone A4.951, American Type Culture Collection), pan-cadherins (rabbit polyclonal, Sigma), cardiac troponin I (clone 19C7, Abcam), human Nkx2.5 (goat polyclonal, R&D), and myosin light chain 2V (rabbit polyclonal, a gift from Dr. K. Chien). To evaluate for the presence of non-cardiac graft elements, we also imunostained with antibodies against the following cell types: neurons (βIII-tubulin, Sigma, St. Louis), endoderm (α-fetoprotein, Dako, Carpinteria, CA), epithelium (pan-cytokeratin cocktail

(AE1/AE3, Dako), endothelium (human-specific CD31/PECAM, Dako; Ulex europaeus, Vector), and skeletal muscle (fast skeletal myosin heavy chain, MY32 clone, Sigma). Host-derived endothelium was identified with a rat-specific anti-endothelial antibody (rat endothelial cell antigen-1, Cambridge, MA). Proliferation was assessed by immunostaining for incorporated BrdU (peroxidase-conjugated mouse anti-BrdU monoclonal antibody, Roche).

The engrafted human cells were identified using *in situ* hybridization with a human-specific pan-centromeric genomic probe [204, 395]. All evaluated sections were either double-labeled with this human-specific marker or an immediately contiguous section was so-labeled. The human-specific pan-centromeric probe is generated by modification of a protocol reported by Weier [395] that involves degenerate PCR with primers against human centromeric sequences; the generated PCR product was labeled with digoxigenin (Dig Hi-Prime labeling kit, Roche, Indianapolis, IN), which was then detected after *in situ* hybridization using a peroxidase-conjugated anti-digoxigenin antibody (Roche). For brightfield studies involving *in situ* hybridization with the pan-centromeric probe, chromagenic detection of the *in situ* probe was performed with diaminobenzidine (Sigma) and any preceding immunohistochemistry used Vector Red (Vector Labs, Burlingame, CA) for detection. For studies requiring confocal microscopy, *the in situ* probe was detected by Alexa Fluo 488 tyramide (Molecular Probes, Eugene, OR), again with preceding immunohisto-chemistry detected by the intrinsic red fluorescence of the Vector Red deposit. Note that, when performed on tissue fixed with methyl Carnoy's, the *in situ* hybridization procedure unfortunately precludes subsequent staining with all available nuclear counterstains. For this reason, we used fast green (cytoplasmic) counterstaining in all brightfield *in situ* studies and no counterstain in fluorescent *in situ* studies. In studies not involving *in situ* hybridization, nuclear counterstaining was done using either routine hematoxylin (brightfield) or Hoechst (fluorescence) dyes. It also is worth noting that, in studies employing the human-specific *in situ* probe in combination with a second cardiac marker (usually β-myosin heavy chain), fine structural details, such as sarcomeric organization, can become difficult to appreciate. First, the relatively rough treatments to the tissue (i.e. acid and proteinase treatment, high temperatures to denature target DNA sequences) necessary for *in situ* hybridization subtly distort the tissue architecture. Second, we have found the only preceding reporter that reliably survives the *in situ* hybridization procedure is the chromagen Vector Red, and so, when we have employed a second marker, it has been detected with this stain. Vector Red is an enzymatic substrate and so generally does not have the crisp

staining pattern possible with a directly-conjugated secondary antibody. For these reasons, when doing studies to specifically evaluate the sarcomeric organization of the grafts, the immunofluorescence was performed, relying on *in situ* hybridization for the human marker on an adjacent section.

While all grafts were confirmed by the human-specific *in situ* probe, the human ESC-derived cardiac implants were also quite distinct morphologically and also could be readily distinguished from the host on the basis of their exclusive immunoreactivity for β-myosin heavy chain, as opposed to the rodent host ventricular myocardium which expressed α-myosin heavy chain. Stated another way, we found all strongly β-myosin heavy chain positive cells to be also positive for the human-specific *in situ* probe. We further confirmed this expected pattern of myosin heavy chain expression on a subset of cell-engrafted hearts using immunofluorescent co-localization by confocal microscopy. For this, sections were double-immunostained using antibodies recognizing β-myosin heavy chain (A4.951 monoclonal primary, followed by tyramide amplification with a sheep anti-mouse IgG HRP-conjugated secondary antibody (Amersham, Piscataway, NJ) and Alexa Fluo 488 tyramide (Molecular Probes, Eugene, OR)) and sarcomeric (i.e. α- and β-) myosin heavy chains (MF-20 monoclonal primary, followed by a biotinylated goat anti-mouse (Vector) and streptavidin-conjugated Alexa 555 (Molecular Probes)). Sections showing close apposition of graft and host muscle were similarly analyzed by confocal microscopy for the presence of shared intercalated disc structures, using dual immunofluorescent labeling for β-myosin heavy chain and cadherins. Similar dual immunofluorescent labeling studies were performed combining β-myosin heavy chain with cardiac troponin I and Nkx2.5. In all cases, slides were then counterstained with Hoechst nuclear dye, mounted with Vectashield (Vector), and visualized on Zeiss LSM510 META confocal microscope using a 10X, 40X, and 63X objectives.

All quantitative histologic studies were performed in a blinded fashion using brightfield microscopy. Cell nuclei counts were obtained using an Olympus BX41 microscope with a 40X objective. Morphometric analyses were performed by acquiring digital photomicrographs of all vibratomed profiles with the stain of interest (via an Olympus SZ-PT dissecting microscope equipped with a Nikon Coolpix 995 digital camera) and then measuring areas using Adobe Photoshop. Morphometric determinations of infarct size were expressed as the percentage of total left ventricular cross-sectional area occupied by picrosirius red-positive infarct zone.

Graft size was expressed as the percentage of picrosirius red-positive infarct area occupied by human β-myosin heavy chain positive graft.

Histology in NHPs.

Paraformaldahyde-fixed macaque hearts were dissected to remove the atria and right ventricle before cross-sections were obtained by sectioning parallel to the short-axis at 2.5 mm thickness on a commercial slicer (Berkel). Weights of the whole heart, left ventricle and each slice were obtained before cutting heart slices to fit tissue cassettes. The tissue then was processed, embedded in paraffin, and four-micrometer sections were cut for staining. For morphometry, infarct regions were identified by Picrosirius red staining; human grafts were identified by anti-human cardiac troponin I or slow skeletal troponin I, stained using avidin-biotin reaction (ABC kits from VectorLabs) followed by chromogenic detection via diaminobenzidine (Sigmafast, Sigma Life Science). The slides were digitized using Nanozoomer scanning and software (Hamamatsu). Resulting images were imported into Image J software (version 1.51k) where area of infarct and graft (region of interest or ROI) were measured. The mass of the ROI was determined by calculating the ratio of ROI area to total tissue area on the slide, and multiplying by the weight of the tissue the slide was cut from. The entire scar or graft was expressed as total weight or percent of LV mass.

For immunohistochemistry, we used the following primary antibodies: primary antibodies then were followed either with fluorescent secondary antibodies (Alexa-conjugated, species-specific antibodies from Molecular Probes) or the avidin biotin reaction (ABC kits from VectorLabs) followed by chromogenic detection via diaminobenzidine (Sigmafast, Sigma Life Science). Immunofluorescent images were collected with either a Nikon A1 Confocal System or a Nikon Ti-E inverted widefield microscope. For high-resolution confocal images, a 60X CFI Plan Apo Water immersion objective lens (NA 1.2) was used. 12-bit images were captured with the pinhole at 1 Airy Unit and field size at 1,024 X 1,024 pixels. For large field immunostained sections, a CFI Pan Apo lambda 4X objective (NA 0.2) was used on the widefield system. Grids of 14-bit Images were captured using a Photometrics CoolSnap HQ2 CCD camera and stitched with NIS Elements vers 4.5 software. For figure preparation, images were exported into Photoshop CS3 (Adobe).

Engrafted human cells were identified using *in situ* hybridization with a human-specific pan-centromeric genomic probe and used to validate human specific antibodies. In brief, the human-specific pan-centromeric probe was generated by modification of a protocol that

involves degenerate PCR with primers against human alpha satellite pan-centromeric repeat sequences. PCR was performed for 30 cycles: denaturation at 94°C for 1 minute; annealing at 45°C for 1 minute; extension at 72°C for 1 minute. We then labeled the PCR product with or biotin (Biotin DecaLabel DNA kit, Thermo Scientific) to generate the in situ probe. The pan-centromeric probe was diluted in hybridization buffer (0.5x SSC, 10% dextran sulfate, 50% deionized formamide, 0.4mg/mL salmon sperm DNA), heated to 80°C to denature the DNA, applied to the slide and hybridized overnight at 37°C. Subsequent detection after in situ hybridization utilized peroxidase-conjugated avidin (ABC kits from VectorLabs). For immunohistochemistry, the *in situ* probe was detected by Alexa Fluor 594 tyramide amplification (Molecular Probes).

Histology in dogs.

Dogs were euthanized by intravenously injecting phenobarbital and phenytoin (Beuthanasia-D). Hearts were removed, rinsed in non-sterile saline, and perfused with 0.9% saline and 4% paraformaldehyde sequentially. A commercial slicer (Berkel) was used to do cross-sectioning parallel to the short-axis at 3mm thicknesses. Tissue morphology and the extent of cardiac fibrosis were determined from hematoxylin and eosin (H&E) and picrosirius red/fast green-stained sections, respectively. The infarct areas were calculated using Nanozoomer scanning and software (Hamamatsu) and Image J software (version 1.47, NIH, Bethesda, MD, USA). The picrosirius red-stained slices were also examined under light microscopy with a linear polarization unit. Fifty collagen fibers per tissue section (5 sections for each dog) were studied where the myocytes were cut longitudinally. A 50-point grid was constructed over the tissue section by an eyepiece reticle. The extinction angle of the collagen fibers intersected by the grid points were measured with a rotating microscope stage. Deviations of the extinction angles were calculated for 50 collagen fibers per tissue section. Lower deviations indicate a more parallel (uniform) alignment of fibers. For immunohistochemistry of formalin-fixed and paraffin embedded tissue, slides were prepared and stained with α-smooth muscle actin antibody at 1:300 (clone 1A4; DAKO) followed by an anti-mouse secondary conjugated to HRP (PowerVision Ms-HRP; Leica) then DAB chromogen (Refine DAB; Leica) and counterstained with hematoxylin 50% in dH_2O (NM-HEM; Biocare). Images were acquired using a Nanozoomer scanner and arteriole numbers were determined in 10 fields of both the infarct and border zones at 10X magnification with the data expressed as the average number of arterioles/mm^2.

3.7. Catheter-based electrophysiology in large animals

The macaques were sedated with ketamine and propofol and intubated. Anesthesia was maintained with sevoflurane. Heart rate, non-invasive blood pressure, and pulse oximetry monitors were connected. R2 pads were placed and connected to a defibrillator. Depending upon the animal and prior vascular access, either the left or right femoral artery was accessed using a hybrid cut down / Seldinger technique. A 7 French hemostatic sheath was placed into the femoral artery. Through this sheath a CARTO NaviStar B-curve, D-curve, or a PENTARAY (Biosense Webster Inc, Diamond Bar, CA) catheter was placed and advanced retrograde through the aortic arch into the left ventricle. If the macaque was in sinus rhythm at the onset of the study, a substrate map was created in sinus rhythm and areas of low voltage annotated. Scar was defined as a voltage of <0.5 mV and / or inability to capture the myocardium at a pacing output of 10 mA at 2 ms pulse width. Diseased myocardium was defined by a voltage of 0.5 – 1.5 mV, and healthy myocardium > 1.5 mV. Following substrate mapping, a ventricular stimulation protocol was performed with an 8-beat drive train with single, double, and triple extrastimuli down to the ventricular effective refractory period. The protocol was repeated at 2 sites and 2 drive train cycle lengths. If non-inducible under baseline conditions, the protocol was repeated on an Isuprel infusion titrated to achieve a 25% increase in baseline heart rate. For induced and spontaneous ventricular arrhythmias, electroanatomic and voltage mapping was performed. The arrhythmia was characterized as focal if there was radial spread of electrical activation from a point source and macro-reentrant if there was an identified circuit of electrical activity with an early-meets-late activation pattern. Activation mapping was performed using the CARTO III system with either a 7-French NaviStar B- or D-curve catheter or a 7-French D-curve PENTARAY catheter (Biosense Webster Inc, South Diamond Bar, CA, USA).

3.8. Statistical analysis

Microsoft Excel (Excel Data Analysis Toolpak, Microsoft) and SPSS 12.0 statistical software were used for statistical analysis. Normality of distribution for each variable was assessed using one-sample Kolmogorov-Smirnov test (K–S test) and the sample frequency distribution was compared with a reference probability distribution. Group comparisons were assessed by independent t-test for variables with unequal variances. For analysis of time course changes in LV size, LV function and HR, a paired t-test analysis of means was used. Paired t-test was also used for comparison of measurements obtained using different MRI sequences

for the same group of animals. ANOVA with post hoc analysis by the Student-Newman-Keuls application for comparison of groups at any single time point. All data were analyzed in a blinded manner, with the breaking of the identifier code only after the data were acquired. Agreement between graft size measurements by MRI and histology and agreement in measurements between different reviewers was assessed using Pearson's correlation coefficient and Bland-Altman plots. The bias between two measurements was examined using the one-sample t-test for the differences between paired measurements. The limits of agreement were calculated as the mean difference ±1.96 standard deviations (SD) of the mean difference. Significance level was defined as $p<0.05$. Values are expressed as means ± standard error of the mean, unless otherwise stated.

4. RESULTS AND DISCUSSION

4.1. Specific Aim 1

To create a technological infrastructure, based on the novel approaches in physics and biophysics, for non-invasive studies of heart in small and large laboratory animals using magnetic resonance imaging and spectroscopy.

The importance of using animal models to study human diseases have been discussed above (part 2.12.). Clinical MRI equipment, including whole body scanners, ECG leads, RF coils and physiological monitoring systems can be used for the large animal scans. Non-invasive magnetic resonance imaging and spectroscopy studies in laboratory animals have been limited in the past because the difficulties in assessing ventricular mass, geometry, and contractile function *in vivo*, especially in murine models of cardiovascular pathology. The extreme fast heart rate, the much smaller body size and size of the heart in comparison with large animals and humans, and weaker electrocardiogram (ECG) gating signal of the murine heart bring substantial difficulties in obtaining good MRI images. A special equipment must be setup to enable small animal studies, special RF coils dedicated for the specific study should be engineered, MRI pulse sequences have to be modified or written de-novo. This part of the work is dedicated to the creating of the technological infrastructure enabling *in vivo* MRI studies of the heart in large and small animals.

Specialized equipment for *in vivo* cardiac MRI on rodents.

Small body size, tiny size of the heart and high heart rate in rodents (300-400 beats per minute, bpm, in rats and 500-600 bpm in mice) are the serious challenges for *in vivo* imaging. Signal-to-noise ratio (SNR) is critical for high quality images. MRI scanners with high magnetic field strength (4.7T and higher) allow significant increase in SNR and shortening of the scan time. However, *in vivo* cardiac MRI studies are also possible using clinical tomographs with the magnetic field strength of 3T and lower. It is well known that SNR decreases as square root of the distance between RF coil and studied tissue. For quantitative studies of the rodent heart imaging must be performed with spatial resolutions that are 5 to 10-fold higher than in humans; this results in SNR losses of 100-1000 % [396]. RF coil should have an optimal size and design to penetrate the distance of the heart inside the rodent's thorax, but not so large that the SNR profile is not optimal.

To maximize SNR in rodent imaging on the clinical tomographs the small surface RF coils (carotid coils or a wrist coil) can be used or small coils designed specifically for rodent

imaging. Several specialized RF coils have been constructed for performing *in vivo* cardiac imaging on rodents in the different scanners (Figure 29). For the rat cardiac MRI studies at the 3T Achieva (Philips, Best, Netherlands) scanner the special coil was built. This is the two-loop solenoid receive-only ^{1}H coil tuned into the 127 MHz with the internal diameter 4.5 cm that fits tightly around the rat thorax to maximize SNR. The coil and the interface box that utilizes the Philips SMC (Synergy Multi Connect) box with preamplifiers, four BNC jacks and blocking circuit logic (cable trap). This coil allows high quality high-resolution images of the rat heart with high SNR (figures 29C and D).

For the cardiac MRI studies at the 4.7T NMR spectrometer (Varian, USA) horizontal bore two coils were built: one 5 cm diameter for rat cardiac exam and second one 2.5 cm diameter for mouse imaging. Both transmit-received coils were tuned unto the 200 MHz. Each coil was placed to the flat plexiglass platform located in the middle of the plexiglass tube cut in half to enable tight fit into the magnet bore. This self-built system allows coil placement to the scanner isocenter. Two capacitors were connected to the coil for fine tuning and matching. Those coils had high homogeneity of the magnetic field for high quality imaging of the rodent heart (figure 29 G, H).

Commercially available coils from the different manufacturers can be used for small animal imaging as well. Many companies that market RF coils for rodent imaging, for example, Philips Medical Research, Rapid Biomedical GmbH, Doty Scientific, XLR Imaging, M2M Imaging, Nova Medical. Each coil is designed to operate at a specific field strength and on a particular MR scanner platform. Advantages of those coils are good homogeneity of the B_0 and presence of the built-in heater elements to maintain body temperature at the physiological level. Disadvantages are high cost ($10000-$40000) and often not an optimal design for the specific needs of the research project. For example, closed coil design is well suitable for the brain imaging, but inconvenient for cardiac scans, where ECG electrodes along with a respiratory pillow have to be fitted into the small closed space. From this perspective the self-designed coils are preferable. Figure figure 29 I, J shows examples of the mouse and rat coils manufactured by the Philips company and *ex vivo* scan of the mouse heart.

The gradient coil strength and speed are important small animal imaging. The MR scanner must have strong and fast switching gradients for achieving the high spatial resolution without substantial image degradation due to cardiac motion. State-of-the-art clinical scanners 1.5T and 3T are equipped with high quality gradients (maximum gradient strength of 80 mT/m

and maximum gradient speed of 200 mT/m/ms), which allows to achieve in-plane resolutions of ~200 μm for cardiac imaging on rodents.

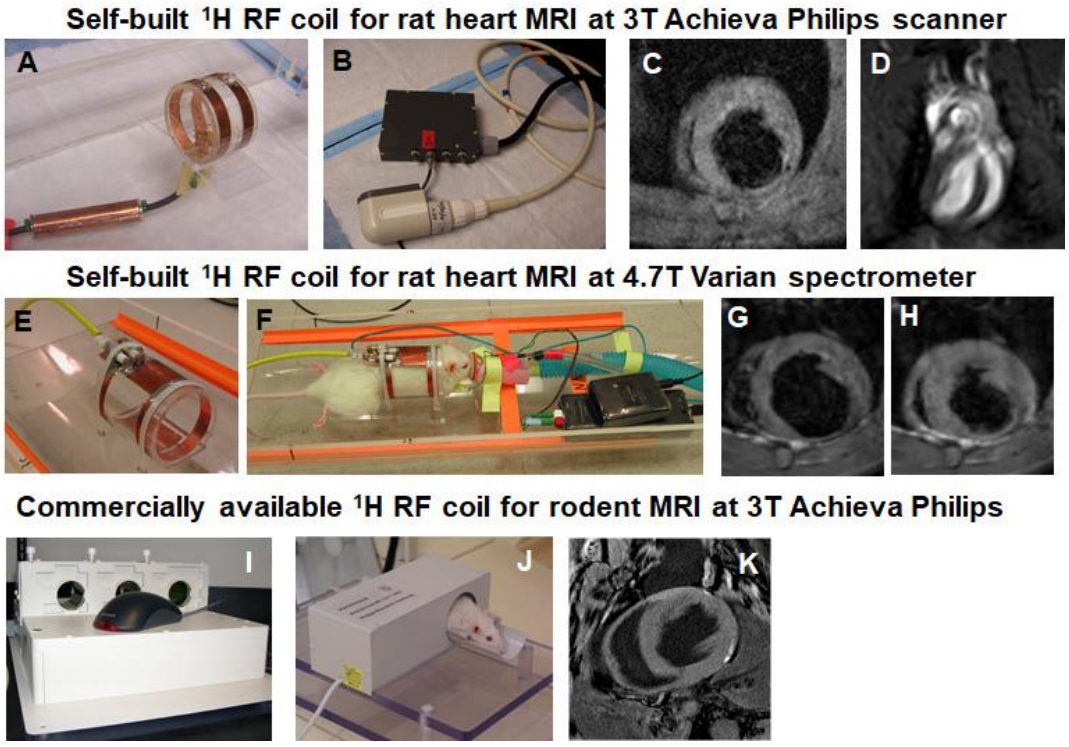

Figure 29. Self-built ^{1}H RF coils for *in vivo* MRI of the rodent heart. **A**: Receive-only coil (4.5 cm diameter) tuned into the 127 MHz with the cable trap balun to reduce the noise. **B**: Interface box for connection if the coil with the Philips scanner. **C**: 2D short axis view of the infarcted rat heart in the diastolic phase. Pulse sequence: prospectively triggered turbo spin echo black blood (TSE BB): slice thickness 1.5 см, repetition time (TR) 632 ms, echo time (TE) 10 ms, flip angle (FA) 90°, acquisition matrix 256x256, 2 signal averages. **D**: Long axis of the rat heart, pulse sequence: prospectively triggered, cartesian turbo-gradient echo cine (TFE CINE): slice thickness 2 mm, TR 7.7 ms, TE 4.4 ms, FA 30°, matrix 128x128, 4 signal averages. **E**: Transmit-receive RF coil (5 cm diameter) tuned into the proton frequency at 4.7T - 200 MHz. **F**: Rat in the cradle with the heart in the coil center and the additional equipment for inhalation anesthesia and ECG-gating. **G**: Short axis of the infarcted rat heart in diastole. Prospectively triggered spin-echo (SE) pulse sequence: **H**: Short axis of the infarcted rat heart in systole. **I**: Mouse "condo" coil (3 cm diameter) for simultaneous imaging of 3 mice. **J**: Rat position in the 4-element solenoid coil (5 cm diameter). **K**: Example of the *ex vivo* mouse heart imaging. 3D scan with matrix 800 x 800; FOV 40 x 40 mm; TE 10.3 ms; TR 53.35ms; FA 45°, water fat shift 6.58 pixels. This image was done by Stephan Fisher at the Philips (Cleveland, USA).

The particular choice and dose of anesthetic are important for rodent imaging, since many sedative drugs suppress the contractile function of the heart. The optimal sedation method for rodent imaging is light inhalation anesthesia with isoflurane (1-1.5%) in oxygen (0.5-1 liter per minute flow rate) that enable stable sleep with minimal impact on cardiac function. Core body temperature in rodents falls quickly under anesthesia, therefore, it is important to monitor and maintain body temperature. MR-compatible rectal probes are available for temperature monitoring. Temperature maintenance can be done by using a

heating blanket with circulating heated water, by blowing hot air over the animal or by using special coils with built-in heater system. An MR-compatible temperature monitoring and heating system is commercially available for small rodent MRI that can regulate temperature variations less than 0.1°C (SA Instruments Inc., Stony Brook, NY, USA).

Cardiac MRI acquisitions require gating to the R-wave of the ECG to capture images at different phases of the cardiac cycle. Needle ECG electrodes are preferable for rodent imaging, because those provide stronger ECG signal. MR-compatible ECG electrodes are recommended, since the ECG signal is often inherently degraded by the magnetohydrodynamic effect, RF pulses, and gradient switching during imaging; all of those effects cause severe noise on ECG signal that interfere with the R-peak triggering. ECG monitoring and gating system for small animal MRI is commercially available from the SA Instruments, Inc. (Stony Brook, NY, USA, figure 30A). This system is developed specifically for small rodent imaging; it accounts for the low amplitude of the ECG signal and the high heart rates. This system provides monitoring of the physiological parameters (ECG, respiratory rate, temperature), MRI compatible and have fiber-optic output to trigger acquisitions. The price for MR-compatible physiological monitoring/gating systems range from $8000 to $22000. To decrease the motion-related artifacts, both, ECG and respiratory signals are important. In this case, the acquisition window is limited to milliseconds (Figure 30B). Standard clinical CMR exams will use breath-holding techniques to suppress respiratory motion. However, these techniques are not possible in small rodents. Pneumatic pillows have been developed specifically for respiratory gating in rodents during an MR exam. Gating is a method of synchronization of imaging with a phase of the cardiac and respiratory cycles. For the effective synchronization R-peaks on ECG should be clearly defined from the noise. SA Instruments provide software tools for skipping the noise related to gradients or arrhythmia, which is especially important for imaging of the infarcted heart with weak noisy ECG. The skipping is also used to trigger on every 2^{nd} or even 3^{rd} R-peak to enable rodent imaging on clinical scanners with the limitations in heart rate <250 bpm.

Because rodents are much smaller than humans, it is important to position the animal and cradle at the isocenter of the scanner where field homogeneity is optimized. Access to the anesthesia lines and ECG leads is important as well, therefore, self-built specialized coils and animal cradles might be preferable over the commercially available standardized equipment.

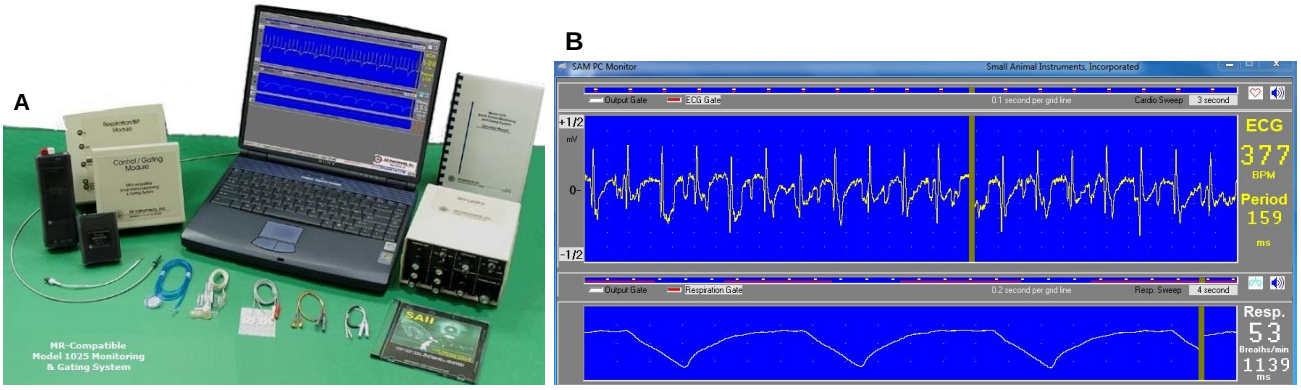

Figure 30. A: Specialized equipment for physiological monitoring and gating of the cardiac acquisitions on small animals (SA Instruments, Inc., Stony Brook, NY, USA) includes ECG/Temperature Module, Respiratory Module, ECG leads, respiratory pillow sensor, temperature sensor, software and other additional equipment. **B**: ECG and respiratory curves from the live rat acquired during cardiac MRI exam.

MRI pulse sequence features for cardiac exam on small animals.

Adjustments of MRI acquisitions are necessary to accommodate the small body size and fast heart rate, especially in small animals. Field of view has to be reduced by almost 10-folds: from 350 cm^2 to 30-40 cm^2 in mice. To visualize fine tissue structures, smaller voxel size and higher image resolution are required. The higher SNR requirements and increased number of signal averages additionally to the above challenges will cause significant increase in scan time. To accommodate the fast heart rate, shorter pulse sequences that use several heart cycles to build the image are preferable. In this conditions short and ultra-short TR and TE are preferable in small animal cardiac scans. Use of several signal averages helps to increase SNR, especially in cases when the respiratory gating is not used. While in large animals and human patients one signal average is commonly used along with the breath hold technique. Standard scan preparation, including automatic shimming, can be used for most small rodent cardiac MR exams. However, if large inhomogeneities are observed in images, manual shimming may be required.

For small animal cardiac MRI exam on different scanners several pulse sequences were developed or adjusted according to the above requirements. One way of heart imaging the end-diastolic and end-systolic phases of cardiac cycle is using a standard spin echo (SE) pulse sequence with short TR and TE, prospective ECG-gating and manual setting the acquisition delay time. For example, for the cardiac SE image in the end-systole the delay time should be set equal to the 30% of the cardiac cycle (R-R interval). For a mouse with the heart rate of 600

bpm the R-R interval is about 100 msec, therefore, acquisition delay time will be 30 msec in SE sequence. For the end-diastolic image, the acquisition should be taken without delay time after R-peak. Examples of the SE cardiac images of the infarcted rat heart are shown in the figure 31.

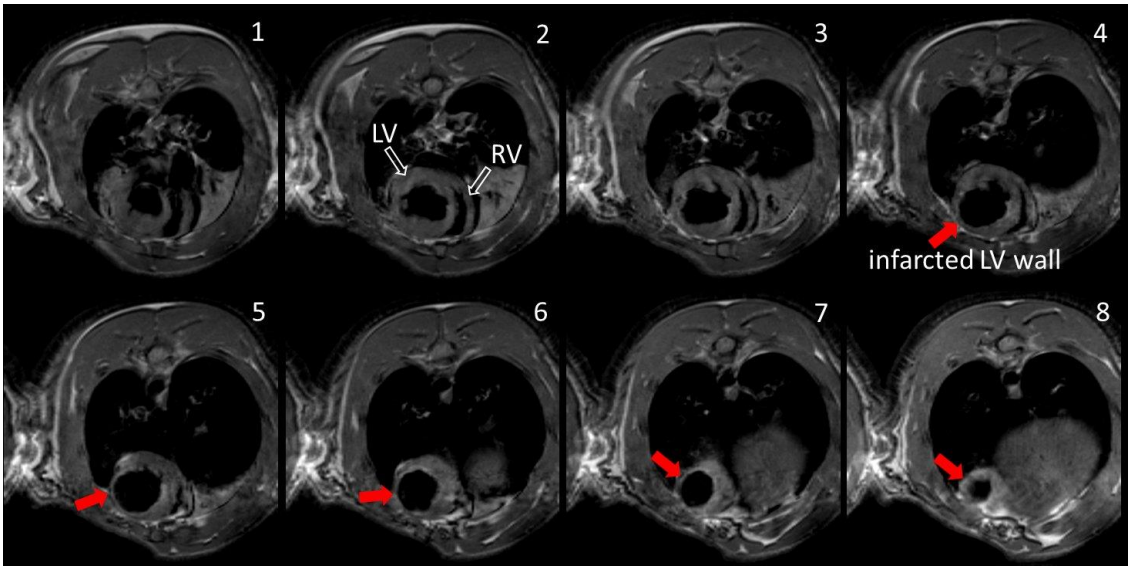

Figure 31. A set of multi-slice short-axis images of the infarcted rat heart from the base (slice 1) to apex (slice 8) at the end-diastolic phase of cardiac cycle acquired at the 4.7T Varian NMR spectrometer. Spin-echo pulse sequence parameters: FOV 50 mm^2; 2D matrix of 256x128; TR 400 ms; TE 13 ms; flip angle 90°, slice thickness 1.5 mm without gap between slices. Each slice was acquired at exactly the same time of R-R interval during cardiac cycle. White arrows point into the left ventricle (LV) and right ventricle (RV) wall of the heart. Red arrows point into the thin infarcted area of the LV.

Recommended slice thickness for assessment of heart geometry and contractile function is 1-1.2 mm in mice; 1.5-2 mm in rats; 4-5 mm in dogs and non-human primates and 6 mm in pigs. Thicker slices are used in scout images. Using thick slices in small animals may cause partial volume artifacts and errors in assessment of cardiac morphology and function.

CINE multislice multiphase imaging is possible in rodents in the high field as well as in the low field clinical scanners using gradient echo pulse (GRE) sequences with short TR and TE and retrospective gating (figure 32). In GRE pulse sequences only one row in k-space is acquired after each R-peak. Therefore, for the complete image of the heart slice in the specific phase of cardiac cycle the prolonged scanning is required. Number of heart beats required for the completion of one slice depends of the phase encoding steps. The imaging time can be estimated by multiplying the time duration of the R-R interval of the ECG with the image matrix size and the number of signal averages. The flip angle is normally between 15-20°. A single slice acquisition can generally be obtained in 1-3 minutes, depending on the matrix size and number of signal averages.

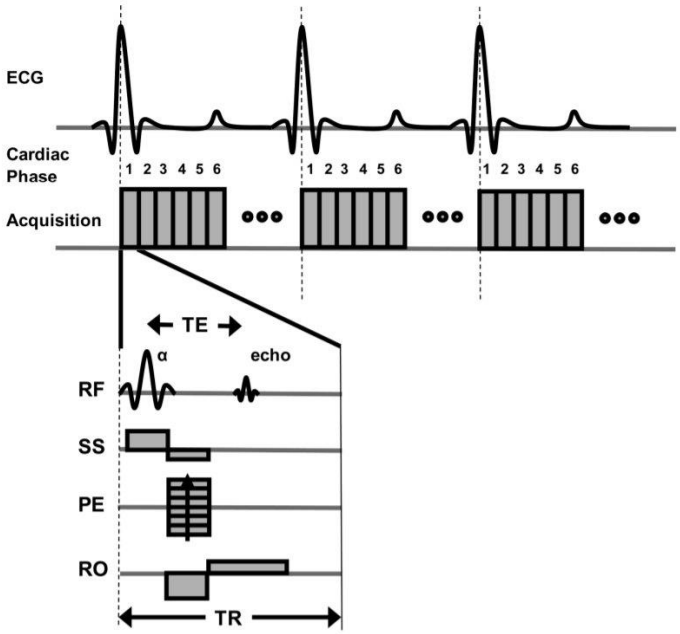

Figure 32. A timing diagram for a cine MRI acquisition using a spoiled gradient echo (GRE) pulse sequence. RF - radiofrequency signal; α - excitation pulse; echo - resulting MR signal, SS - slice-select gradient, PE - phase encode, RO - readout gradient, TE - echo time, TR - repetition time. Individual images are acquired at different phases (e.g. 1,2,3,4,5,6,…) of the cardiac cycle. Индивидуальные изображения получают в разные фазы сердечного цикла (1,2,3,4,5,6,…). The maximum number of cardiac phases that can be acquired is determined by the TR and the time interval between R waves of consecutive heart beats Figure from [397].

Representative mid-ventricular short-axis images from a CINE MRI acquisition of the mouse heart are shown in the Figure 33. In spoiled GRE images, the blood pool appears bright and the myocardium dark. The clear border definition between the blood pool and the myocardial tissue enables CINE MRI to be an accurate technique for measuring ventricular volumes and mass. Table 3 clearly represent the differences in the left ventricle chamber volumes, myocardial mass and contractile function between healthy and infarcted rats.

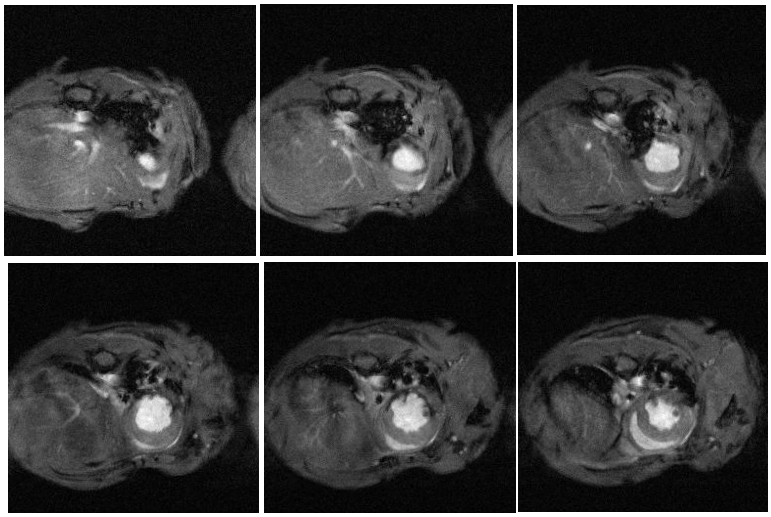

Figure 33. Flow compensated turbo gradient-echo CINE pulse sequence for imaging of the infarcted mouse heart at the 14T Bruker Biospec spectrometer. TR 6ms, TE 1.64 ms, slice thickness 1 mm, FA 15°, FOV 25x25mm; acquisition matrix: 256x256, na=4.

Table 3. MRI measurements taken from the normal and infarcted rat hearts. Infarcted hearts are characterized by enlarged left ventricle chamber dimensions in the end-systole (ESV) and end-diastole (EDV) and decreased contractile function (ejection fraction, EF).

	Body weight, g	Heart rate, bpm	ESV, mm^3	EDV, mm^3	SV, ml	LV mass, mg	CO, mm^3/min	EF, %
Normal rats, n=5	318.0±4.9	422.4±15.6	161.5±7.8	419.9±9.2	258.5±8.7	689.1±17.4	108913±4058	61.4±1.63
Infarcted rats, n=11	323.0±7.0	359.6±11.0**	419.6±26.5***	677.5±20.9***	257.9±15.7	755.3±20.5	92554±5977	38.5±2.7***

All values are reported as Mean ± St. Error of mean.
Statistically significant difference with the control group (normal rats): * $p<0.05$; ** $p<0.01$; *** $p<0.001$.

Delayed contrast-enhanced MRI is used in large and small animals for the infarct visualization. T_1-weighted inversion-recovery pulse sequence is run at 10-30 minutes after the gadolinium (Gd) contrast agent administration (0.1-0.2 mM/kg). Gd-based contrast agents are shortening the T_1 relaxation time of the tissues. Since Gd-contrast accumulates in the fibrotic scar that area of myocardium restores the magnetization faster and appears hyper-enhanced, while the contrast agent is washed out quickly from the viable myocardial tissues which appear dark with the correct inversion time (TI). In rodents the contrast agent is usually delivered via a self-built catheter inserted into the right femoral vein or to the tail vein, however, intra-peritoneal (i.p.) injection of gadolinium is also producing good results in scar visualization. Contrast agent dose is usually higher for ip injections ~ 0.3-0.6-mmol/kg. In large animals, Gd is injected intravenously (i.v.) via jaguar or hand vein catheter.

Imaging of infarction in mice was performed using a 14T Bruker NMR spectrometer (^{1}H frequency 600 MHz). For assessment of heart contractile function, a generic form of steady-state free precession imaging technique, fast low angle shot (FLASH), was used. FLASH technique is a spoiled gradient echo sequence that destroys transverse coherences and yields T_1 contrast that incorporate transverse coherences into the steady-state signal. An ECG-triggered 2D CINE spoiled gradient echo pulse sequence was used in 10-12 short axis slices of the heart with a slice thickness of 1 mm and a zero-filled, in-plane resolution of 100×100 μm^2. The TE was 1.8 ms; TR 4.8 ms; FOV 30 mm^2; FA 30°; 30 cardiac phases were acquired within the R-R interval. The same line of k-space was collected for each phase during 1 heart cycle. This was repeated until all the phase-encoding steps were acquired. Although spatial resolution in the phase-encode direction could be increased by scanning for longer periods, the acquisition of 192 lines served to balance spatial and temporal resolutions. For infarct

visualization (after i.p. injection of MRI contrast agent), an inversion-recovery (IR) technique was used with the same slice thickness (1 mm) and same slice positioning as for CINE. To increase T_1-weighting for contrast-enhanced imaging flip angle was increased to 60° with TE 1.7 ms, TR 700 ms, TI 300 ms, FOV 30 mm^2. Examples of the CINE and IR images of the normal and infarcted mouse heart are shown in the Figure 34. On visual comparison, the contrast-enhanced regions in the IR images were found to correspond closely to the regions of the left ventricle with thin wall and absence of wall motion as defined by CINE. In cases when the gadolinium administration cannot be performed, the scar size might be estimated as areas of the left ventricle thinning due to infarction (systolic wall thickness <0.5 mm in mice) and compared with that of viable (thick) LV tissue; a score might be assigned as a percent of overall ventricular circumference [375]. For each heart, the mean score can be determined from all of the image slices.

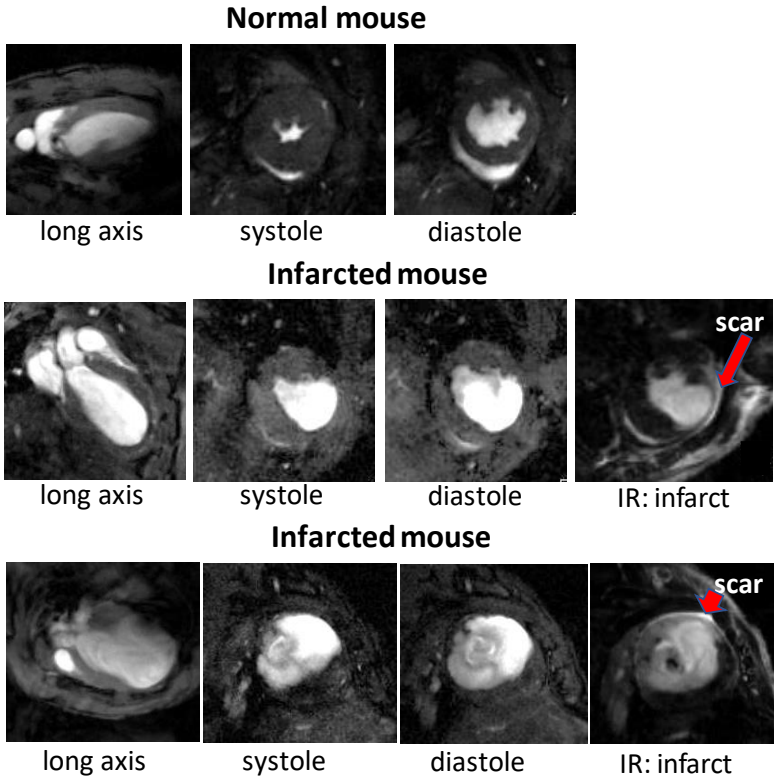

Figure 34. Examples of the cardiac MRI scans of the normal and infarcted mice at the 14T Bruker spectrometer. Normal mouse heart is characterized by good contractility and LV wall motion as well as small size of the heart. Infarcted heart has enlarged LV chamber (remodeling), weak ECG signal, arrhythmia, decreased contractile function and absence of the LV wall motion in the scar zone (red arrow).

Cardiac MRI exam in large infarcted animals is also complicated by the weak ECG signal accompanied with arrhythmia, which brings additional challenges to already complicated animal imaging technology (figure 35). Often CINE multislice sequence with

retrospective gating cannot be completed due to high arrhythmia (abrupted scans); in these cases, the prospective gating can be used or the special noise-skipping software tool in the SA Instrument equipment (that is normally used for small animals) can be implemented to gate cardiac acquisitions in large animals (figure 35).

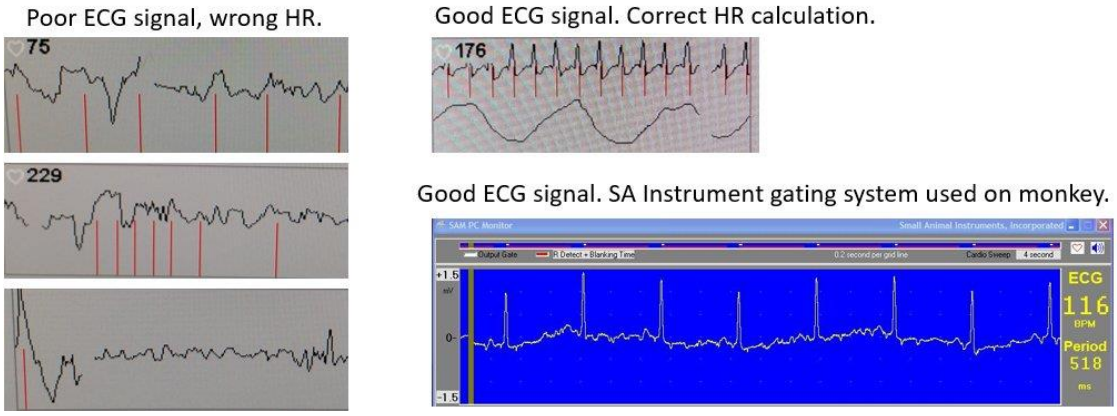

Figure 35. Examples of the bad ECG (on left) and good ECG signal (right column) from the infarcted monkey heart. It is possible to use Small Animal Monitoring and Gating system (SA Instruments, Inc.) for gating cardiac MRI on large animals (monkey in the current example). HR – heart rate in beats per minute (bpm).

For the infarct size measurement, short-axis IR images spanning the LV should be acquired, endocardial and epicardial borders manually delineated, regions of interest (ROI) selected in the non-enhanced viable myocardium and in the hyper-enhanced non-viable myocardium for the signal intensity threshold calculation using the full-width half-maximum or mean plus 5 standard deviation (5 SD) criterion. The infarct volume is calculated by summing the volumetric ROIs from each slice. The infarct size is reported as a percentage of the left ventricle (LV) mass. Scar location visualized in IR images is usually well correlated with the location of edema identified with the T_2-weighted pulse sequence (figure 36).

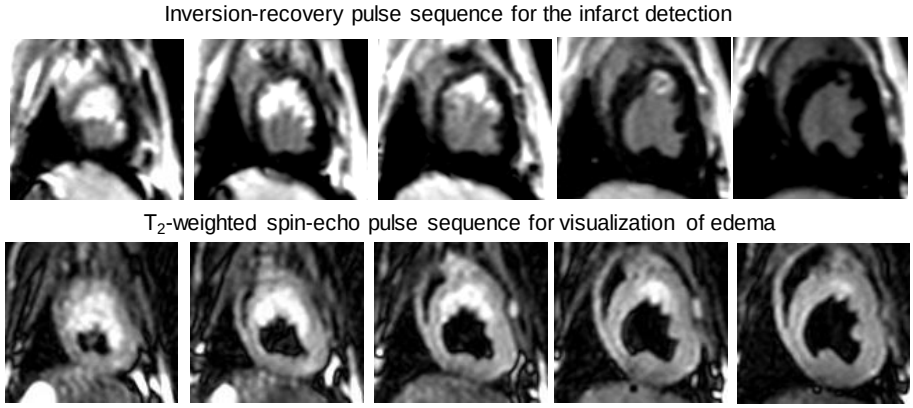

Figure 36. MRI of the infarct zone (top row) and edema (lower row) in the dog 2 weeks after myocardial infarction at the 3T Achieva Philips. Inversion-recovery pulse sequence: FOV 250x250 mm, slice thickness 5 mm, TR/TE = 6/3 msec, TI ~300 msec, FA 25°, matrix 156x114, na 2. T_2-weighted SE: FOV 250x250 mm, 5 mm slice, TR/TE = 1200/40 msec, FA 90°, matrix 144x120, na 2.

Dynamic contrast enhanced (DCE) MRI acquisitions are used for quantitative assessment of myocardial perfusion in a variety of diseases. The use of first-pass contrast-enhanced MRI to identify myocardial perfusion deficits at rest or under stress has shown prognostic value in detecting significant coronary occlusive disease, assessing the risk of cardiovascular events, and identifying the presence of hibernating myocardium after infarction [397-403]. Fast-scan perfusion methods have been used to track the passage of a bolus of a MRI contrast agent through the heart and demonstrate qualitative or semi-quantitative perfusion information. Qualitative assessment may include visualization of the areas of perfusion deficit that is seen as dark zones in myocardium after injection of the Gd-based contrast agent. To provide semi-quantitative and quantitative myocardial blood flow measurements, MRI intensity data must be fit to a model that relates signal intensity changes to tissue perfusion. Calculation of absolute myocardial blood flow is possible using the Kety model, modified to account for extravascular movement of the contrast agent [404]. Combining myocardial blood flow measurements with estimates of extracellular volume it should be possible to discriminate among normal, ischemic, reperfused, and infarcted myocardium.

DCE MRI can be done in animals after specific modifications of the acquisition protocol. DCE sequence modifications include using single-shot saturation recovery TFE acquisition, shortening of TR (from 275 msec in patients to 3 msec in animals), decreasing flip angle from 50 to 20 degrees, decreasing slice thickness from 9 mm in humans to 5 mm in large animals. DCE image resolution in human patients is about 0.4 pixels per mm, voxel size: 2.4 mm^2. DCE image resolution in large animals is about 0.7 pixels per mm, voxel size 1.4 mm^2. Due to small infusion volume for animals, the clinical contrast agent injectors cannot be used. There are commercially available mini-injectors for animals, but this requires a catheter setup for the contrast agent and saline administration. Contrast agent bolus injections can be done manually during the acquisition (a person should be present in the scanner room for injection) followed by a saline flush. Unlike DCE data in tumors, myocardial DCE data have lower diversity among tissue uptake curves, higher temporal resolution, and sharper AIF curve with significant saturation even at relatively low-contrast doses. The examples of DCE MR images in the dog heart are shown in the figure 37. Temporal resolution of these images is high – one

image per second; this allows to follow the dynamic of the contrast agent via the heart chambers and myocardial tissue.

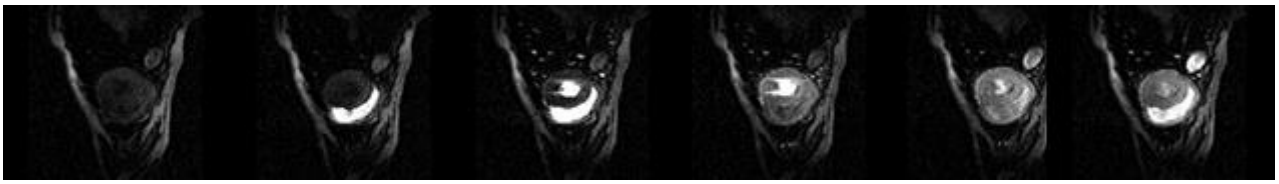

Figure 37. First pass perfusion in the dog heart to estimate blood supply and tissue permeability. Dynamic perfusion sequence: mid-ventricle single-slice, single-shot saturation recovery TFE, 20° flip angle, 5 mm slice thickness, TR/TE of 3.0/1.4 msec, in-plane resolution of 1.99 mm × 1.96 mm.

Disadvantage of the high-speed imaging techniques in the dynamic studies of the beating heart is low SNR. Several postprocessing techniques were developed for automated registration of the arterial input function (AIF) and noise attenuation. Noise and contrast agent dynamics can be modeled as random processes, then noise can be reduced using Kalman filtering methods [405] to rapidly compute linear minimum mean square error estimates of the noise-free images. Motion removal can be accomplished by minimizing the squared difference of images [406]. As a result, the new algorithm, Kalman filtering, registration, and smoothing (KFRS), has been developed [407]. KFRS algorithm enables analysis of DCE images, where temporal changes in the intensity of individual pixels can be modeled. We have used the KFRS algorithm for the motion correction noise filtering in DCE imaging and perfusion parameters extraction in large animal studies (figure 38). Details of the DCE analysis are discussed in the part 4.4.

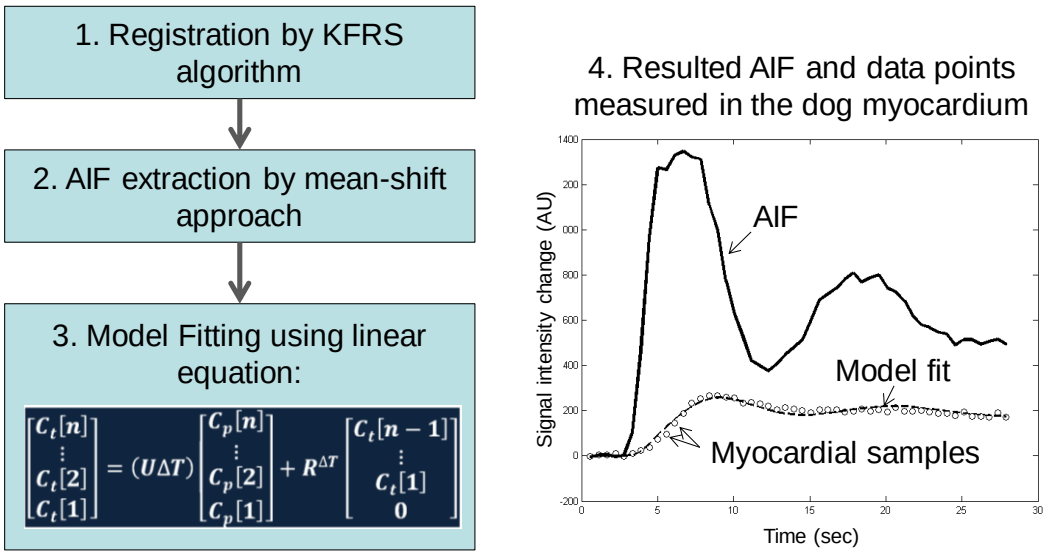

Figure 38. Scheme of the kinetic analysis of the DCE MRI and the resulted curves for the arterial input function (AIF) and myocardial tissue enhancement in dog. AU - arbitrary units.

Spatially localized ^{31}P MR spectroscopy on rodents requires special coil design and pulse sequence development. The unique custom coil assemblies were built for the combined $^{1}H/^{31}P$ MR exam in the different spectrometers with different magnetic field strength (figure 39).

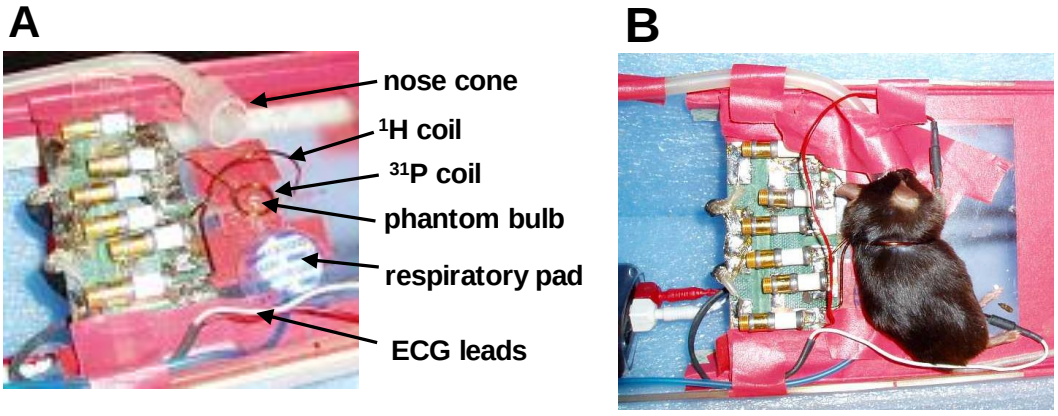

Figure 39. Custom RF coil assembly for *in vivo* ^{1}H MRI and ^{31}P MRS of the mouse heart at the 4.7T GE Omega NMR spectrometer. **A**: Transmit-receive ^{1}H solenoid coil (25 mm diameter) tuned into the 200 MHz and ^{31}P surface coil (10 mm diameter) tuned to 81 MHz (^{31}P coil) with the phantom bulb in the middle of the coil. **B:** Mouse position in the ^{1}H coil with the heart centered over the ^{31}P coil.

The original design of the $^{1}H/^{31}P$ coil assembly has been proposed by Dr. Chacko at the Johns Hopkins University (Baltimore, MD, USA) for *in vivo* MRI/MRS studies of the mouse heart at the GE Omega NMR spectrometer equipped with a 4.7T Oxford magnet (40 cm horizontal bore) and a 15 cm actively shielded Accustar^{TM} gradient set. This coil assembly consists of a single loop proton coil 2.5 cm diameter placed on the flat Plexiglas platform and another single loop phosphorus solenoid surface coil (1 cm diameter) placed in the orthogonal direction to the ^{1}H coil. ^{1}H and ^{31}P coils each are connected to the tuning and matching capacitors for the fine tuning/matching of the coil to the right frequency. A phantom bulb (5 mm diameter) filled with 500 mM phenyl-phosphonic acid (PPA) is placed in the middle of the surface ^{31}P coil. The highly concentrated PPA solution has large chemical shift (~20 ppm), therefore, its peak is easy detectable in ^{31}P spectra. The phantom is also used for spatial localization of 1D spectral slices. Animal position in the coil assembly is very important. The anesthetized mouse should be placed inside of the proton solenoid coil and rotated to its left side to place the heart over the ^{31}P coil. The correct position of the animal over the phosphorus coil is verified using scout ^{1}H images, where the PPA bulb is seen as well as mouse heart. The coil assembly design and position on the large open plexiglass platform enables easy access to animal, capacitors, ECG electrodes and for placing respiratory pillow and rectal probe if

needed. This simple self-made probe design proved its reliability in use and quality of resulted images and spectral acquisitions.

Several different methods were developed for obtaining image-localized ^{31}P MRS from the hearts of humans and animals, as it was discussed in the part 2.5. We found that for ^{31}P MRS on small animals a one-dimensional chemical shift imaging sequence (1D-CSI) sequence provides the best possible spectra with high spatial localization. A small 1 cm diameter (comparable to the size of mouse heart) surface ^{31}P coil allows sufficient signal penetration for obtaining spectral slices from the anterior LV wall with minimal signal contamination from the chest muscles and blood. Magnetic field homogeneity is very important for obtaining high quality spectra. ^{1}H solenoid coil has been used for shimming on a thick slice containing the heart. After optimization of the magnetic field homogeneity, spatially localized ^{31}P MR spectra were acquired using 1D-CSI pulse sequence with 32 phase encode steps in the direction perpendicular to the plane of the coil. The time of the phase encode gradient was 0.5 msec, the field of view 32 mm, the recycle delay 1s, and 64 averages were obtained per phase encode step. Adiabatic pulses with a flip angle of 45° were used for uniform excitation. Total acquisition time was ~34 min without ECG or respiratory motion compensation. With this protocol, well-resolved spectra from 1-mm slices from the antero-septal region of the mouse heart parallel to the coil were obtained (figure 40).

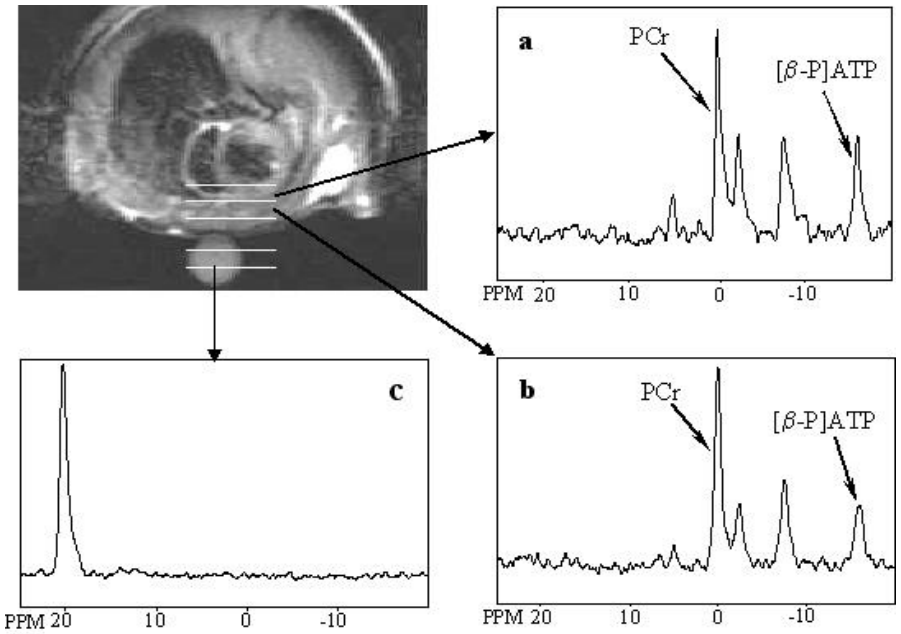

Figure 40. Typical transverse short axis ^{1}H MRI of a mouse thorax through a mid-LV slice of the heart at end-diastole. Selected 1-mm ^{31}P NMR spectral slices containing the myocardium (a), skeletal muscle (b) and a bulb with phenylphosphonic acid (c) are shown.

The same principle has been used for building $^{1}H/^{31}P$ coil assembly for *in vivo* MR spectroscopy on mouse heart at the 14T Bruker spectrometer vertical bore (figure 41). The ^{1}H saddle coil (25 mm diameter) has been combined with ^{31}P surface coil (10 mm diameter); the PPA phantom (500 mM) has been inserted in the middle of the ^{31}P surface coil. ^{1}H coil with distributed capacitance tuned to 600 MHz was used for localized shimming and anatomic imaging. The ^{31}P and the ^{1}H coils were decoupled from each other on the basis of their geometry so that mutual interference was minimized. Coordinate axes were defined with z parallel to the static magnetic field magnitude (B_0) and xz as the RF coil plane. Both coils were curved to allow optimal contact with the chest wall of the animal. The coil assembly has been placed to the shielded mouse cradle 30 mm diameter.

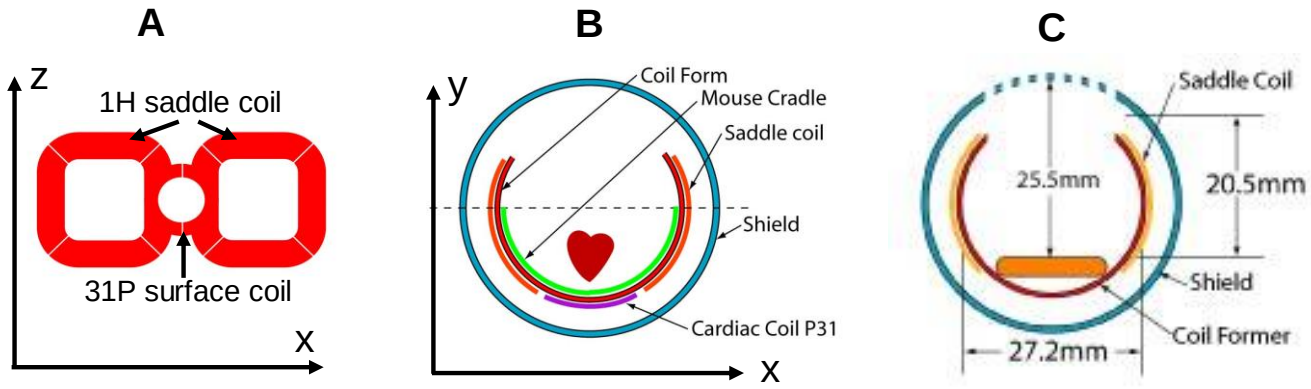

Figure 41. Custom RF coil assembly for *in vivo* ^{1}H MRI and ^{31}P MRS of the mouse heart at the 14T Bruker NMR spectrometer. **A**: Transmit-receive two-loop ^{1}H saddle coil (25 mm diameter) tuned into the 600 MHz and ^{31}P surface coil (10 mm diameter) tuned to 241 MHz (^{31}P coil) with the phantom bulb in the middle of the coil. **B**: Cross-section of the coil assembly with description of the parts. C: Specific measurements of the $^{1}H/^{31}P$ coil assembly. position in the ^{1}H coil with the heart centered over the ^{31}P coil. Coordinate axes are shown as z - parallel to the static magnetic field magnitude (B_0) and xz coordinates in the ^{31}P RF coil plane.

Next step was search for optimal pulse power settings. To match the coil loading, a mouse-like phantom was made from the glove finger filled with 100 mM solution of inorganic phosphate K_2PO_4 (Pi). Non-localized ^{31}P block- and adiabatic pulses with long TR for complete relaxation were used to calibrate power for each pulse duration spectroscopy with. For the adiabatic pulse, pulse duration was gradually increased from 0.5 msec to 2 msec. The adiabatic pulse calibration results are shown in the figure 42. Then 1D SCI was performed on the same phantom with optimal pulse power and global shimming (50% spectral linewidth of 48.8 Hz after shimming).

Nuclei:	Excitation pulse:	Area
Ref Attn Ch1	Attenuation	
30	4.5	3057264
20	-5.5	2431645
40	14.5	2405529
38	12.5	2814439
36	10.5	2987997
34	**8.5**	**3171979**
32	6.5	3131020
33	7.5	3061139

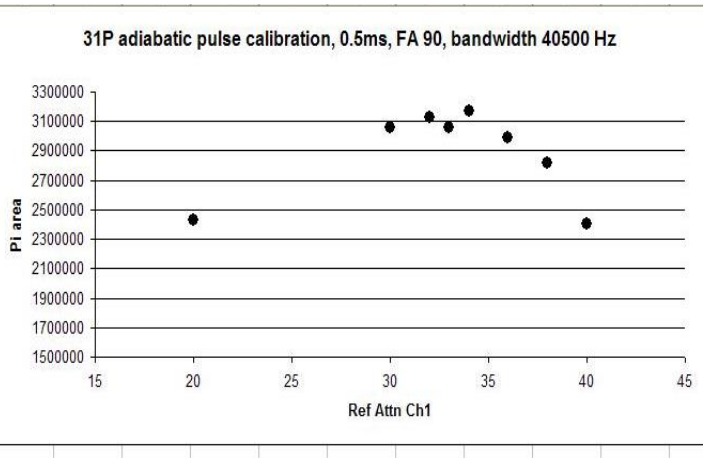

Figure 42. Power calibration for the adiabatic pulse ('sech') 0.5 msec pulse length, 90° flip angle, 40500 Hz bandwidth.

Processing of CSI spectra have shown gradual drop off in the signal intensity away from the coil. Maximal inorganic phosphate peak area was at power of 34 dB, which corresponded to 8.5 dB attenuation of excitation pulse power (figure 42). The resulted non-localized spectra obtained with the optimal power settings using block- and adiabatic pulses and a mouse-like phantom are shown in the figure 43.

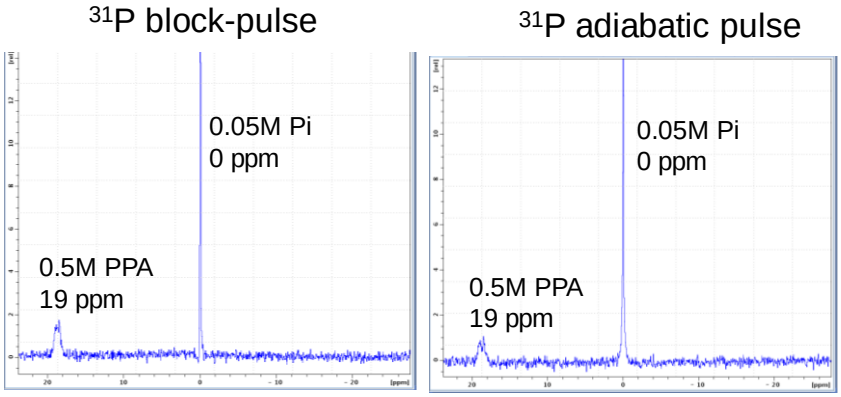

Figure 43. Acquired ^{31}P spectra using calibrated for an optimal power block- and adiabatic pulses. Non-localized ^{31}P block-pulse parameters: TR 2 sec, 0.1ms pulse length, 90° flip angle, Ref. attenuation Ch1: 30 dB (optimal power). Non-localized ^{31}P adiabatic-pulse parameters: TR 2 sec, 0.5 ms pulse length, 90° flip angle, Ref. attenuation Ch1: 34 dB (optimal power).

To continue the adiabatic pulse power optimization and to test the coil sensitivity at the 14T spectrometer, a new phantom was built that contained three 3mm NMR tubes filled inorganic phosphate solution K_2PO_4 in final concentration of 0.1 M and different pH: 2.0; 7.0 and 11, to create chemical shift effect. Three NMR tubes were inserted into the 25ml Falcon tube filed with 1% agarose (figure 44). Two tubes that were located closer to the surface ^{31}P coil were "visible" on the ^{31}P spectroscopy; the 3rd one was not detected. Therefore, the sensitivity depth of the 10 mm diameter ^{31}P surface coil is about 10 mm.

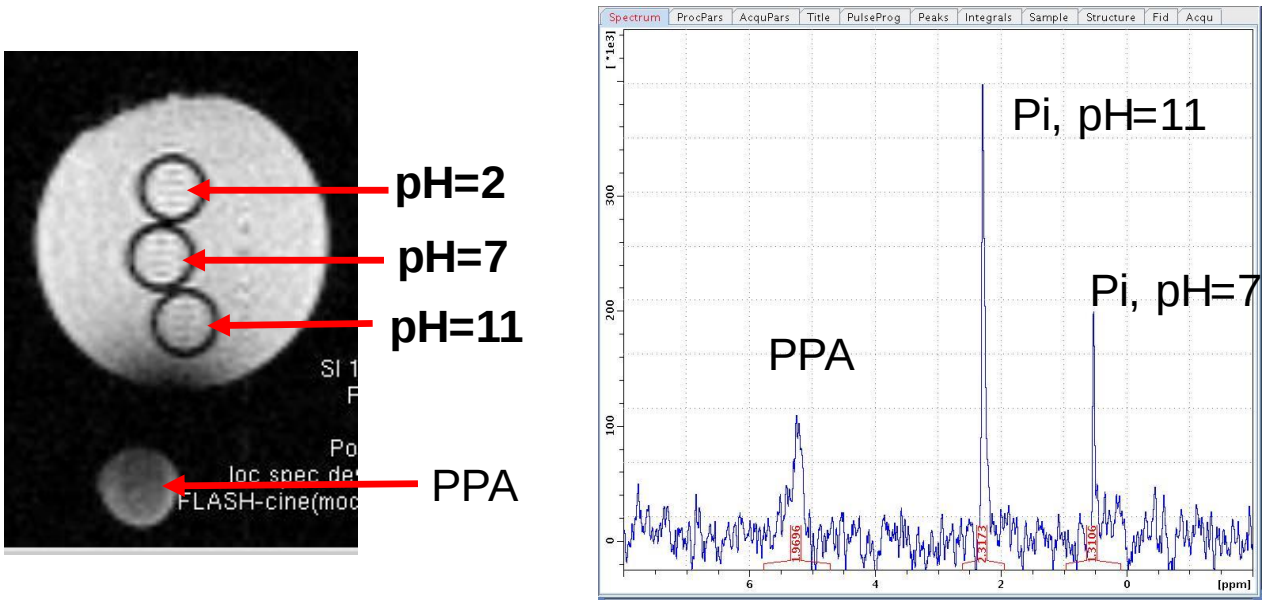

Figure 44. ^{1}H MRI (FLASH pulse sequence) showing three 3mm NMR tubes filled with 10 mM K_2PO_4, pH 2, 7 and 11. Spectra from two Pi peaks are detectable, 3rd tube (pH 2) is invisible (too far from the coil). 50% spectral linewidth after global shimming was 27 Hz.
Non-localized ^{31}P block pulse**:** TR 2 sec, 10° FA, na = 32.

For further power optimization, three tubes in the phantom were located at the same distance to the ^{31}P surface coil (parallel to the coil). The sensitivity profiling with different power settings are shown in the figure 45. The optimal pulse power for 1D-CSI was found about 32 dB.

The coil sensitivity was also tested by using mouse-like phantom (glove finger) filled with different concentrations of Pi. We found that ^{31}P surface coil is sensitive enough to detect signal from the low-concentration (10 mM) phantom, therefore, the *in vivo* ^{31}P MRS should be possible with the self-built coil assembly. To perform spatially localized cardiac ^{31}P MRS in live mouse, nose cone was placed into the mouse holder for the inhalation anesthesia supply; ECG leads and respiratory pillow were used to trigger MR imaging and spectroscopic acquisitions. In opposite to the lower field magnets, the 14T spectrometer is highly sensitive to noise, therefore both ECG and respiratory gating are required for obtaining high quality data. Good shimming is critical in spectroscopic acquisitions. First, we optimized shimming protocol on a mouse-like phantom; the global and voxel-localized shimming protocols were used: mapshim (with Bruker macros, matrix 64×64×64), fastmap and PRESS-waterline (6 mm^3 voxel).

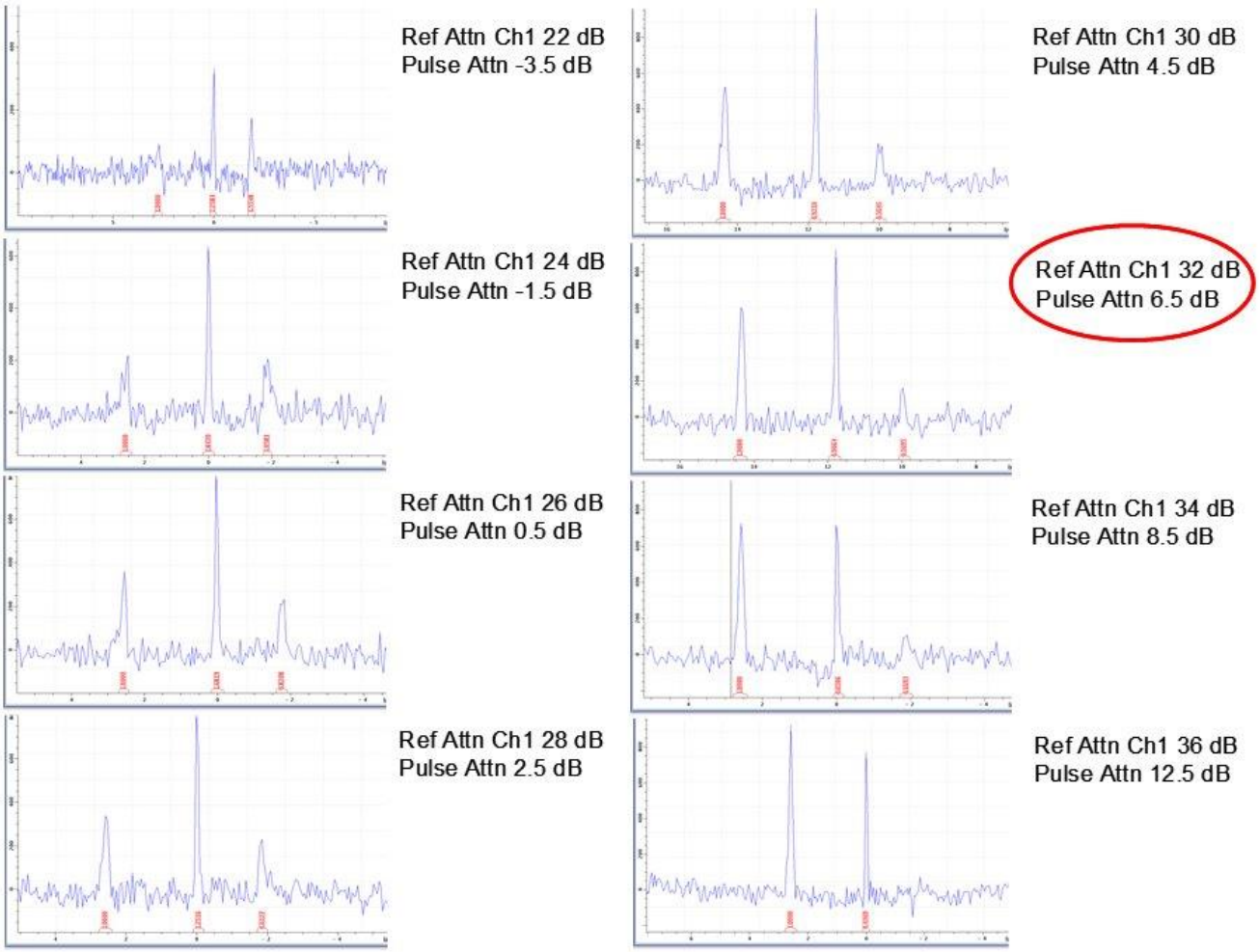

Figure 45. The sensitivity profiling with different power settings for three 3mm NMR tubes filled with 10 mM Pi, pH 2, 7 and 11. 50% spectral linewidth after global shimming 36.6 Hz. Non-localized 1D-CSI ^{31}P adiabatic-pulse parameters: TR 2 sec, 0.5 ms pulse length, FA 90°.

Next step was shimming optimization on the living anesthetized mouse (~25 gram). Global and voxel-localized shimming protocols (mapshim, fastmap and PRESS-waterline) were used. The best shimming results were achieved with PRESS-waterline protocol and large voxel size 12×12×12 mm covering whole heart. Global shimming: 50% linewidth 293 Hz. PRESS-waterline for localized shimming: 50% linewidth 48.8 Hz. Disadvantage of the manual shimming – it is time consuming; it takes 40-50 min to get a 50% linewidth of 48.8 Hz. Non-localized ^{31}P spectra from live mouse at the 14T Bruker Biospec NMR spectrometer is shown in the Figure 46.

Non-localized ^{31}P block-pulse

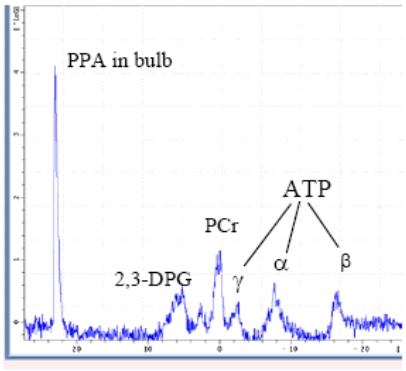

Non-localized ^{31}P adiabatic pulse

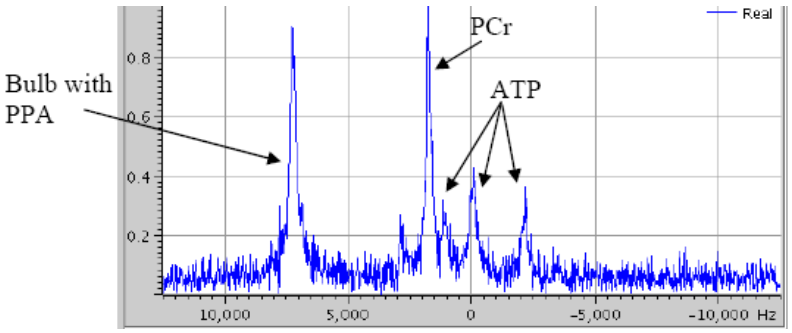

Figure 46. Non-localized ^{31}P spectra from live mouse at the 14T Bruker Biospec spectrometer. Block-pulse parameters: TR 2 sec, 0.1ms pulse length, FA 90°, bandwidth 12800 Hz, na 128, power 30 dB. Adiabatic pulse parameters: TR 2 sec, 0.5 ms pulse length, FA 90°, na=128, bandwidth 40500 Hz, power 32 dB, acquisition time 4 min.

Spatial localization was achieved with the use of 1D chemical shift imaging with the PHASE encoding direction in y-axis perpendicular to the plane of the surface coil, while READ gradient should be turned off. The optimal 1D-CSI pulse parameters for the localized 31P MRS on live mouse were found as following: FOV (READ direction) 3.2 cm; matrix READ (number of points in Read direction) 512; matrix P1 (number of points in PHASE direction) 32; FOV divided by the number of phase encode steps gives the thickness of the voxel in the phase encode direction (the slice thickness of the 1D slices: 32 1D slices, each 1 mm thick); note that FOV can be decreased to 16 mm and with 16 phase encode steps would give the same 1mm thick CSI, but may give severe aliasing; TR 1-2 s; flip angle 90°; slice orientation: axial; TE should be shortest (around 0.7 ms); readout direction L-R; excitation RF pulse: adiabatic (sech); increase the sweep width to at least 10,000 Hz in order to cover the full ^{31}P spectrum (best spectral coverage at 15,000 Hz); receiver gain = 2050 (for maximum ^{31}P signal); 32 signal averages is the minimal for live mouse MRS (the more the better). The examples of the mouse ^{1}H image and spatially localized ^{31}P spectra are shown in the figure 47.

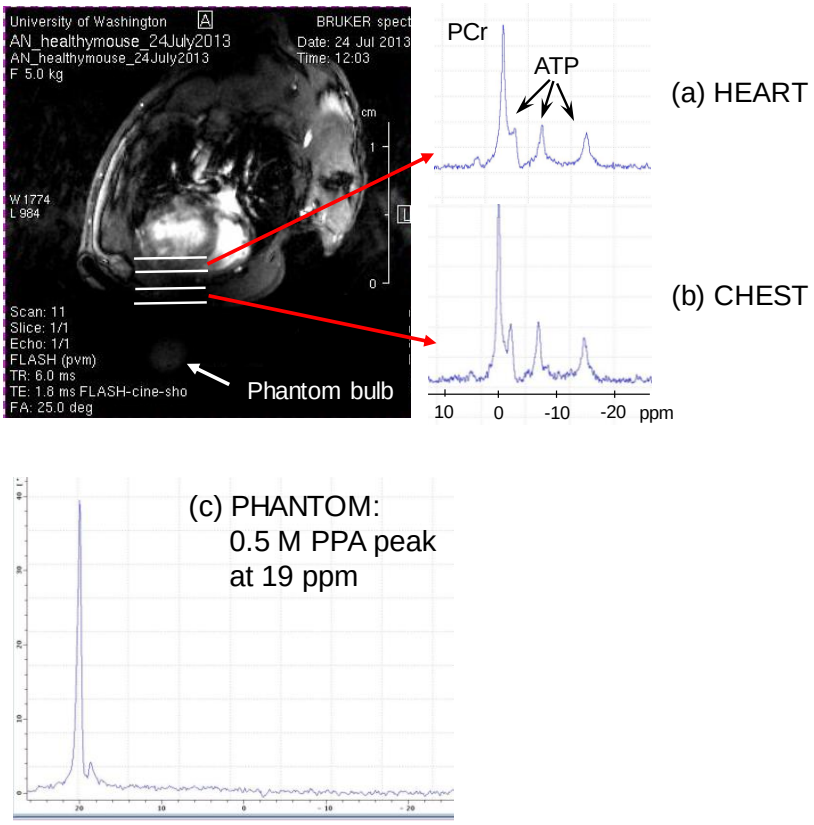

Figure 47. Transverse short-axis ^{1}H MR image of a mouse thorax through the heart and selected ^{31}P spectra taken from 1-mm slices located in the left ventricle of the mouse heart (a), mouse chest (b) and a phantom bulb filled with 500 mM PPA solution. ^{1}H MRI: cine FLASH sequence, TE 1.8 ms, TR 6 ms, slice thickness 1 mm, FOV 25 mm, na 2. ^{31}P MRS: 1D CSI, adiabatic pulse with 32 phase encode steps in the direction perpendicular to the plane of the surface coil, TE 0.7 msec; 64 averages per phase encode step, field of view 32 mm, recycle delay 1s, flip angle 90°.

^{31}P spectra were analyzed with a Bruker Topspin and ImageJ (NIH Image, Bethesda, MD) software. The PCr/ATP ratio was determined from the integrated peak areas of the creatine phosphate and [γ-P]ATP resonances from voxels centered on skeletal muscle in the anterior chest or on cardiac muscle identified from the high-resolution ^{1}H MR images. Voxel shifting was performed when necessary to optimize slice alignment with cardiac structures and minimize skeletal muscle contamination of cardiac spectra [48]. The PCr/ATP ratios were corrected for partial saturation effects using a factor determined in separate studies that included fully relaxed acquisitions [12, 128, 129, 377]. Infarcted, non-viable myocardium lacks PCr and ATP [408, 409]. In prior ^{31}P MRS studies of infarcted rodent hearts the detected PCr and ATP signals were attributed to the surviving viable regions, even when the entire infarcted region was contained within the region studied by MRS [410-412]. Based on this accepted practice and our efforts through animal positioning and slice selection to minimize infarcted tissue within the volume of interest, the cardiac PCr/ATP ratios reported here derive

almost entirely from surviving, viable myocardium. The mean PCr/ATP ratios in intact heart and in skeletal muscle are ~2.0 and ~3.0, respectively.

In summary, the result of this part of work was creation of a technological infrastructure, based on the novel approaches in physics and biophysics, enabling non-invasive studies of heart morphology, physiology and metabolism in small and large laboratory animals using magnetic resonance imaging and spectroscopy. Main requirements for this type of studies are the following: 1) achievement of the stable ECG signal for efficient triggering of MRI acquisitions; 2) engineering of the specialized radiofrequency coils that allow improvements of the magnetic field homogeneity and increase in SNR; 3) right choice of the anesthesia methods and maintenance of the physiological body temperature; 4) use of multiple cardiac cycles for k-space acquisition and multiple signal averages for SNR increase; 5) short TR and TE; 6) thin slices (1-2 mm for imaging of the rodent heart and 4-6 mm in large animals) to decrease partial volume artifacts due to the small size of the heart.

4.2. Specific Aim 2

Using ^{1}H MRI, to evaluate the extend of structural and functional restoration of the heart in small and large laboratory animals after infarction and cell transplantation.

Methods of experimental biophysics and bioengineering developed at the Specific Aim 1 of this work have been applied to the non-invasive studies of heart regeneration after infarction and transplantation of the human embryonic stem cell derived cardiomyocytes (hESC-CM) to the small and large laboratory animals. Previously published studies have demonstrated that hESC-CM have the capacity to form new myocardium in the uninjured heart [203-205]. No studies have explored the suitability of hESCs to repair the heart after myocardial infarction injury. First question is whether the grafted cardiomyocytes survive in the harsh environment of the infarcted tissue to form enough new myocardium to replace the tissue lost to infarction, and to prevent immune rejection of the allogeneic cells. Second question is whether human cardiomyocytes can improve the structure and contractile function of the injured heart. Third question is related to the mechanisms of heart repair, whether cardiomyocytes directly participate in the heart contractility or indirectly, via paracrine stimuli. To answer these questions, we have conducted studies of hESC-CM transplantation to the infarcted hearts of small (rodents) and large (non-human primates) laboratory animals.

4.2.1. hESC-CM transplantation to the rat heart

Infarcts were induced in the immunodeficient rats by 60 minutes of ischemia followed by reperfusion. Animals were studied by echocardiography 2 days after myocardial infarction (MI) to establish a pre-treatment functional baseline. To stratify animals into groups with comparable infarct severities, rats with a baseline fractional shortening >40% or subsequently shown to have no histologically identifiable infarct were excluded from the study. Four days post-infarction (and two days following the baseline echocardiography) 10 million direct-differentiated hESC-derived cardiomyocytes were transplanted into the infarcted region in the Pro-survival cocktail (PSC) enhancing transplanted cell survival and retention in the heart. Control rats received injections into the infarct of PSC without cells, serum-free media without cells or non-cardiac cells (hESC-derived fibroblasts). At 4 weeks post-engraftment, rat heart function was assessed again by echocardiography and MRI using the biophysical approaches in *in vivo* imaging on rodents developed in the part 4.1. MRI studies were conducted at the 4.7T Varian NMR spectrometer using a custom-built cardiac coil, developed at the Specific Aim 1. After the study the rats were euthanized, their hearts were harvested for histologic determinations of infarct size as well as graft size, distribution, and composition. Picrosirius red histochemical staining was used to define the boundaries of the infarct zone on histologic sections, and subsequent histomorphometry indicated that infarct size did not differ among the three groups, averaging 10.6±1.3% of the left ventricle in PSC + cardiomyocytes, 9.2±0.7% in hearts receiving PSC-only, 10.6±0.8% in hearts receiving serum-free medium-only and 11.2 ±1.5 in hearts receiving non-cardiac cells.

In some cases, the grafts had remuscularized a significant portion of the infarct zone (Figure 48). The human myocardium was readily visualized by strong expression of β-myosin heavy chain (Figures 48a-h), in contrast to the expression of α-myosin heavy chain in the rat myocardium (Figure 48e). Additionally, all β-myosin-positive cells also stained with a human-specific pan-centromeric *in situ* probe (Figure 48 a-b, d), whereas the surrounding rat cells were uniformly negative for this probe. Human myocardial graft size averaged 4.1±0.9% of the infarct with a maximum size of 10.7% of the infarct. The hESC-derived were still proliferating within the infarct zone, as evidenced by immunostaining for the thymidine analogue 5-bromodeoxyuridine (BrdU) positive on 1.4 ± 0.2% of the graft cardiomyocytes after a one hour pulse.

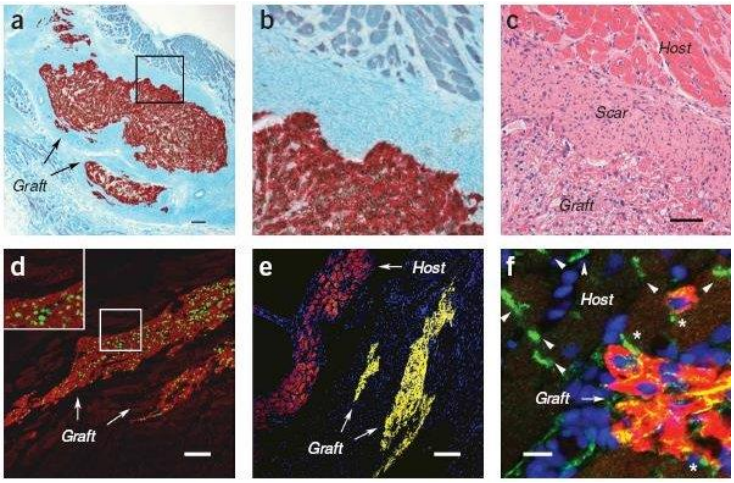

Figure 48. Histological evaluation of human myocardial grafts in the rat heart at 4 weeks after transplantation. Panels a–c: brightfield microscopic images from rat heart 4 weeks post-transplantation. Panels d–i**:** three laser confocal microscope images. (**a**) Combined human pan-centromeric *in situ* hybridization and β-myosin heavy-chain immunostaining. Fast green counterstain. Scale bar, 100 mm. (**b**) High magnification of box in **a**. All of the β-myosin-positive cells (red stain) have nuclear staining with the pan-centromeric probe (huCent, brown-black stain), whereas rat nuclei in the surrounding scar or myocardial tissue are unstained. (**c**) Hematoxylin and eosin stain of the box in (a). The graft cells have a vacuolated appearance due to the presence of glycogen. Scale bar, 50 mm. (**d**) Colocalization of human pan-centromeric *in situ* hybridization and β-myosin heavy chain (red). Scale bar, 100 mm; inset shows the corresponding boxed area magnified twofold. (**e**) Graft and host myosin heavy chain expression pattern, double-immunostaining for sarcomeric myosin heavy chain (sMHC all striated muscle; red) and β-myosin heavy chain (human cardiac muscle; green). The human myocardial graft is clearly identified by the dual staining for sarcomeric and β-myosin, which appears yellow in this merged image. The surviving subendocardial rat myocardium is identified by the red staining for sarcomeric myosin. The surrounding infarct scar tissue is unstained. Scale bar, 100 mm. (**f**) Host-graft contact illustrated by this section double-immunostained for β-myosin heavy chain (red) and cadherins (green). Scale bar, 10 mm.

To determine the physiologic consequences of implanting direct-differentiated hESC-CMs in PSC onto infarcted hearts, functional outcome with these cells was compared to that observed with control hearts receiving either PSC or serum-free medium (SFM) only. A third control was performed to specifically test the importance of using the highly cardiac-enriched preparation, generated using the previously described directed differentiation protocol. To generate cells for this "non-cardiac" control group, undifferentiated H7 hESCs were subjected to equivalent high-density monolayer culture conditions, but treatment with activin A and BMP-4 was omitted. While still promoting differentiation, these conditions were poorly cardiogenic, and resultant cells contained only a mean of 0.8% cardiomyocytes. Recipients of these "non-cardiac" cells were otherwise equivalently treated, i.e. receiving 10 million of the non-cardiac hESC-derived cells in the presence of PSC four days post-infarction.

Echocardiography demonstrated that, when lightly anesthetized, non-infarcted athymic rats had left ventricular end diastolic dimensions (LVEDD) of 6.4 ± 0.1 mm, left ventricular

end systolic dimensions (LVESD) of 3.6 ± 0.1 mm, and fractional shortening (FS) of 44 ± 1%. Two days after infarction (but two days prior to cell transplantation) all groups showed ventricular dilation and reduced fractional shortening, but there were no differences among groups. Overall, at two days post-infarction LVEDD increased by ~10%, LVESD increased by ~42%, and fractional shortening decreased by ~40%. By 28 days after hESC-CM or vehicle injection, all groups showed progressive ventricular dilation relative to their baseline studies two days after infarction (Figure 49). Quantification of rat heart dimensions and contractile function is shown in the Table 4.

Table 4. Echocardiographic and MRI assessment of the rat heart contractility.

Parameter	**PSC+Cells**	**PSC only**	**SFM Only**
Infarct area (% LV area)	10.6 ± 1.3	8.9 ± 0.7	10.6 ± 0.8
Echocardiographic			
LVEDD, 48 hrs. (mm)	6.9 ± 0.2	7.2 ± 0.1	7.1 ± 0.2
LVESD, 48 hrs. (mm)	4.8 ± 0.2	5.4 ± 0.2	5.2 ± 0.2
Fractional shortening, 48 hrs. (%)	28.1 ± 0.7	25.5 ± 1.6	25.4 ± 2.2
Heart rate, 48 hrs. (bpm)	394.3 ± 7.4	397.4 ± 6.3	404.9 ± 11.5
LVEDD, 4 weeks (mm)	8.2 ± 0.2	9.2 ± 0.3	9.2 ± 0.2
LVESD, 4 weeks (mm)	5.8 ± 0.2	7.7 ± 0.3	8.0 ± 0.1
Fractional shortening, 4 weeks (%)	28.1 ± 1.5	16.5 ± 1.7	13.4 ± 1.3
Heart rate, 4 weeks (bpm)	366.6 ± 5.8	357.6 ± 6.4	341.4 ± 8.1
MRI			
EDV (mm^3)	592.87±33.02	638.20±14.31	710.20±27.20
ESV (mm^3)	302.53±28.50	352.30±16.86	414.40±28.27
LV mass (mg)	718.53±32.43	727.80±13.45	759.00±34.46
LV EF (%)	50.27±2.03	45.00±1.56	42.00±1.92
Infarct wall thickening (%)	27.53±3.34	11.50±1.87	8.80±1.66
Opposite wall thickening (%)	40.47±3.45	43.10±2.18	33.40±4.43
Mid-septal wall thickening (%)	54.47±2.75	53.60±2.52	52.20±5.12

Abbreviations: PSC, Pro-Survival cocktail; LV, left ventricle; MRI, magnetic resonance imaging; EDV, end diastolic volume; ESV, end systolic volume; EF, ejection fraction.

In hearts receiving hESC-CM, however, there was attenuation of ventricular dilation compared to controls. Specifically, there was a difference in LV diastolic dilation amongst the cardiac cell-treated hearts (8.2 ± 0.2 mm), the PSC-only treatment (9.2 ± 0.3 mm), serum-free medium treatment (9.2 ± 0.2 mm) and the non-cardiac cell treatment (9.1 ± 0.4 mm) by ANOVA ($p = 0.01$). In contrast, the increase LVESD was markedly attenuated in hearts receiving hESC-derived cardiomyocytes (Figure 50). The LVESD in cell-engrafted hearts was 5.8 ± 0.2 mm vs. 7.7 ± 0.3 mm in PSC-only, 8.0 ± 0.1 mm in serum-free medium-only and 7.3 ± 0.5 mm in non-cardiac cell receiving rats (**$p<0.01$ vs cardiac cell-treated cohort for all

groups). There was no difference in LVESD amongst PSC, SFM or non-cardiac cell control groups at 4 weeks.

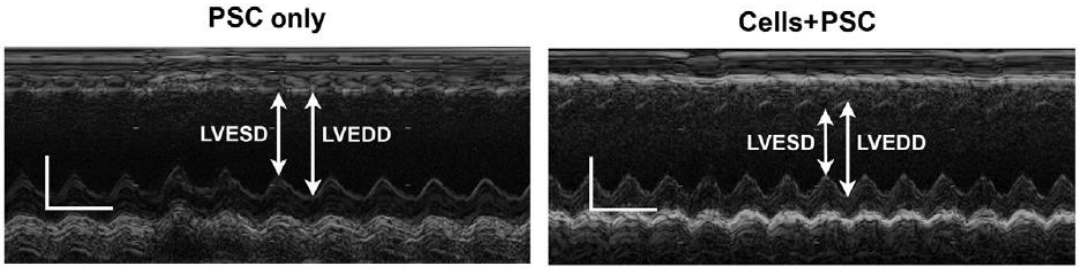

Figure 49. M-Mode echocardiograms of the infarcted rat heart. Upper panel: Representative control heart receiving PSC-only. The left ventricular cavity is dilated and the anterior wall shows akinesis. Left arrow indicates left ventricular end-systolic dimension (LVESD); right arrow indicates left ventricular end-diastolic dimension (LVEDD). Vertical scale bar = 5 mm; horizontal scale bar = 250 msec. Lower panel: Representative heart receiving hESC-derived cardiomyocytes in PSC (Cells+PSC). There is reduced left ventricular dilation relative to the above PSC-only control. The anterior wall moves inward during systole, indicating preservation of wall motion. Left arrow indicates left ventricular end-systolic dimension (LVESD); right arrow indicates left ventricular end-diastolic dimension (LVEDD). Vertical scale bar = 5 mm; horizontal scale bar = 250 msec.

Left ventricular contractile function, measured by fractional shortening, declined significantly in vehicle-injected hearts over the four weeks test period, decreasing to 16.5 ± 1.7% in PSC-only hearts, 13.4 ± 1.3% in hearts receiving serum-free medium, and 20.3 ± 3.5% in the non-cardiac cell treated group. (# $p<0.05$ for pair wise comparison of each group at –2 days vs. 28 days). In contrast, transplantation of hESC-derived cardiomyocytes prevented the decline in fractional shortening (Figure 50c). In the cardiac cell-treated hearts, fractional shortening at day –2 was 28.2 ± 0.7% vs. 28.4 ± 1.5% at day 28 ($p = 0.98$ for –2 days vs. 28 days). At 28 days after engraftment, the hESC-derived cardiomyocyte treated cohort had a significantly greater fractional shortening compared to either PSC-only, serum-free medium-only controls or non-cardiac cell treated rats (** $p<0.01$ for all cohorts vs cardiac cell treated group). Interestingly, there was no difference in fractional shortening between PSC-only, serum-free only or non-cardiac cell treated cohorts at 28 days.

Assessment of the rat heart function by MRI demonstrated the dramatic but expected changes in heart function and geometry by 4 weeks after infarction: left ventricle chamber dimensions was significantly increased, and ejection fraction was reduced in all hearts as compared with control non-infarcted animals ($p<0.01$, Table 4). Transplantation of hESC-derived cardiomyocytes into infarcted recipients significantly attenuated the changes in left ventricle geometry and improved cardiac function. In particular, left ventricle chamber

volumes at end-systole (ESV) and end-diastole (EDV) were decreased in the cardiac cell-treated group as compared to the SFM-only group (*p<0.05, online Table 4), and there was a similar positive trend relative to other controls.

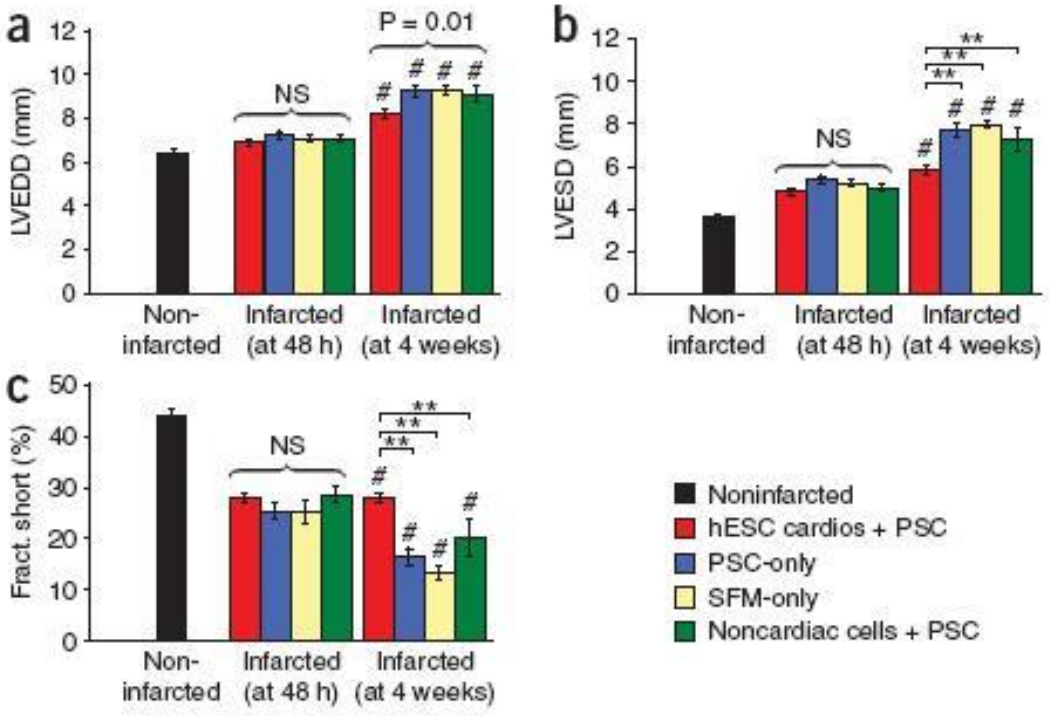

Figure 50. Echocardiographic effects of hESC-CM grafts on postinfarct ventricular function in rats. (**a–c**) Echocardiography results (for n = 11 uninfarcted rats, n = 15 infarcted rats receiving hES cell cardios+PSC, n = 16 infarcted rats receiving PSC-only, n = 7 infarcted rats receiving SFM-only and n = 6 infarcted rats receiving noncardiac cells in PSC). (**a**) Left-ventricular end-diastolic dimension (LVEDD). All groups showed ventricular dilation at 48 h post-infarction, but there were no baseline differences among the groups (NS, no significant difference). Over the course of 4 weeks, each group dilated their LV end diastolic dimension compared with their paired, baseline value at 48 h (#, p< 0.05). At 4 weeks, there was a trend toward reduced LVEDD in the hESC cardios + PSC group (p<0.01 by ANOVA). (**b**) Left-ventricular end-systolic dimension (LVESD). All groups had comparably increased LVESD at 48 h post-infarction. Over the course of 4 weeks, each group dilated their LV end systolic dimension compared with their paired, baseline value at 48 h (#, p<0.05). At 4 weeks, hearts receiving hESC-CM had significantly smaller LVESD compared with those receiving PSC-only, SFM-only, or noncardiac cells+PSC (**, p<0.01). (**c**) Fractional shortening. All groups had comparable decreases in fractional shortening at 48 h post-infarction. Over the course of 4 weeks, each group except for the cardiac cell treated cohort exhibited a worsened fractional shortening compared with their paired, baseline value at 48 h (#, p<0.05). At 4 weeks, fractional shortening was significantly greater in the hearts receiving cardiomyocytes compared with those receiving PSC-only, SFM-only or noncardiac cells+PSC (**, P<0.01).

Representative MR images of the control and cell-treated rat hearts are shown in Figure 51. The left ventricular ejection fraction of the injured hearts after cardiomyocyte engraftment was enhanced in comparison with controls: 50.3 ± 2% in cells + PSC vs. 45 ± 1.6 % in PSC-only, 42 ± 1.9 % in serum-free medium or 43 ± 4% in non-cardiac cell cohort (p < 0.05). The effects of human cardiomyocyte transplantation were even most apparent after analysis of the

regional contractile function. In the infarct region of cardiomyocyte-engrafted hearts, left ventricle wall thickening averaged 27.5±3.3%, compared to 11.5±1.9% in the PSC-only group, 8.8±1.7% in the serum-free medium-only group or 9.8 ± 2.0% in the group receiving non-cardiac cells (**p<0.01 vs cardiac cell treated cohort). Wall thickening in the non-infarcted region was comparable among all four groups (Figure 51f).

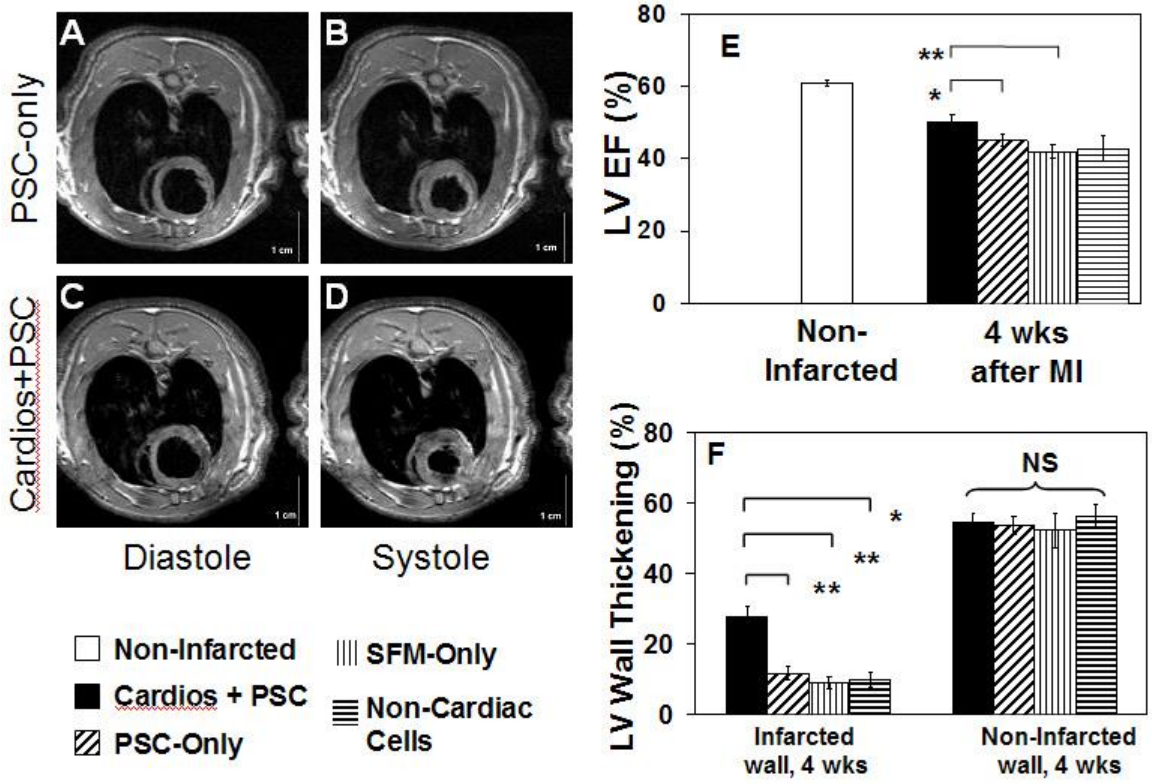

Figure 51. MRI evaluation of the contractile function of the infarcted rat heart at one month after transplantation of hESC-CM. **A-D:** Representative short-axis ^{1}H cardiac MRI show hearts receiving hESC-CM in the prosurvival cocktail (Cardios + PSC) or the cocktail alone (PSC-only). **E**: Left ventricle (LV) ejection fraction; **F**: Regional LV wall motion. * - Statistically significant difference between groups, p<0.01; ** p<0.001.

Taken together, these data suggest that formation of human myocardium in the infarcted rat heart significantly attenuates the progression of heart failure, manifested by reduced ventricular dilation (LVESD, LVEDD), improved global function (fractional shortening and ejection fraction) and increased regional wall motion when compared to non-cell controls. This study is the first to demonstrate that transplanted hESC-derived cardiomyocytes can positively influence cardiac structure and contractile function following acute myocardial infarction. The most obvious and straightforward explanation is that the implanted human cardiomyocytes beat synchronously with the host myocardium and thereby directly contribute systolic force. In support of this, the infarcted walls of hearts receiving the highly enriched hESC-derived cardiomyocytes showed 2.5-fold greater thickening during systole versus saline, PSC, or non-

cardiac+PSC controls (Figure 51f). On the other hand, the force could have been generated by host cells, which had been indirectly influenced by the transplanted human cells. Indeed, there is good experimental evidence for such indirect ("paracrine") effects on the infarcted heart with other cell types [191, 413, 414]. The indirect mechanisms include enhanced angiogenesis, production of trophic factors, extracellular matrix improvement or immune modulation, culminating in reduced anatomical remodeling. However, after transplantation of the non-cardiac preparation, the beneficial effects were less impressive than those obtained with the enriched cardiac preparation. While there were trends toward improvements in echocardiographic and MRI parameters in recipients of non-cardiac cells, we found no statistically significant differences when compared with the no-cell controls. Furthermore, the recipients of the non-cardiac cells showed a worsened LVESD and thinner infarct zones at four weeks than those receiving cardiomyocytes. Probably, the implanted cardiomyocytes provide new contracting cardiac muscle, while the non-cardiac graft cells do not. Another possibility is that, while both cell preparations mediate the paracrine effects, the cardiomyocytes may contribute systolic force in addition to activating beneficial paracrine signaling. Admitting some uncertainties about mechanism of action, the beneficial effects observed with hESC-CM for the infarcted rat heart are robust. It will be important to directly determine whether the grafts are electromechanically coupled with the host myocardium. If the grafts are not beating synchronously, this would imply a paracrine mechanism is responsible. It would also imply that an additional increment of improvement can be expected when hESC-CM are delivered to hearts of larger species with slower heart rates, including humans.

Human cardiomyocyte transplantation to the chronic infarction in rats.

The ability to restore heart structure and function in the setting of chronic heart failure would be highly desirable from a clinical standpoint. The chronically infarcted heart may be a hostile environment for cell engraftment, e.g. fibrous scar tissue with low vascularization. The question, whether hESC-CM transplantation could exert a beneficial effect in the chronically infarcted heart that already underwent adverse remodeling, remains unanswered. We evaluated long-term effects of hESC-CM transplantation in a chronic model of myocardial infarction. For this, the same type of myocardial injury in athymic Sprague Dawley rats was performed, as described above, but $10x10^6$ hESC-CM were transplanted at 4 weeks after MI. Animals were randomly assigned to one of the 4 following groups: 1) hESC-CM group receiving cardiomyocytes suspended in pro-survival cocktail (PSC), 2) non-cardiac group receiving non-

cardiac hESC derivatives suspended in PSC, 3) PSC group receiving PSC only and 4) SFM group receiving intracardiac injections of serum-free media.

Histomorphometry performed on picrosirius red-stained sections showed infarcted area size 18.6±4.7% of the left ventricle. Using β-MHC immunostaining, human cardiomyocytes grafts representing 0.83±0.22% of the left ventricle (Figure 52A-C), however, human cardiomyocytes did not show robust sarcomere organization (Figure 52D). Interestingly, many of the vascular structures present in the grafts contained human endothelial cells; the lumens of these microvessels contained erythrocytes (Ter119 positives cells) that are connected to the host coronary vasculature (Figure 52E).

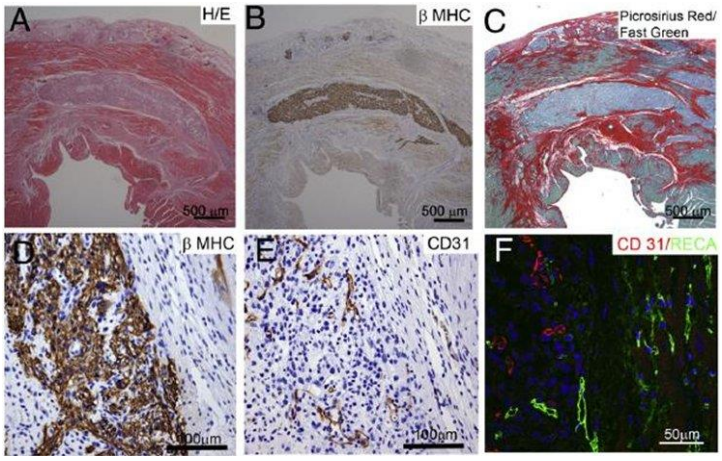

Figure 52. Histological evaluation of a human myocardial graft at 1 month after transplantation into the rat heart (2 months after MI). **A, B, C:** Transverse section of the rat heart with representative human intramyocardial graft visualized by hematoxylin eosin staining (**A**) or β-MHC immunostaining (**B**, brown chromagen, DAB) or picrosirius red/fast green staining (**C**). **D–F:** Higher magnification of a human graft showing the presence of human cardiomyocytes (**D**, β-MHC immunostaining) and human endothelial cell arranged in a vessel-like structure within the human graft (**E**, human CD31 immunostaining). Confocal microscopy confirmed the presence of human endothelial cells located only within the human graft (**F**, red) whereas rat endothelial cells (RECA immunostaining, green) are present in both host and graft tissue.

At three months after intramyocardial injection, human cardiomyocytes were present in all 13 rats identified by staining and β-MHC and our human pan centromeric *in situ* hybridization probe. Double immunostaining with β-MHC and BrdU antibodies revealed that human grafts were still proliferative and had developed immature but readily identifiable sarcomeres.

MRI analyses performed in all animals at the 3-month time point did not show any improvement in heart size or contractile function in cell-treated group (Figure 53). Two-way ANOVA analysis with paired data revealed that systolic and diastolic volume of the left ventricle, left ventricular mass and ejection fraction were significantly worsened between the

1-month and the 3-month time point ($p<0.0003$), thus confirming progressive left ventricular remodeling. However, cardiac MRI did not show any difference among groups in any cardiac parameter at any time point of the study. Taken together, the MRI data strongly indicate that neither hESC-CM, noncardiac cells nor the PSC has a beneficial effect on cardiac function in the rat chronic infarct model.

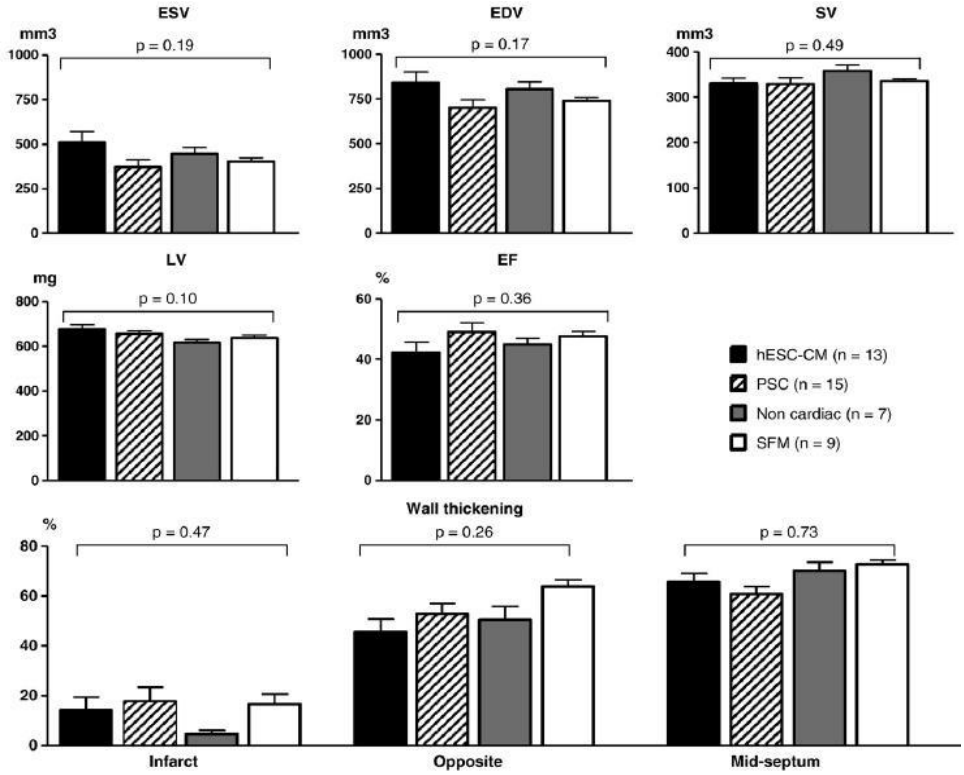

Figure 53. Assessment of post-infarct left ventricular function of the rat heart by MRI 3 months after hESC-CM transplantation. ESV: end-systolic volume, volume of the left ventricle at the end of systole (in mm^3); EDV: end-diastolic volume, volume of the left ventricle at the end of diastole (in mm^3); SV: left ventricle stroke volume, calculated as the difference between EDV and ESV (in mm^3); LV mass: left ventricular mass (in mg); EF: left ventricular ejection fraction, calculated from the relative difference in end-diastolic and end-systolic cavity volumes; wall thickening was evaluated at the infarcted segment, at the opposite wall and at mid septum level.

To summarize the study of hESC-CM transplantation to the chronic MI model in rats, the MRI showed that the engrafted cardiomyocytes are insufficient to restore heart function or to alter adverse remodeling in these settings. The need for adequate vascularization is increasingly recognized in cardiac cell transplantation [415]. In the acute myocardial injection protocol, we have shown that vascular structures within grafts were mostly host-derived, i.e. rat endothelium (part 4.2.1). In contrast, after injecting apparently comparable preparations in established scars, we observed vascular structures of human origin one month later. These human microvessels contained blood cells, indicating connection with the host circulation. However, we did not observe any human-derived endothelial cells. The loss of human

endothelium may have occurred during maturation of the grafts' wound-like environment (endothelial apoptosis is common as granulation tissue evolves into scar) [416], or those cells may have been killed by immune mechanisms. The humoral and innate arms of the immune system remain intact in the athymic rats. Furthermore, athymic rats develop oligoclonal T cell populations as they age [417, 418]. Sarcomere organization was not observed at the 1-month time point, but at 3-months striation was readily observed in some transplanted cardiomyocytes.

Therefore, a cell therapy product seems to be more effective when provided in the acute or subacute phase of myocardial infarction rather than at the chronic phase of myocardial infarction. This study demonstrated that hESC-CMs injected into the scar tissue of a chronic infarct model still engraft, survive and form striated cardiomyocytes graft similar to observed in acute myocardial infarction studies. However, although hESC-CM transplantation can attenuate the progression of heart failure in an acute model, the same hESC-CM injection protocol is insufficient to restore heart function or to alter adverse remodeling of a chronic myocardial infarction model.

Testing hESC-derived cardiomyocytes in a rat xenotransplant model has several limitations. Many issues related to immunogenicity would be expected to differ compared to human allogeneic transplantation. Also, the rat's high heart rate could mask arrhythmias generated by pacemaker activity or re-entrant circuits, which would still occur in slower heart rate species. Finally, the effectiveness of human cardiomyocytes might be underestimated in the rat, if they cannot keep pace with the rat myocytes but could in larger species. The ability of human cardiomyocytes to improve structure and function in the infarcted rat heart provides important proof of concept for this cell type. This study cannot be completed without the biophysical methods developed in the Specific Aim 1. MRI played key role in non-invasive determination of the structure and contractile function of the infarcted rat heart *in vivo* after hESC-CM transplantation.

4.2.2. Non-invasive visualization of the infarcted heart in non-human primates (NHPs)

Biophysical non-invasive visualization of heart structure and contractility in primates after transplantation of hESC-CM have not been done previously. It is unknown whether human cardiomyocytes can restore cardiac function in a physiologically relevant large animal model. In order to assess the impact of hESC-CM transplantation on left ventricular structure

and function, we developed techniques for cardiac MRI in the macaque. In the pilot studies, myocardial infarction in macaques was created by occluding the distal part of the left anterior descending (LAD) coronary artery for 90 min, followed by reperfusion. This protocol gave a minimal reduction in ejection fraction, from ~65% at baseline to ~60% after infarction. For the functional studies here, we induced larger infarcts by occluding the mid-LAD for 3 hours, followed by reperfusion. This induced large transmural infarcts and reduced ejection fraction to ~40% two weeks after infarction, creating a greater window for detecting functional improvement. With this new infarction protocol in place, we undertook an efficacy study. Electrodes for EKG telemetry were implanted at the time of infarction to assess spontaneous arrhythmias. Immunosuppressive agents were administered starting 5 days before cell delivery. 750 million hESC-CMs or vehicle (RPMI/pro-survival cocktail, PSC) were administered ~14 days post-infarction by surgically exposing the heart and injecting intramuscularly into the infarct region and the border zones. MRI was performed one day prior to cell delivery and ~27 days after cell delivery, with all scans independently evaluated by 3 blinded observers. A subset of the animals underwent catheter-based electrophysiological studies at approximately day 14, described in a subsequent section. Most macaques were euthanized ~28 days after cell transplantation, with the exception of two hESC-CM treated and one control animal, which were given prolonged immunosuppression and studied by MRI at 12 weeks post-injection to assess durability of the functional effects.

Seventeen non-human primates (*Macaca nemestrina*) were enrolled in this study initially without randomization, and another two were enrolled for targeted mechanistic studies, described below. Eight animals were excluded from final MRI analysis due to protocol design or complications outlined in the Figure 54, only one of which was related to cell delivery, but 9 successfully completed the infarction, cell or vehicle injection, and multiple MRI scans. One additional animal was added to the cell-treated group later to increase statistical power and to confirm the results. MRI studies were done at the 3T Achieva Philips clinical scanner with 8-elenent knee coil or combination of two-element Flex-M and Flex-L surface coils, depends on animal’s size. Scheme of MRI protocol is shown in the Figure 55. For image reconstruction and analysis, the standard Philips software tools (Philips Intellispace Portal), free software ImageJ 1.34u (NIH, Bethesda, MD, USA) as well as a specially developed analytical methods in Matlab (The Mathworks, Natick, MA, USA). Specifically, custom-developed Matlab

program has been used for automated extraction of the perfusion parameters from the dynamic contrast enhanced (DCE) images using the method described in the Specific Aim 4.

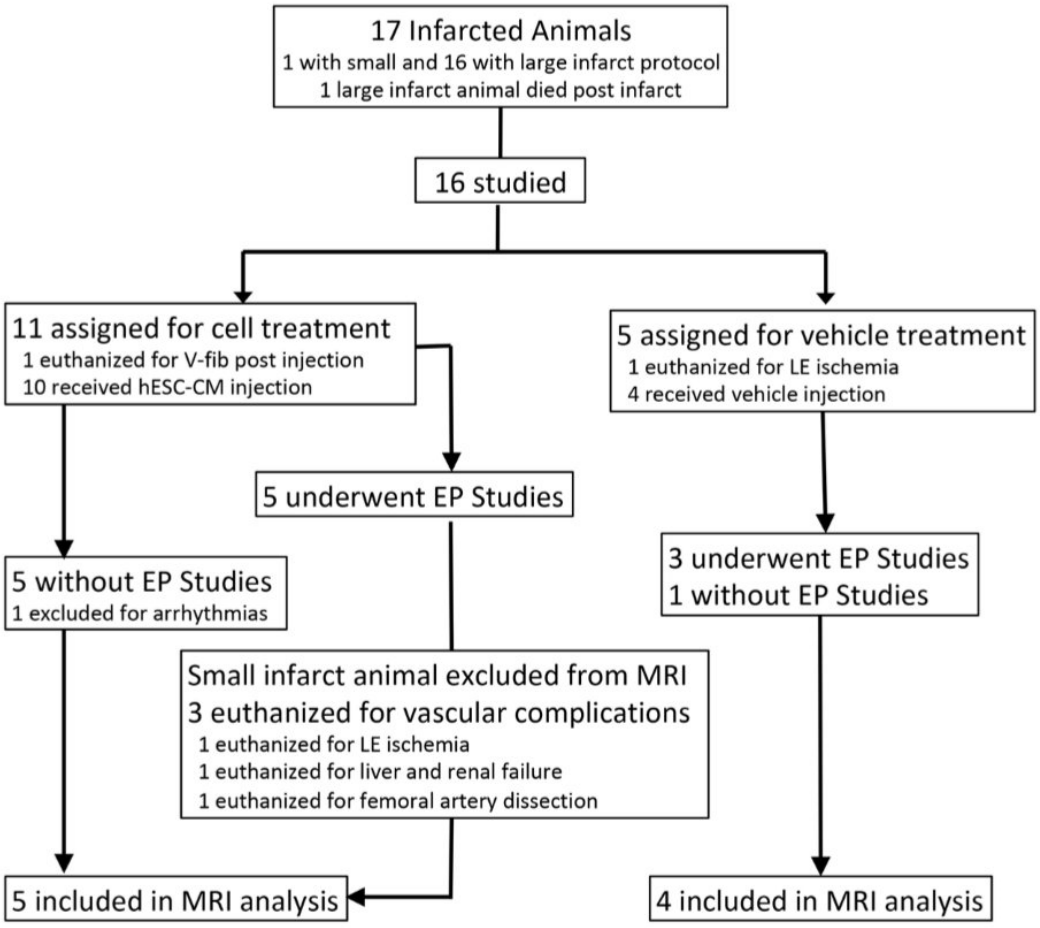

Figure 54. Flow diagram for animal assignment and inclusion in MRI and electrophysiology (EP) studies.

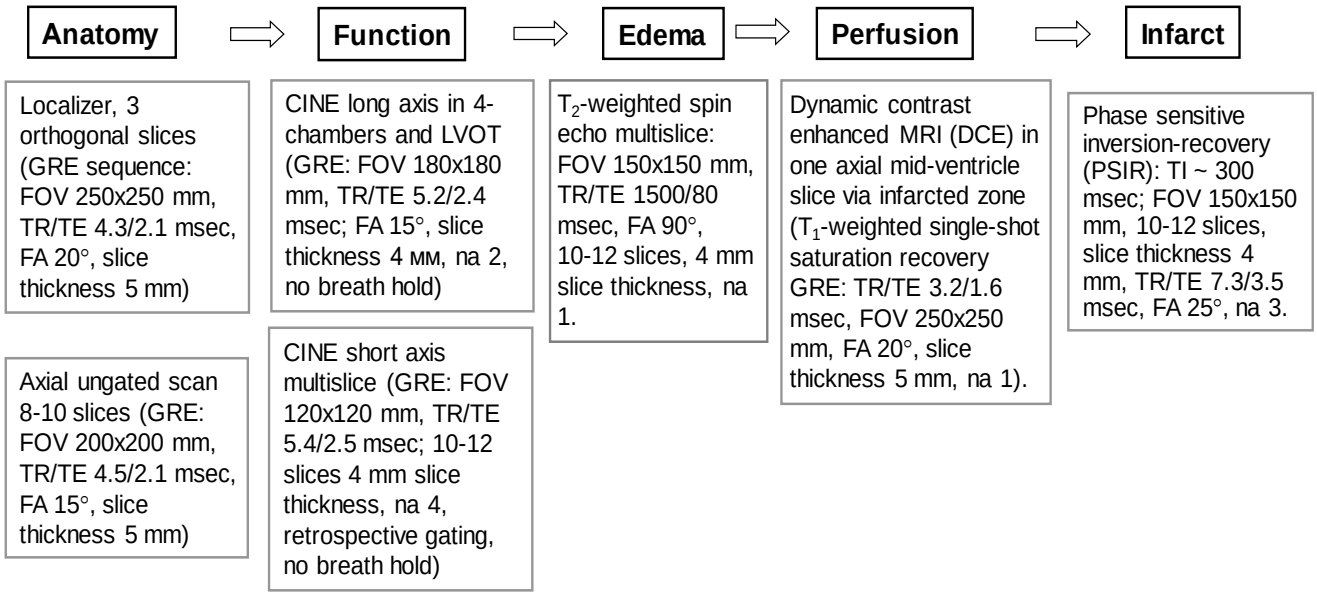

Figure 55. Scheme of cardiac MRI protocol that was used for assessment of the physiological effects of hESC-CM into the infarcted heart of non-human primates.

Non-invasive imaging studies have shown that prior to treatment, both groups exhibited comparably depressed EF, averaging 37.9 ± 2.3% in control animals and 39.3± 2.2% in hESC-CM-treated animals (p = NS). At 4 weeks post treatment, transplantation of hESC-CMs significantly improved left ventricular ejection fraction (LVEF: hESC-CM vs. control: 50.0 ± 2.4% vs. 40.5 ± 2.2%, p = 0.01, Table 5). The effects of hESC-CM transplantation also could be seen by comparing the change in ejection fraction between day -1 and day 27: the control group showed an improvement of 2.5 ± 0.8%, whereas the hESC-CM-treated group improved by 11.0 ± 0.3% (p = 0.001). Representative cardiac MR images at the end-diastolic and and-systolic phases of cardiac cycle for control and cell-treated animals are shown in the figure 56.

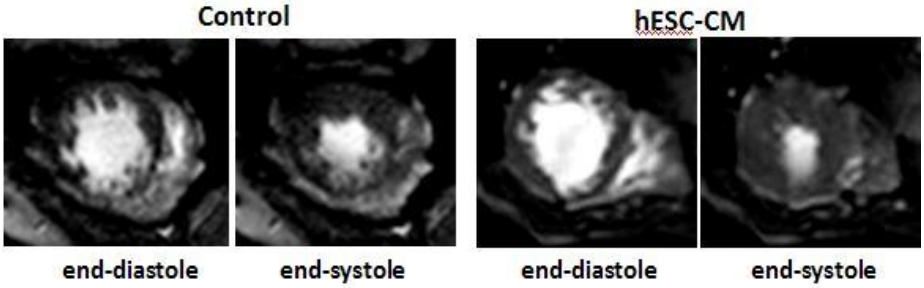

Figure 56. Representative short-axis CINE MRI at end-diastolic and end-systolic phases of the cardiac cycle at 4 weeks after treatment (6 weeks after MI). Blood in the chamber appears bright. There is greater ejection of blood in the hESC-CM heart during systole.

The benefits of hESC-CM transplantation also were apparent after analyzing regional contractile function, as assessed by systolic wall thickening. In the infarct region before therapy, all animals had 0% systolic LV wall thickening. All of the control hearts had 0% systolic LV wall thickening at 4 weeks. In contrast, after hESC-CM transplantation, wall thickening in the infarct improved to 23.0 ± 15% of the LV wall. However, because the improvement ranged from 0-67%, this was of borderline statistical significance (p = 0.055; Figure 57d). Wall thickening in the non-infarcted region was not different between these two groups at any time, and there was no significant effect of cardiomyocyte transplantation on left ventricular end-diastolic volume. Taken together, these data indicate that formation of human myocardium in the infarcted NHP's heart improves LV function. To test for the durability of the functional benefit, we studied three macaques at 3 months post-engraftment (2 cell-treated and 1 control; Figure 57e). In the control animal, the LVEF decreased from 43.9% at day 27 to 40.4% at 3 months. In both hESC-CM-treated animals, LVEF improved from 51.1% at day 27 to 60% and 66% at 3 months. Thus, the benefit from hESC-CM therapy appears to be durable for 3 months, with the potential for further improvement in function between 1 and 3 months.

Table 5. MRI data for individual macaques in study (4 control and 5 cell-treated animals).

						Baseline characteristics					4 weeks after treatment				
Animal #	Sex	Age	Weight, kg	Infarct size (histology), % to LV	Graft size, % to infarct	LVEDV, ml	LVESV, ml	LVEF, %	Infarcted LVTh, %	Infarct size, % to LV	LVEDV, ml	LVESV, ml	LVEF, %	Infarcted LVTh, %	Infarct size, % to LV
Control															
P14	M	6y 10mo	12.6	10.9	NA	18.0	10.2	43.9	0	19	20.7	11.4	44.8	0	18
P15	F	9y 7mo	11.7	6.6	NA	19.0	11.6	39.1	0		23.6	13.4	43.1	0	13
P18	F	10y 9mo	11.4	5.2	NA	16.1	10.7	33.4	0	15	18.3	11.9	34.7	0	13
P20	F	6y 0mo	10.6	8.9	NA	15.5	10.0	35.5	0	17	13.0	7.9	39.3	0	13
Mean		**8**	**11.6**	**7.9**	**NA**	**17.2**	**10.6**	**37.9**	**0**	**17.0**	**18.2**	**11.2**	**40.5**	**0**	**14.0**
SEM		**1**	**0.4**	**1.2**	**NA**	**0.8**	**0.4**	**2.3**	**0**	**1.0**	**2.2**	**1.2**	**2.2**	**0**	**1.3**
hESC-CM															
P22	F	15y 7mo	7.05	10.6	10.1	13.2	8.6	34.5	0	31	12.3	6.6	46.3	14	26
P23	F	11y 6mo	10.7	11.6	29.4	16.1	9.6	40.1	0	15	13.3	6.5	51.1	67	10
P24	F	12y 2mo	9.5	18.6	11.1	15.2	9.9	34.7	0	25	16.1	8.8	45.6	0	20
P25	F	6y 7mo	5.2	7.5	ND	11.7	6.6	43.5	0	17	13.8	6.1	55.8	10	11
P39	F	14y 6mo	9.2			13.7	7.6	44.0	0	16	11.2	5.5	51.0	18	13
Mean		**12**	**8.3**	**12.1**	**16.8**	**14.0 ****	**8.5****	**39.3**	**0**	**21**	**13.3***	**6.7****	**49.95****	**22**	**16**
SEM		**2**	**1.1**	**2.3**	**6.3**	**1**	**0.7**	**2.2**	**0**	**3.7**	**0.8**	**0.6**	**2.4**	**15**	**3.8**

Statistically significant difference between control and cell-treated groups: * p< 0.05, ** p < 0.01.

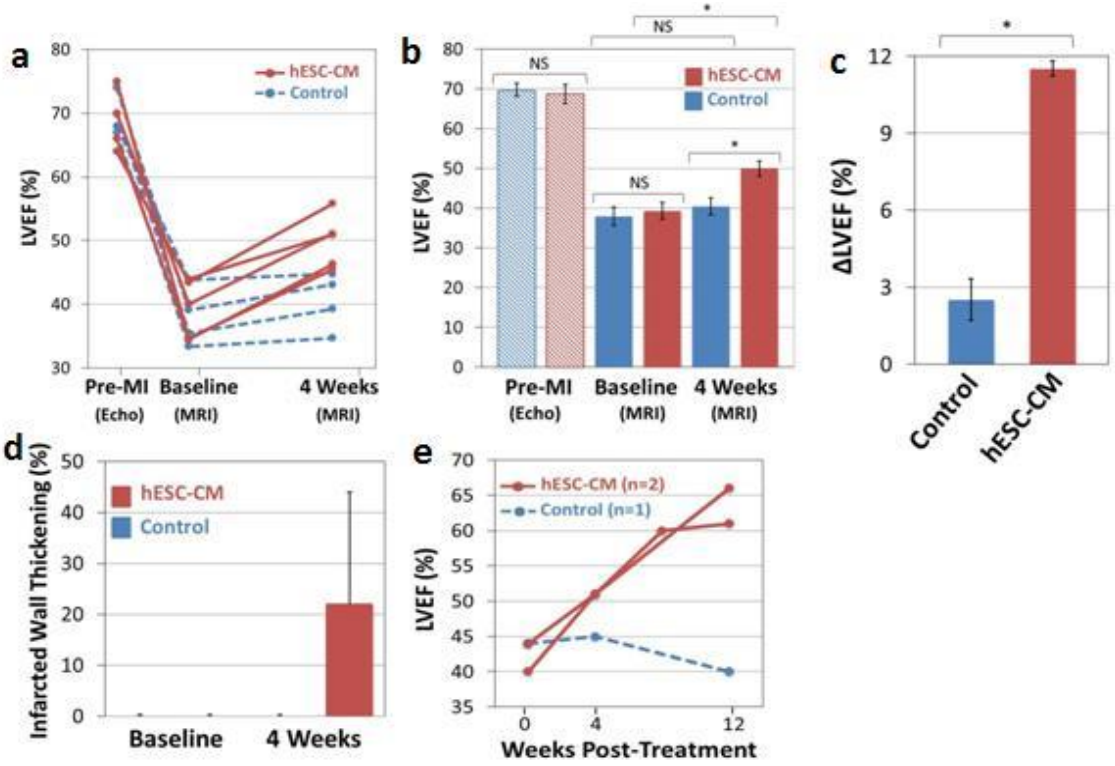

Figure 57. MRI study of the hESC-CM transplantation on cardiac function of NHPs. (**a**) Plot of left ventricular ejection fraction (LVEF) for individual subjects from baseline (day prior to injection) to 1-month post treatment. All hESC-CM hearts show significant improvement, while there is minimal improvement in controls. (**b**) Mean LVEF is comparable between groups at baseline but shows a significant improvement after hESC-CM treatment ($p<0.05$). (**c**) Change in LVEF (ΔLVEF) from baseline to 4 weeks is significantly greater in hESC-CM hearts than in controls. (**d**) There is a trend ($p=0.055$) toward increased systolic thickening of the infarcted wall in hESC-CM treated animals. (**e**) Extending survival to 12 weeks demonstrates a modest reduction in LVEF in control hearts and an improvement with hESC-CM treatment.

To study spontaneous arrhythmias, the EKG telemetry system was used. Cardiac rhythms were recorded for 24-hour periods at 3-day intervals, and episodes of sustained ventricular tachycardia or accelerated idioventricular rhythm were quantified in hours/day. Arrhythmias data are highly variable, however, cell-treated animals exhibited more extensive ventricular arrhythmias, including both ventricular tachycardia and accelerated idioventricular rhythm, which is likely were due to the human cardiomyocyte graft.

The large size of these grafts made visualization by cardiac MRI possible. Using delayed gadolinium enhancement, two animals showed the appearance of islands of new tissue (viable Gd-negative tissue) within the infarcted anterior wall and septum at 1 and 3 months after treatment (Figure 58). These islands were ~1 cm in maximal dimension. By carefully cross-registering histology and MRI scans, we identified regions of human myocardium more than 1 cm in maximal dimension, that corresponded to these Gd-negative regions in the MRI images. Masses of this size are easily visualized by MRI, leading us to conclude that it is possible to image large-scale regeneration from human cardiomyocyte grafts.

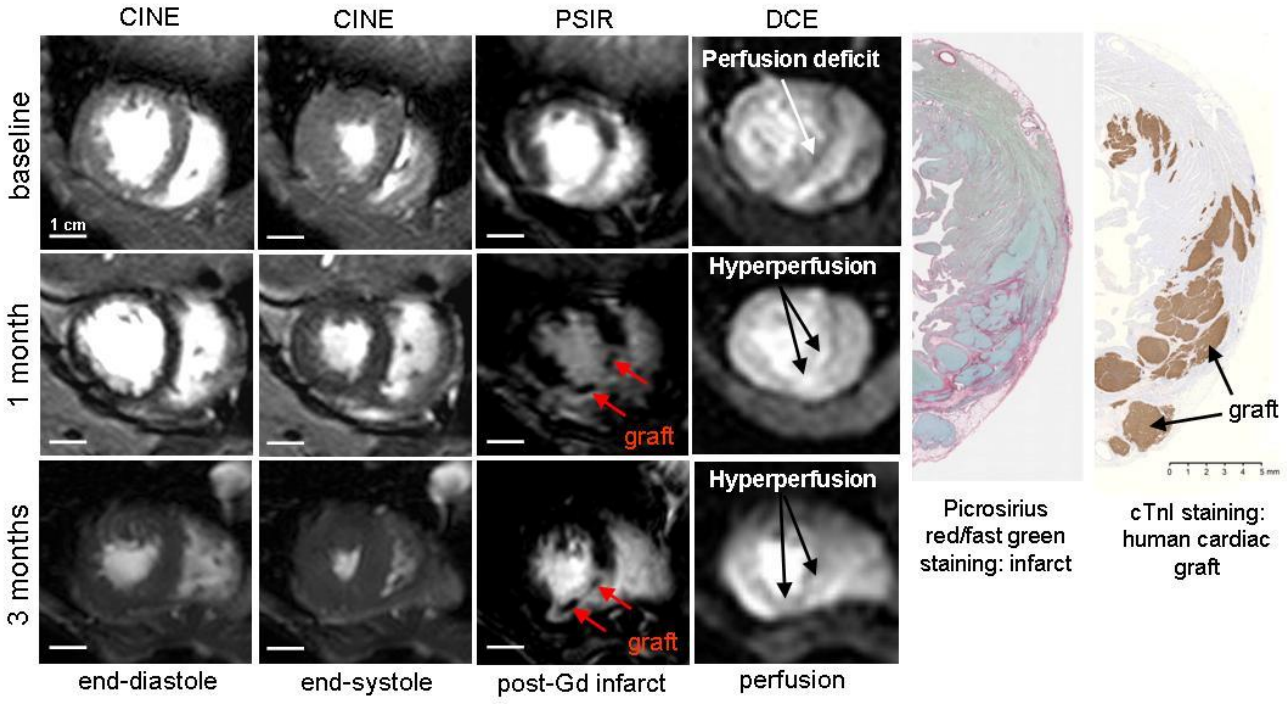

Figure 58. MRI visualiazation of the primate's heart contractility (**CINE**), infarct zone (**PSIR**) and myocardial perfusion (**DCE**) in 1 and 3 months after hESC-CM transplantation. MRI pulse sequence CINE GRE shown axial mid-ventricle slice in the end-diastolic and end-systolic phase of cardiac cycle. Infarct is seeing in PSIR images as homogenous contrast-enhanced zone of the left ventrile. Two islands of new viable (dark) myocardium are seeing within the scar zone after transplantation of hESC-CM (red arrows point into the graft). White arrow point into the zone of perfusion deficit on DCE images; black arrows point into the bright areas of hyper-perfusion. Histological staining picrosirius red shows fibrosis in red. Histological staining with the cTnI antibody depict human graft as brown areas in the monkey's myocardium.

Graft size ranged from 10-29% of the infarct area (16.8 ± 6.3%) and 1.1-3.4% of the LV (2.2 ± 0.7%). Representative low-magnification images for 3 different engrafted hearts are presented in Figure 59.

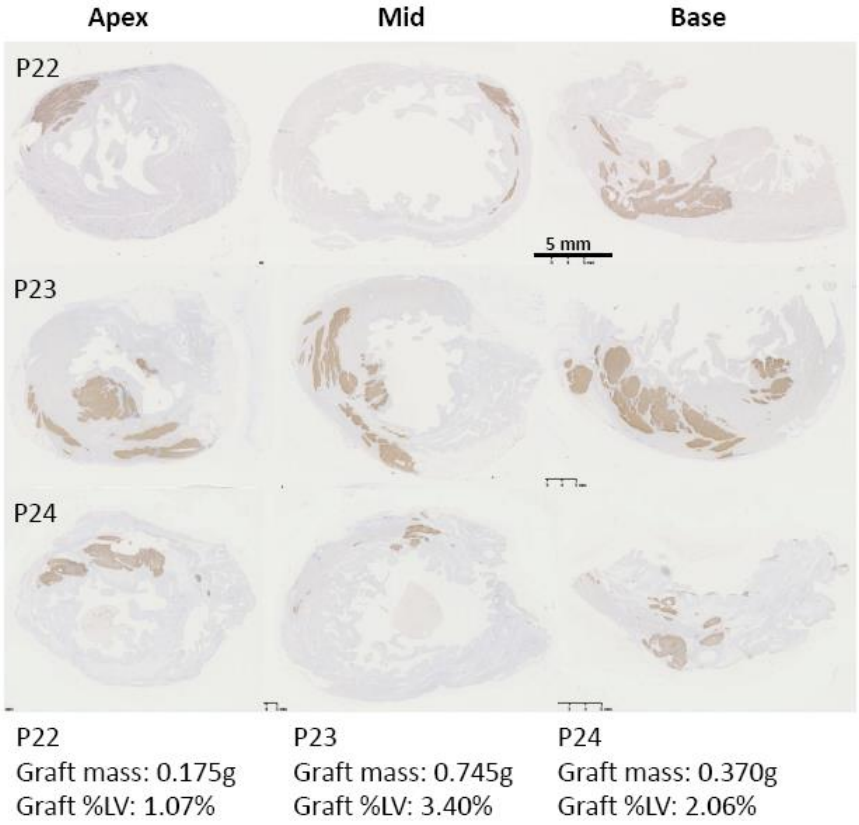

Figure 59. Low magnification whole-slide scans from 3 hearts receiving hESC-CM grafts, stained for human cTnI (brown). Apical section is on the left and basal section is on the right. Extensive areas of remuscularization are present in all hearts. Scale bar, 5 mm.

This study had shown that hESC-CM can remuscularize infarcts in macaque monkey hearts, reduce scar size and restore contractile function. The infarcts studied here were large, reducing ejection fraction from 65% to ~40%. No significant spontaneous recovery occurred in the vehicle-injected group (~2.5%), whereas all hESC-CM-treated hearts showed significant recovery at 4 weeks (~11%). Based on studies on two macaques extended to 3 months, the benefit to cardiac function appears durable, with the potential for further functional improvement between 1 and 3 months. Importantly, although pluripotent stem cell derivatives have the potential to cause teratomas [419-421], none were observed in the current study. The mechanical benefit could result from direct mechanical force from the graft and/or paracrine signals [422] that enhance function of the host myocardium. The increased hypertrophy and maturation of engrafted cardiomyocytes further supports their possible direct participation in generating mechanical force.

Other reported studies with mouse ESC-derived cardiomyocytes grafted into the infarcted mouse heart have shown increased spontaneous arrhythmias [423, 424] and decreased susceptibility to pacing-induced arrhythmias [425]. When human ESC-CMs were transplanted into injured guinea pig hearts no effects on spontaneous arrhythmias and reduced susceptibility to pacing-induced arrhythmias were found [368]. In contrast, when human cardiomyocytes were transplanted into the hearts of macaque monkeys with small infarcts, they induced transient ventricular arrhythmias [369]. Similar arrhythmias were noted when allogeneic monkey iPSC-derived cardiomyocytes were transplanted into infarcted monkey hearts [426]. The functional recovery seen in the current study on the non-human primates was larger than were observed in rats (part 4.2.1.) or guinea pigs [368], even though grafts occupied a similar fraction of the ventricle. It is likely that the greater physiological match between human and macaque is the basis for a more profound improvement in contractile function. This therapeutic effect may be further augmented when human cardiomyocytes are transplanted into diseased human hearts.

4.2.3. Allogeneic bone marrow fibroblasts in the infarcted canine heart

Different cell types were reported in literature to repair infarcted heart; however, conclusions from cell-based therapies in pre-clinical studies and clinical trials remain controversial. In the current study the canine bone marrow-derived fibroblasts, DS-1 cells [427], were evaluated as the potential treatment of the myocardial infarction in dogs. Previously, it was shown that a single intravenous infusion of DS-1 cells reduced radiation-induced lung fibrosis, improved pulmonary function and prevented the progression of radiation-induced lung injury in the canine model [428]. There are other potential advantages to investigating the use of DS-1 cells in the treatment of myocardial infarction. First, the single intravenous injection of DS-1 cells eliminates the need to inject cells directly into the myocardial infarct or the coronary arteries. Second, since the DS-1 cells do not engraft, but are instead cleared from the body of immune-competent animals in 48-72 hours, there is no need for histocompatibility matching. Third, DS-1 cells are a clonal population of fibroblasts that provide an unlimited number of homogeneous cells which allows for consistent results and enables mechanistic studies.

Six adult mongrel dogs (5 male and 1 female, weighing 13.9-18.1 kg) were used in the study. Percutaneous transluminal coronary artery catheterization technique was used to create myocardial infarction via ischemia-reperfusion injury. A specialized shape guiding catheter

was used to engage the left coronary artery and then inflated a percutaneous transluminal coronary angioplasty balloon catheter (2.5mm/8mm, ApexTM monorail balloon catheter, Boston Scientific) for 90 minutes to occlude all flow distal to the first diagonal branch of the left anterior descending coronary artery (LAD). MI was confirmed by ECG and subsequent post-MI 24-hour serum cardiac troponin I (cTnI) assay (Phoenix Central Laboratories, Everett, WA). A diagram of the study protocol is shown in the Figure 60. All the study dogs received I-R procedure and had infarctions in the LV anterior wall and septum which was proven by coronary angiography, ECG and serum cardiac troponin I assay. All the dogs were enrolled into one of two groups: vehicle-treated controls (n=3) and DS-1-treated (n=3).

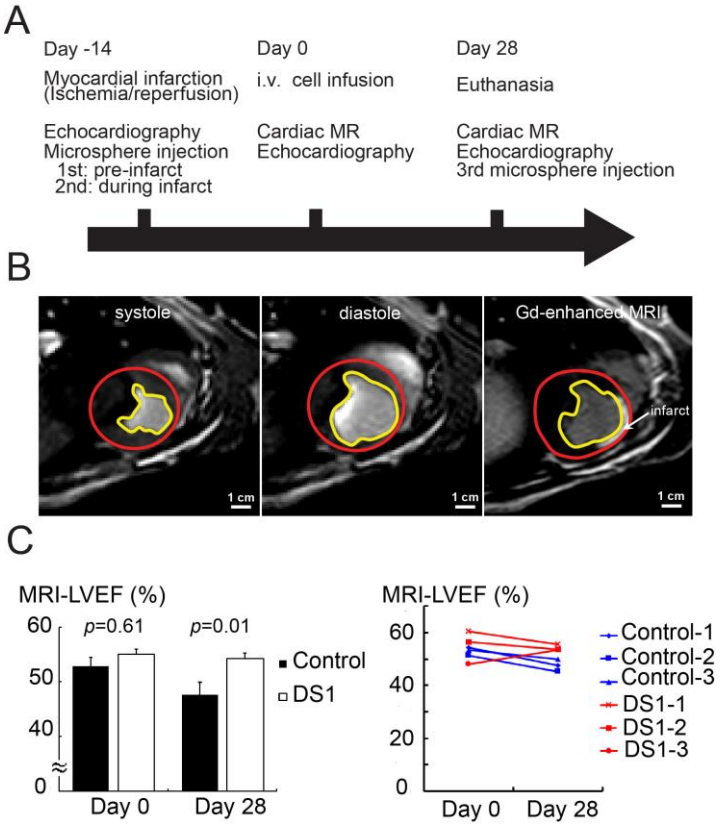

Figure 60. Study protocol and LV systolic function evaluation by cardiac MRI. A, Study protocol. **B**, Representative CMR images for assessing LV systolic function. The endocardial boundaries were traced in CINE gradient-echo images as indicated by red lines at end-systole (left graph) and end-diastole (middle graph) to obtain end-diastolic volume (EDV) and end-systolic volume (ESV). Late gadolinium enhancement images showed an anterior-anteroseptal myocardial infarction (right graph). **C**, EF was measured prior to treatment (day 0) and 28 days after treatment. Black bars indicate control dogs, and white bars indicate DS-1 cell-treated dogs.

There was no significant difference of ejection fraction between the control (vehicle-treated) animals and the DS-1 cell-treated animals prior to treatment (14 days after myocardial infarction). At 28 days after treatment, the DS-1 treated animals had better LV systolic function. At 28 days after treatment, five out of six studied animals presented significantly

deteriorated EF (figure 60C). One cell-treated dog has shown improvement in the ejection fraction.

Table 6. Left ventricular contractile function of the DS1-treated dogs and the control dogs.

	Day -14			Day 0			Day 28		
	Vehicle-treated	DS1-treated	*p*	Vehicle-treated	DS1-treated	*p*	Vehicle-treated	DS1-treated	*p*
Cardiac MRI study									
LV EDV index	NA	NA	NA	66.6 ± 17.4	58.9 ± 8.3	0.53	76.0 ± 6.3	74.0 ± 9.8	0.78
LV ESV index	NA	NA	NA	31.2 ± 7.2	26.2 ± 1.2	0.30	39.9 ± 3.5	33.8 ± 4.3	0.13
MRI-LV EF (%)	NA	NA	NA	52.9 ± 1.6	55.0 ± 6.3	0.61	47.6 ± 2.3	54.2 ± 1.2	0.01
Echocardiographic study									
GLS (%)	-19.3 ± 0.7	-20.0 ± 0.3	0.17	-15.7 ± 0.9	-15.3 ± 1.4	0.65	-13.6 ± 1.7	-16.0 ± 0.8	0.045
Mitral E/A	1.4 ± 0.2	1.3 ± 0.2	0.51	1.9 ± 0.4	2.0 ± 0.4	0.76	1.8 ± 0.9	1.2 ± 0.3	0.37
Mitral E/e’	7.0 ± 0.9	7.4 ± 2.0	0.75	10.6 ± 3.8	13.8 ± 2.1	0.27	14.6 ± 1.3	7.3 ± 1.2	0.002
LAV index	16.8 ± 3.3	15.1 ± 1.1	0.45	23.0 ± 1.9	20.7 ± 6.3	0.58	23.0 ± 1.0	15.2 ± 1.2	<0.001

Abbreviations: EDV, end-diastolic volume; EF, ejection fraction; ESV, end-systolic volume; E/A, the ratio of the early to late ventricular filling velocities; E/e’, the ratio of early transmitral velocity to tissue Doppler imaging annular early diastolic velocity; GLS, global LV peak systolic longitudinal strain; LAV, left atrial volume; LV, left ventricular.

As an additional way of assessing systolic function, we used global longitudinal strain (GLS), which has been shown in several studies to be a more objective and sensitive parameter than 2D-EF to evaluate LV systolic function and contractility. Therefore, we performed 2-dimensional strain analysis (table 6) and GLS showed better LV systolic function in the DS-1-treated dogs than the control dogs at 4 weeks after treatment (DS-1 cell treated dogs vs. vehicle-treated dogs; -16.0 ± 0.8 % vs. -13.6 ± 1.7 %, p = 0.045, table 6). Taken together, the CMR and GLS data suggest that DS-1 cell i.v. infusion prevented deterioration of LV systolic function in the infarcted dogs. In the current study, we used mitral E/e’ and LAVi, to evaluate LV diastolic function. Either LAVi or mitral E/e’ showed that all the dogs had LV diastolic dysfunction at 2 weeks after myocardial infarction (LAVi for the control animals paired t-test p = 0.03; mitral E/e’ for the DS-1 treated animals paired t-test p = 0.04); nevertheless, LV diastolic function was significantly improved at 28 days after DS-1 cell infusion (mitral E/e’ for the DS-1 treated animals paired t-test p = 0.04; table 6).

There was no difference between groups in infarct size (% of LV) at 28 days after cell therapy (DS-1 treated dogs vs. vehicle-treated dogs; 5.4 ± 5.6 % vs. 4.6 ± 5.7 %, p = 0.87). The collagen fiber orientation in the infarcted myocardium in both groups was examined. The

angle deviation of the control dogs was larger than that of the DS-1-treated dogs (DS-1 treated dogs vs. vehicle-treated dogs; 25.9 ± 3.1° vs. 31.1 ± 4.1°, p = 0.01).

This study describes the effect of intravenously administration a cloned population of allogeneic marrow fibroblasts in a canine subacute MI model. The results indicate that a single infusion of DS-1 cells, which do not engraft, during the subacute stage of an MI (post-MI day 14) facilitated the preservation of LV systolic function in one out of three treated animals and a reduction in the extent of collagen fiber disarrangement in the infarcted myocardium. Severe cardiac fibrosis is known to increase LV stiffness, leading to LV diastolic dysfunction [429, 430]. In this study the DS-1-treated dogs did not demonstrate decreased infarct size in comparison with the controls, but histological analysis showed more parallel alignment of collagen fibers in the infarcted areas of DS-1-treated dogs. Disarrangement of the heart's collagen fibers is correlated with a stiffer LV and both systolic and diastolic dysfunction [431]. Here we used echocardiography-derived TDI E/e' to evaluate diastolic function and LV stiffness, as recommended by the American Society of Echocardiography [430]. We speculate that the reduction in LV stiffness in the DS-1-treated dogs might be due to better uniformity of the collagen fiber orientation in the infarcted area. The major limitation of the present study is the small number of animals in each group.

In summary, this study did not show benefits of intravenously infusing DS-1 cells at the subacute MI period: the contractile function and infarct size have not changed. The DS-1 cells do not contribute to the myocardial regeneration after infarction; therefore, we do not plan continuation of using this cell type in cardiac regeneration studies.

4.3. Specific Aim 3

Using spatially-localized ^{31}P MRS, to evaluate changes in myocardial energetics of the mouse heart during stress as well as following myocardial infarction and pharmacological interventions.

4.3.1. ^{31}P MRS in mouse heart in dobutamine stress conditions

Mice are frequently used as models to study human physiology and disease because transgenic manipulations are more easily accomplished in that species. Despite the importance of mice in research and for transgenic manipulations, very little is understood about *in vivo* murine myocardial metabolic regulation. This, in part, is due to the very small size (~0.1g) and very fast heart rates (500~600/min) of normal mouse hearts. Studies of high-energy phosphate metabolism using ^{31}P MRS have been reported in isolated mouse hearts [432, 433]. However,

studies on isolated heart preparations do not truly reflect the physiologic conditions present in the intact *in vivo* settings. Recently, our research group implemented and validated image-guided, spatially localized ^{31}P MRS techniques to study murine cardiac metabolism *in vivo* [12, 129]. These studies demonstrated that the normal murine cardiac PCr/ATP ratio under baseline conditions is similar to that in larger species, including humans [434-436]. Studies in isolated cardiac mitochondria [45, 437, 438] indicate that increases in respiration are regulated by changes in high-energy phosphates, while most studies in intact large animals including humans [434, 436, 439] demonstrate that global levels of high-energy phosphates do not regulate metabolism since they are unchanged during stress that increases heart rate. No *in vivo* studies of myocardial regulation have been conducted to date in very small animals, such as mice, at extremely fast heart rates. The aim of the current study was to utilize image-guided, spatially localized ^{31}P MRS to study murine cardiac metabolism under resting and stress conditions *in vivo* to test the hypothesis that global levels of high-energy phosphates do not regulate myocardial respiration during substantial increases in cardiac demand in the normal mouse heart.

Ten animals completed the entire ^{31}P MRS dobutamine protocol and their data are presented here. The mean baseline heart rate for all ten animals was 482 ± 46/min (mean ± SD). Intravenous infusion of dobutamine at the dose of 24 μg/min/kg body weight significantly increased the mean heart rate by ~39% to 669 ± 77/min. The maximum ß-adrenergic effect of dobutamine was detected approximately 12 minutes after initiation of dobutamine administration. Heart rates returned to baseline levels within a few minutes of stopping the dobutamine infusion.

After acquisition of high-resolution ^{1}H MR anatomic image, the spatially localized ^{31}P MR spectra were obtained from myocardium, skeletal muscle, and the phenylphosphonic acid standard using 1D-CSI pulse sequence as described in the part 4.1. The mean PCr/ATP ratios in intact heart and in skeletal muscle at baseline were 2.1±0.5 and 3.0±0.6, respectively. These are similar to those reported before in normal mice [12]**.** During intravenous administration of dobutamine the myocardial PCr/ATP ratio remained unchanged at 2.1±0.5 ($p>0.05$). The PCr/ATP ratio in skeletal muscle was also unchanged during dobutamine stimulation: 3.0±0.6 and 3.2±0.5, respectively (Figure 61). Our data are in agreement with studies in large species such as dogs, pigs, and humans, where increased heart rates did not result in a significant change in the cardiac PCr/ATP ratio [128, 435, 437, 439, 440]. Therefore, increased

mitochondrial respiration during adrenergic stimulation does not depend on changes in the relative global concentrations of myocardial phosphocreatine and ATP. This is consistent with the conclusion that global levels of high-energy phosphates do not regulate myocardial respiration, even in small animals, such as mice, with very rapid heart rates up to 750 bpm. It is more likely that mitochondrial respiration is rather controlled by delivery of substrates, subsequent changes in the NADH/NAD redox, or mitochondrial calcium status [439, 441]. Despite the small size and rapid heart rates, our current studies demonstrate that it is feasible to perform studies of cardiac high-energy phosphate metabolism during sustained, reproducible dobutamine stress in intact mice, with heart rates as high as 750 bpm, using image-guided, spatially-localized ^{31}P MRS.

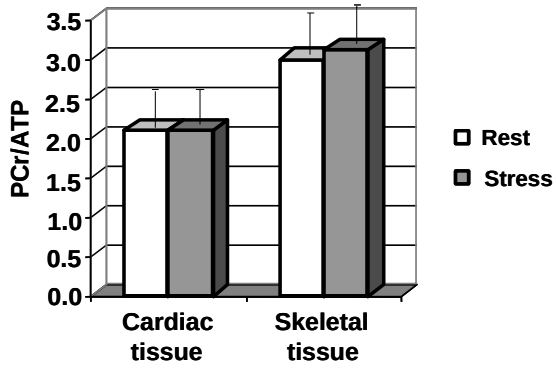

Figure 61. Mean PCr/ATP ratios in heart and skeletal muscle under baseline and dobutamine stress conditions in intact mice.

Others have used MRI to demonstrate an increase in heart rate, cardiac output, and ejection fraction as well as a significant decrease of end-diastolic and end-systolic left ventricular volumes in normal mice following intraperitoneal injection of dobutamine. We subjected three animals to separate functional testing with MRI during intravenous dobutamine infusion and also observed a similar increase in ejection fraction, cardiac output and smaller end-systolic volumes during dobutamine stress (data not shown). Both intraperitoneal and intravenous dobutamine approaches result in increased heart rates but the latter provides the opportunity for a more reproducible, graded, prolonged, and rapidly reversible method for adrenergic stimulation without uncertainties about dobutamine absorption.

In summary, it is now possible to study energetics at rest and during graded adrenergic stress in intact mice under physiologic conditions. We report that a 40% increase in heart rate does not result in a significant change in the murine cardiac PCr/ATP ratio suggesting that

global levels of high-energy phosphates and ADP do not regulate myocardial metabolism even in small mammals with extremely fast heart rates.

4.3.2. ^{31}P MRS in the infarcted mouse heart after pharmacological interventions.

Ventricular remodeling occurs following myocardial infarction (MI) in many species, including humans, and is typically characterized by progressive ventricular dilatation, eccentric hypertrophy, and contractile dysfunction [442-444]. Patients with post-MI remodeling experience increased rates of heart failure and cardiovascular mortality while interventions that reduce geometric ventricular remodeling improve outcomes [442, 445]. In addition to the geometric and contractile abnormalities associated with post-MI remodeling, adverse changes in energy metabolism also occur [410, 446]. Abnormalities in energy metabolism after MI include reductions in ATP, creatine phosphate (PCr), and in the activity of the creatine kinase (CK) reaction, the primary energy reserve reaction of the heart [21, 125, 139, 446]. Inhibitors of CK significantly increase mortality following experimental infarction [447]. The reduction in cardiac PCr/ATP ratio in experimental post-infarction remodeling is similar to that observed in human heart failure which in turn correlates with clinical severity and predicts overall and cardiovascular mortality [131, 132, 137, 139]. Taken together, the energetic consequences of post-MI remodeling are similar to those of heart failure and offer an additional potential mechanism that may contribute to progressive dysfunction and geometric changes.

Xanthine oxidase (XO) is important in purine metabolism and its expression and activity are increased in heart failure [448]. XO is also a major source of free radicals, such as superoxide, that can impair energy metabolism and reduce energetic efficiency [449, 450]. In non-ischemic experimental and human heart failure, inhibition of XO improves mechano-energetic coupling by improving contractile performance relative to a reduced energetic demand [449, 450]. Targeted XO blockade impacts on the progression of postischemic cardiomyopathy in mice [451] and attenuates LV remodeling processes after experimental MI [452]. Despite the evidence for improved mechano-energetic coupling with XO inhibition in non-ischemic heart failure, the metabolic and contractile effects of XO inhibition on post-infarction remodeling and the effects of XO inhibitors on depressed energetics in failing hearts have not been characterized.

There were two aims to this study: 1) to determine the extent to which geometric, contractile and metabolic remodeling occur *in vivo* following non-reperfused MI in the mouse; and 2) to test the hypothesis that XO inhibitors improve bioenergetics and contractile function

in the failing heart. This is based on the mechanism observed in non-ischemic heart failure where XO inhibitors improve mechano-energetic coupling by improving contractile performance relative to a reduced energetic demand such that improved energetics, as indexed by the cardiac PCr/ATP, would be expected to be associated with improved contractile function.

Myocardial infarction was modeled in 30 adult mice (20-30 g body weight) by complete ligation of the left main coronary artery. After verification that coronary occlusion had occurred by blanching of the tissue distal to the suture, the ribs were closed with suture and the mice recovered. Immediately following MI surgery, XO inhibited mice received either allopurinol (0.5 mM) or oxypurinol (1 mM) in the drinking water while control animals had neither. Because few pharmacologic agents are completely specific, we studied both allopurinol and oxypurinol to increase the likelihood that any observed metabolic or contractile effects were due to XO inhibition and not due to another effect of one agent. All animals underwent MRI/MRS studies four weeks after surgery. Since there were no significant anatomic, functional or metabolic differences between allopurinol- and oxypurinol-treated hearts, the groups were combined (MI+XOI) (Table 7).

Table 7. ^{1}H MRI studies of cardiac function in normal, infarcted mice and after xanthine oxidase inhibition (XOI).

Group	n	ESV (mm^3)	EDV (mm^3)	SV (mm^3)	CO (mm^3/min)	LV mass (mg)	LVmass/ ESV	LVmass/ EDV	MI size (%)	EF (%)
Normal mice, control (without MI)	9	13±5	31±7	18±2	8900±1500	80±11	6.8±2.2	2.6±0.4	-	59±8
MI group (4 weeks after surgery)	11	182±129 *	203±133 *	21±9	9600±4700	162±29 *	1.4±0.9 *	1.2±0.7 *	55±11	14±9 *
MI mice + allopurinol (0.5 mM)	7	84±29 *	108±36 *	23±11	10500±49000	139±16 *	1.8±0.6 *	1.4±0.5 *	48±8	21±7 *#
MI mice + oxypurinol (1 mM)	11	104±66 *	131±75 *	28±14	13200±7300	159±32 *	2.0±0.9 *	1.4±0.9 *	50±9	24±10 * †
XOIs (allopurinol and oxypurinol combined)	18	96±54 * †	122±62 * †	26±13	12200±6400	151±28 *	1.9±0.8 *	1.4±0.5 *	49±9	23±9 * &

Values are means ± SD. ∗ - $p<0.005$ vs control (normal mice). #, $p=0.08$ vs MI group. †, $p\leq0.03$ vs MI group. &, $p=0.01$ vs MI group.

Representative ^{1}H MR cardiac images acquired at end-systole and end-diastole are shown in Figure 62 for a normal mouse (control) and in another following myocardial

infarction (MI). Four weeks following MI there is a significant increase in mean LV mass, a several-fold increase in LV chamber dimensions and a significant reduction in EF, as shown in Table 7.

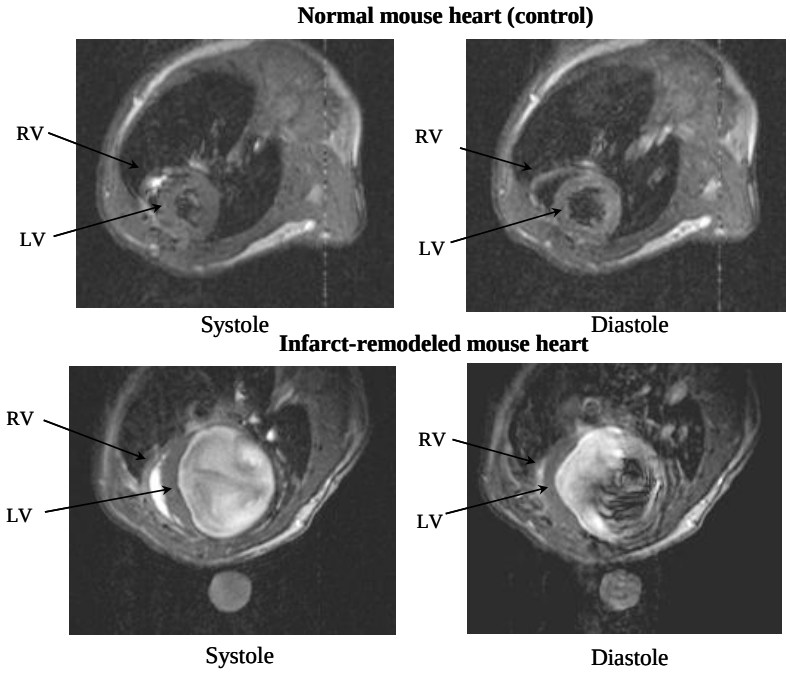

Figure 62. Transverse short-axis ^{1}H MR images of mouse thorax at the level of the heart at end-systole (left) and end-diastole (right) for a normal mouse (top) and another four-weeks after MI (bottom). Following infarction there is a several-fold increase in left ventricular dimensions and a relative decrease in the amount of blood ejected. The blood in the left ventricular chamber appears dark in the normal mouse because blood with excited spins has exited the chamber during the time of the spin-echo sequence. In contrast, blood in the ventricular chamber remains bright in the post-MI heart with the same spin-echo sequence because only a small fraction of the chamber blood with excited spins has exited the LV chamber.

End-systolic and end-diastolic dimensions of the left ventricle at the were increased in the infarcted mouse heart by more than six-fold and mean LV ejection fraction decreased from approximately 60% to 15% (Table 7). Following infarction LV mass doubled ($p<0.001$) and the ratio of myocardial mass/chamber volume was reduced several-fold ($p<0.001$, Table 7), consistent with prior observations in infarct-remodeled hearts [443, 444]. Together these findings in MI mice demonstrate a marked degree of geometric remodeling and LV dysfunction that occurs in this model of permanent left main coronary artery occlusion.

To determine whether myocardium remote from infarction demonstrates energetic abnormalities in the mouse similar to those observed in larger animals, we used non-invasive image-guided ^{31}P MRS to quantify cardiac high-energy phosphates. Representative *in vivo* cardiac ^{31}P MR spectra from normal and infarct animals are shown in Figure 63.

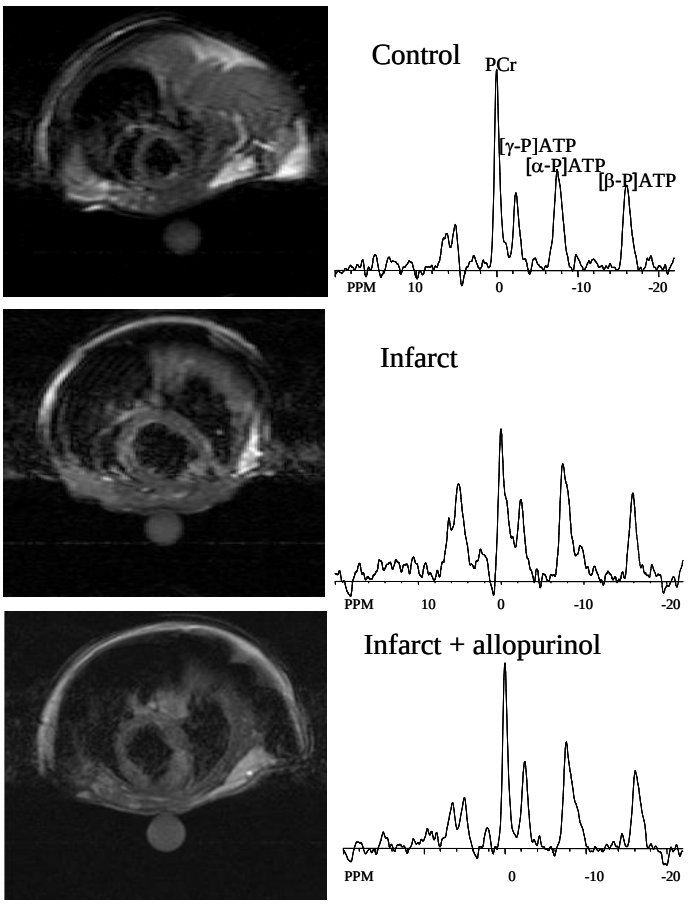

Figure 63. MR images (left column) and ^{31}P spectra (right column) in normal (upper), infarct-remodeled (middle), and infarct-remodeled with XO inhibitor allopurinol mouse hearts. The ^{31}P MR spectra with 1D chemical shift imaging were nominally obtained from 1-mm slices from the antero-septal region of the mouse heart parallel to the coil (white lines on images, left column). The cardiac PCr/ATP ratio is reduced in failing myocardium and normalized with chronic allopurinol administration.

In control mice the mean PCr/ATP ratio is 3.0±0.6 in chest skeletal muscle and 2.1±0.5 in heart. These agree well with previously published values in mice [12, 129] as well as those in larger species, including humans [22, 128, 377]. The infarct-remodeled myocardium is characterized by a significant 30% decrease in the mean cardiac PCr/ATP ratio to 1.4±0.6 ($p<0.02$). XO inhibitor therapy did not affect the increase in LV mass that develops following infarction but did significantly attenuate the marked degree of ventricular dilatation that occurs (Table 7). Specifically, XO inhibitors (XOIs) attenuated the dramatic increase in ESV ($p=0.02$) and EDV ($p=0.03$) following infarction (Table 7). In addition, LV EF was significantly higher in all MI+XOI hearts (23±9%) than in MI hearts (14±9%, $p=0.01$). Infarct size did not significantly differ between control and XOI hearts (55±11% and 49±9%, $p=0.10$, Table 7), in accord with prior histopathologic findings in this model [451].

XO inhibition with allopurinol and oxypurinol following infarction normalized myocardial PCr/ATP ratios (Figure 64). The mean myocardial PCr/ATP ratios were 2.1±0.7 and 1.9±0.4 for allopurinol and oxypurinol, respectively. The cardiac PCr/ATP was significantly higher in MI+XOI (2.0±0.5) than in MI mice (1.4±0.6, $p<0.04$) and similar to that in normal, non-infarcted mice. There was a correlation between the metabolic and functional parameters in MI and MI+XOI hearts in that the correlation coefficient between PCr/ATP ratio and ESV was -0.7 ($p<0.05$); and between PCr/ATP ratio and EF, $r=0.65$ ($p<0.05$). Thus, XO inhibition normalizes the reduced cardiac PCr/ATP in these failing, infarct-remodeled mouse hearts and this is associated with improved contractile function.

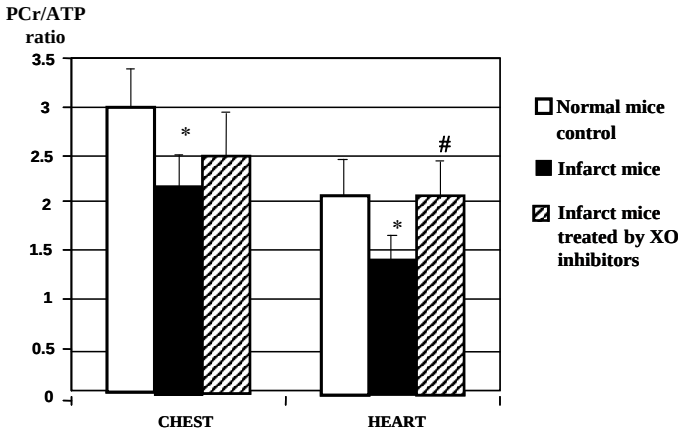

Figure 64. In vivo PCr/ATP ratios in chest muscle (left) and cardiac muscle (right) from control (open bars, n=10), MI (solid bars, n=9), MI+XOI (cross-hatched, n=10) mice.
∗ - statistically significant difference with control group (normal mice), $p<0.02$.
- statistically significant difference with MI group, $p<0.02$.

The geometric, functional and energetic consequences of post-MI remodeling were non-invasively characterized in a murine model of heart failure as well as the effects of XOIs on that process. We conclude that significant ventricular geometric remodeling occurs four weeks following permanent coronary ligation in the mouse as evidenced by a doubling in LV mass, several-fold increases in EDV and ESV, as well as a marked reduction in LV EF ($p<0.001$). The magnitude of these changes is comparable or larger than observed in other species [443]. Less dramatic changes in mass, chamber dimensions, and EF have been reported in mice following reperfused infarction [116] and earlier than four weeks following permanent coronary ligation [374]. Less remodeling was also observed in other studies where smaller infarct sizes (18±2%) were induced than in this study (~50%), likely due to more proximal coronary ligation in our approach [453]. The decrease in the ratio of LV mass to chamber

volume is similar to that reported in other models with large infarctions following coronary occlusion [443, 444].

In addition, a significant 30% reduction in the *in vivo* myocardial PCr/ATP ratio in infarcted hearts was observed. These data demonstrate metabolic remodeling, at least in relation to the CK reaction, occurs in vivo in the post-infarction, failing mouse and they are in agreement with prior observations in patients and in larger animals following infarction [131, 410, 446]. Taken together, they demonstrate that remodeling occurs in the mouse and suggest that transgenic murine lines may offer novel avenues for investigating additional mechanisms underlying post-infarction anatomic and energetic remodeling.

XO activity is increased in this mouse infarction model and that oral allopurinol suppresses this increase and improves both *in vitro* and *in vivo* contractile function as well as survival [451]. The current MRI findings in different animals confirm the prior observation made with echocardiography that XO inhibition improves *in vivo* contractile function following infarction in the mouse and does so without preventing hypertrophy. In the earlier work, the improved contractile function with XOI was not associated with increased activator calcium or a left-shift in calcium sensitivity, but rather was due to an increase in force production during maximal calcium activation [451]. Because allopurinol restored myofilament force generation to near-normal values without altering $[Ca^{2+}]_i$, the hypothesis was generated that XO inhibition improves the poor coupling between energy production and mechanics in failing hearts. In other words, the ability to generate more force without augmenting activator calcium predicts an improved efficiency of myocardial energy utilization.

Energy metabolism fuels normal myocardial contractile function and for decades it has been hypothesized that a deficit in energy metabolism may contribute to the contractile deficit in heart failure [124, 125]. Likewise, a deficit in energy metabolism could contribute to the progressive dysfunction and geometric changes following infarction [446]. The creatine kinase reaction reversibly converts the major cardiac form of chemical energy, ATP, with the prime energy reserve metabolite, creatine phosphate. Animal models of heart failure and patients with heart failure typically exhibit abnormalities in the creatine kinase reactants with modest reductions in [ATP], larger reductions in [PCr] and total creatine, and significant reductions in the cardiac PCr/ATP [132, 137, 446, 447]. Abnormalities, such as a reduced PCr/ATP, correlate with the severity of the heart failure, improve with clinical recovery, and are stronger predictors of mortality than usual clinical indices of left ventricular ejection fraction and New

York Heart Association class [454]. All of these observations are consistent with, but do not prove, that abnormalities in energy metabolism may contribute to the pathophysiology of the contractile dysfunction in heart failure. To test the energy starvation hypothesis of heart failure, one needs to determine whether a metabolic intervention that improves energetics results in improved contractile function in failing hearts. Evidence that over-expression of a glucose transporter in pressure-overload mice attenuates the development of heart failure [455] and that ranolizine, a free fatty acid inhibitor, improves mechanical efficiency in dogs with heart failure [456] both indicate that metabolic interventions can be important in heart failure. However, here the energetic changes may be secondary to improved excitation-contraction coupling, rather than reflecting a primary metabolic effect.

In this regard, the current studies on XO inhibition in remodeled mouse myocardium provide important insights. XO inhibition improves mechano-energetic coupling in failing hearts by reducing energetic demand in both animals and people [449, 450]. Improved mechano-energetic efficiency with XO inhibition occurs in failing but not normal hearts and is due to a reduction in myocardial oxygen consumption while maintaining or improving contractile function. XO inhibition represents one strategy for evaluating the energy starvation hypothesis of heart failure.

XO inhibition normalized the reduced myocardial PCr/ATP ratio in failing mouse hearts. The improvement in cardiac PCr/ATP with XOI is not likely due to an effect on infarct size since it is similar in control and infarcted hearts [451] and because infarcted tissue does not contain significant PCr or ATP [408, 409]. XOI is one of the first metabolic interventions that normalize reduced cardiac energetics in any model of heart failure. Moreover, improved energetics with XO inhibitors are associated with improved contractile function (Table 7). Although angiotensin converting enzyme inhibition prevents the decrease of *in vitro* creatine kinase activity in infarcted rat hearts [457], ACE inhibition has many effects including those on LV hypertrophy and cardiac demand that can secondarily affect metabolism. Therefore, XO inhibition represents a metabolic approach to improve altered energetics following infarction in a failing heart and this is associated with a significant improvement in contractile function in that setting.

Myocardial PCr/ATP falls acutely during ischemia as a result of an imbalance of oxygen supply and demand whereby PCr is consumed to buffer or delay a decline in ATP. In the more chronic setting of heart failure, there is evidence that classic ischemia is not present,

in that deoxymyoglobin cannot be detected in several animal models of heart failure [435, 446]. However, a slow loss in ATP does occur in heart failure that is accompanied by a more rapid and greater loss of total creatine [458]. Creatine depletion acts to attenuate or prevent an increase in ADP as ATP falls [458]. Because creatine is not synthesized in muscle cells, if expression of the major creatine transport proteins in animal models and patients with heart failure is depressed [411], then this may be the likely mechanism for the decrease in total creatine in heart failure. It seems likely that by improving mechano-energetic coupling in dysfunctional myocardium and/or blocking adenine nucleotide degradation, XO inhibition attenuates the initial ATP loss and the resultant more dramatic decline in PCr/ATP. An alternative explanation is that XOIs fundamentally alter crossbridge kinetics such that more force is generated per ATP consumed; such a mechanism has been proposed to underlie the effects of agents, such as XOIs, that increase maximal calcium-activated force without shifting the calcium-force relationship [411]. We cannot exclude the possibility that XO inhibition exerts an anti-oxidant protective effect in the heart. The present data do not distinguish among these various mechanisms, which merit further dissection.

In conclusion, geometric, functional and metabolic remodeling occurs in this mouse post-infarction model and the magnitude of the changes is similar or greater than those observed in other larger mammals. XO inhibition attenuates but does not prevent the geometric changes, significantly improves contractile function, and completely normalizes depressed cardiac high-energy phosphate ratios. The observation that a metabolic intervention normalizes energetics and results in improved contractile function directly supports the long-debated energy starvation hypothesis of heart failure.

4.4. Specific Aim 4

To develop non-invasive physiologically meaningful method of myocardial perfusion quantitation using kinetic modeling of the contrast agent dynamics in tissues.

Myocardial perfusion studies using dynamic contrast-enhanced cardiac MRI could provide valuable, quantitative information regarding heart physiology in diseases that lead to myocardial damage. The goal of this work was to develop an intuitive but physiologically meaningful method for quantifying myocardial perfusion by cardiac MRI and to test its ability to detect global myocardial differences in the infarcted heart of non-human primates and in a dog model of Duchenne muscular dystrophy (DMD). Perfusion cardiac MRI studies may

provide quantitative information regarding myocardial physiology through approaches based on contrast agent kinetic modeling [101, 459]. Such quantitative information can be especially valuable in cardiac pathologies leading to diffuse changes in myocardial properties that are too subtle to recognize based on direct inspection of the images themselves. Among the challenges in applying quantitative perfusion cardiac MRI to diseases such as DMD is the potential for global changes in perfusion that cannot be recognized as regional differences. This challenge is compounded by the lack of a concise display and simple interpretation of the quantitative results. Previous methods for quantifying perfusion cardiac MRI results have focused either on semi-quantitative measurements, such as the upslope of the myocardial uptake curve, or kinetic models with specific physiological measurements, such as the mean transit time [113, 404, 459-462]. These measurements often lack a clear physiological context or else portray information that is difficult to understand by those who are not familiar in the underlying model.

Thus, the purpose of this study was three-fold. First, we sought to develop an analysis approach that automatically extracts a map of perfusion characteristics and communicates the characteristics in terms of intuitive but physiologically meaningful parameters. Second, we tested this approach in a canine model of DMD and third, in the non-human primates with myocardial infarction. DMD-affected dogs represent the only animal model that faithfully mimics human DMD, reproducing many of its elements including cardiomyopathy. The affected dogs typically die from cardiac or respiratory malfunctions within 2 to 4 years of birth [463], making this a meaningful preclinical model for testing out the approach. Non-human primates (NHPs) are the closest to human animal species that are used for pre-clinical evaluations of therapeutic interventions. The utility of cardiac MRI to study myocardial perfusion in heart failure in NHP has not been described.

4.4.1. Kinetic model

To model the contrast agent dynamics, we used a discrete time approximation of the Kety model as previously used in perfusion cardiac MRI [404] and given by

$$C_t(t) = K^{trans} \int_0^t C_p(\tau) e^{-k_{ep}(t-\tau)} d\tau, \qquad \text{(Equation 1)}$$

where K^{trans} is the transfer constant and k_{ep} is the transfer rate constant, $C_p(t)$ is the plasma concentration, and $C_t(t)$ is the tissue concentration. Equation 1 has also been formulated in terms of the myocardial blood flow (*MBF*), extraction efficiency (*EE*), and

partition coefficient (λ) which are related by $K^{trans} = MBF \times EE$ and $k_{ep} = MBF \times EE/\lambda$ [460]. Numerical integration of this function under an assumption of piece-wise constant plasma concentration yields

$$C_t[n] = U\sum_{i=1}^{n} R^{n-i} C_p[i], \qquad \text{(Equation 2)}$$

where $C_p[n]$ and $C_t[n]$ are, respectively, the plasma and tissue concentrations in frame n of the image series, $U = K^{trans}\Delta T$ and $R = e^{Kep\Delta T}$, and ΔT is the time step between image frames. Alternatively, this model can be written

$$C_t[n] = UC_p[n] + RC_t[n-1] \qquad \text{(Equation 3)}$$

which invites a simple interpretation of the model components. First, $UC_p[n]$ is the total forward flux of contrast agent into the tissue over one time frame. The term $RC_t[n\text{-}1]$ is the amount of contrast agent still remaining in the tissue from the previous time frame (i.e. the amount not lost to efflux). We refer to the parameters U and R as the uptake and retention, respectively. To solve for U and R, we set up the linear equation

$$\begin{bmatrix} C_t[n] \\ \vdots \\ C_t[2] \\ C_t[1] \end{bmatrix} = U \begin{bmatrix} C_p[n] \\ \vdots \\ C_p[2] \\ C_p[1] \end{bmatrix} + R \begin{bmatrix} C_t[n-1] \\ \vdots \\ C_t[1] \\ 0 \end{bmatrix}. \qquad \text{(Equation 4)}$$

Finally, to eliminate the dependence of the model parameters on ΔT, we normalize the results to 1-second intervals and define the uptake and retention coefficients as $U_{1sec}=U/\Delta T \times 100\%$, $R_{1sec}=R/\Delta T \times 100\%$.

The U_{1sec} parameter describes for a given blood concentration of the agent how fast the tissue concentration would rise due to entry from the blood. For example, if the blood held 1 μM per liter and the uptake coefficient was 10% per second, then the increase in tissue concentration would occur at a rate of: (1 μM /liter) × (10% per sec) = (0.1 μM per liter per second).

The R_{1sec} parameter describes the reverse process - how fast the tissue concentration drops in the absence of any blood concentration. For example, if the tissue concentration was 1 μM per liter and the efflux coefficient was 10% per second, the concentration would drop to 0.9 μM per liter after 1 second, to 0.81 μM per liter after 2 seconds (i.e. 10% of 0.9 is gone), to 0.729 μM per liter after 3 seconds (i.e. 10% of 0.81 is gone). In reality, both of these processes are happening at the same time and moving toward an equilibrium state.

The discrete kinetic model was implemented into a custom quantitative perfusion analysis package programmed in Matlab (The Mathworks, Natick, MA) and based on similar analysis tools for perfusion analysis of artery wall images [407, 464]. In this program, a time series of frames was extracted from the dynamic sequence starting at the frame immediately before bolus arrival in the right ventricle and ending 30 seconds later. The frame with approximately maximal enhancement of the left ventricle chamber was also identified. Then, an automatic registration algorithm [407] was run in both directions from the frame of maximal enhancement within an 8.75 cm × 8.75 cm region of interest centered on the left ventricle. Each frame was matched to the previous one by identifying the in-plane shift that minimized the sum of the square roots of the absolute differences between pixel values. Next, an automatic arterial input function (AIF) extraction algorithm [464] was used to identify an enhancement-versus-time curve representing the blood within the left ventricle chamber. Enhancement-versus-time curves were extracted from all pixels within a 7-pixel × 7-pixel region at the center of the chamber. For each pixel, all pixels with similar curves were identified via a mean shift algorithm, and the mean curve for those pixels was found. The AIF was identified as the mean curve based on at least 5 pixels, with maximal enhancement.

Finally, maps of the uptake and retention coefficients were computed for every pixel within the region of interest using Equation 4. Concentration was assumed to be proportional to the change in signal intensity. In addition, an average tissue curve for the entire myocardium was extracted by averaging all pixels within manually drawn epicardial and endocardial boundaries. The model parameters were then extracted from this average curve to obtain a single overall value for the myocardium. For the overall value, model parameters were obtained from the non-linear Equation 2 using a gradient descent algorithm with R constrained to be less than or equal to 100%. The non-linear formulation was found to yield less fitting error than Equation 4 for quantitative analyses.

4.4.2. Myocardial perfusion in dogs with Duchenne muscular dystrophy (DMD)

One potential application of quantitative perfusion MRI is assessing the degree of cardiac involvement in Duchenne muscular dystrophy (DMD). DMD is a fatal, X-linked, recessive muscle disease caused by lack of dystrophin due to mutations in the dystrophin gene. DMD affects both skeletal and cardiac muscles [465, 466]. Due to the increasingly common use of ventilatory support, cardiomyopathy has become the leading cause of morbidity and mortality (~40%) in DMD patients [467, 468]. In addition, more than 50% of DMD carriers

also present with cardiac symptoms [467-469]. Cardiac MRI may be helpful in staging and detecting early impacts of DMD in the myocardium. In particular, perfusion cardiac MRI may reveal vascular changes or the existence of diffuse fibrosis in the myocardium. Previous reports have shown that DMD patients exhibit a high prevalence of scar by delayed enhancement cardiac MRI [470-472]. Perfusion studies involving PET and SPECT imaging have reported deficits in patients with DMD [473, 474]. Studies of the DMD involving perfusion cardiac MRI, however, have not been reported.

The study involved 5 dogs with DMD and 6 normal controls. Ages for dogs with DMD averaged 41 ± 38 months (range: 12 to 98) and weight averaged 14.33±1.8 kg (range 11.7 to 16.5kg). Healthy controls had mean age 20 ± 4 months (range: 15 to 25) and weight averaged 12.2±3.26 kg (range 9.3 to 16.3 kg). All DMD dogs were confirmed by genotyping and increased serum creatine kinase level. Clinical signs of the disease varied among the 5 dogs. While the 3 younger DMD-affected dogs (aged 12, 13 and 17 months) showed obvious clinical symptoms, including difficulties in eating, walking and breathing, the two older affected dogs (aged 5 years 2 months, and 8 years 2 months) were in generally good health.

Cardiac functional parameters for dogs with DMD and healthy controls are summarized in Table 8. Dogs with DMD had higher heart rates compared to normal controls (170 versus 111 bpm, p=0.01). EF tended to be lower in dogs with DMD (p=0.06). Comparisons of end-diastolic and end-systolic images from dogs with DMD and normal controls are shown in Figure 65. No evidence of focal delayed enhancement was observed in any dogs, indicating a lack of identifiable infarcted tissue.

Table 8. Cardiac functional parameters (mean ± SD) comparing dogs with DMD to healthy controls.

Parameter	DMD	Control	P value
Heart Rate (BPM)	170±39	111±20	0.01
End-systolic Volume (ml)	17.4±12.1	14.6±6.2	0.6
End-diastolic Volume (ml)	32.6±14.7	32.6±9.3	1.0
Stroke volume (ml)	15.1±4.5	18.0±3.5	0.3
Cardiac Output (l/min)	2.4±0.2	2.0±0.7	0.2
Ejection Fraction (%)	45.2±10.4	56.6±6.4	0.06
LV Mass (g)	46.5±9.8	46.9±12.8	0.8

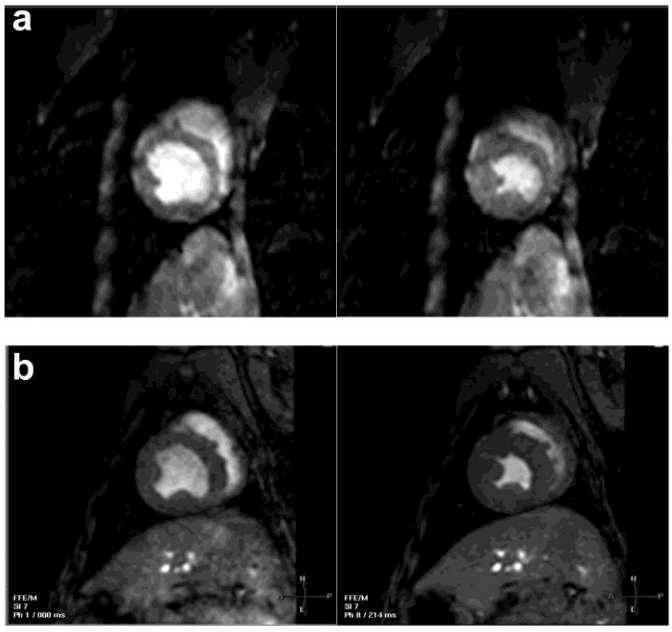

Figure 65. Examples of CINE images at end-diastole and end-systole from a dog with DMD with ejection fraction (EF) of 52.0% (a) and a normal control with EF 57.2% (b).

Perfusion analysis was successfully performed for all dogs with DMD and 5 (83%) healthy controls. In the one remaining healthy control, weak enhancement was observed within the chamber, but no measurable tissue enhancement was seen. This was attributed to partial failure of the injection and this dog was excluded from further analysis. In the remaining dogs, visual evaluation confirmed that the automatic registration algorithm effectively eliminated translational motion due to breathing. Average values of *U* and *R* for both groups are plotted in Figure 66. Dogs with DMD exhibited significantly higher uptake with mean *U* (± SD) of 6.76% (± 2.41%) compared to 2.98% (± 1.46%) in controls (p=0.03). Additionally, retention appeared lower with mean *R* of 82.2% (± 5.8%) in dogs with DMD compared to 90.5% (± 6.6%) in controls (p=0.12).

Representative perfusion maps of the uptake and retention coefficients are shown in Figure 67 for a dog with DMD and a healthy control. Maps of both *U* and *R* show fairly uniform values within the myocardium, which is easily distinguished from surrounding regions. These examples confirm on a pixel scale the observed tendency for higher uptake and reduced retention in dogs with DMD.

	U (%)	R (%)
DMD	6.8 ± 2.4	82 ± 6
Control	3.0 ± 1.5	91 ± 7
P	0.03	0.12

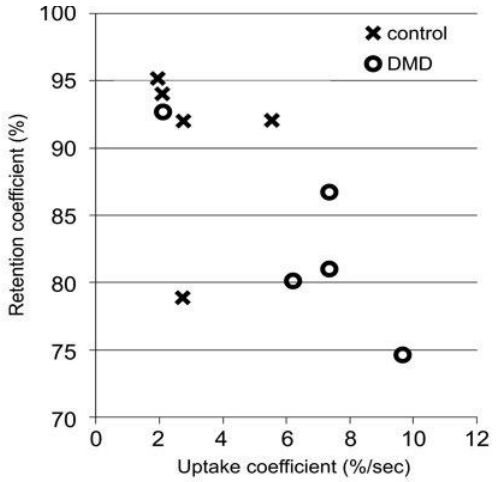

Figure 66. Values of the uptake and retention coefficients measured in 5 dogs with DMD versus 5 healthy controls. Averaged over the entire myocardium, DMD dogs exhibited higher uptake and lower retention than normal controls.

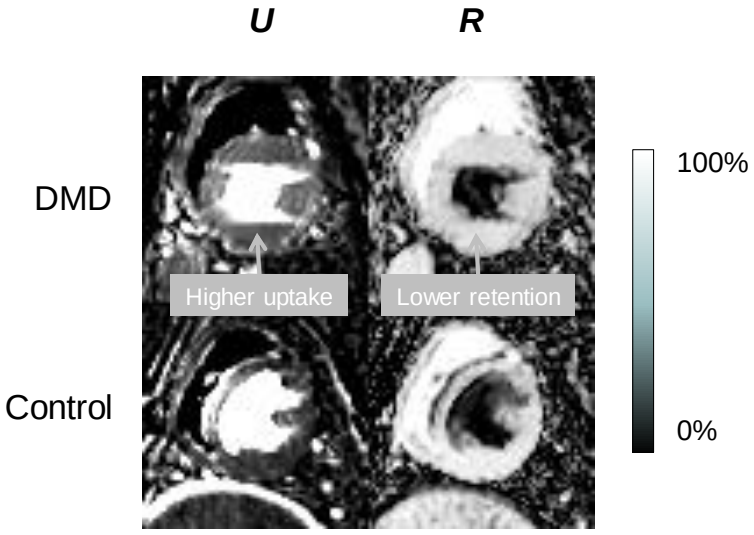

Figure 67. Parametric maps of the uptake (*U*) and retention (*R*) coefficients for healthy and DMD dog. Averaged over the entire myocardium, DMD dogs exhibited higher uptake and lower retention than normal controls. Perfusion maps are showing an intuitive representation of the rates of wash-in and wash-out.

The left ventricle chamber is characterized by 100% uptake and 0% retention. The right ventricle chamber, on the other hand, exhibits a non-physical model result with 0% uptake and 100% retention. This is attributed to the time lag between bolus arrival in the right and left ventricles, which is not captured in the model.

This study illustrates the potential utility of a discrete approximation of the Kety model for quantitative perfusion analysis by cardiac MRI. By parameterizing the model in terms of uptake and retention coefficients, perfusion maps are presented in an intuitive representation of the rates of wash-in and wash-out, respectively. Using this framework, the clinician can

quickly assess whether abnormal contrast enhancement is due to altered delivery of the agent, increased retention of the agent, or both. On the other hand, a direct relationship exists between U and R and the kinetic parameters K^{trans}, k_{ep}, MBF, EE, and λ. This permits the discrete parameters to be translated into those more traditional physiological quantities.

The application of this technique to a study of DMD in dogs demonstrated its ability to reliably and automatically extract qualitative and quantitative representations of cardiac perfusion. Few prior studies of contrast agent uptake in DMD exist. A study in skeletal muscle in a mouse model found that early in the disease, enhanced perfusion is likely due to active degeneration/regeneration processes in muscle, with reduced perfusion in later stages of the disease [475]. In humans, a high prevalence of myocardial scar has been observed which typically is associated with perfusion deficits [470-472]. In this study, no myocardial scar was observed; however, it does not exclude ongoing inflammation or fibrosis. Because of the lack of scar and enhanced perfusion in dogs with DMD, our results are consistent with an early-stage disease model.

A major motivation for this study was a desire to use this technique in the future to monitor changes in cardiac function over time for disease staging or monitoring therapy, first in the preclinical DMD dogs and then translating into human DMD patients. Whether myocardial perfusion transitions from a hyperperfused state to a hypoperfused state in later stages of DMD remains to be determined. In principle, the technique described here provides a robust, automated, and quantitative approach to address such questions. In addition to investigating myocardial perfusion in DMD, this study also examined quantitative cardiac function based on cross-sectional CINE images. Reduced EF has been frequently observed in echocardiographic studies of DMD [476-478]. The results here indicated a trend toward reduced EF in dogs with DMD. We also observed elevated heart rates within the DMD group. One question that arises is whether the apparent changes in perfusion observed are a consequence or contributing cause of the altered functional parameters. Investigating this question will prove critical in determining which parameters are of most value for assessing cardiac involvement in DMD.

Regarding the discrete kinetic model implementation, insight can be gained by considering a hypothetical case in which the AIF rises to a concentration C for one time interval before returning to zero. In this case, the tissue concentration would rise to UC over the interval and then decay at a rate proportional to R^t. In actual situations, the contrast agent

kinetics can be viewed as the superposition of such impulse responses due to the concentration in each interval [459]. From this, we see that two aspects of contrast agent dynamics are neglected in the model. First, changes in the AIF over the interval are not modeled, and second, the model does not account for any contrast agent that enters and leaves the tissue within the same interval. The impact of both of these assumptions is minimized by using short intervals, such as single heart beats. In this study, the interval was typically on the order of 0.5 sec. In this study, we also explored two methods for fitting the model to the data. For producing parametric images, we used the linear solution of Equation 4, which could be rapidly computed for every pixel in the image. The results, however, were not as accurate as those from direct fitting of Equation 2 because the presence of tissue concentrations on both sides of Equation 4 can lead to numerical instabilities. The differences were not apparent when viewing parametric images, but for quantitative reporting, we chose to use non-linear fitting of Equation 2.

The major limitation for this study was the small group size. In many cases, compelling trends were observed, such as the reduced retention coefficient in dogs with DMD, but did not achieve statistical significance. The small size also precluded multiparametric analyses to assess interactions between variables. Most notably, the influence of the larger distribution in ages of the dogs with DMD compared to the healthy controls was not assessed. Nevertheless, the small study size was sufficient to demonstrate the potential of this approach for future studies.

In conclusion, this study illustrates the potential utility of a discrete model of contrast agent kinetics to investigate myocardial perfusion characteristics. While the automatic AIF extraction algorithm has been previously applied to study atherosclerotic plaque lesions in human patients [464], this technique has been used for the first time for cardiac applications in large animals. Model parameters describing uptake and retention of the contrast agent were automatically extracted in all cases on a pixel level. When applied to the study of DMD in dogs, the model was consistent with enhanced perfusion associated with the disease.

4.4.3. Temporal changes in myocardial perfusion after human cardiomyocyte transplantation in non-human primates

Perfusion MRI sequence was tested in 8 non-human primates *Macaca nemestrina* (10±2 kg, 9±2 years old, both sexes) 2 weeks after MI (before transplantation of 750 million hESC-CMs) and one month after cell therapy using a 3T clinical scanner (Philips Achieva, Best, Netherlands). The dynamic perfusion scans were acquired in single-slice between mid-

ventricle and apex, sequence was single-shot saturation recovery TFE acquisition with TR/TE of 3.0/1.4 msec, 20 degree flip angle, 4 mm slice thickness and in-plane resolution of 1.99 mm × 1.96 mm. During the acquisition, 0.2 mmol/kg Gd-DTPA (ProHance, Bracco Diagnostics Inc., Princeton, NJ) was manually injected, followed by a saline flush. Perfusion analysis was performed using a discrete-time model that estimates the transfer constant (K^{trans}) that describes the uptake (U) of contrast agent into the tissue and the contrast retention coefficient (R). The AIF extraction algorithm generated similar curves for all animals, consisting of a fast-rising first peak followed by a second smaller peak due to bolus recirculation. The model produced qualitatively excellent fit results for the average myocardial enhancement curve (figure 68).

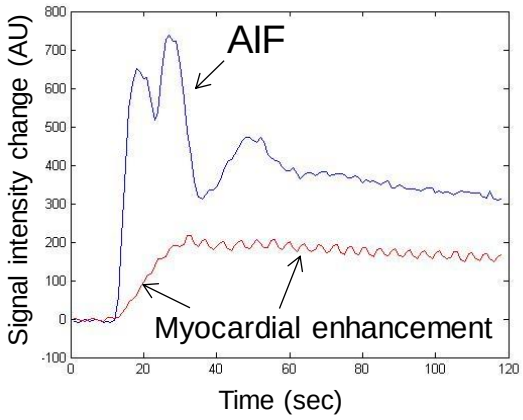

Figure 68. An automatic arterial input function (AIF) extraction algorithm was used to identify an enhancement-versus-time curve representing the blood within the left ventricle chamber (blue curve) and the enhancement of the myocardial tissue (red curve) in the non-human primates. AU - arbitrary units.

Automated quantification of the contrast uptake and retention showed the tendency to the increased perfusion from 3.6±0.1% (before cell transplantation) to 5.9±4.2% (1 month after cell transplantation) compared to 2.84±0.9% and 4.1±1.5% in no cell control animals at the same time points. One animal was excluded from the perfusion analysis due to failed cardiac triggering during injection. Another cell-treated animal showed decrease in U from 3.62 (baseline) to 1.29 (1 month); it correlated with the histology data showing loss of human graft. Also, myocardium of the cell-treated animals was described by decreased contrast retention in comparison with non-treated control (figure 69). Improvement in perfusion correlated with the improved contractility in the cell-treated group (part 4.2.2).

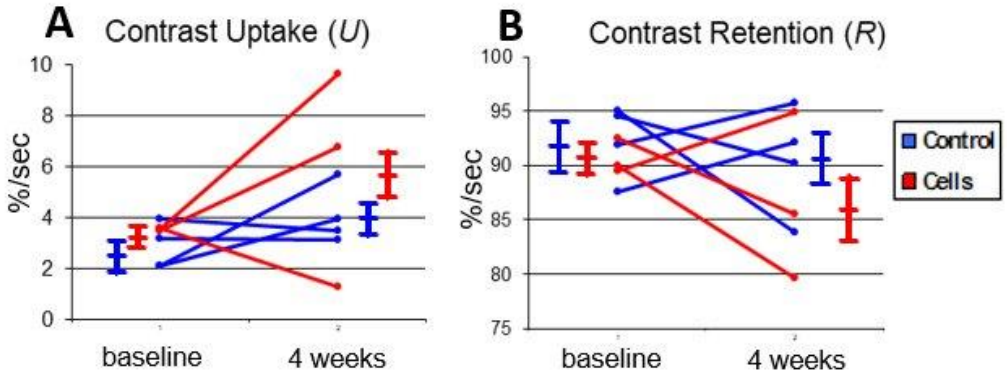

Figure 69. Changes in myocardial perfusion (contrast uptake and retention) in the individual studied non-human primates before (baseline) and one month after hESC-CM transplantation.

Observed tendency in perfusion increase after hESC-CM transplantation might be related to the neovasculature in graft area, as we have shown previously in heart of non-human primates [379], or might be related to viable mass increase and presence of large human cardiac grafts. Interestingly, the areas of the large human graft were characterized by the myocardial hyper-perfusion, as shown in the figure 70 (DCE). The areas of perfusion deficit are shown in the DCE images as hypo-intensity (dark) zones (figure 70). Maps of uptake and retention show uniform values within the myocardium and blood pool; maps can be shown in the Matlab program in any chosen color (here uptake is shown in red; retention in green).

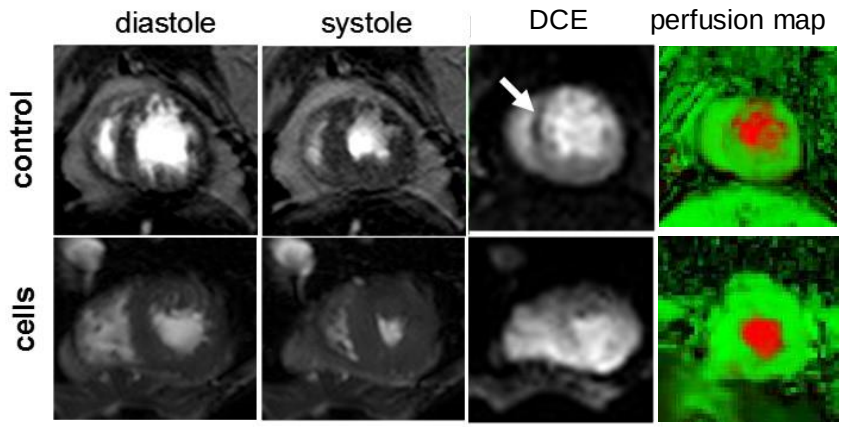

Figure 70. Examples of a single slice CINE in systole and diastole, DCE images and perfusion images from an infarcted no-cell control animal and a non-human primate after hESC-CM transplantation. Arrow indicates perfusion deficit in control that is not seen in the cell-treated animal. *U* is red, *R* – green color.

Analysis of contrast agent perfusion by MRI shows potential for the study of myocardial perfusion in the assessment of cell transplantation benefits. Future studies involving larger numbers of animals are needed to statistically assess the therapeutical benefits of hESC-CMs in terms of perfusion.

4.5. Specific Aim 5

To explore the possibility of using the new processing method of the post-contrast MRI, 3D-TRIPS, for infarct visualization.

T_1-weighted inversion-recovery (IR) MRI acquisitions are commonly used in detection of myocardial scar after contrast agent administration. After applying a 180° RF inversion pulse the appropriate inversion time (TI) should be chosen, so the tissues with relatively long T_1 have negative longitudinal magnetization (polarity) in the reconstructed image, while the tissues accumulating gadolinium-based MRI contrast agent have shorter T_1 and bright enhancement in IR images. The correctly chosen TI is typically set to null the normal myocardium signal to maximize the contrast between the normal and infarcted myocardium. An error in selecting the optimum null time leads to a reduced infarct to myocardium contrast ratio and may also cause artifact appearance due to the loss of polarity information. The contrast agent has its own kinetics; washes out rates are different for the normal and infarcted tissues. The T_1 increases as the contrast agent washes out of the tissue. With a fixed TI value that nulls the healthy myocardial tissue at the start of a multislice acquisition, the contrast degrades at the final slice, which is acquired several minutes later, due to the increasing T_1.

Phase-sensitive detection has been used to improve infarct to myocardium contrast by preserving the sign of the desired magnetization during IR and reduce the dependence on prescribing at exact TI time. Phase-sensitive reconstruction achieves consistently good contrast ratio between normal and infarcted myocardium during multislice acquisition by decreasing the sensitivity to changes in the value of tissue T_1 with increasing delay from the time of the contrast agent injection. Phase-sensitive inversion recovery (PSIR) is now the standard MRI method for scar imaging [118]. However, phase-sensitive reconstruction requires acquisition of an additional phase-reference image acquired after magnetization recovery, which cause the scan time increase. Short scan time is critical for the heart failure patients and for the infarcted animals with severe myocardial damage.

Additional complications of a reference phase map of the areas with heterogeneous anatomical structures are associated with the separation of high SNR regions, such as blood in the left ventricular blood chamber, from low-SNR regions, such as normal myocardium with “nulled” signal. The reference-free methods [479-481] attempt to solve this problem, but those methods are vulnerable to error propagation problems, where a small number of voxels with incorrectly estimated polarity can ultimately lead to errors across a large region of the image.

The basis for majority of the reference-free phase-sensitive reconstruction methods is that the added background-phase changes smoothly within the field of view [480, 482]. Therefore, in the background phase map, the difference between neighboring voxels with sufficient SNR should be smaller than $\pi/2$. If the difference φ_{dif} between the phase φr of a voxel and the background phase of its neighboring voxels is smaller than $\pi/2$ (Figure 71a), φr is assigned as the background phase of this voxel, otherwise, $\pi - \varphi r$ is assigned as the background phase (Figure 71b).

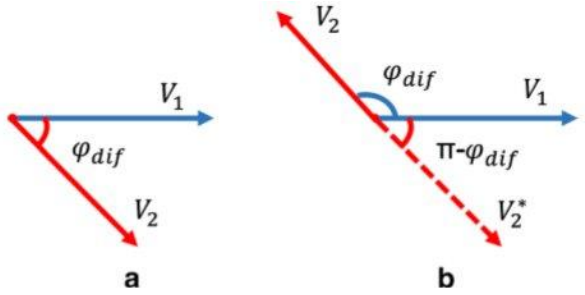

Figure 71. Background phase determination based on the phase difference. **a:** Two neighboring vectors V_1 and V_2 have a phase difference $\varphi_{dif} \leq \pi/2$. **b**: Two neighboring vectors V_1 and V_2 with phase difference $\varphi_{dif} > \pi/2$, in which case the phase difference between V_1 and the conjugate of V_2 (V_2^*) is smaller than $\pi/2$. Figure from [483].

The region growing processing methods for the background-phase estimation processes the neighboring voxels as continuation of the voxels that have already been processed; then voxels with small phase differences are prioritized from lower phase differences to larger phase differences to optimize the region growing track (sequence of the processed voxels). This technique is susceptible to errors when noise is present due to pre-existing background-phase differences. For example, voxel V_1 and its reference V_{ref} have a phase difference of 20° (Figure 72a). After adding noise to V_1, the phase difference may change to either 25° with $V_{1,noise1}$ (Figure 72b) or to 5° with $V_{1,noise2}$ (Figure 72c). With phase-only based region-growing methods, $V_{1,noise1}$ will have a lower priority relative to $V_{1,noise2}$, even if the SNR of $V_{1,noise1}$ is actually higher than that of $V_{1,noise2}$. Error propagation from low- to high-SNR voxels can be avoided if SNR is taken into account.

A new cardiac MRI technique for the 3D-late gadolinium enhancement (LGE) imaging and phase-sensitive reconstruction has been recently developed at the University of Washington [473]. The 3D True Polarity Recovery with Independent Phase Estimation Using Multi-layer Stacks Based Region-Growing (3D-TRIPS) technique allows shortening imaging time by direct reconstruction of 3D phase sensitive images without need for a separate

reference scan. 3D-TRIPS image reconstruction method is taking in consideration not only the phase, but also SNR of each voxel. In 3D-TRIPS voxels are primarily prioritized by signal intensity, mitigating the phase-error propagation from low-SNR voxels. The flow-chart of the 3D-TRIPS reconstruction algorithm is show in the figure 73. The full description of all steps in image processing are in [473].

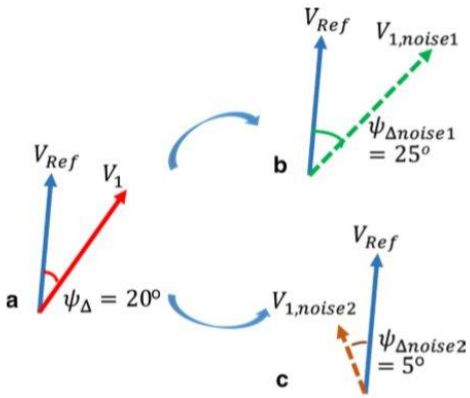

Figure 72. Scheme of error propagation in phase-based region growing image processing method (from Liu et al, 2017). **a**: A preexisting phase difference 20° between voxel V_1 and its reference V_{ref}. After adding noise to V_1, the phase difference may increases to 25° for $V_{1,noise1}$ (**b**) and to 5° for $V_{1,noise2}$ (**c**). In phase-based region growing, $V_{1,noise2}$ has a higher priority than $V_{1,noise1}$ because of the apparently smaller phase difference. Figure from [483].

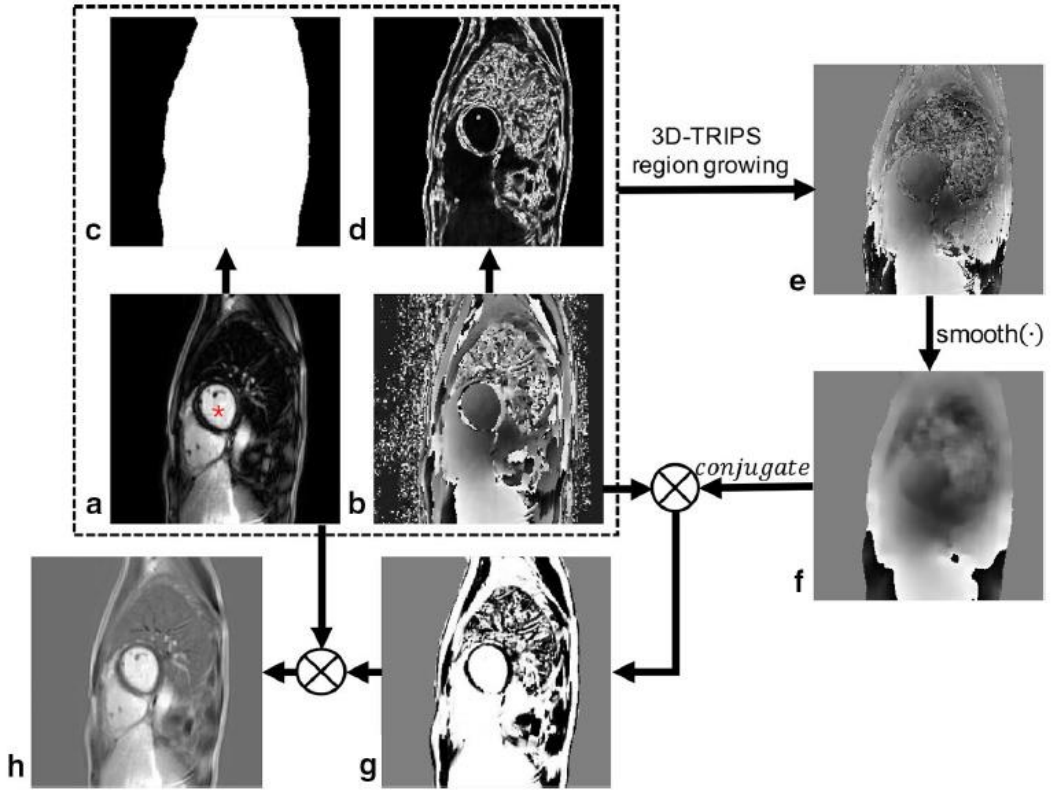

Figure 73. Flow chart for 3D-TRIPS. Magnitude of the acquired T_1-weighted image, with the red star marking the starting point of region growing (a). Corresponding phase image (b). The mask M global calculated from a (c). Maximum neighboring phase-difference map M_{dif} (d). Background phase using the proposed 3D-TRIPS method (e). Smoothed background-phase map (f). Polarity map (g). Final phase-sensitive 3D-TRIPS image (h). Figure from [483].

3D-TRIPS method is based on two assumptions, compared with phase-only region growing methods: 1) The error ratio of the background-phase estimation negatively correlates with SNR; and 2) Prioritizing voxels with high SNR can improve the background-phase estimation of low-SNR voxels.

3D-TRIPS uses signal intensity as a surrogate for SNR to evaluate the reliability of voxels for background-phase calculation. To reduce the influence of voxels in polarity transition regions or regions with non-smooth background phase, 3D-TRIPS uses the maximum neighboring phase difference to adjust voxel priority during region growing. The three tier stack bank used in 3D-TRIPS prioritizes signal intensity (Figure 74). 3D-TRIPS reduces error propagation in region growing by prioritizing the most reliable voxels. 3D-TRIPS directly reconstructs image polarity by comparing the phase difference with the preset π/2 threshold and is therefore computationally efficient for phase-sensitive reconstruction.

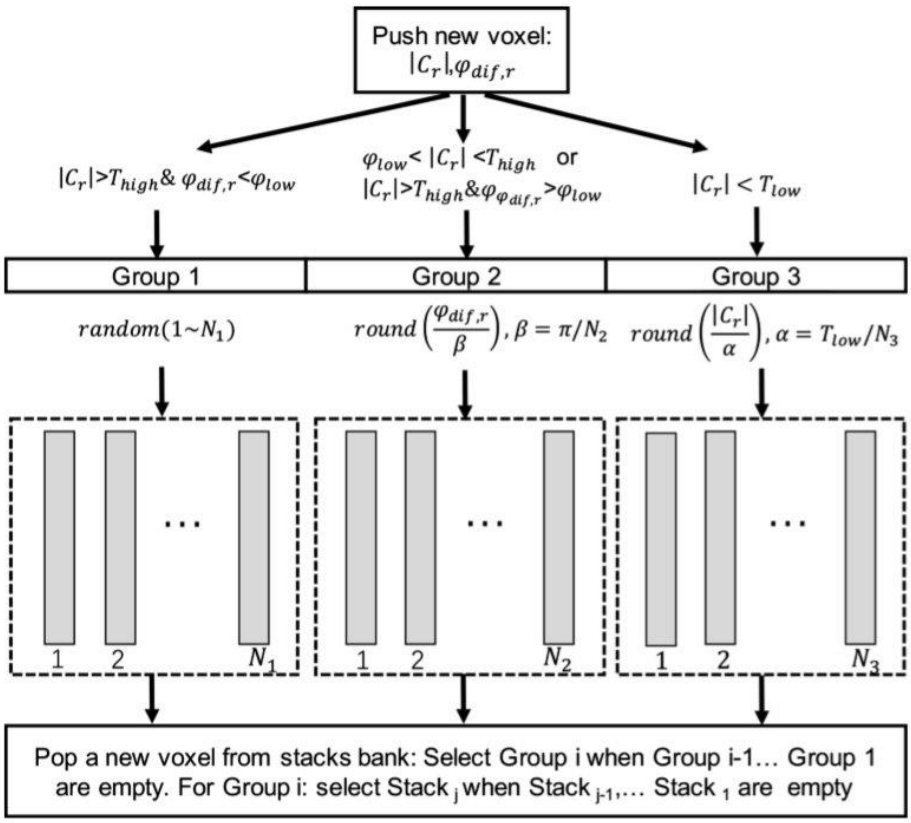

Figure 74. Scheme of the three-tier stack bank during region growing. When a new voxel is pushed into the stack bank, the classification function determines which stack to use based on the magnitude of the voxel $|C_r|$ and its maximum phase difference with neighboring voxels $\varphi_{dif,r}$. The stack bank always pops a new voxel from the nonempty stack with highest priority. Figure from [483].

Equivalent image quality for 3D-TRIPS and PSIR acquisitions has been demonstrated on patients with nonischemic cardiomyopathy [483]. Aim of this study was to evaluate 3D-

TRIPS method in imaging of myocardial infarction on non-human primates, which are the preferred large animal species for pre-clinical evaluations of therapeutic interventions due to their physiological similarity to humans.

Myocardial infarction was induced in ten *Macaca nemestrina* by 3 hours mid-LAD balloon inflation followed by reperfusion. Infarct size was evaluated noninvasively with MRI using 3T Achieva Philips clinical scanner (Best, Netherlands) and Flex-M/Flex-L or knee coils (depends of the animal size). 3D-LGE images were acquired at 5 minutes after intravenous injection of 0.2 mmol/kg Gd-DTPA ProHance (Bracco Diagnostics Inc., Princeton, NJ). 3D-LGE sequence parameters included: TI ~ 180 ms; FOV 150×150×48 mm^3, slice thickness 4 mm no gap, TR/TE 7.0 /3.5 ms, FA 25°, TFE factor 16, 112 shots, FTE shot interval 1 beat, 3 signal averages, acquired voxel size 1.2/1.2/4 mm reconstructed to 0.63/0.63/2 mm^3. Scan time 5.38 min. 2D-PSIR images were acquired at ~10 minutes after contrast agent administration with following parameters: TI 280-350 msec; FOV 150×150 mm^2, 12 slices, slice thickness 4 mm, TR/TE 7.0/3.5 ms, FA 25°, TFE factor 17, FTE shots 7, FTE shot interval 1 beat, PSIR flip angle 5°, 3 signal averages, scan time ~8.36 min. Prospective ECG triggering was used without breath hold. 2D-PSIR images were reconstructed with the Philips IntelliSpace Portal software. 3D-LGE images were reconstructed using the 3D-TRIPS method at the custom-written Matlab software [483]. Infarct size was measured as percentage of the enhanced area to total LV area with the threshold set as full-width-half-max. Signal intensities of the infarcted and non-infarcted areas of LV as well as inside of LV chamber (blood) were measured. Signal intensity ratios (SIR) were calculated between infarcted and non-infarcted area as well as between infarct and blood. Signal-to-noise (SNR) and contrast-to-noise (CNR) were measured in all images.

Our results have shown advantages of using 3D-TRIPS reconstruction vs. standard PSIR method for MR imaging of infarct. First, the acquisition time without acquiring phase reference image was reduced in 1.5-fold. Second, the SIR between infarcted and non-infarcted LV wall was significantly higher for 3D-TRIPS images, 1.50 ± 0.13, compared to 1.10 ± 0.08 in PSIR ($p<0.001$, Table 9). Third, PSIR images often suffer from the poor contrast between infarct and blood; however, 3D-TRIPS provided higher SIR, 1.10 ± 0.08, than 1.01 ± 0.01 in PSIR ($p<0.001$), which enable better visualization of endocardium and differentiation it from blood. Infarct size measurements between 3D-TRIPS and PSIR were similar, 14.10 ± 2.81% in 3D-TRIPS and 14.25 ± 4.33% in PSIR; however, the standard deviation was higher in PSIR

measurements. The SNR for 3D-TRIPS processed images was lower than in 2D-PSIR, which might be related to higher sensitivity of 3D-TRIPS technique to the presence of magnetic field inhomogeneities. Examples of the non-human primate's heart reconstructed with 3D-TRIPS and PSIR are shown in the Figure 75.

Table 9. Comparison 3D-TRIPS and 2D-PSIR images of the infarcted monkey heart (n=10).

	Infarct size, %	SI infarct	SI LV	SI blood	SIR infarct/LV	SIR infarct/blood
3D-TRIPS	14.10 ± 2.81	2959 ± 526	1982 ± 321	2705 ± 463	1.5 ± 0.13 #	1.10 ± 0.08 #
PSIR	14.25 ± 4.33	2311 ± 91	2062 ± 50	2289 ± 91	1.12 ± 0.05	1.01 ± 0.01

All values are shown as means ± St. Deviation. # marks statistically significant difference between groups, $p<0.001$ (t-test for independent variables).

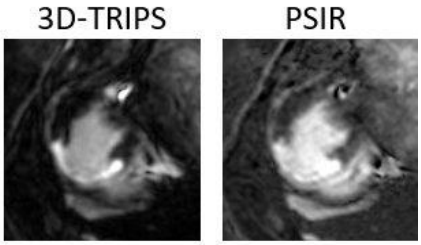

Figure 75. Example of the short axis images of the infarcted non-human primate heart processed in 3D-TRIPS and 2D-PSIR.

3D-TRIPS used a 1-RR acquisition scheme that may reduce the probability of the subject's movement and eliminate the chance of artifact propagation from a phase-reference scan. If higher 3D-TRIPS SNR is desired, a 2-RR repetition time (time between inversion pulses) can be used; it still will eliminate complications associated with a reference scan, such as artifact propagation. There are couple of disadvantages of this method. 1) 3D-TRIPS cannot separate the phase introduced by tissues with a chemical shift relative to water from other phase sources. Fat has a chemical shift of 3.5 ppm relative to water and thus could introduce phase errors in the reconstruction. 2) 3D-TRIPS was developed based on the assumption of a spatially smooth background-phase map. This assumption, however, may not be valid in regions with poor magnetic field homogeneity. There were noticed artifacts in the processed 3D-TRIPS images of the non-human primate's heart related to the presence of the implanted wires or recent surgery.

In summary, this is the first application of the recently developed 3D-TRIPS reconstruction method to the infarcted heart imaging. The new technique not only shortens scan time by almost 2-folds, but also improves image quality and robustness of infarct detection by improving contrast between infarcted and non-infarcted areas of LV as well as

between scar tissue and blood. The scan time shortening is critical for patients and animals with severe heart damage, where prolonger anesthesia cannot be tolerated.

4.6. Specific Aim 6

To explore the feasibility of visualization and quantification of the cardiac grafts by overexpressing MRI gene-reporter ferritin.

Current methods of studying cell engraftment rely on postmortem histological sampling. There is a lack of suitable imaging technology for serial non-invasive tracking of therapeutic cell after their engraftment. Cells have to be labeled in the order to be visualized after transplantation. The standard cell labeling strategy is using superparamagnetic iron oxide nanoparticles (SPIOs) for detection with MRI [237, 282]. However, the MRI signal hypointensity caused by particles does not reflect the actual cell number after several rounds of cell division due to particle dilution. MRI signal from SPIOs does not represent live cells; particles released from dead cells can be phagocytosed by host cells, thereby misleading MRI tracking [260, 261]. Both of these reasons preclude monitoring of long-term stem cell engraftment. Molecular tagging of graft cells by overexpression of non-toxic MRI-detectable probes, such as the iron-binding protein, ferritin, is an alternative approach that may solve the cell tracking problem [224, 336]. The use of reporter genes for MRI-based cell tracking offers two important advantages over particle-based techniques: 1) gene expression is correlated much more tightly with cell viability than is particle retention; and 2) when integrated into the genome, transgene based reporters are much less susceptible to signal loss through cell division and therefore are uniquely suited for longitudinal monitoring of cell transplants.

The unique structure and properties of ferritin make it valuable as an MRI reporter. Ferritin is the main intracellular iron storage protein and has a globular structure 12 nm in diameter, accumulating significant amounts of hydrous ferric oxide iron in its core [310]; therefore, ferritin can be considered as an “endogenous nanoparticle”. The protein shell isolates iron from the cytoplasm, preventing elevation of hydroxyl radical formation [289, 307]. It has been shown that ferritin overexpression can be detected by MRI in C6 glioma tumors [223], used for *in vivo* studies in the mouse brain [336, 346] and for imaging of subcutaneous inoculation of undifferentiated mouse embryonic stem cells [344]. The potential of using ferritin overexpression for non-invasive imaging of cells transplanted into infarcted heart has not been explored. This study aimed to develop a genetically-based technique for molecular imaging of ferritin-tagged cells transplanted into infarcted rodent hearts. Our principal

hypotheses for this study were: 1) ferritin overexpression is non-toxic for transduced cells, i.e. it does not affect cell viability, proliferation or differentiation; 2) ferritin overexpression in transduced cells is detectable by MRI *in vitro* and *in vivo* after transplantation into infarcted murine heart; 3) tagging of transplanted cells by ferritin permits accurate quantification of graft size in the heart.

Ferritin expression vector design

The murine ferritin heavy-chain cDNA with an HA (influenza hemagglutinin) epitope tag (HA-ferritin) was obtained from Dr. Neeman and Dr. Cohen at the Weizmann Institute, Israel [223]. BamHI and HindIII double digestion was used for identifying of HA-ferritin presence in the pGEM-T vector (figure 76).

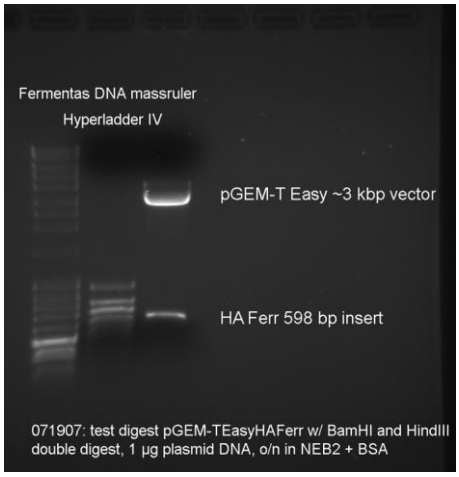

Figure 76. Test-digestion of the pGEM-T plasmid using BamHI and HindIII restriction enzymes to identify the vector backbone (pGEM-T Easy 1 kbp and HA-Ferritin insert ~600 bp. Two DNA ladders were used Fermentas DNA massruler and Hyperladder IV). Electrophoresis in 1% agarose.

HA-ferritin insert was released from pGEM-T vector backbone using EcoRI restriction sites and was then ligated into the pcDNA3 vector plasmid downstream of the cytomegalus virus (CMV) promoter, thus enabling strong transgene expression and selection of stably transduced cells via neomycin (G418) resistance. DNA sequencing confirmed fidelity of the construct. Mouse C2C12 myoblasts were used as a test system to develop the ferritin tagging system. C2C12 cells were transfected with pcDNA3-HA-ferritin cDNA using FuGENE6 reagent and cells were cultured on gelatin-coated tissue culture dishes in growth medium (DMEM, Invitrogen) supplemented with 20% fetal bovine serum (HyClone, Logan, UT), 2 mM L-glutamine (Invitrogen) and penicillin/streptomycin. Neomycin (G418) was added to the cell culture media at 1.2 mg/mL to select for stably transduced cells. G418-selected colonies were trypsinized, replated as mixed mass cultures and maintained in G418 containing growth

media until use. C2C12 subclones were created by dilute plating of cells and isolation of the subclones using cloning rings.

Ferritin over-expression did not affect C2C12 proliferation and differentiation into the multi-nucleated myotubes. C2C12 differentiation was induced using a myogenic differentiation protocol where growth media is replaced by DMEM containing 5% horse serum. Myosin heavy chain was visualized using monoclonal anti-fast skeletal myosin heavy chain antibody MY32 (1:400 dilution). Strong expression of the ferritin has been confirmed with Western Blot using primary antibodies: anti-HA mouse non-conjugated monoclonal antibody (1:1000; Covance, Inc., Emeryville, CA), and rabbit non-conjugated monoclonal anti-ferritin antibody (1:2000; Abcam Ltd., Cambridge, MA); secondary antibodies horseradish peroxidase–conjugated goat anti-rabbit antibody (ferritin detection), sheep anti-mouse antibody (HA-tag detection), 1:5000 dilution in TBS-T. Prussian Blue staining is a sensitive technique for iron detection; it confirmed significant accumulation of iron in the cytoplasm of transduced cells after iron supplementation of the media, whereas no blue cells were observed in iron-supplemented WT controls. Thus, significant overexpression of ferritin was achieved with increased iron-storage capacity. We noticed that supplementation of cell media with iron citrate in high doses (1 mM) reduced the expansion of both wild type C2C12 and transduced cells. However, high iron concentration in the cell media was more toxic for the wild type cells than for cells overexpressing ferritin ($p<0.05$). This indicates an advantage for proliferation and/or survival of the ferritin-expressing cells in the presence of high levels of iron.

Measurements of T_2 relaxation time by MRI in cell samples

To test the capability of MRI to detect ferritin overexpression, T_2 relaxation times were measured in suspensions of wild type (WT) and ferritin-transduced C2C12 cells cultured with and without ferric citrate supplementation (1 mM for 48 hours). $6x10^7$ cells of each type were imaged alive in Eppendorf tubes in 300µl of 2% agarose and in 1 ml of media. T_2 measurements were obtained from a single slice aligned through the center of the live cell pellets on a 3T Achieva Philips scanner with a custom-built solenoid coil. A multiple spin-echo pulse sequence with 32 equally spaced echoes (10 msec echo spacing) and repetition time TR 5000 msec was used. A T_2 map was reconstructed from variable TE images by pixel-based fit of a single-exponential signal equation: $I = I_0 e^{-TE/T2}$, where I was the signal intensity, proton density (I_0) and T_2 were fitted parameters. T_2 values were measured from the T_2 map in

homogenous regions-of-interest placed in the center of each sample. T_1 values of the cell samples were measured using inversion-recovery sequence with 12 inversion times (TI) in a range 50-4000 ms, TE 9 msec and TR 6000 msec.

The ferritin overexpressing cells were readily detectable by MRI *in vitro*, yielding significant changes in T_2 compared to WT cells (figure 77). T_2 of transgenic cells decreased by ~25% compared to non-modified control cells (500 msec and 629 msec, respectively). Supplementation of growth media by ferric citrate caused additional shortening of T_2 with further amplification of the difference between WT and transgenic cells (467 msec in control and 259 msec in the transgenic cells).

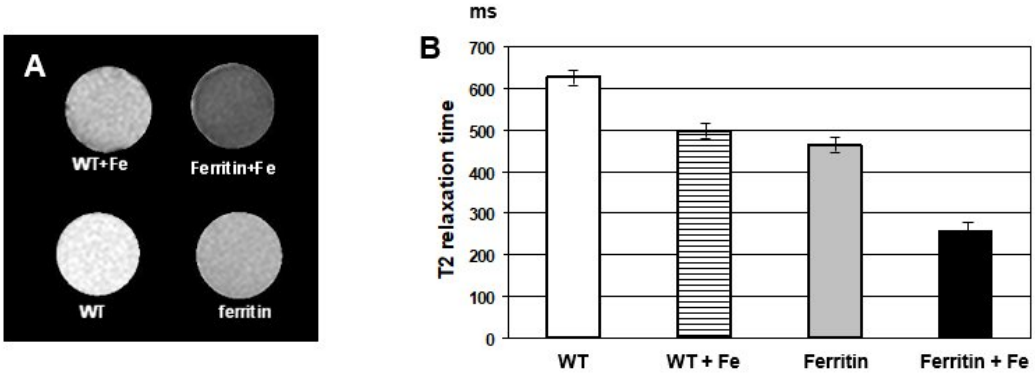

C

	WT C2C12 control, no Fe	WT C2C12 + Fe citrate	Transfected C2C12, no Fe	Transfected C2C12 + Fe
T2, ms	629 ± 4	500 ± 4	467 ± 3	259 ± 4
T1, ms	2858 ± 39	2588 ± 15	2705 ± 24	1985 ± 25

Figure 77. *In vitro* MRI of wild type (WT) and transgenic C2C12 overexpressing ferritin. **A**: Transverse relaxation (T_2) map of WT cells and C2C12 transduced by pcDNA3-HAferritin construct with and without iron supplementation (Fe:1 mM). **B**: Quantification of changes in T_2 relaxation time of WT C2C12 and cells transduced by pcDNA3-HAFerritin with and without iron citrate supplementation. Error bars indicate standard deviation of T_2 within region of interest on the parametric map. **C**: Mean T_1 and T_2 values of the cell samples ± SD.

Cell injection into the infarcted mouse heart and MRI.

To validate the hypothesis that ferritin overexpression is suitable as a MRI reporter for non-invasive imaging of grafted cells, we transplanted wild type and ferritin-overexpressing myoblasts into the infarcted hearts of syngeneic C3H mice. The C2C12 myoblast line was originally derived from the C3H mouse [378] and, therefore, we chose this mouse strain as recipient to minimize immunological rejection of engrafted cells. Myocardial infarction was modeled by permanent ligation of the left anterior descending artery. 150,000

or 500,000 C2C12 cells suspended in 7µl of serum/antibiotics-free medium were directly injected into the border of infarcted region of the left ventricle. Six C3H mice received 150,000 cells ferritin-tagged cells, 13 syngeneic C3H mice received 500,000 C2C12 cells overexpressing ferritin and 6 animals received wild type unlabeled C2C12 cells (control).

The important part of this work was design of an optimal imaging protocol and evaluation of different MRI sequences as tools for detection and morphological measurements of ferritin-labeled grafts *in vivo*. Toward this overall goal, this study aimed to investigate contrast properties of grafts overexpressing ferritin in bright- and black-blood cardiac imaging sequences similar to those used in human cardiac MRI. Further aims of this study were to quantify MRI signal intensity changes in transgenic grafts overexpressing ferritin in the infarcted mouse heart for the above sequences and to identify an optimal MRI sequence for visualization of ferritin-labeled cardiac grafts.

Three imaging techniques were compared. 1) The standard bright-blood cine gradient-echo (GRE) imaging sequence, which is an essential technique in the majority of cardiac imaging protocols. Based on the choice of the echo time (TE), this technique can enable T_2*-weighted contrast, which is beneficial for graft detection. 2) A widely used black-blood sequence based on the double inversion-recovery (DIR) magnetization preparation [485] combined with fast spin-echo (FSE) signal readout [94]. The DIR blood suppression method achieves effective elimination of the blood signal by applying two consecutive inversion pulses (non-selective and slice-selective) followed by the delay corresponding to the zero-crossing point on the curve of blood magnetization recovery [485]. The DIR-FSE sequence [94] is currently recognized as an essential approach for accurate evaluation of cardiac morphology. 3) The third sequence is a new black-blood imaging method based on the motion-sensitized driven equilibrium (MSDE) preparation, which has been recently improved (iMSDE) [486]. In the iMSDE technique, the blood suppression effect is achieved via generating two consecutive spin echoes in the presence of flow-dephasing gradients, followed by restoring magnetization with a flip-back pulse (Figure 78). The key advantage of the iMSDE technique is its time efficiency, since the preparation period in MSDE requires much shorter time than that in the DIR sequence. It also has been demonstrated that MSDE blood suppression is more effective than DIR for elimination of slow-flow artifacts [487]. For the purposes of this study, the iMSDE technique is of particular interest, since it allows combination with a fast cardiac-gated cine GRE sequence, thus enabling black-blood imaging with T_2*-weighted contrast.

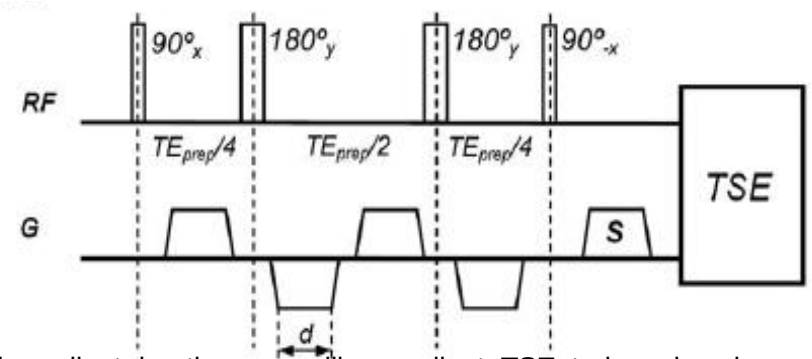

d: gradient duration, **s**: spoiling gradient, **TSE**: turbo spin echo.

Figure 78. Schematic representation of the black-blood improved motion-sensitized driven equilibrium (iMSDE). Figure from [486].

At one month after the surgery, mouse hearts were imaged on a 3T Philips Achieva clinical scanner (42 cm horizontal bore, gradient strength 80 mT/m) and a single-channel solenoid mouse coil (Philips Research Laboratories, Hamburg, Germany) with a built-in heating system maintaining physiological body temperature. To obtain high resolution *in vivo* MR images of the mouse heart, we used ECG-gated proton-density weighted black-blood double inversion-recovery turbo spin echo (PD TSE BB) multislice sequence (TE 10 ms; TR ~ 1100-1200 ms dependent of the heart rate, matrix 248×245; flip angle 90°; field of view 50×50 mm; 4 signal averages, image resolution 202×204 μm). The PD TSE BB sequence allowed clear delineation of the left ventricle borders in the mouse heart and excellent blood suppression.

To detect iron accumulated in the overexpressed ferritin complexes bright- and black-blood T_2*-weighted sequences were tested. Bright-blood imaging was performed using used T_2* weighted cine gradient echo (GRE) multislice sequence (TR/TE = 14/9 msec; slice thickness 1 mm; flip angle 15°; echo train length 1; field of view 50×50 mm, matrix 200×198; 6 signal averages, image resolution 250×250 μm). For black-blood imaging of transgenic grafts a recently introduced [486] improved motion sensitized driven equilibrium (iMSDE) preparative sequence was executed prior to the GRE imaging sequence. The advantage of this MRI sequence for visualization of iron accumulation is the presence of a T_2*-prepulse along with a good suppression of blood flow and improved soft-tissue signal-to-noise and contrast-to-noise ratio values. iMSDE preparation parameters: gradient amplitude 12 mT/m, first gradient moment 500 mT.ms2/m and slew rate 100 mT/(m.ms). The imaging parameters were as follows: TR/TE=16/8ms; flip angle 13°; slice thickness 1 mm, field of view 50×50 mm, 8 signal averages, image resolution 298×303 μm. *Ex vivo* imaging was conducted with 3D

multiple gradient-echo sequence (range 4.9-21.8 msec, echo spacing 4.2 msec); TR 61.8 msec; flip angle 10°; slice thickness 0.5 mm; resolution 197×120 μm; two signal averages.

Both, wild type C2C12 and ferritin-tagged cells successfully grew in mouse hearts and formed skeletal muscle grafts (Figure 79). The presence of transgenic grafts in the infarcted mouse heart was detected by T_2*-weighted MRI as areas of hypointensity caused by accumulation of iron in overexpressed ferritin complexes. Cine MRI techniques did not detect any contractile activity of the area containing skeletal muscle grafts, consistent with previous reports of their lack of electromechanical coupling [160, 188].

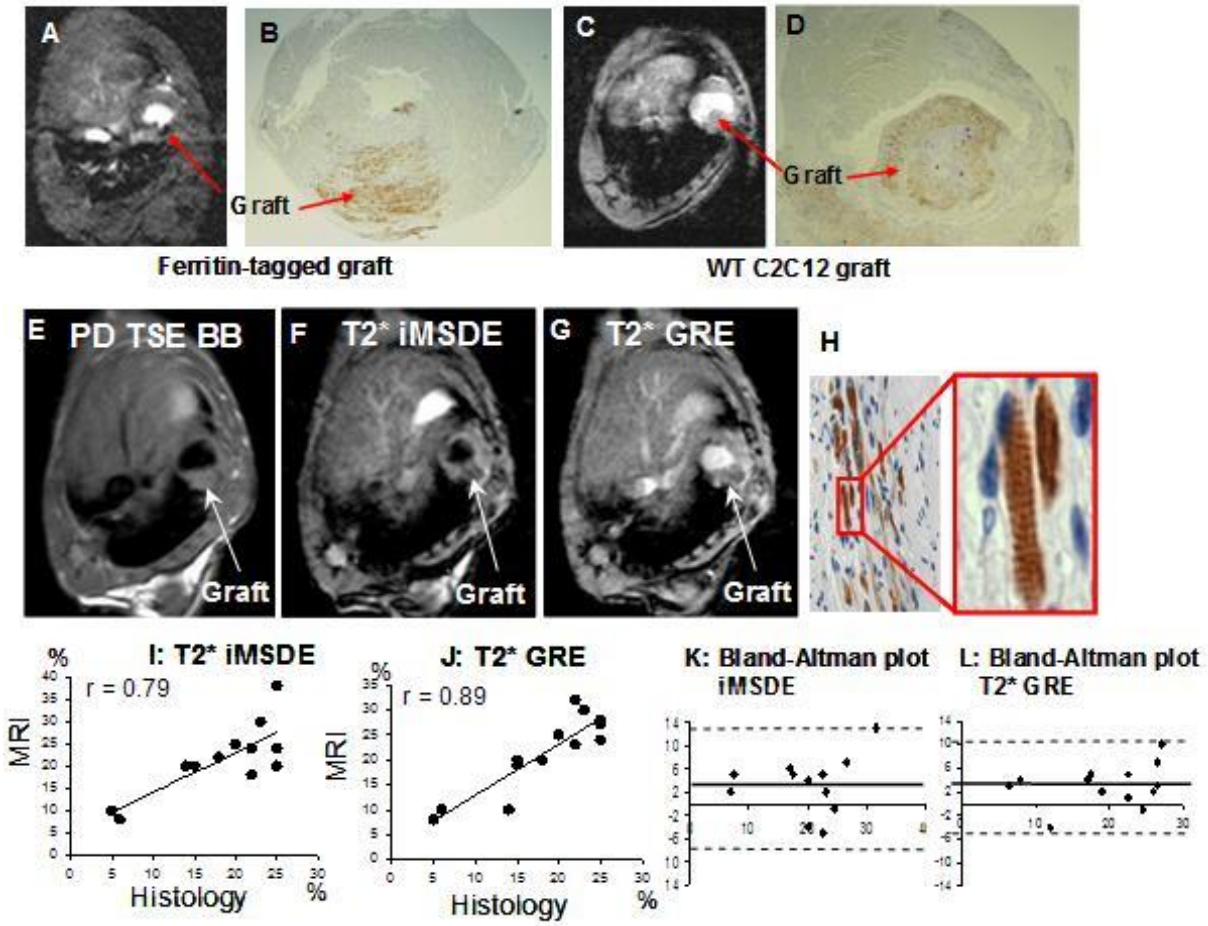

Figure 79. *In vivo* MRI of wild type (WT) and transgenic C2C12 overexpressing ferritin. **A**: Stable signal void T_2*-weighted MRI revealed in the left ventricle indicating presence of transgenic ferritin-tagged graft. Graft localization is confirmed with histology. **B**: Embryonic skeletal myosin heavy chain staining of the mouse heart reveals presence of the large skeletal muscle graft. **C**: Large skeletal muscle graft is well defined as non-contracting invagination into left ventricle chamber of the heart. No signal void is detected by T_2* sequence in the area of wild-type graft. **D**: Areas of calcification are detected in the middle of the large skeletal grafts. **E**: PD TSE BB. F: T2* iMSDE black-blood. **G**: T_2* GRE bright blood. **H**: Graft cells are well differentiated and contain sarcomeres. **I**: Correlation of the graft size measurements between T_2* iMSDE and histology. **J**: Correlation of the graft size measurements between T_2* GRE and histology. **K**: Bland-Altman plot for T_2* iMSDE vs. histology measurements. **L**: Bland-Altman plot for T2* GRE vs. histology measurements. r – correlation coefficient. Solid line on Bland-Altman plots is representing a mean difference of graft size estimated by MRI and histology. Dashed lines represent 1.96% SD of mean differences in measurements.

MRI signal void in the graft area was detected *in vivo* one month after transplantation of transgenic cells overexpressing ferritin (Figure 79A). No signal void areas were detected by MRI in wild type grafts (Figure 79C). Signal intensity ratio (SIR) of the wild-type C2C12 grafts was about 1, i.e., showing no difference from the surrounding myocardium (Table 10). Unlabeled skeletal muscle grafts in the mouse heart could only be detected by MRI as a considerable thickening of the left ventricle wall. No contractile activity was detected in areas of skeletal muscle graft by cine MRI. Embryonic skeletal myosin staining confirmed the presence of skeletal muscle grafts in the left ventricle of mouse heart after transplantation of wild type C2C12 (Figure 79D) as well as ferritin-overexpressing cells (Figure 79B). Graft cells were well differentiated and contained sarcomeric structures (Figure 79H).

To determine the optimal method of imaging the ferritin-overexpressing grafts, we compared graft size measurements using different MRI pulse sequences to the histological graft size as a gold standard. Only T_2*-weighted iMSDE and T_2*-weighted GRE MRI sequences were used for graft size measurements, since the PD TSE BB sequence did not provide sufficient contrast between graft and cardiac tissues. The area of signal hypointensity was measured in each MR image at the short-axis plane of the heart. Graft size was assessed as a ratio of graft area to the left ventricle (LV) in each slice. Average graft-to-LV ratio in mouse hearts 3 weeks after transplantation of 150,000 cells was 9.4% (assessed by MRI) and 13.3% (assessed by histology). The T_2* bright-blood GRE and T_2* black-blood iMSDE sequences provided similar graft size measurements after transplantation of 500,000 cells, with no statistically significant difference detected (21.23±7.81% and 21.85±7.64%, correspondingly, p=0.84). Both measurements were significantly correlated with histology, but a significantly stronger correlation was observed for the bright-blood GRE sequence (r=0.79 for T_2*-weighted iMSDE, and r=0.89 for T_2*-weighted GRE, Figure 79 I, J). Bland-Altman analysis indicated significant bias similar for both sequences (3.3±4.9, p=0.01 for T_2*-weighted iMSDE, figure 39K; and 3.0±3.6, p=0.04 for T_2*-weighted GRE, figure 39L). This bias corresponds to approximately 10-15% overestimation of the graft size by MRI and may be explained by mild (20-30%) changes in contrast of ferritin-tagged grafts or by a slight extension of the region of signal attenuation beyond the anatomical boundaries of the ferritin-tagged grafts.

C2C12 grafts overexpressing ferritin did not change tissue contrast in the PD TSE BB sequence (SIR=1.02). However, MRI signal intensity of ferritin-tagged grafts was significantly reduced when T_2*-weighted GRE and T2*-weighted iMSDE sequences were used for graft

detection (Table 10). Specifically, transgenic C2C12 grafts overexpressing ferritin reduced SIR by 30% in bright-blood GRE (mean SIR=0.7) and by 20% in black-blood iMSDE sequences (mean SIR=0.8). The SIR of transgenic grafts was significantly different from SIR of unlabeled control grafts ($p<0.0001$). All acquired MRI images were characterized by high signal-to-noise ratio, SNR (Table 10). T_2*-weighted GRE images had the highest contrast-to-noise ratio (CNR) among all used sequences ($p<0.0001$).

Table 10. Quantification of signal intensity changes in transgenic C2C12 grafts overexpressing ferritin and in unlabeled wild-type (WT) control grafts.

	WT graft (n=6)			Ferritin-tagged graft (n=13)		
	SIR	SNR graft	CNR graft	SIR	SNR graft	CNR graft
PD TSE BB	1,0 ± 0,1	59,5±7.4	-2,1±5,3	1,0 ± 0,1	46,1±21,1	-1,3±6,6
T_2* iMSDE	1,2 ± 0,4 #	33,2±6,6	-1,8±6,7	0,8 ± 0,2 #**	19,7± 9,9	4,9±4,3
T_2* GRE	1,0 ± 0,1 ##	36,0±4,4	1,5±2,3	0,7 ± 0,1 ##**	29,6±11,5	11,5±5,7 ##

All values shown as mean ± standard deviation.
Statistically significant difference between ferritin-tagged and control groups in SIR measured using the same pulse sequence (independent t-test, unequal variances) is shown as # for $p < 0.05$, and ## for $p < 0.0001$. Statistically significant difference from PD TSE BB in SIR measured in the same animal group (paired t-test) is shown as ** for $p < 0.0001$.

Reproducibility of hypointensity area appearance on bright- and black-blood images provided additional proof of the presence of ferritin-tagged grafts. The areas of signal reduction were reproducible on both image types, and therefore distinguishable from flow artifacts. Our studies showed the persistence of signal void areas in the same short axis slices of the heart *in vivo* and *ex vivo* shortly after sacrificing of the mouse (Figure 80C). Increase of echo time from 4.9 ms to 21.8 ms on ex vivo images revealed a magnetic susceptibility effect of iron accumulation in transgenic graft. However, longer echo time compromised the signal-to-noise ratio (Figure 80, C1-C5).

Ferritin overexpression provided sufficient MRI contrast to make transduced cells detectable *in vitro* and *in vivo* in murine hearts. The optimal MRI protocol for visualization and quantification of ferritin-tagged grafts in the mouse heart should include multiple sequences. The proton density weighted turbo-spin echo black blood (PD TSE BB) sequence provided the highest SNR and excellent blood suppression and was used for high resolution assessment of the mouse heart morphology. However, this sequence was not sensitive for detection of iron accumulation in overexpressed ferritin complexes, and signal intensities of ferritin-tagged grafts and unlabeled wild-type C2C12 grafts were essentially the same. Therefore, the PD TSE BB pulse sequence can only be used for evaluation of heart morphology, not for detection of ferritin-tagged grafts.

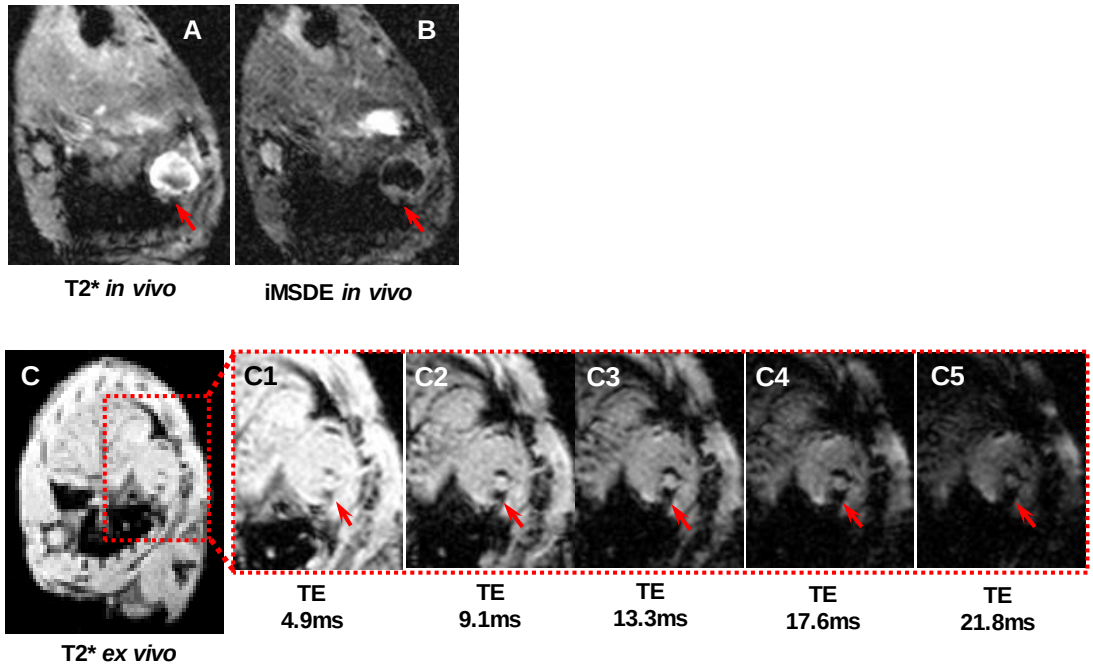

Figure 80. Reproducibility of detection of transgenic ferritin-overexpressing grafts in the infarcted mouse heart. **A:** *In vivo* T2*-weighted bright-blood turbo gradient echo cine sequence, TR 15ms; TE 9.3ms; flip angle 15°; slice thickness 0.8 mm; acquisition voxel size 0.25/0.25mm, reconstruction voxel size 0.10/0.10mm; 6 signal averages. **B:** *In vivo* 2D iMSDE-prepared (improved motion sensitized driven equilibrium) black blood turbo spin-echo pulse sequence: TR 16ms; TE 9.8ms; flip angle 15°; slice thickness 0.8mm; acquisition voxel size 0.26/0.26mm, reconstruction voxel size 0.10/0.10 mm; 10 signal averages. **C:** *Ex vivo* detection of the graft on post-mortem images (10 min after euthanasia) using multiple gradient echoes. Increase of the echo time (TE) makes MR images more T_2*-weighted and thus makes a cellular graft better visible in the mouse heart (arrow). Sequence parameters: 3D gradient echo, TR 61.8ms; FA 10°; slice thickness 0.5mm; acquisition matrix 248×248; 2 signal averages.

Black-blood and bright-blood T_2* weighted MRI sequences were sensitive for detection of transgenic C2C12 grafts overexpressing ferritin. Quantification of MRI signal intensity changes showed 30% reduction of signal intensity in ferritin-tagged areas in T_2* bright-blood GRE images and 20% in T_2* black-blood iMSDE images. Furthermore, MRI allowed morphological graft size measurements with reasonable accuracy and precision, taking into account limitations of the histological approach itself, which may be subject to tissue deformation, shrinkage, and subsequent registration difficulties between imaging and histological sectioning planes

It is important to note that the bright-blood T_2* GRE images provided the highest CNR among all used sequences (Table 10) and enabled more precise graft size measurements. However, this sequence frequently suffers from signal non-uniformity and voids in the ventricles caused by complex flow patterns. It is advisable therefore to use bright-blood T_2*-weighted GRE images in combination with black-blood images, allowing reliable localization

of the cardiac wall. The use of a black-blood T_2*-weighted technique could potentially provide an all-in-one solution, enabling both morphological information and the capability of graft measurements based on tissue contrast properties. However, graft contrast and precision of graft size measurements by the iMSDE black-blood sequence appeared inferior to those from the bright-blood sequence. This might be associated with a lower SNR for this sequence (Table 10). An iMSDE preparative sequence has been proposed for highly efficient blood signal suppression. This method has been shown to considerably improve the quality of blood suppression as compared to the standard double inversion-recovery technique, while enabling much better time-efficiency. However, iMSDE produces a rather strong effect on the static tissue signal, mainly due to the T_2-weighting effect introduced by this preparative sequence. While SNR loss in the iMSDE sequence appeared critical for morphological measurements in the current experimental setup (mouse imaging on a human whole-body scanner), this sequence also showed a good potential for graft imaging as evidenced by a significant signal decrease caused by ferritin and the clear visibility of grafts.

Since transverse MRI relaxivity of ferritin is much higher than its longitudinal relaxivity, we were able to detect ferritin-tagged cells using T_2*-weighted bright- and black-blood image sequences in a clinical 3T scanner. It has been shown that transverse relaxivity ($1/T_2$) linearly increases with increase of field strength; therefore, we would expect more effective visualization of ferritin-tagged grafts in higher magnetic field strength. Natural iron storage protein ferritin will be useful for noninvasive long-term monitoring of transplanted cells into the infarcted heart. It has been shown that overexpression of the ferritin H-chain induces expression of the transferrin receptor and increases iron uptake [318]. Therefore, there are natural mechanisms that shift the iron pool the into ferritin bound storage form; this restores iron homeostasis and prevents iron cytotoxicity. Transgenic cells overexpressing ferritin are characterized by increase of iron content as well as by up-regulation of transferrin receptors [344]. These data indicate that ferritin overexpression can effectively tag cells transplanted into the heart. Potential future applications of this technique include studying the dynamics of adult or pluripotent stem cells after transplantation.

One limitation of ferritin-based imaging of tissue grafts, which generally pertains to any cell labeling strategies based on negative contrast, is that the signal void caused by iron accumulation is almost indistinguishable from that caused by hemosiderin. In normal conditions, ferritin provides a natural rapid mechanism to sequester excess iron intracellularly

in a dispersed soluble form preventing elevation of hydroxyl-radical formation [289, 307]. With further increases in cytosolic iron, ferritin is collected in lysosomes [321], where the ferritin shell denatures and the iron core aggregates in insoluble masses of hemosiderin for long-term storage [488, 489]. Under pathological conditions, the total amount of tissue iron can increase, and the proportion stored as hemosiderin rises, while the capacity of ferritin to store iron is overwhelmed [303]. Therefore, overexpression of ferritin in transplanted cells might have a protective effect as a quick mechanism to prevent toxic effects of free iron in damaged tissues. However, the challenge for imaging of ferritin-tagged grafts is to distinguish their MRI signal changes from iron deposited in hemosiderin.

In this study, we occasionally observed hemosiderin deposition in the infarcted myocardial tissue of animals receiving WT cells; those areas were distinguishable by MRI as areas of hypointensity. This effect might be caused by enhanced ferritin content or by hemosiderin deposition in damaged tissue [490, 491]. We compared localization and size of the signal void areas in MRI with histological data determining localization of C2C12 graft (embryonic myosin staining) and hemosiderin deposition (Prussian blue staining). In most of the studied cases large morphologically distinct skeletal muscle grafts were spatially isolated from areas of hemosiderin deposition; therefore signal void caused by hemosiderin did not affect SIR measured in C2C12 graft. In future studies, however, careful interpretation of the areas of signal void must be provided, especially for small grafts that cannot be precisely identified by a known anatomical location. New technical approaches, such as analysis of non-monoexponential signal decay [492, 493] or phase-contrast imaging [494] might be helpful to distinguish different sources of signal void, though more research is necessary to identify the possibility of their applications *in vivo*.

In summary, this is the first use of MRI for detection of ferritin gene expression in cardiac grafts. The major findings are: 1) stable overexpression of ferritin in C2C12 mouse skeletal myoblasts is feasible; 2) ferritin overexpression does not affect cell viability, proliferation or differentiation; 3) ferritin-tagged cells are detectable by MRI *in vitro*, yielding significant changes in signal intensity compared to wild-type cells; 4) the presence of transgenic grafts in the infarcted mouse heart can be detected by MRI as areas of signal hypointensity; 5) graft size assessed by MRI correlates well with histological measurements; 6) the optimal MRI pulse sequences were determined for visualization of ferritin-labeled graft;

and 7) *in vivo* MRI signal properties of cardiac grafts overexpressing ferritin were quantitatively assessed at the 3T clinical scanner.

4.7. Specific Aim 7

To compare the standard nanoparticle-based cell labeling methods with expression of MRI gene reporters for longitudinal tracking of transplanted cells in the infarcted heart.

MRI is often used as a tool for non-invasive serial imaging of transplanted cell migration and engraftment. Typically labeling of cells prior transplantation is required for discrimination of graft from the surrounding host tissue. The most robust method of cell labeling for MRI detection is loading of cells with synthetic superparamagnetic nanoparticles (10-200 nm diameter) containing high concentrations of iron oxide inside of the shell composed of dextran or other bio-compatible materials. These nanoparticles can be easily delivered to cells in culture dish with or without use of transfection reagents and accumulated in cytoplasm without altering cell viability and function. The presence of iron causes local disturbance of the magnetic field in the area of injected cells that can be detected by MRI as areas of hypointensity (that is, dark) in T_2* weighted images.

Another way of cell tagging is genetic overexpression of the endogenous protein ferritin. MRI relaxivity increases with increased iron uptake by ferritin [340, 341, 495]. Importantly, there is no essential dependence of ferritin-based MRI contrast on exogenous substrate administration [223, 224]. Some studies however suggest that exogenous iron supplementation increases MRI signal hypointensity of ferritin-expressing tissues [343]. No direct comparison between cells labeled by iron oxide particles and cells overexpressing ferritin was done so far to determine efficacy of MRI to detect live transplanted cells. Previously we have demonstrated the feasibility of MRI detection of cardiac grafts overexpressing ferritin and identified the optimal MRI sequences for detection and morphological measurements of ferritin-labeled grafts in rodent heart *in vivo* (part 4.6 of the dissertation). Purpose of this study was to compare two labeling techniques, iron oxide particles versus genetic manipulations leading to ferritin overexpression, for MRI detection of transplanted cell survival in the infarcted heart.

C2C12 cells were labeled by overnight co-cultivation with superparamagnetic iron oxide particles (Bangs Laboratories, Fishers, IN). The particles have size 1.63 μm and

composed of 42.5% magnetite and a fluorescent dye Dragon Green (excitation/emission 660/690 nm). The particles were directly added to C2C12 media at 1:1000 dilutions from the commercial stock without use of transfection reagents. In parallel, other C2C12 cells were genetically modified to overexpress endogenous ferritin, as described in the part 4.6. Viability of mouse myoblasts was evaluated with every passage by Trypan Blue exclusion assay; almost 100% of the cells remained viable after labeling by either particles or ferritin. Prussian blue staining confirmed iron accumulation in cytoplasm after C2C12 labeling with iron oxide particles and in cells overexpressing ferritin. Western blot with a rabbit monoclonal antibody specific to ferritin detected high levels of ferritin in transduced cells, but not in wild type control. Both particle-labeled and ferritin-tagged mouse skeletal myoblasts were well differentiated into myotubes. No difference in differentiation pattern or timing was found.

45 C3H mice were included in the study (weight 20-25 g). $5x10^5$ C2C12 cells suspended in 7 µl of serum/antibiotics-free medium were injected into the border of infarcted region of the left ventricle of the mice. Two groups of animals received live C2C12 cells: first group received wild type C2C12 cells labeled with iron oxide particles (n=10); second group received live C2C12 genetically modified to overexpress ferritin (n=13). Along with live cell transplantation, other two groups of mice were injected with dead C2C12 cells (cells were killed by repeated freeze-thaw cycles): one of those groups received wild-type C2C12 previously labeled in culture with iron oxide particles (n=12), other group received transgenic cells overexpressing ferritin (n=10). C2C12 cells labeled with ferritin and iron oxide particles were injected at the same day to different animals to minimize the study variability.

MRI detection of live ferritin- and particle-tagged grafts in the mouse heart.

Wild-type C2C12 cells labeled by iron oxide particles as well as transgenic C2C12 cells overexpressing ferritin and transplanted alive to the infarcted mouse heart formed large skeletal muscle grafts detected by MRI as significant thickening of the left ventricle wall (Figure 81). The presence of the live grafts was confirmed by immunostaining for embryonic skeletal muscle myosin heavy chain (Figure 81F, K, M). Live C2C12 grafts labeled by particles and by ferritin were detected in T_2*-weighted GRE sequences as dark areas of signal hypointensity in the left ventricle wall of the mouse heart (Figure 81, red arrows).

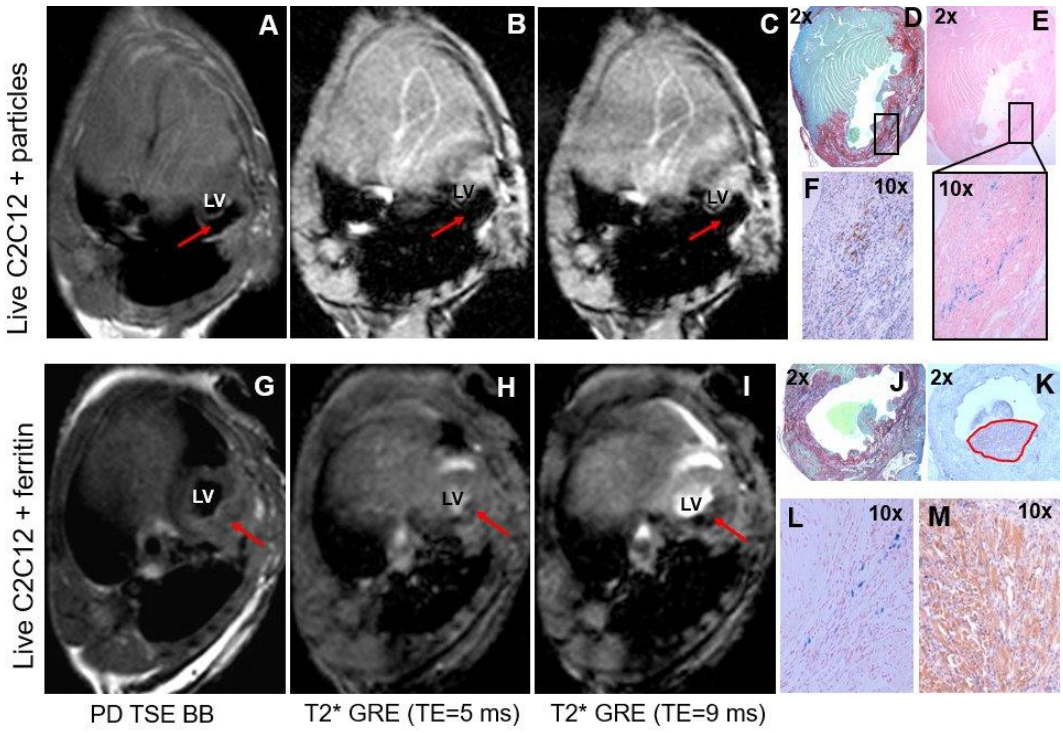

Figure 81. *In vivo* MRI identification of the live transplanted cells labeled by iron oxide particles (top) or transgenic C2C12 overexpressing ferritin (bottom). Red arrows point to the graft area in the left ventricle of the mouse heart. A-F: Live C2C12 graft labeled with iron oxide particles. G-M: Live transgenic C2C12 graft overexpressing ferritin. A and G: PD TSE black-blood MRI sequence. B and H: T2* GRE black-blood sequence with TE 5 ms. C and I: T2* GRE bright-blood sequence with TE 9 ms. D and J: Picrosirius red (collagen-specific)/fast green staining to define the infarct zone. E (with magnification) and L: Prussian blue staining depicting iron accumulation in cardiac tissue. F, K and M: Embryonic skeletal myosin heavy chain staining to identify C2C12 graft. Black rectangle (in D) shows matching area of iron accumulation (E) and graft location (F).

Graft-to-myocardium signal intensity ratio (SIR) in the live transgenic grafts overexpressing ferritin was 0.71±0.13 at the T_2* weighted GRE, which corresponds to 30% MRI signal decrease (Table 11). The longer TE of 9 msec visualized iron accumulated in overexpressed ferritin complexes better than a 5 msec TE (figure 81H, I). Live grafts overexpressing ferritin did not cause signal intensity change in PD TSE BB images (SIR 1.02±0.14).

Live C2C12 graft labeled with iron-oxide particles caused greater signal intensity change in T_2*-weighted GRE sequences: MRI signal decreased up to 80% (SIR=0.23±0.08, figure 81A-C). The difference in signal intensity between ferritin-tagged and particle-labeled grafts was statistically significant ($p<0.001$). A 50% signal decrease caused by presence of iron oxide particles was detected also in PD TSE BB images (SIR 0.48±0.20).

Table 11. *In vivo* imaging properties of iron-oxide particle labeled C2C12 grafts and grafts overexpressing ferritin in the mouse heart.

Studied groups	PD TSE BB			T2* GRE		
	SIR	SNR	CNR	SIR	SNR	CNR
Live C2C12+ferritin (n=13)	1.02±0.14	48.25±21.91	-1.59±6.47	0.71±0.13^	28.88±12.33	11.27±5.59^
Dead C2C12+ferritin (n=10)	1.05±0.06	63.74±8.51	-3.35±3.68	0.96±0.11^	34.99±4.17	1.74±4.22^
Live C2C12+particles (n=10)	0.48±0.20 *	13.60±7.02	14.25±5.21	0.23±0.08 *	4.05±2.06	13.12±3.15
Dead C2C12+particles (n=12)	0.55±0.20 #	11.46±5.68	8.86±4.02	0.22±0.08 #	3.08±1.42	11.02±3.06

Abbreviations: CNR, contrast-to-noise ratio; GRE, gradient echo; PD TSE BB, black-blood proton density weighted turbo spin echo; SIR, signal intensity ratio; SNR, signal-to-noise ratio. All values are shown as mean ± SD. * Statistically significant difference between ferritin-live and particle-live graft in SIR measured using the same pulse sequence (independent t-test, unequal variances): $p<0.0001$.
Statistically significant difference between ferritin-dead and particle-dead groups in SIR measured using the same pulse sequence (independent t-test, unequal variances): $p<0.0001$.
^ Statistically significant difference between ferritin-live and ferritin-dead groups in SIR and CNR measured using the same pulse sequence (independent t-test, unequal variances): $p<0.0001$.

Change in MRI contrast after injection of dead ferritin- and particle-labeled cells

The injection of dead cells pre-labeled with iron-oxide particles also caused strong signal void effect; graft-like areas were detected in the left ventricle of the mouse heart with no live graft present (Figure 82A-C). T_2* signal attenuation in dead particle-labeled C2C12 group resembled signal void effect of the live particle-labeled grafts (SIR=0.22±0.08 and 0.23±0.08, correspondingly, $p>0.05$). Dark areas in the left ventricle were also detected in PD TSE BB images (SIR 0.55±0.20).

In contrast to injection of dead C2C12 cells pre-labeled with iron-oxide particles, injection of dead transgenic C2C12 genetically modified to overexpress ferritin did not cause MRI signal intensity change in any slice of the left ventricle (SIR 1.05±0.06 in PD TSE BB and 0.96±0.11 in T_2*-weighted GRE, difference in SIR with cells labeled by dead particle was statistically significant). All acquired images were characterized by high SNR and CNR ratio (Table 11).

There was a statistically significant difference in SIR and CNR between ferritin-live and ferritin-dead groups ($p<0.0001$). The same assessment did not show any difference in SIR and CNR between particle-live and particle-dead groups (Table 11). This emphasizes high specificity of MRI signal hypointensity caused by ferritin overexpression to identify live transplanted cells, while artificial iron oxide particles cannot distinguish live and dead graft.

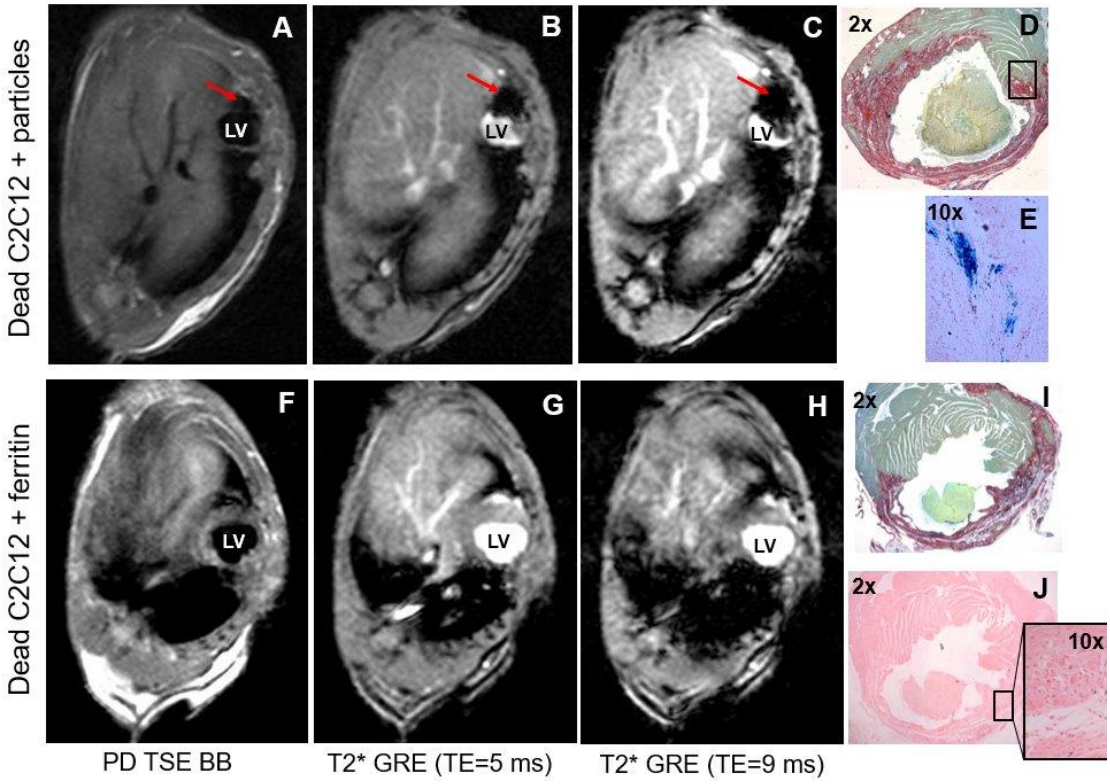

Figure 82. MRI identification of the dead injected cells labeled by iron oxide particles (top) or transgenic C2C12 overexpressing ferritin (bottom). The injection of dead cells pre-labeled with iron-oxide particles caused strong signal void effect (red arrows); in contrast, injection of dead transgenic C2C12 genetically modified to overexpress ferritin did not cause MRI signal intensity change. **A-E**: pre-labeled with iron oxide particles C2C12 cells, injected dead. **F-I**: transgenic C2C12 ferritin-tagged, injected dead. **A** and **F**: PD TSE black-blood MRI sequence. **B** and **G**: T2* GRE black-blood sequence with TE 5 ms. **C** and **H**, T2* GRE bright-blood sequence with TE 9 ms. **D** and **I**: Picrosirius red (collagen-specific)/fast green staining to define the infarct zone. **E**: Positive Prussian blue staining depicting iron accumulation in myocardial tissue after injection of dead C2C12 cells prelabeled with iron oxide particles. **J**: Negative Prussian Blue staining after injection of dead transgenic ferritin-tagged C2C12.

In this study, two methods of cell labeling for MRI detection of transplanted cell survival in the infarcted heart were evaluated: exogenous paramagnetic iron oxide particles and genetic overexpression of the endogenous iron storage protein ferritin. Both particle-labeled C2C12 and transgenic myoblasts overexpressing ferritin survived well after transplantation to the infarcted mouse heart and were visualized by MRI as significant thickening of the left ventricle wall in proton density weighted black blood pulse sequence. Live labeled C2C12 grafts were also detected by T_2* weighted gradient echo sequence as areas of signal hypointensity. Not surprisingly, grafts labeled by iron oxide particles exhibited very strong effect on T_2* GRE decreasing signal intensity up to 80%, while transgenic grafts overepressing ferritin moderately decreased signal intensity by 30%. Grafts labeled by iron oxide particles also decreased signal intensity in PD TSE BB images by 50%.

Series of experiments with injection of dead cells that were particle-labeled or ferritin-tagged before performing repeated freeze-thaw cycles showed MRI signal void caused by iron accumulation persistance after cell death. The pattern of signal persistence 4 weeks after injection of dead cells pre-labeled with iron oxide particles was similar to that in live particle labeled graft. In spite of the fact that dead cells do not form grafts, false-positive MRI signal depicted areas of iron oxide particles localization in myocardium and size of those areas extended beyond left ventricle boundaries (figure 82 B, C).

In contrast to particle labeled cells, dead transgenic cells overexpressing ferritin were not detected by T_2* weighted MRI sequences. This important finding suggests that genetically based expression of natural iron storage protein ferritin has advantages for live cell imaging over the standard cell labeling approach with artificial iron oxide particles. Despite of the lower signal void effect on MRI from the ferritin-tagged graft the signal void areas represent live transplanted cells with functioning DNA; conversely, the strong signal from iron oxide particles does not represent live cells, but image particle location instead. In addition to ferritin's advantages in detecting viable cells, iron oxide particles are diluted with each round of cell division while the integrated ferritin transgene is expressed in each daughter's cell.

Studies by other research groups also suggest that iron oxide particles are not a reliable marker to monitor transplanted stem cell location and survival. Amsalem et al showed that after engrafted cell death enhanced MRI signals arise from cardiac macrophages that engulfed the iron oxide particles [260]. Terrovitis et al described cardiac-derived stem cells transplantation into intact rat heart [261]. Despite detectable MRI signal in the xenogeneic model, there were no surviving cells by histology and the source of detectable MRI signal was cardiac macrophages. Our study shows that ferritin overexpression shows a difference in MRI signal between live and dead transplants suggesting that genetic labeling is a better option for stem cell tracking than use of exogenous iron oxide nanoparticles.

The main limitation of this study is the lack of serial imaging (only one MRI exam one month after cell transplantation); therefore, we were not able to follow transplanted cells over time. It is also unknown how quickly ferritin-based MRI signal would fade and disappear if transplanted cells die in the host tissue, or vice versa, how quickly ferritin complexes in proliferating graft can accumulate endogenous iron to be detectable by non-invasive imaging. Live ferritin cells detection by MRI at the time of cell transplantation can be improved by pre-incubation in iron-rich media prior to transplantation. In contrast to dead cells, live ferritin

overexpression leads to increased iron accumulation in transplanted cells thereby result in increasingly better visualization. In this study MRI was conducted 4 weeks after transplantation. A serial study is required to demonstrate the increased iron accumulation by ferritin and remains to be demonstrated in forthcoming studies.

In conclusion, this study demonstrated a dramatic discordance between MRI signal persistence and viability of grafted cells labeled by iron oxide particles before transplantation. Thus, use of iron oxide nanoparticles only provides particle localization rather than imaging of cell survival and engraftment. In contrast, genetically based cell tagging, such as ferritin overexpression, despite the lower signal intensity in comparison with iron oxide particles, represent live transplanted cells.

5. CONCLUSION

The current work created a technological infrastructure, based on the state-of-the-art approaches in physics and biophysics, enabling non-invasive studies of heart morphology, physiology and metabolism in small and large laboratory animals using magnetic resonance imaging and spectroscopy. Specific developments included engineering of the specialized radiofrequency coils for cardiac imaging and spectroscopy studies on animals; modification of the existent pulse sequences and new developments for animal imaging and transplanted cell tracking; usage of the additional equipment for ECG/respiratory monitoring on small animals and triggering of MRI acquisitions; right choice of the anesthesia methods and maintenance of the physiological conditions.

Physical and technological developments of this work played key role in multiple biomedical projects involving non-invasive studies of the heart in different animal species. Specifically, novel data on the infarcted heart regeneration after human cardiomyocyte transplantation into the infarcted heart of rodents and non-human primates has been obtained using the biophysical and bioengineering approaches developed during this work. The recovery of the heart contractile function was more apparent in the non-human primates in comparison with the rodents, which is likely due to the greater physiological match between human and non-human primates. These findings created a foundation for transplantation of human cardiomyocytes to patients.

The geometric, functional and energetic consequences of post-myocardial remodeling were non-invasively characterized in a murine model of heart failure as well as possibility of pharmacological correction of the myocardial damage. Further directions include ^{31}P magnetic resonance spectroscopy studies of myocardial energy metabolism after human cardiomyocyte transplantation to the heart of large animals and humans.

A novel physiologically meaningful method for quantifying myocardial perfusion by cardiac MRI has been developed based on the kinetic modeling of the contrast agent dynamics in the myocardial tissue. The discrete kinetic model was implemented into a custom quantitative perfusion analysis package programmed in Matlab. The algorithm enables automatic extraction of the arterial input function and coefficients of the contrast agent uptake and retention in tissues. The global differences in the perfusion characteristics of the non-human primates' heart after infarction and in a dog model of Duchenne muscular dystrophy has been shown with the developed model. Analysis of contrast agent perfusion by MRI shows

potential for the study of myocardial perfusion in the assessment of cell transplantation benefits.

Developed methods of quantitative evaluation of myocardial structure, perfusion and metabolism enable longitudinal non-invasive studies of heart on animals and potentially on humans. Novel postprocessing method, 3D-TRIPS, has been used for the first time to evaluate myocardial scar in large animals. The new technique not only shortens scan time by almost 2-folds, but also improves image quality and robustness of infarct detection by improving contrast between infarcted and non-infarcted areas of LV as well as between scar tissue and blood. The scan time shortening is critical for patients and animals with severe heart damage, where prolonger anesthesia cannot be tolerated.

To follow the transplanted cell fate and to measure graft size non-invasively, MRI gene-reporter ferritin has been used in cardiac applications for the first time. Genetic modification of the cells for ferritin over-expression enables visualization of transgenic cells *in vitro* and *in vivo*, evaluation of graft size and viability. Advantage of the genetic tagging over the standard nanoparticle-based cell labeling technique is the correspondence of the MRI signal to the cell viability, while MR imaging of nanoparticles only provides particle localization rather than imaging of cell survival and engraftment. In future, we plan to extend *in vivo* visualization techniques to imaging multimodality including PET, SPECT and bioluminescence.

6. MAIN FINDINGS OF THE WORK

1. A unified approach to non-invasive assessment of myocardial structure, function, energy metabolism and transplanted cell tracking in laboratory animals has been created combining state-of-the-art biophysical technology and bioengineering.

2. Unified infrastructure based on the modern physical methods and biophysical techniques has been created for comprehensive non-invasive studies of the heart using magnetic resonance imaging and spectroscopy. Developments in bioengineering included installation of the specialized imaging equipment for physiological monitoring and gating of ECG and respiratory signals with MR acquisitions, construction of the specialized radiofrequency coils, selection of anesthesia methods, development and optimization of pulse sequences for cardiac MRI on small and large animals.

3. For the first time ^{1}H MRI methods were applied to the evaluation of heart structure and contractile function in rodents and primates after modeling myocardial infarction and transplantation of human cardiomyocytes. Possibility of the infarct regeneration with hESC-CM has been shown for the first time. Specifically, after transplantation of 10 million human cardiomyocytes the ejection fraction of the left ventricle in the infarcted rat heart increased to 50.3 ± 2%, while the heart contractility in control group (without cells) was only 42 ± 1.9%. Regional thickening of the infarcted wall increased by 2.5-fold in comparison with the control ($p < 0.001$). The recovery of the heart contractile function was more apparent in the non-human primates. Specifically, after transplantation of 750 million of hESC-CM left ventricle ejection fraction increased from 39.3 ± 2.2% to 50 ± 2.4% in four weeks; then EF further increased to 60 ± 3.4% by 3 months ($p = 0.01$). Regional LV wall thickening in the infarct area of the cell-treated animals increased to 20.8 ± 3.7% (0% in the control group, $p = 0.055$). Mean hESC-CM graft size was 16.9 ± 6.3% of the infarct zone.

4. Specialized combined $^{1}H/^{31}P$ radiofrequency coils were engineered for conducting of MRI and spatially localized phosphorus MR spectroscopy studies of the heart of small laboratory animals *in vivo* at the same examination. Using 1D-CSI pulse sequence PCr/ATP was measured in the normal mouse heart that was 2.1 ± 0.5; PCr/ATP decreased in 30% after myocardial infarction to 1.4 ± 0.6 ($p<0.02$). Xantine oxidase inhibitors normalized PCr/ATP in the mouse heart (2.0 ± 0.5, $p<0.05$). Improvement in energy metabolism of the infarcted mouse heart correlated with improvement of the contractile function ($r = 0.65$). Therefore, the metabolic correction of the heart contractility and energy metabolism has been shown.

5. New method of myocardial perfusion quantitation using kinetic modeling of the contrast agent dynamics in tissues has been developed. The coefficients of the contrast uptake *U* and retention *R* by the tissues were offered for perfusion characterization. This model has shown the differences in myocardial perfusion between dogs with Duchenne muscular dystrophy and healthy animals. Canine model of DMD was characterized by increased *U* (6.76 ± 2.41%) in comparison with the control dogs (2.98 ± 1.46%), $p < 0.05$. *R* coefficient was lower in DMD dogs in comparison with healthy animals, 82.2 ± 5.8% and 90.5 ± 6.6%, correspondingly ($p = 0.12$). New kinetic model has also shown the tendency to the improved myocardial perfusion after hESC-CM transplantation and decrease in the contrast agent retention in tissues, however, the differences were not statistically significant due to small sample size.

6. New phase-sensitive reconstruction method for the 3D late gadolinium enhanced images, 3D-TRIPS, has been used for assessment of the infarct zone in the non-human primates. Advantages of the 3D-TRIPS are shorter scan time by 1.5-2 folds due to elimination of the reference scan and higher signal intensity ratio between the infarct zone and blood pool in the LV chamber in comparison with the standard 2D-PSIR technique (1.10 ± 0.08 and 1.01 ± 0.01, correspondingly, $p<0.05$), which increases precision in the infarct size measurements.

7. Feasibility of over-expression of the natural endogenous protein ferritin for MRI visualization of the cardiac grafts has been shown. Optimal MRI pulse sequences (T_2*-GRE bright blood and T_2*-iMSDE black blood) has been developed for precise evaluation of the graft size with high correlation with histology ($r=0.89$ for T_2*-weighted GRE and $r=0.79$ for T_2*-weighted iMSDE). Signal intensity of the ferritin-tagged grafts decreased in 20-30% in T_2*-weighted MR images, which is caused by iron accumulation in the cytoplasm of the transgenic cells, while WT transplant has not changed the relaxation properties of the myocardial tissue.

8. MRI gene-reporter ferritin is better suitable for the long-term monitoring of the live transplanted cells in comparison with the standard cell labeling method using superparamagnetic iron oxide nanoparticles SPIO. Despite stronger decrease in MRI signal intensity caused by SPIO labeling (80%) in comparison with ferritin (30%), SPIO signal does not reflect the transplanted cell viability. The genetically based cell tagging with ferritin is more reliable indicator of the transplant viability and graft size.

7. LIST OF PUBLICATIONS BASED ON THIS WORK

Publications in the referred scientific journals cited at the databases Web of Science (WOS), Scopus, RSCI (IF – impact factor of the journal during last 5 years):

1. **Naumova AV**, Weiss RG, Chacko VP. Regulation of Murine Myocardial Energy Metabolism During Adrenergic Stress Studied by In Vivo Phosphorus-31 NMR Spectroscopy // *Am J Physiol Heart Circ Physiol.* – 2003. – Vol. 285. – N. 5. – P. H1976-1979. **IF: 3.567**. *WOS, Scopus.*

2. **Naumova AV**, Chacko VP, Ouwerkerk R, Stull L, Marban E, Weiss RG. Xanthine Oxidase Inhibitors Improve Energetics and Function Following Infarction in the Failing Mouse Heart // *Am J Physiol Heart Circ Physiol.* – 2006. – Vol. 290. – P. H837-H843. **IF: 3.567**. *WOS, Scopus.*

3. Laflamme MA, Chen KY, **Naumova AV**, Muskheli V, Fugate JA, Dupras SK, Xu C, Hassanipour M, Police S, O'Sullivan C, Collins L, Minami E, Gill E.A, Ueno S, Yuan C, Gold J, Murry CE. Delivery of Human Embryonic Stem Cell Cardiomyocytes in Pro-Survival Factors Enhances the Function of Infarcted Hearts // *Nature Biotechnol.* – 2007. – Vol. 25. – P. 1015–1024. **IF: 46.223**. *WOS, Scopus.*

4. **Naumova AV**, Reinecke H, Yarnykh V, Deem J, Yuan C, Murry CE. Ferritin Overexpression for Noninvasive MRI-Based Tracking of Stem Cells Transplanted into the Heart // *Mol Imaging.* – 2010. – Vol. 9. – N. 4. – P. 201-210. **IF: 1.926.** *WOS, Scopus.*

5. Fernandes S, **Naumova AV,** Zhu WZ, Laflamme MA, Gold J, Murry CE. Human embryonic stem cell-derived cardiomyocytes engraft but do not alter cardiac remodeling after chronic infarction in rats // *J Molecul Cell Cardiol.* – 2010. – Vol. 49. – P. 941-949. **IF: 5.13.** *WOS, Scopus.*

6. **Naumova AV**, Yarnykh VL, Balu N, Reinecke H, Murry CE, Yuan C. Quantification of MRI Signal of Transgenic Grafts Overexpressing Ferritin in Murine Myocardial Infarcts // *NMR Biomed*. – 2012. – Vol. 25. – N.10. – P.1187-1195. **IF: 3.523.** *WOS, Scopus.*

7. Kerwin WS, **Naumova A**, Storb R, et al. Mapping contrast agent uptake and retention in MRI studies of myocardial perfusion: case control study of dogs with Duchenne muscular dystrophy // *Int J Cardiovasc Imaging.* – 2013. – Vol. 29. – P. 819-826. **IF: 1.845.** *WOS, Scopus.*

8. Maslov LN, Podoksenov YuK, Portnichenko AG, Naumova AV. Hypoxic Preconditioning of Stem Cells as a New Approach to Increase the Efficacy of Cell Therapy for Myocardial Infarction // *Annals of the Russian Academy of Medical Sciences.* – 2013. – Vol. 12. – P. 16–25. **IF: unknown.** *Scopus.*

9. **Naumova AV**, Balu N, Yarnykh VL, Reinecke H, Murry CE, Yuan C. MRI Tracking of Graft Survival in the Infarcted Heart: Iron Oxide Particles vs. Ferritin Overexpression Approach // *J Cardiovasc Pharmacol Ther*. – 2014. – Vol. 19. – N. 4. – P. 358-367. **IF: 2.43.** *WOS, Scopus.*

10. **Naumova AV**, Yarnykh VL, Balu N, Reinecke H, Murry CE, Yuan C. MRI Tracking Of Transplanted Cells In The Mouse Heart With Iron Oxide Nanoparticles And Ferritin Expression // *Izvestia VUZOV: Physics.* – 2015. – Vol. 58. – N. 12/2. – P. 43-51. **IF**: **0.671.** *WOS, Scopus.*

11. **Naumova AV**, Modo M, Moore A, Murry CE, Frank JA. Clinical imaging to track cell fate and function in regenerative medicine // *Nature Biotechnol.* – 2014. – Vol. 32. – N. 8. – P. 804-818. **IF: 46.223.** *WOS, Scopus.*

12. **Naumova AV**, Modo M, Moore A, Frank JA, Murry CE. Response to cardiac regeneration validated // *Nature Biotechnol*. – 2015. – Vol. 33. – N. 6. – P. 587. **IF: 46.223.** *WOS, Scopus.*

13. **Naumova AV**, Yarnykh VL Assessment of the Heart Microstructure: From Mouse to Man // *Circulation.* – 2014. – Vol. 129. – N. 17. – P. 1720-1722. **IF: 17.14.** *WOS, Scopus.*

14. **Naumova A**, Yarnykh V, Ferguson M, Rosenfeld M, Yuan C. MR histology of advanced atherosclerotic lesions of ApoE- knockout mice // *Journal of Physics: Conference Series.* – 2016. – Vol. 677. – N. 1. – P. 012008. **IF: нет.** *WOS.*

15. **Naumova AV**, Vande Velde G. Genetically encoded iron-associated proteins as MRI reporters for molecular and cellular imaging // *Wiley Interdiscip Rev Nanomed Nanobiotechnol.* – 2018. – Vol. 10. – N. 2. doi: 10.1002/wnan.1482. **IF: 4.571.** *WOS, Scopus.*

16. Liu Y-W, Iwata M, Minami E, Abrams VK, Don C, **Naumova AV**, Martinson AM, Kadota S, Lee W-H, Yang L-T, Liao I-C, Tsai H-W, Murry CE, Torok-Storb B. A clonal population of allogeneic bone marrow fibroblasts indirectly mitigates damage in myocardial infarction // *Adv Tissue Eng Regen Med Open Access. – 2017.* – Vol. 3. – N. 1. – P. 00055. **IF: 18.456.** *WOS.*

17. Liu Y-W, Chen B, Yang X, Fugate JA, Kalucki FA, Futakuchi-Tsuchida A, Couture L, Vogel KW, Astley CA, Baldessari A, OgleJ, Don CW, Steinberg ZL, Seslar SP, Tuck SA, Tsuchida H, **Naumova AV**, Dupras SK, Lyu MS, Lee J, Hailey DW, Reinecke H, Pabon L, Fryer BH, MacLellan WR, Thies RS, Murry CE. Human ESC-Derived Cardiomyocytes Restore Function in Infarcted Hearts of Non-Human Primates // *Nature Biotechnol. – 2018. In press.* **IF: 46.223.** *WOS, Scopus.*

18. **Naumova AV**, Murry CE. Indirect Cell Labeling for Magnetic Resonance Imaging of Cardiac Grafts. In: MRI of Stem Cell Applications. Nova Publisher, 2014. *WOS.*

8. REFERENCES

1. Chen I.Y., Wu J.C. Cardiovascular molecular imaging: focus on clinical translation // Circulation. – 2011. – Vol. 123. – P. 425–443.
2. Youn H., Chung K.J. Reporter gene imaging // Am J Roentgenol. – 2013. – Vol. 201. – P. 206–214.
3. Kooreman N.G., Ransohoff J.D., Wu J.C. Tracking gene and cell fate for therapeutic gain // Nat Mater. – 2014. – Vol. 13. – P. 106–109.
4. Nguyen P.K., Riegler J., Wu J.C. Stem cell imaging: from bench to bedside // Cell Stem Cell. – 2014. – Vol. 14. – P. 431–444.
5. Dash R., Chung J., Ikeno F., et al. Dual manganese-enhanced and delayed gadolinium-enhanced MRI detects myocardial border zone injury in a pig ischemia-reperfusion model // Circ Cardiovasc Imaging. – 2011. – Vol. 4. – P. 574–582.
6. Mezer A., Yeatman J.D., Stikov N., et al. Quantifying the local tissue volume and composition in individual brains with magnetic resonance imaging // Nat Med. – 2013. – Vol. 19. – P. 1667–1672.
7. Wedeen V.J., Hagmann P., Tseng W.Y., et al. Mapping complex tissue architecture with diffusion spectrum magnetic resonance imaging // Magn Reson Med. – 2005. – Vol. 54. – P. 1377–1386.
8. Sosnovik D.E., Mekkaoui C., Huang S., et al. Microstructural impact of ischemia and bone marrow-derived cell therapy revealed with diffusion tensor magnetic resonance imaging tractography of the heart in vivo // Circulation. – 2014. – Vol. 129. – P. 1731–1741.
9. Ward K.M., Aletras A.H., Balaban R.S. A new class of contrast agents for MRI based on proton chemical exchange dependent saturation transfer (CEST) // J Magn Reson. – 2000. – Vol. 143. – P. 79–87.
10. Yarnykh V.L. Fast macromolecular proton fraction mapping from a single off-resonance magnetization transfer measurement // Magn Reson Med. – 2012. – Vol. 68. – N 1. – P. 166–78.
11. Chan K.W., Liu G., Song X., et al. MRI-detectable pH nanosensors incorporated into hydrogels for in vivo sensing of transplanted-cell viability // Nat Mater. – 2013. – Vol. 12. – P. 268–275.
12. Chacko V.P., Aresta F., Chacko S.M., et al. MRI//MRS assessment of in vivo murine cardiac metabolism, morphology, and function at physiological heart rates // Am J Physiol. – 2000. – Vol. 279. – P. H2218–H2224.
13. Haris M., Singh A., Cai K., et al. A technique for in vivo mapping of myocardial creatine kinase metabolism // Nat Med. – 2014. – Vol. 20. – P. 209–214.
14. Robbers L.F., Nijveldt R., Beek A.M., et al. Cell therapy in reperfused acute myocardial infarction does not improve the recovery of perfusion in the infarcted myocardium: a cardiac MR imaging study // Radiology. – 2014. – Vol. 272. – P. 113–122.
15. Naresh N.K., Chen X., Roy R.J., et al. Accelerated dual-contrast first-pass perfusion MRI of the mouse heart: development and application to diet-induced obese mice // Magn Reson Med. – 2015. – Vol. 73. – P. 1237–1245.
16. Kerwin W.S., Zhao X., Yuan C., et al. Contrast-enhanced MRI of carotid atherosclerosis: dependence on contrast agent // J Magn Reson Imaging. – 2009. – Vol. 30. – P. 35–40.
17. Henningsson M., Greil G.F., Burch M., et al. Coronary magnetic resonance angiography in heterotopic heart transplant recipient // Circulation. – 2014. – Vol. 129. – P. 1453–1455.
18. Stadlbauer A., Zimmermann M., Heinz G., et al. Magnetic resonance imaging biomarkers for clinical routine assessment of microvascular architecture in glioma // J Cereb Blood Flow Metab. – 2017. – Vol. 37. – N 2. – P. 632–643.
19. Vande Velde G., Baekelandt V., Dresselaers T., et al. Magnetic resonance imaging and spectroscopy methods for molecular imaging // Q J Nucl Med Mol Imaging. – 2009. – Vol. 53. – P. 565–585.
20. Vandsburger M.H., Radoul M., Cohen B., et al. MRI Reporter Genes: Application to Imaging of Cell Survival, Proliferation, Migration, and Differentiation // NMR Biomed. – 2013. – Vol. 26. – P. 872–884.

21. Ingwall J.S. Phosphorus nuclear magnetic resonance spectroscopy of cardiac and skeletal muscles // Am J Physiol Heart Circ Phisiol. – 1982. – Vol. 242. – P. H729–H744.
22. Menon R.S., Hendrich K., Hu X., et al. 31P NMR spectroscopy of the human heart at 4T: detection of substantially uncontaminated cardiac spectra and differentiation of subepicardium and subendocardium // Magn Reson Med. – 1992. – Vol. 26. – P. 368–376.
23. Wagers A.J. The stem cell niche in regenerative medicine // Cell Stem Cell. – 2012. – Vol. 10. – P. 362–369.
24. Shapiro E.M., Sharer K., Skrtic S., et al. In vivo detection of single cells by MRI // Magn Res Med. – 2006. Vol. 55. – P. 242–249.
25. Shapiro E.M., Skrtic S., Sharer K., et al. MRI detection of single particles for cellular imaging // Proc Natl Acad Sci USA. – 2004. – Vol. 101. – P. 10901–10906.
26. de Vries I.J., Lesterhuis W.J., Barentsz J.O., et al. Magnetic resonance tracking of dendritic cells in melanoma patients for monitoring of cellular therapy // Nature Biotechnology. – 2005. – Vol. 23. – P. 1407–1413.
27. Dahnke H., Schaeffter T. Limits of detection of SPIO at 3.0 T using T2 relaxometry // Magn Res Med. – 2005. – Vol. 53. – P. 1202–1206.
28. Thu M.S., Bryant L.H., Coppola T., et al. Self–assembling nanocomplexes by combining ferumoxytol, heparin and protamine for cell tracking by magnetic resonance imaging // Nature Medicine. – 2012. – Vol. 18. – P. 463–467.
29. Gutova M., Frank J.A., D'Apuzzo M., et al. Magnetic resonance imaging tracking of ferumoxytol-labeled human neural stem cells: studies leading to clinical use // Stem Cells Translational Medicine. – 2013. – Vol. 2. – P. 766–775.
30. Partlow K.C., Chen J., Brant J.A., et al. 19F magnetic resonance imaging for stem//progenitor cell tracking with multiple unique perfluorocarbon nanobeacons // FASEB J. – 2007. – Vol. 21. – P. 1647–1654.
31. Ruiz–Cabello J., Barnett B.P., Bottomley P.A., et al. Fluorine (19F) MRS and MRI in biomedicine // NMR in biomedicine. – 2011. – Vol. 24. – P. 114–129.
32. Streeter D.D. Jr, Hanna W.T. Engineering mechanics for successive states in canine left ventricular myocardium. II. Fiber angle and sarcomere length // Circ Res. – 1973. – Vol. 33. – P. 656–664.
33. Laflamme M.A., Murry C.E. Heart regeneration // Nature. – 2011. – Vol. 473. – N. 7347 – P. 326–335.
34. Soonpaa M.H., Kim K.K., Pajak L., et al. Cardiomyocyte DNA synthesis and binucleation during murine development // Am J Physiol. – 1996. – Vol. 271. – N 5 Pt 2. – P. H2183–H2189.
35. Quaini F., Cigola E., Lagrasta C., et al. End-stage cardiac failure in humans is coupled with the induction if proliferating cell nuclear antigen and nuclear mitotic division in ventricular myocytes // Circ Res. – 1994. – Vol. 75. – N 6. – P. 1050–1063.
36. Brodsky W.Y., Arefyeva A.M., Uryvaeva I.V. Mitotic polyploidization of mouse heart myocytes during the first postnatal week // Cell Tissue Res. – 1980. – Vol. 210. – N 1. – P. 133–144.
37. Lundy S.D., Zhu Z.W., Regnier M., et al. Structural and Functional Maturation of Cardiomyocytes Derived From Human Pluripotent Stem Cells // Stem Cells Dev. – 2013. – Vol. 22. – N 14. – P. 1991–2002.
38. Saggin L., Gorza L., Ausoni S., et al. Troponin I switching in the developing heart // J Biol Chem. – 1989. – Vol. 264. – N 27. – P. 16299–16302.
39. Hunkeler N.M., Kullman J., Murphy A.M. Troponin I isoform expression in human heart // Circ Res. – 1991. – Vol. 69. – N 5. – P. 1409–1414.
40. Xu X.Q., Soo S.Y., Sun W., et al. Global expression profile of highly enriched cardiomyocytes derived from human embryonic stem cells // Stem Cells. – 2009. – Vol. 27. – N 9. – P. 2163–2174.
41. Louch W.E., Sejersted O.M., Swift F. There goes the neighborhood: pathological alterations in T-tubule morphology and consequences for cardiomyocyte Ca2+ handling // J Biomed Biotechnol. – 2010. – Vol. 2010. – P. 503906.

42. Angst B.D., Khan L.U., Severs N.J., et al. Dissociated spatial patterning of gap junctions and cell adhesion junctions during postnatal differentiation of ventricular myocardium // Circ Res. – 1997. – Vol. 80. – N 1. – P. 88–94.
43. Taegtmeyer H. Energy metabolism of the heart: from basic concepts to clinical applications // Curr Probl Cardiol. – 1994. – Vol. 19. – P. 59–113.
44. Neely J.R., Liebermeister H., Battersby E.J., et al. Effect of pressure development on oxygen consumption by isolated rat heart // Am J Physiol. – 1967. – Vol. 212. – P. 804–814.
45. Chance B., Williams G.R. The Respiratory Chain And Oxidative Phosphorylation // Adv Enzymol. – 1956. – Vol. 17. – P. 65–130.
46. Schaper J., Meiser E., Stammler G. Ultrastructural morphometric analysis of myocardium from dogs, rats, hamsters, mice, and from human hearts // Circ Res. – 1985. – Vol. 56. – N 3. – P. 377–391.
47. Lopaschuk G.D., Jaswal J.S. Energy metabolic phenotype of the cardiomyocyte during development, differentiation, and postnatal maturation // J Cardiovasc Pharmacol. – 2010. – Vol. 56. – N 2. – P. 130–140.
48. Bottomley P.A., Hardy C.J., Roemer P.B., et al. Problems and expediencies in human 31P spectroscopy. The definition of localized volumes, dealing with saturation and the technique-dependence of quantification // NMR Biomed. – 1989. – Vol. 2. – 284–289.
49. Barker P.B., Sibisi S. Non-linear least squares analysis of in vivo 31P NMR data // Soc Magn Res Med. – 1990. – P. 1089.
50. Lopez A.D., Mathers C.D., Ezzati M., et al. Global and regional burden of disease and risk factors, 2001: systematic analysis of population health data // Lancet. – 2006. – Vol. 367. – P. 1747–1757.
51. Go A., Mozaffarian D., Roger V.L., et al. Executive Summary: Heart Disease and Stroke Statistics–2014 Update: A Report From the American Heart Association // Circulation. – 2014. – Vol. 129. – P. 399–410.
52. Porrello E.R., Mahmoud A.I., Simpson E., Hill et al. Transient regenerative potential of the neonatal mouse heart // Science. – 2011. – Vol. 331. – P. 1078–1080.
53. Bergmann O., Bhardwaj R.D., Bernard S., et al. Evidence for cardiomyocytes renewal in humans // Science. – 2009. – Vol. 324. – N 5923. – P. 98–102.
54. Beltrami C.A., Finato N., Rocco M., et al. Structural basis of end-stage failure in ischemic cardiomyopathy in humans // Circulation. – 1994. – Vol. 89. – N 1. – P. 151–163.
55. Hockman J.S., Bulkley B.H. Expansion of acute myocardial infarction: an experimental study // Circulation. – 1982. – Vol. 65. – N 7. – P. 1446–1450.
56. Frangogiannis N.G., Smith C.W., Entman M.L. The inflammatory response in myocardial infarction // Cardiovasc Res. – 2002. – Vol. 53. – P. 31–47.
57. Frangogiannis N.G. Regulation of the inflammatory response in cardiac repair // Circ Res. – 2012. – Vol. 110. – P. 159–173.
58. Lehnart S.E., Maier L.S., Hasenfuss G. Abnormalities of calcium metabolism and myocardial contractility depression in the failing heart // Heart Failure Reviews. – 2009. – Vol. 14. – N 4. – P. 213–224.
59. Sciarretta S., Paneni F., Palano F., et al. Role of the reninangiotensin-aldosterone system and inflammatory processes in the development and progression of diastolic dysfunction // Clinical Science. – 2009. – Vol. 116. – P. 467– 477.
60. Jessup M., Brozena S. Heart failure // N Engl J Med. – 2003. – Vol. 348. – P. 2007–2018.
61. Goldberg L.R. In the clinic. Heart failure // Annals of Internal Medicine. – 2010. Vol. 152. – P. 11–15.
62. Burchfield J.S., Xie M., Hill J.A. Pathological ventricular remodeling: mechanisms // Circulation. – 2013. – Vol. 128. – N 4. – P. 388–400.
63. Cohn J.N., Ferrari R., Sharpe N. Cardiac remodeling — concepts and clinical implications: a consensus paper from an international forum on cardiac remodeling // J Am Coll Cardiol. – 2000. – Vol. 35. – N 3. – P. 569–582.

64. Ohtani T., Mohammed S.F., Yamamoto K., et al. Diastolic stiffness as assessed by diastolic wall strain is associated with adverse remodelling and poor outcomes in heart failure with preserved ejection fraction // European Heart Journal. – 2012. – Vol. 33. – N 14. – P. 1742–1749.
65. Harvey P.A., Leinwand L.A. The cell biology of disease: cellular mechanisms of cardiomyopathy // The Journal of Cell Biology. – 2011. – Vol. 194. – N 3. – P. 355–365.
66. Ford E.S., Ajani U.A., Croft J.B., et al. Explaining the decrease in U.S. deaths from coronary disease, 1980–2000 // N Engl J Med. – 2007. – Vol. 356. – P. 2388–2398.
67. Herfkens R.J., Higgins C.B., Hricak H., et al. Nuclear magnetic resonance imaging of the cardiovascular system: normal and pathologic findings // Radiology. – 1983. – Vol. 147. – P. 749–759.
68. Lanzer P., Botvinick E., Schiller N.B., et al. Cardiac imaging using gated magnetic resonance // Radiology. – 1984. – Vol. 150. – P. 121–127.
69. Haase A., Frahm J., Matthaei D., et al. FLASH imaging: rapid NMR imaging using low flip angle pulses // J Magn Reson. – 1986. – Vol. 67. – P. 258–266.
70. Frahm J., Haase A., Matthaei D. Rapid NMR imaging of dynamic processes using the FLASH technique // Magn Reson Med. – 1986. – Vol. 3. – P. 321–327.
71. Frahm J., Merboldt K.D., Bruhn H., et al. 0.3–second FLASH MRI of the human heart // Magn Reson Med. – 1990. – Vol. 13. – P. 150–157.
72. Lenz G., Haacke E.M., White R.D. Retrospective cardiac gating: a review of technical aspects and future directions // Magn Reson Imaging. – 1989. – Vol. 7. – P. 445–455.
73. Edelman R.R., Wallner B., Singer A., et al. Segmented turbo FLASH: method for breath-hold MR imaging of the liver with flexible contrast // Radiology. – 1990. – Vol. 177. – P. 515–521.
74. Atkinson D.J., Edelman R. Cineangiography of the heart in a single breath hold with a segmented TurboFLASH sequence // Radiology. – 1991. – Vol. 178. – P. 357–360.
75. Ruff J., Wiesmann F., Hiller K.H., et al. Magnetic resonance microimaging for noninvasive quantification of myocardial function and mass in the mouse // Magn Reson Med. – 1998. – Vol. 40. – P. 43–48.
76. Peters D.C., Ennis D.B., McVeigh E.R. High-Resolution MRI of Cardiac Function With Projection Reconstruction and Steady-State Free Precession // Magn Reson Med. – 2002. – Vol. 48. – P. 82–88.
77. Bieri O., Scheffler K. Fundamentals of balanced steady state free precession MRI // J Magn Reson Imaging. – 2013. – Vol. 38. – N 1. – P. 2–11.
78. Carr J.C., Simonetti O., Bundy J., et al. Cine MR Angiography of the Heart with Segmented True Fast Imaging with SteadyState Precession // Radiology. – 2001. – Vol. 219. – N 3. – P. 828–834.
79. Berr S.S., Roy R.J., French B.A., et al. Black blood gradient echo cine magnetic resonance imaging of the mouse heart // Magn Reson Med. – 2005. – Vol. 53. – P. 1074–1079.
80. Ginat D.T., Fong M.W., Tuttle D.J., et al. Cardiac imaging: Part I, MR pulse sequences, imaging planes, and basic anatomy // AJR Am J Roentgenol. – 2011. – Vol. 197. – P. 808–815.
81. Cootes T.F., Hill A., Taylor C.J., et al. The Use of Active Shape Models for Locating Structures in Medical Images // Image and Vision Computing. – 1994. – Vol. 12. – N 6. – P. 355–366.
82. Noble N.M., Hill D.L., Breeuwer M., et al. Myocardial Delineation via Registration in a Polar Coordinate System // Acad Radiol. – 2003. – Vol. 10. – N 12. – P. 1349–1358.
83. Hoffmann U., Globits S., Stefenelli T., et al. The effects of ACE inhibitor therapy on left ventricular myocardial mass and diastolic filling in previously untreated hypertensive patients: a cine MRI study // J Magn Reson Imaging. – 2001. – Vol. 14. – P. 16–22.
84. Moon J.C., Messroghli D.R., Kellman P., et al. Myocardial T1 mapping and extracellular volume quantification // J Cardiovasc Magn Reson. – 2013. – Vol. 15. – P. 92.
85. Look D.C., Locker D.R. Time saving in measurement of NMR and EPR relaxation times // Rev Sci Instrum. – 1970. – Vol. 41. – N 2. – P. 250e1.
86. Kellman P., Hansen M.S. T1-mapping in the heart: accuracy and precision // J Cardiov Magn Reson. – 2014. – Vol. 16. – N 1. – P. 2.

87. Piechnik S.K., Ferreira V.M., Dall'Armellina E., et al. Shortened Modified Look-Locker Inversion recovery (ShMOLLI) for clinical myocardial T1-mapping at 1.5 and 3 T within a 9 heartbeat breathhold // J Cardiovasc Magn Reson. – 2010. – Vol. 12. – P. 69.
88. Dass S., Suttie J.J., Piechnik S.K., et al. Myocardial tissue characterization using magnetic resonance noncontrast t1 mapping in hypertrophic and dilated cardiomyopathy // Circ Cardiovasc Imaging. – 2012. – Vol. 5. – N 6. – P. 726–733.
89. Everett R.J., Stirrat C.G., Semple S.I., et al. Assessment of myocardial fibrosis with T1 mapping MRI // Clinical Radiology. – 2016. – Vol. 71. – P. 768–778.
90. Roujol S., Weingärtner S., Foppa M., et al. Accuracy, precision, and reproducibility of four T1 mapping sequences: a head-to-head comparison of MOLLI, ShMOLLI, SASHA, and SAPPHIRE // Radiology. – 2014. – Vol. 272. – N 3. – P. 683–689.
91. Mavrogeni S., Apostolou D., Argyriou P., et al. T1 and T2 Mapping in Cardiology: “Mapping the Obscure Object of Desire” // Cardiology. – 2017. – Vol. 138. – P. 207–217.
92. Abdel-Aty H., Simonetti O., Friedrich M.G. T2-weighted cardiovascular magnetic resonance imaging // J Magn Reson Med. – 2007. – Vol. 26. – N 3. – P. 452–459.
93. Pruessmann K.P., Weiger M., Scheidegger M.B., et al. SENSE: sensitivity encoding for fast MRI // Magn Reson Med. – 1999. – Vol. 42. – N 5. – P. 952–962.
94. Simonetti O.P., Finn J.P., White R.D., et al. "Black blood" T2-weighted inversion-recovery MR imaging of the heart // Radiology. – 1996. – Vol. 199. – N 1. – P. 49–57.
95. Giri S., Chung Y.-C., Merchant A., et al. T2 quantification for improved detection of myocardial edema // J Cardiovasc Magn Reson. – 2009. – Vol. 11. – P. 56.
96. McNamara M.T., Higgins C.B., Schechtmann N., et al. Detection and characterization of acute myocardial infarction in man with use of gated magnetic resonance // Circulation. – 1985. – Vol. 71. – P. 717–724.
97. Huang T.-Y., Liu Y.-J., Stemmer A., et al. T2 measurement of the human myocardium using a T2-prepared transient-state TrueFISP sequence // Magn Reson Med. – 2007. – Vol. 57. – P. 960–966.
98. Sprinkart A.M., Luetkens J.A., Träber F., et al. Gradient Spin Echo (GraSE) imaging for fast myocardial T2 mapping // J Cardiovasc Magn Reson. – 2015. – Vol. 17. – P. 12.
99. Akçakaya M., Basha T.A., Weingärtner S., et al. Improved quantitative myocardial T2 mapping: Impact of the fitting model // Magn Reson Med. – 2015. – Vol. 74. – N 1. – P. 93–105.
100. Butler C.R., Thompson R., Haykowsky M., et al. Cardiovascular magnetic resonance in the diagnosis of acute heart transplant rejection: a review // J Cardiovasc Magn Reson. – 2009. – Vol. 11. – P. 7.
101. Coelho-Filho O.R., Rickers C., Kwong R.Y., et al. MR myocardial perfusion imaging // Radiology. – 2013. – Vol. 266. – P. 701–725.
102. Tsekos N.V., Zhang Y., Merkle H., et al. Fast anatomical imaging of the heart and assessment of myocardial perfusion with arrhythmia insensitive magnetization preparation // Magn Reson Med. – 1995. – Vol. 34. – N 4. – P. 530–536.
103. Kellman P., Arai A.E. Imaging Sequences for First Pass Perfusion // J Cardiovasc Magn Reson. – 2007. – Vol. 9. – P. 525–537.
104. Detre J.A., Zhang W., Roberts D.A., et al. Tissue specific perfusion imaging using arterial spin labeling // NMR Biomed. – 1994. – Vol. 7. – N 1–2. – P. 75–82.
105. Vandsburger M.H., Janiczek R.L., Xu Y., et al. Improved arterial spin labeling after myocardial infarction in mice using cardiac and respiratory gated look-locker imaging with fuzzy C-means clustering // Magn Reson Med. – 2010. – Vol. 63. – N 3. – P. 648–657.
106. Wang J., Licht D.J., Silvestre D.W., et al. Why perfusion in neonates with congenital heart defects is negative: technical issues related to pulsed arterial spin labeling // Magn Reson Imaging. – 2006. – Vol. 24. – N 3. – P. 249–254.
107. Di Bella E.V., Parker D.L., Sinusas A.J. On the dark rim artifact in dynamic contrast-enhanced MRI myocardial perfusion studies // Magn Reson Med. – 2005. – Vol. 54. – N 5. – P. 1295–1299.

108. Ortiz-Pérez J.T., Rodríguez J., Meyers S.N., et al. Correspondence between the 17-segment model and coronary arterial anatomy using contrast-enhanced cardiac magnetic resonance imaging // JACC Cardiovasc Imaging. – 2008. – Vol. 1. – N 3. – P. 282–293.
109. Penzkofer H., Wintersperger B.J., Knez A., et al. Assessment of myocardial perfusion using multisection firstpass MRI and color-coded parameter maps: a comparison to 99mTc Sesta MIBI SPECT and systolic myocardial wall thickening analysis // Magn Reson Imaging. – 1999. – Vol. 17. – N 2. – P. 161–170.
110. Christian T.F., Aletras A.H., Arai A.E. Estimation of absolute myocardial blood flow during first-pass MR perfusion imaging using a dual-bolus injection technique: comparison to single-bolus injection method // J Magn Reson Imaging. – 2008. – Vol. 27. – N 6. – P. 1271–1277.
111. Gatehouse P.D., Elkington A.G., Ablitt N.A., et al. Accurate assessment of the arterial input function during high-dose myocardial perfusion cardiovascular magnetic resonance // J Magn Reson Imaging. – 2004. – Vol. 20. – N 1. – P. 39–45.
112. Al-Saadi N., Nagel E., Gross M., et al. Noninvasive Detection of Myocardial Ischemia from Perfusion Reserve based on Cardiovascular Magnetic Resonance // Circulation. – 2000. – Vol. 101. – P. 1379–1383.
113. Nagel E., Thouet T., Klein C., et al. Noninvasive determination of coronary blood flow velocity with cardiovascular magnetic resonance in patients after stent deployment // Circulation. – 2003. – Vol. 107. – N 13. – P. 1738–1743.
114. Kim R.J., Fieno D.S., Parrish T.B., et al. Relationship of MRI delayed contrast enhancement to irreversible injury, infarct age, and contractile function // Circulation. – 1999. – Vol. 100. – P. 1992–2002.
115. Kim R.J., Wu E., Rafael A., et al. The use of contrast-enhanced magnetic resonance imaging to identify reversible myocardial dysfunction // N Engl J Med. – 2000. – Vol. 343. – P. 1445–1453.
116. Yang Z., Berr S.S., Gilson W.D., et al. Simultaneous evaluation of infarct size and cardiac function in intact mice by contrast-enhanced cardiac magnetic resonance imaging reveals contractile dysfunction in noninfarcted regions early after myocardial infarction // Circulation. – 2004. – Vol. 109. – P. 1161–1167.
117. French B.A., Beyers R.J., Sureau F.C., et al. Imaging infarct expansion in mice using a contrast enhanced inversion recovery MRI sequence // J Cardiovasc Magn Reson. – 2005. – Vol. 7. – P. 172–173.
118. Kellman P., Arai A.E., McVeigh E.R., et al. Phase-sensitive inversion recovery for detecting myocardial infarction using gadolinium-delayed hyperenhancement // Magn Reson Med. – 2002. – Vol. 47. – N 2. – P. 372–383.
119. Yee K., Malliaras K., Kanazawa H., et al. Allogeneic cardiospheres delivered via percutaneous transendocardial injection increase viable myocardium, decrease scar size, and attenuate cardiac dilatation in porcine ischemic cardiomyopathy // PLoS One. – 2014. – Vol. 9. – N 12. – P. e113805.
120. Hu T.C., Pautler R.G., MacGowan G.A., et al. Manganese enhanced MRI of mouse heart during changes in inotropy // Magn Reson Med. – 2001. – Vol. 46. – P. 884–890.
121. Hu T.C., Bao W., Lenhard S.C., et al. Simultaneous assessment of left-ventricular infarction size, function and tissue viability in a murine model of myocardial infarction by cardiac manganese-enhanced magnetic resonance imaging (MEMRI) // NMR in Biomedicine. – 2004. – Vol. 17. – P. 620–626.
122. Wallimann T. Bioenergetics. Dissecting the role of creatine kinase // Curr Biol. – 1994. – Vol. 4. – N 1. – P. 42–46.
123. Bessman S.P., Carpenter C.L. The creatine-creatine phosphate energy shuttle // Annu Rev Biochem. – 1985. – Vol. 54. – P. 831–862.
124. Katz A.M. Is the failing heart energy depleted? // Cardiol Clin. – 1998. – Vol. 16. – P. 633–644.
125. Ingwall J.S., Weiss R.G. Is the failing heart energy starved? On using chemical energy to support cardiac function // Circ Res. – 2004. – Vol. 95. – N 2. – P. 135–145.

126. Conway M.A., Bristow J.D., Blackledge M.J., et al. Cardiac metabolism during exercise measured by magnetic resonance spectroscopy // Lancet. – 1988. – Vol. 861. – P. 692.
127. Menon R.S., Hendrich K., Hu X., et al. 31P NMR spectroscopy of the human heart at 4T: detection of substantially uncontaminated cardiac spectra and differentiation of subepicardium and subendocardium // Magn Reson Med. – 1992. – Vol. 26. – P. 368–376.
128. Weiss R.G., Bottomley P.A., Hardy C.J., et al. Regional myocardial metabolism of high-energy phosphates during isometric exercise in patients with coronary artery disease // N Engl J Med. – 1990. – Vol. 323. – P. 1593–1600.
129. Weiss R.G., Chatham J.C., Georgakopoulos D., et al. An increase in the myocardial PCr/ATP ratio in GLUT4 null mice // FASEB J. – 2002. – Vol. 16. – P. 613–615.
130. Zhang J., Duncker D.J., Xu Y., et al. Transmural bioenergetic responses of normal myocardium to high workstates // Am J Physiol. – 1995. – Vol. 268. – P. H1891–H1905.
131. Yabe T., Mitsunami K., Inubushi T., et al. Quantitative measurements of cardiac phosphorus metabolites in coronary artery disease by 31P magnetic resonance spectroscopy // Circulation. – 1995. – Vol. 92. – P. 15–23.
132. Neubauer S., Krahe T., Schindler R., et al. 31P Magnetic resonance spectroscopy in dilated cardiomyopathy and coronary artery disease: altered cardiac high-energy phosphate metabolism in heart failure // Circulation. – 1992. – Vol. 86. – P. 1810–1818.
133. Diamant M., Lamb H.J., Groeneveld Y., et al. Diastolic dysfunction is associated with altered myocardial metabolism in asymptomatic normotensive patients with well-controlled type 2 diabetes mellitus // J Am College Cardiol. – 2003. – Vol. 42. – N 2. – P. 328–335.
134. Scheuermann-Freestone M., Madsen P.L., Manners D., et al. Abnormal cardiac and skeletal muscle energy metabolism in patients with type 2 diabetes // Circulation. – 2003. – Vol. 107. – N 24. – P. 3040–3046.
135. Crilley J.G., Boehm E.A., Blair E., et al. Hypertrophic cardiomyopathy due to sarcomeric gene mutations is characterized by impaired energy metabolism irrespective of the degree of hypertrophy // J Am College Cardiol. – 2003. – Vol. 41. – N 10. – P. 1776–1782.
136. Bottomley P., Herfkens R., Smith L., et al. Altered phosphate metabolism in myocardial infarction: P-31 MR spectroscopy // Radiology. – 1987. – Vol. 165. – N 3. – P. 703–707.
137. Conway M.A., Allis J., Ouwerkerk R., et al. Detection of low phosphocreatine to ATP ratio in failing hypertrophied human myocardium by 31P magnetic resonance spectroscopy // Lancet. – 1991. – Vol. 338. – P. 973–976.
138. Hove M.T., Neubauer S. MR spectroscopy in heart failure – clinical and experimental findings // Heart Failure Rev. – 2007. – Vol. 12. – N 1. – P. 48–57.
139. Neubauer S., Horn M., Pabst T., et al. Cardiac high-energy phosphate metabolism in patients with aortic valve disease assessed by P-31-magnetic resonance spectroscopy // J Invest Med. – 1997. – Vol. 45. – N 8. – P. 453–462.
140. Fragasso G., Perseghin G., De Cobelli F., et al. Effects of metabolic modulation by trimetazidine on left ventricular function and phosphocreatine//adenosine triphosphate ratio in patients with heart failure // Eur Heart J. – 2006. – Vol. 27. – N 8. – P. 942–948.
141. Robitaille P.M., Merkle H., Sublett E., et al. Spectroscopic imaging and spatial localization using adiabatic pulses and applications to detect transmural metabolite distribution in the canine heart // Magn Reson Med. – 1989. – Vol. 10. – P. 14–37.
142. Cho Y.K., Merkle H., Zhang J., et al. Noninvasive measurements of transmural myocardial metabolites using 3-D (31)P NMR spectroscopy // Am J Physiol Heart Circ Physiol. – 2001. – Vol. 280. – N 1. – P. H489– H497.
143. Brown T.R., Kincaid B.M., Ugurbil K. NMR chemical shift imaging in three dimensions // Proc Natl Acad Sci USA. – 1982. – Vol. 79. – N 11. – P. 3523–3526.
144. Tyler D.J., Emmanuel Y., Cochlin L.E., et al. Reproducibility of 31P cardiac magnetic resonance spectroscopy at 3 T // NMR Biomed. – 2009. – Vol. 22. – N 4. – P. 405–413.
145. Pohmann R., von Kienlin M. Accurate phosphorus metabolite images of the human heart by 3D acquisition-weighted CSI // Magn Reson Med. – 2001. – Vol. 45. – N 5. – P. 817–826.

146. Robson M.D., Tyler D.J., Neubauer S. Ultrashort TE chemical shift imaging (UTE–CSI) // Magn Reson Med. – 2005. – Vol. 53. – N 2. – P. 267–274.
147. Flogel U., Jacoby C., Godecke A., et al. In Vivo 2D Mapping of Impaired Murine Cardiac Energetics in NO-Induced Heart Failure // MRM. – 2007. – Vol. 57. – P. 50–58.
148. Katz L.A., Swain J.A., Portman M.A., et al. Relation between phosphate metabolites and oxygen consumption of heart in vivo // Am J Physiol. – 1989. – Vol. 256. – N 1 Pt 2. – P. H265–H274.
149. Ye Y., Wang C., Zhang J., et al. Myocardial creatine kinase kinetics and isoform expression in hearts with severe LV hypertrophy // Am J Physiol Heart Circ Physiol. – 2001. – Vol. 281. – N 1. – P. H376–H386.
150. Bottomley P.A., Ouwerkerk R., Lee R.F., et al. Four-angle saturation transfer (FAST) method for measuring creatine kinase reaction rates in vivo // Magn Reson Med. – 2002. – Vol. 47. – N 5. – P. 850–863.
151. Bottomley P.A., Atalar E., Weiss R.G. Human cardiac high-energy phosphate metabolite concentrations by 1D-resolved NMR spectroscopy // Magn Reson Med. – 1996. – Vol. 35. – N 5. – P. 664–670.
152. Weiss R.G., Gerstenblith G., Bottomley P.A. ATP flux through creatine kinase in the normal, stressed, and failing human heart // Proc Natl Acad Sci USA. – 2005. – Vol. 102. – N 3. – P. 808–813.
153. Bottomley P.A., Ouwerkerk R. Optimum flip-angles for exciting NMR with uncertain T1 values // Magn Reson Med. – 1994. – Vol. 32. – N 1. – P. 137–141.
154. Bittl J.A., Ingwall J.S. Reaction rates of creatine kinase and ATP synthesis in the isolated rat heart. A 31P NMR magnetization transfer study // J Biol Chem. – 1985. – Vol. 260. – N 6. – P. 3512–3517.
155. Martin J.F., Guth B.D., Griffey R.H., et al. Myocardial creatine kinase exchange rates and 31P NMR relaxation rates in intact pigs // Magn Reson Med. – 1989. – Vol. 1. – N 1. – P. 64–72.
156. Vinnakota K.C., Bassingthwaighte J.B. Myocardial density and composition: a basis for calculating intracellular metabolite concentrations // Am J Physiol Heart Circ Physiol. – 2004. – Vol. 286. – N 5. – P. H1742–H1749.
157. Gibbs C. The cytoplasmic phosphorylation potential. Its possible role in the control of myocardial respiration and cardiac contractility // J Mol Cell Cardiol. – 1985. – Vol. 17. – N 8. – P. 727–731.
158. Daar A.S., Greenwood H.L. A proposed definition of regenerative medicine // J Tissue Eng Regen Med. – 2007. – Vol. 1. – P. 179–184.
159. Jain M., DerSimonian H., Brenner D.A., et al. Cell therapy attenuates deleterious ventricular remodeling and improves cardiac performance after myocardial infarction // Circulation. – 2001. – Vol. 103. – N 14. – P. 1920–1927.
160. Leobon B., Garcin I., Menasche P., et al. Myoblasts transplanted into rat infarcted myocardium are functionally isolated from their host // Proc Natl Acad Sci USA. – 2003. – Vol. 100. – N 13. – P. 7808–7811.
161. Murry C.E., Wiseman R.W., Schwartz S.M., et al. Skeletal myoblast transplantation for repair of myocardial necrosis // J Clin Invest. – 1996. – Vol. 98. – N 11. – P. 2512–2523.
162. Horackova M., Arora R., Chen R., et al. Cell transplantation for treatment of acute myocardial infarction: unique capacity for repair by skeletal muscle satellite cells // Am J Physiol Heart Circ Physiol. – 2004. – Vol. 287. – N 4. – P. H1599–H1608.
163. Taylor D.A., Atkins B.Z., Hungspreugs P., et al. Regenerating functional myocardium: improved performance after skeletal myoblast transplantation // Nat Med. – 1998. – Vol. 4. – N 8. – P. 929–933.
164. Atkins B.Z., Hueman M.T., Meuchel J.M., et al. Myogenic cell transplantation improves in vivo regional performance in infarcted rabbit myocardium // J Heart Lung Transplant. – 1999. – Vol. 18. – N 12. – P. 1173–1180.
165. Li R.K., Jia Z.Q., Weisel R.D., et al. Smooth muscle cell transplantation into myocardial scar tissue improves heart function // J Mol Cell Cardiol. – 1999. – Vol. 31. – P. 513–522.

166. Liu J., Wang H., Wang Y., et al. Exendin-4 pretreated adipose derived stem cells are resistant to oxidative stress and improve cardiac performance via enhanced adhesion in the infarcted heart // PLoS One. – 2014. – Vol. 9. – N 6. – P. e99756.
167. Yang J.J., Yang X., Liu Z.Q., et al. Transplantation of adipose tissue-derived stem cells overexpressing heme oxygenase-1 improves functions and remodeling of infarcted myocardium in rabbits // Tohoku J Exp Med. – 2012. – Vol. 226. – N 3. – P. 231–241.
168. Zhang D.Z., Gai L.Y., Liu H.W., et al. Transplantation of autologous adipose-derived stem cells ameliorates cardiac function in rabbits with myocardial infarction // Chin Med J (Engl). – 2007. – Vol. 120. – N 4. – P. 300–307.
169. Wang J.S., Shum-Tim D., Galipeau J., et al. Marrow stromal cells for cellular cardiomyoplasty: feasibility and potential clinical advantages // J Thorac Cardiovasc Surg. – 2000. – Vol. 120. – P. 999–1005.
170. Toma C., Pittenger M.F., Cahill K.S., et al. Human mesenchymal stem cells differentiate to a cardiomyocyte phenotype in the adult murine heart // Circulation. – 2002. – Vol. 105. – P. 93–98.
171. Orlic D., Kajstura J., Chimenti S., et al. Bone marrow cells regenerate infarcted myocardium // Nature. – 2001. – Vol. 410. – P. 701–705.
172. Murry C.E., Soonpaa M.H., Reinecke H., et al. Haematopoietic stem cells do not transdifferentiate into cardiac myocytes in myocardial infarcts // Nature. – 2004. – Vol. 428. – P. 664–668.
173. Penn M.S., Francis G.S., Ellis S.G., et al. Autologous cell transplantation for the treatment of damaged myocardium // Prog Cardiovasc Dis. – 2002. – Vol. 45. – P. 21–32.
174. Strauer B.E., Brehm M., Zeus T., et al. Repair of infarcted myocardium by autologous intracoronary mononuclear bone marrow cell transplantation in humans // Circulation. – 2002. – Vol. 106. – P. 1913–1918.
175. Shake J.G., Gruber P.J., Baumgartner W.A., et al. Mesenchymal stem cell implantation in a swine myocardial infarct model: engraftment and functional effects // Ann Thorac Surg. – 2002. – Vol. 73. – P. 1919–1925; discussion, 1926.
176. Min J.Y., Sullivan M.F., Yang Y., et al. Significant improvement of heart function by cotransplantation of human mesenchymal stem cells and fetal cardiomyocytes in postinfarcted pigs // Ann Thorac Surg. – 2002. – Vol. 74. – P. 1568–1575.
177. Mangi A.A., Noiseux N., Kong D., et al. Mesenchymal stem cells modified with Akt prevent remodeling and restore performance of infarcted hearts // Nat Med. – 2003. – Vol. 9. – P. 1195–1201.
178. Oh H., Bradfute S.B., Gallardo T.D., et al. Cardiac progenitor cells from adult myocardium: homing, differentiation, and fusion after infarction // Proc Natl Acad Sci USA. – 2003. – Vol. 100. – P. 12313–12318.
179. Barile L., Messina E., Giacomello A., et al. Endogenous Cardiac Stem Cells // Prog Cardiovasc Dis. – 2007. – Vol. 50. – N 1. – P. 31–48.
180. Smith R.R., Barile L., Cho H.C., et al. Regenerative Potential of Cardiosphere-Derived Cells Expanded From Percutaneous Endomyocardial Biopsy Specimens // Circulation. – 2007. – Vol. 115. – N 7. – P. 896–908.
181. Malliaras K., Zhang Y., Seinfeld J., et al. Cardiomyocyte proliferation and progenitor cell recruitment underlie therapeutic regenerationafter myocardial infarction in the adult mouse heart // EMBO Mol Med. – 2013. – Vol. 5. – N 2. – P. 191–209.
182. Mummery C., Ward–van Oostwaard D., Doevendans P., et al. Differentiation of human embryonic stem cells to cardiomyocytes: role of coculture with visceral endoderm-like cells // Circulation. – 2003. – Vol. 107. – P. 2733–2740.
183. Klug M.G., Soonpaa M.H., Koh G.Y., et al. Genetically selected cardiomyocytes from differentiating embryonic stem cells form stable intracardiac grafts // J Clin Invest. – 1996. – Vol. 98. – P. 216–224.

184. Kehat I., Kenyagin-Karsenti D., Snir M., et al. Human embryonic stem cells can differentiate into myocytes with structural and functional properties of cardiomyocytes // J Clin Invest. – 2001. – Vol. 108. – P. 407–414.
185. Etzion S., Battler A., Barbash I.M., et al. Influence of embryonic cardiomyocyte transplantation on the progression of heart failure in a rat model of extensive myocardial infarction // J Mol Cell Cardiol. – 2001. – Vol. 33. – P. 1321–1330.
186. Takahashi K., Yamanaka S. Induction of pluripotent stem cells from mouse embryonic and adult fibroblast cultures by defined factors // Cell. – 2006. – Vol. 126. – P. 663–676.
187. Yu J., Vodyanik M.A., Smuga-Otto K., et al. Induced pluripotent stem cell lines derived from human somatic cells // Science. – 2007. – Vol. 318. – P. 1917–1920.
188. Reinecke H., Murry C.E. Transmural replacement of myocardium after skeletal myoblast grafting into the heart. Too much of a good thing? // Cardiovasc Pathol. – 2000. – Vol. 9. – N 6. – P. 337–344.
189. Reinecke H., Poppa V., Murry C.E. Skeletal muscle stem cells do not transdifferentiate into cardiomyocytes after cardiac grafting // J Mol Cell Cardiol. – 2002. – Vol. 34. – N 2. – P. 241–249.
190. Gardner O.F., Alini M., Stoddart M.J. Mesenchymal Stem Cells Derived from Human Bone Marrow // Methods Mol Biol. – 2015. – Vol. 1340. – P. 41–52.
191. Mirotsou M., Zhang Z., Deb A., Zhang et al. Secreted frizzled related protein 2 (Sfrp2) is the key Akt-mesenchymal stem cell-released paracrine factor mediating myocardial survival and repair // Proc Natl Acad Sci USA. – 2007. – Vol. 104. – P. 1643–1648.
192. Balsam L.B., Wagers A.J., Christensen J.L., et al. Haematopoietic stem cells adopt mature haematopoietic fates in ischaemic myocardium // Nature. – 2004. – Vol. 428. – P. 668–673.
193. Dimmeler S., Zeiher A.M., Schneider M.D. Unchain my heart: the scientific foundations of cardiac repair // J Clin Invest. – 2005. – Vol. 115. – P. 572–583.
194. Le Blanc K. Immunomodulatory effects of fetal and adult mesenchymal stem cells // Cytotherapy. – 2003. – Vol. 5. – P. 485–489.
195. Meyer G.P., Wollert K.C., Lotz J., et al. Intracoronary bone marrow cell transfer after myocardial infarction: eighteen months' follow-up data from the randomized, controlled BOOST (BOne marrOw transfer to enhance ST-elevation infarct regeneration) trial // Circulation. – 2006. – Vol. 113. – N 10. – P. 1287–1294.
196. Bianco P., Cao X., Frenette P.S., et al. The meaning, the sense and the significance: translating the science of mesenchymal stem cells into medicine // Nat Med. – 2013. – Vol. 19. – N 1. – P. 35–42.
197. Hutcheson K.A., Atkins B.Z., Hueman M.T., et al. Comparison of benefits on myocardial performance of cellular cardiomyoplasty with skeletal myoblasts and fibroblasts // Cell Transplant. – 2000. – Vol. 9. – P. 359 –368.
198. Fujii T., Yau T.M., Weisel R.D., et al. Cell transplantation to prevent heart failure: a comparison of cell types // Ann Thorac Surg. – 2003. – Vol. 76. – P. 2062–2070; discussion 2070.
199. Chimenti I., Smith R.R., Li T.S., et al. Relative roles of direct regeneration versus paracrine effects of human cardiosphere-derived cells transplanted into infarcted mice // Circ Res. – 2010. – Vol. 106. – P. 971–980.
200. Messina E., De Angelis L., Frati G., et al. Isolation and expansion of adult cardiac stem cells from human and murine heart // Circ Res. – 2004. – Vol. 95. – P. 911–921.
201. Andersen D.C., Andersen P., Schneider M., et al. Murine ‘cardiospheres’ are not a source of stem cells with cardiomyogenic potential // Stem Cells. – 2009. – Vol. 27. – P. 1571–1581.
202. Zandstra P.W., Bauwens C., Yin T., et al. Scalable production of embryonic stem cell-derived cardiomyocytes // Tissue Eng. – 2003. – Vol. 9. – P. 767–778.
203. Kehat I., Khimovich L., Caspi O., et al. Electromechanical integration of cardiomyocytes derived from human embryonic stem cells // Nat Biotechnol. – 2004. – Vol. 22. – P. 1282–1289.
204. Laflamme M.A., Gold J., Xu C., et al. Formation of human myocardium in the rat heart from human embryonic stem cells // Am J Pathol. – 2005. – Vol. 167. – P. 663–671.

205. Xue T., Cho H.C., Akar F.G., et al. Functional integration of electrically active cardiac derivatives from genetically engineered human embryonic stem cells with quiescent recipient ventricular cardiomyocytes: insights into the development of cell-based pacemakers // Circulation. – 2005. – Vol. 111. – P. 11–20.
206. Takahashi K., Tanabe K., Ohnuki M. Induction of pluripotent stem cells from adult human fibroblasts by defined factors // Cell. – 2007. – Vol. 131. – P. 861–872.
207. Yoshida Y, Yamanaka S. Recent stem cell advances: induced pluripotent stem cells for disease modeling and stem cell–based regeneration // Circulation. – 2010. – Vol. 122. – N.1. – P. 80–87.
208. Okita K, Ichisaka T, Yamanaka S. Generation of germline–competent induced pluripotent stem cells // Nature. – 2007. – Vol. 448. – P. 313–317.
209. Nakagawa M, Koyanagi M, Tanabe K, et al. Generation of induced pluripotent stem cells without Myc from mouse and human fibroblasts // Nat Biotechnol. – 2008. – Vol. 26. – P. 101–106.
210. Aoi T, Yae K, Nakagawa M, et al. Generation of pluripotent stem cells from adult mouse liver and stomach cells // Science. – 2008. – Vol. 321. – P. 699–702.
211. Stadtfeld M, Brennand K, Hochedlinger K. Reprogramming of pancreatic Beta cells into induced pluripotent stem cells // Curr Biol. – 2008. – Vol. 18. – P. 890–894.
212. Kim JB, Zaehres H, Wu G, et al. Pluripotent stem cells induced from adult neural stem cells by reprogramming with two factors // Nature. – 2008. – Vol. 454. – P. 646–650.
213. Eminli S, Utikal J, Arnold K, et al. Reprogramming of neural progenitor cells into induced pluripotent stem cells in the absence of exogenous Sox2 expression // Stem Cells. – 2008. – Vol. 26. – P. 2467–2474.
214. Hanna J, Markoulaki S, Schorderet P, et al. Direct reprogramming of terminally differentiated mature B lymphocytes to pluripotency // Cell. – 2008. – Vol. 133. – P. 250–264.
215. Aasen T, Raya A, Barrero MJ, et al. Efficient and rapid generation of induced pluripotent stem cells from human keratinocytes // Nat Biotechnol. – 2008. – Vol. 26. – P. 1276–1284.
216. Loh YH, Agarwal S, Park IH, et al. Generation of induced pluripotent stem cells from human blood // Cell Stem Cell. – 2009. – Vol. 113. – P. 5476–5479.
217. Rossbach B, Hildebrand L, El–Ahmad L, et al. Generation of a human induced pluripotent stem cell line from urinary cells of a healthy donor using an integration free vector // Stem Cell Res. – 2016. – Vol. 16. – N. 2. – P. 314–317.
218. Hanna J, Wernig M, Markoulaki S, et al. Treatment of sickle cell anemia mouse model with iPS cells generated from autologous skin. – Science. – 2007. – Vol. 318. – P. 1920–1923.
219. Wernig M, Zhao JP, Pruszak J, et al. Neurons derived from reprogrammed fibroblasts functionally integrate into the fetal brain and improve symptoms of rats with Parkinson's disease. Proc Natl Acad Sci USA. – 2008. – Vol. 105. – P. 5856–5861.
220. Xu D, Alipio Z, Fink LM, et al. Phenotypic correction of murine hemophilia A using an iPS cell–based therapy // Proc Natl Acad Sci USA. – 2009. – Vol. 106. – P. 808–813.
221. Nelson TJ, Martinez–Fernandez A, Yamada S, et al. Repair of acute myocardial infarction by human stemness factors induced pluripotent stem cells // Circulation. – 2009. – Vol. 120. – P. 408–416.
222. Cho IK, Wang S, Mao H, Chan AWS. Genetic engineered molecular imaging probes for applications in cell therapy: emphasis on MRI approach // Am J Nucl Med Molecul Imag. – 2016. – Vol. 6. – P. 234–261.
223. Cohen B, Dafni H, Meir G, et al. Ferritin as an endogenous MRI reporter for noninvasive imaging of gene expression in C6 glioma tumors // Neoplasia. – 2005. – Vol. 7. – P. 109–117.
224. Genove G, DeMarco U, Xu H, et a. A new transgene reporter for in vivo magnetic resonance imaging // Nat Med. – 2005. – Vol. 11. – P. 450–454.
225. Vande Velde G, Raman Rangarajan J, Vreys R, et al. Quantitative evaluation of MRI–based tracking of ferritin–labeled endogenous neural stem cell progeny in rodent brain // Neuroimage. – 2012. – Vol. 62. – P. 367–380.

226. Koretsky A LY, Schorle H, Jaenisch R. Genetic control of MRI contrast by expression of the transferrin receptors // Proceedings ISMRM. – 1996.
227. Moore A, Josephson L, Bhorade RM, et al. Human transferrin receptor gene as a marker gene for MR imaging // Radiology. – 2001. – Vol. 221. – P. 244–250.
228. Deans AE, Wadghiri YZ, Bernas LM, et al. Cellular MRI contrast via coexpression of transferrin receptor and ferritin // Magn Reson Med. – 2006. – Vol. 56. – P. 51–59.
229. Bartelle BB, Szulk KU, Suero–Abreu GA, et al. Divalent metal transporter, DMT1: a novel MRI reporter protein // Magn Reson Med. – 2013. – Vol. 70. – P. 842–850.
230. Chen TT, Li L, Chung DH, et al. TIM–2 is expressed on B cells and in liver and kidney and is a receptor for H–ferritin endocytosis // J Exp Med. – 2005. – Vol. 202. – P. 955–965.
231. Todorich B, Zhang X, Slagle–Webb B, et al. Tim–2 is the receptor for H–ferritin on oligodendrocytes // Journal of Neurochemistry. – 2008. – Vol. 107. – P. 1495–1505.
232. Patrick PS, Rodrigues TB, Kettunen MI, et al. Development of Timd2 as a reporter gene for MRI // Magn Reson Med. – 2016. – Vol. 75. – P. 1697–1707.
233. van Zijl PC, Yadav NN. Chemical exchange saturation transfer (CEST): what is in a name and what isn't? // Magn Reson Med. – 2011. – Vol. 65. – P. 927–948.
234. Shapiro MG RR, Sperling LJ, Sun G, et al. Genetically encoded reporters for hyperpolarized xenon magnetic resonance imaging // Nat Chem. – 2014. – Vol. 6. – P. 629–634.
235. Arbab AS, Liu W, Frank JA. Cellular magnetic resonance imaging: current status and future prospects // Expert Rev Med Devices. – 2006. – Vol. 3. – P. 427–439.
236. de Vries IJ, Lesterhuis WJ, Barentsz JO, et al. Magnetic resonance tracking of dendritic cells in melanoma patients for monitoring of cellular therapy // Nature Biotechnol. – 2005. – Vol. 23. – P. 1407–1413.
237. Bulte JW, Kraitchman DL. Monitoring cell therapy using iron oxide MR contrast agents // Curr Pharm Biotechnol. – 2004. – Vol. 5. – P. 567–584.
238. Ahrens ET, Bulte JW. Tracking immune cells in vivo using magnetic resonance imaging // Nature Rev Immunol. – 2013. – Vol. 13. – P. 755–763.
239. Partlow KC, Chen J, Brant JA, et al. 19F magnetic resonance imaging for stem//progenitor cell tracking with multiple unique perfluorocarbon nanobeacons // FASEB J. – 2007. – Vol. 21. – P. 1647–1654.
240. Zhen Z, Xie J. Development of manganese–based nanoparticles as contrast probes for magnetic resonance imaging // Theranostics. – 2012. – Vol. 2. – P. 45–54.
241. Bara C, Ghodsizad A, Niehaus M, et al. In vivo echocardiographic imaging of transplanted human adult stem cells in the myocardium labeled with clinically applicable CliniMACS nanoparticles // J Am Soc Echocardiogr. – 2006. – Vol. 19. – P. 563–568.
242. Bulte JW. In vivo MRI cell tracking: clinical studies // AJR Am J Roentgenol. – 2009. – Vol. 193. – P. 314–325.
243. Zhu J, Zhou L, Xing, Wu F. Tracking neural stem cells in patients with brain trauma // N Engl J Med. – 2006. – Vol 355. – P. 2376–2378.
244. Laskey WK, Feinendegen LE, Neumann RD, Dilsizian V. Low–level ionizing radiation from noninvasive cardiac imaging: can we extrapolate estimated risks from epidemiologic data to the clinical setting? //JACC Cardiovascular Imaging. – 2010. – Vol. 3. – P. 517–524.
245. Brenner W, Aicher A, Eckey T, et al. 111In–labeled CD34+ hematopoietic progenitor cells in a rat myocardial infarction model // J Nucl Med. – 2004. – Vol. 45. – P. 512–518.
246. Wolfs E, Struys T, Notelaers T, et al. 18F–FDG labeling of mesenchymal stem cells and multipotent adult progenitor cells for PET imaging: effects on ultrastructure and differentiation capacity // J Nucl Med. – 2013. – Vol. 54. – P. 447–454.
247. Wu C, Ma G, Li J, et al. In vivo cell tracking via (1)(8)F–fluorodeoxyglucose labeling: a review of the preclinical and clinical applications in cell–based diagnosis and therapy. – Clin Imaging. – 2013. – Vol. 37. – P. 28–36.
248. Artemov D, Mori N, Ravi R, Bhujwalla ZM. Magnetic Resonance Molecular Imaging of the HER–2//neu Receptor // Cancer Research. – 2003. – Vol. 63. – P. 2723–2727.

249. Winter PM, Morawski AM, Caruthers SD, et al. Molecular imaging of angiogenesis in early–stage atherosclerosis with alpha(v)beta3–integrin–targeted nanoparticles // Circulation. – 2003. – Vol. 108. – N. 18. – P. 2270–2274.
250. Sosnovik DE, Schellenberger EA, Nahrendorf M, et al. Magnetic resonance imaging of cardiomyocyte apoptosis with a novel magneto–optical nanoparticle // Magn Reson Med. – 2005. – Vol. 54. – N. 3. – P. 718–724.
251. Nahrendorf M, Jaffer FA, Kelly KA, et al. Noninvasive vascular cell adhesion molecule–1 imaging identifies inflammatory activation of cells in atherosclerosis // Circulation. – 2006. – Vol. 114. – N. 14. – P. 1504–1511.
252. Lipinski MJ, Amirbekian V, Frias JC, et al. MRI to detect atherosclerosis with gadolinium–containing immunomicelles targeting the macrophage scavenger receptor // Magn Reson Med. – 2006. – Vol. 56. – N. 3. – P. 601–610.
253. Kang HW, Josephson L, Petrovsky A, et al. Magnetic resonance imaging of inducible E–selectin expression in human endothelial cell culture // Bioconjug Chem. – 2002. – Vol. 13. – N. 1. – P. 122–127.
254. Sipkins DA, Cheresh DA, Kazemi MR, et al. Detection of tumor angiogenesis in vivo by alphaVbeta3–targeted magnetic resonance imaging // Nat Med. – 1998. – Vol. 4. – N. 5. – P. 623–626.
255. Storrs RW, Tropper FD, Li HY, et al. Paramagnetic polymerized liposomes as new recirculating MR contrast agents // J Magn Reson Imaging. – 1995. – Vol. 5. – N. 6. – P. 719–724.
256. Anderson SA, Rader RK, Westlin WF, et al. Magnetic resonance contrast enhancement of neovasculature with alpha(v)beta(3)–targeted nanoparticles // Magn Reson Med. – 2000. – Vol. 44. – N. 3. – P. 433–439.
257. Lanza GM, Abendschein DR, Yu X, et al. Molecular imaging and targeted drug delivery with a novel, ligand–directed paramagnetic nanoparticle technology // Acad Radiol. – 2002. – Vol. 9. – Suppl 2. – P. S330–331.
258. Weissleder R, Lee AS, Fischman AJ, et al. Polyclonal human immunoglobulin G labeled with polymeric iron oxide: antibody MR imaging // Radiology. – 1991. – Vol. 181. – N. 1. – P. 245–249.
259. Zhao M, Beauregard DA, Loizou L, et al. Non–invasive detection of apoptosis using magnetic resonance imaging and a targeted contrast agent // Nat Med. – 2001. – Vol. 7. – N. 11. – P. 1241–1244.
260. Amsalem Y, Zweigerdt R, Schwanke K, et al. Iron–oxide labeling and outcome of transplanted mesenchymal stem cells in the infarcted myocardium // Circulation. – 2007. – Vol. 116. – P. I38–I45.
261. Terrovitis J, Stuber M, Youssef A, et al. Magnetic resonance imaging overestimates ferumoxide–labeled stem cell survival after transplantation in the heart // Circulation. – 2008. – Vol. 117. – P. 1555–1562.
262. Pawelczyk E, Arbab AS, Chaudhry A, et al. In vitro model of bromodeoxyuridine or iron oxide nanoparticle uptake by activated macrophages from labeled stem cells: implications for cellular therapy // Stem Cells. – 2008. – Vol. 26. – P. 1366–1375.
263. Pawelczyk E, Jordan EK, Balakumaran A, et al. In vivo transfer of intracellular labels from locally implanted bone marrow stromal cells to resident tissue macrophages // PloS One. – 2009. – Vol. 4. – P. e6712.
264. Arbab AS, Frank JA. Cellular MRI and its role in stem cell therapy // Regenerative Medicine 2008. – Vol. 3. – P. 199–215.
265. Schafer R, Kehlbach R, Müller M, et al. Labeling of human mesenchymal stromal cells with superparamagnetic iron oxide leads to a decrease in migration capacity and colony formation ability // Cytotherapy. – 2009. – Vol. 11. – P. 68–78.
266. Kostura L, Kraitchman DL, Mackay AM, et al. Feridex labeling of mesenchymal stem cells inhibits chondrogenesis but not adipogenesis or osteogenesis // NMR Biomed. – 2004. – Vol. 17. – P. 513–517.

267. Arbab AS, Yocum GT, Rad AM, et al. Labeling of cells with ferumoxides–protamine sulfate complexes does not inhibit function or differentiation capacity of hematopoietic or mesenchymal stem cells // NMR Biomed. – 2005. – Vol. 18. – P. 553–559.
268. Campan M, Lionetti V, Aquaro GD, et al. Ferritin as a reporter gene for in vivo tracking of stem cells by 1.5–T cardiac MRI in a rat model of myocardial infarction // Am J Physiol Heart Circ Physiol. – 2011. – Vol. 300. – P. H2238–2250.
269. Gyongyosi M, Blanco J, Marian T, et al. Serial noninvasive in vivo positron emission tomographic tracking of percutaneously intramyocardially injected autologous porcine mesenchymal stem cells modified for transgene reporter gene expression // Circ Cardiovasc Img. – 2008. – Vol. 1. – P. 94–103.
270. Willmann JK, Paulmurugan R, Rodriguez–Porcel M, et al. Imaging gene expression in human mesenchymal stem cells: from small to large animals // Radiology. – 2009. –Vol. 252. – P. 117–127.
271. Yaghoubi SS, Jensen MC, Satyamurthy N, et al. Noninvasive detection of therapeutic cytolytic T cells with 18F–FHBG PET in a patient with glioma // Nature clinical practice. Oncology. – 2009. – Vo. 6. – P. 53–58.
272. Zhang Y, Ruel M, Beanlands RS, et al. Tracking stem cell therapy in the myocardium: applications of positron emission tomography // Curr Pharm Des. – 2008. – Vol. 14. – N. 36. – P. 3835–3853.
273. Yaghoubi SS, Campbell DO, Radu CG, Czernin J. Positron emission tomography reporter genes and reporter probes: gene and cell therapy applications // Theranostics. – 2012. – Vol. 2. – N. 4. – P. 374–391.
274. Tannous BA, Grimm J, Perry KF, et al. Metabolic biotinylation of cell surface receptors for in vivo imaging // Nat Methods. – 2006. – Vol. 3. – N. 5. – P. 391–396. Erratum in: Nat Methods. 2006. – Vol. 3. – N. 8. – P. 657.
275. So PW. Kalber T, Hunt D, et al. Efficient and rapid labeling of transplanted cell populations with superparamagnetic iron oxide nanoparticles using cell surface chemical biotinylation for in vivo monitoring by MRI // Cell Transplantation. – 2010. – Vol. 19. – N. 4. – P. 419–429.
276. Templin C, Zweigerdt R, Schwanke K, et al. Transplantation and tracking of human–induced pluripotent stem cells in a pig model of myocardial infarction: assessment of cell survival, engraftment, and distribution by hybrid single photon emission computed tomography/computed tomography of sodium iodide symporter transgene expression // Circulation. – 2012. – Vol. 126. P. 430–439.
277. Zhou J, Payen JF, Wilson DA, et al. Using the amide proton signals of intracellular proteins and peptides to detect pH effects in MRI // Nat Med. – 2003. – Vol. 9. – P. 1085–1090.
278. Bar–Shir A, Liu G, Greenberg MM, et al. Synthesis of a probe for monitoring HSV1–tk reporter gene expression using chemical exchange saturation transfer MRI // Nat Protoc. – 2013. – Vol. 8. – N. 12. – P. 2380–2391.
279. Berger C, Flowers ME, Warren EH, Riddell SR. Analysis of transgene–specific immune responses that limit the in vivo persistence of adoptively transferred HSV–TK–modified donor T cells after allogeneic hematopoietic cell transplantation // Blood. – 2006. – Vol. 107. – N. 6. – P. 2294–2302.
280. Seggewiss R, Pittaluga S, Adler RL, et al. Acute myeloid leukemia is associated with retroviral gene transfer to hematopoietic progenitor cells in a rhesus macaque // Blood. – 2006. – Vol. 107. – N. 10. – P. 3865–3867.
281. Bauer LM, Situ SF, Griswold MA, Samia AC. Magnetic Particle Imaging Tracers: State–of–the–Art and Future Directions // J Phys Chem Lett. – 2015. – Vol. 6. – P. 2509–2517.
282. Zheng B, Vazin T, Goodwill PW, et al. Magnetic Particle Imaging tracks the long–term fate of in vivo neural cell implants with high image contrast // Sci Rep. – 2015. – Vol. 5. – P. 14055.
283. Zheng B, von See MP, Yu E, et al. Quantitative Magnetic Particle Imaging Monitors the Transplantation, Biodistribution, and Clearance of Stem Cells In Vivo // Theranostics. – 2016. – Vol. 6. – P. 291–301.

284. Bulte JW, Walczak P, Janowski M, et al. Quantitative "Hot Spot" Imaging of Transplanted Stem Cells using Superparamagnetic Tracers and Magnetic Particle Imaging (MPI) // Tomography. – 2015. – Vol.1. – P. 91–97.
285. Shi Y, Do JT, Desponts C, et al. A combined chemical and genetic approach for the generation of induced pluripotent stem cells // Cell Stem Cell. – 2008. – Vol. 2. – P. 525–528.
286. Kilcoyne SH, Cywinski R. Ferritin: a model superparamagnet // Journal of Magnetism and Magnetic Materials. – 1995. – Vol. 140. – P. 1466–1467.
287. Pantopoulos K, Porwal SK, Tartakoff A, Devireddy L. Mechanisms of mammalian iron homeostasis // Biochemistry. – 2012. – Vol. 51. – P. 5705–5724.
288. Fenton HJH. Oxidation of tartaric acid in presence of iron // J Chem Soc Trans. – 1894. – Vol. 65. – N. 65. – P. 899–911.
289. Crichton RR, Wilmet S, Legssyer R, Ward RJ. Molecular and cellular mechanisms of iron homeostasis and toxicity in mammalian cells // J Inorg Biochem. – 2002. – Vol. 91. – P. 9–18.
290. Wang J, Pantopoulos K. Regulation of cellular iron metabolism // Biochem J. – 2011. – Vol. 434. – P. 365–381.
291. Hentze MW, Muckenthaler MU, Galy B, Camaschella C. Two to tango: regulation of mammalian iron metabolism // Cell. – 2010. – Vol. 142. – P. 24–38.
292. Ponka P, Lok CN. The transferrin receptor: role in health and disease // Int J Biochem Cell Biol. - 1999. – Vol. 31. – P. 1111–1137.
293. Wada HG, Hass PE, Sussman HH. Transferrin receptor in human placental brush border membranes. Studies on the binding of transferrin to placental membrane vesicles and the identification of a placental brush border glycoprotein with high affinity for transferrin // J Biol Chem. – 1979. – Vol. 254. – P. 12629–12635.
294. Davies M, Parry JE, Sutcliffe RG. Examination of different preparations of human placental plasma membrane for the binding of insulin, transferrin and immunoglobulins // J Reprod Fertil. - 1981. – Vol. 63. – P. 315–324.
295. Gatter KC, Brown G, Trowbridge IS, et al. Transferrin receptors in human tissues: their distribution and possible clinical relevance // J Clin Pathol. – 1983. – Vol. 36. – P. 539–545.
296. Enns CA, Shindelman JE, Tonik SE, Sussman HH. Radioimmunochemical measurement of the transferrin receptor in human trophoblast and reticulocyte membranes with a specific anti–receptor antibody // Proc Natl Acad Sci USA. – 1981. – Vol. 78. – P. 4222–4225.
297. Thorstensen K, Romslo I. The role of transferrin in the mechanism of cellular iron uptake // Biochem J. – 1990. – Vol. 271. – P. 1–9.
298. Anderson GJ, Vulpe CD. Mammalian iron transport // Cell Mol Life Sci. – 2009. – Vol. 66. – P. 3241–3261.
299. Aisen P. Entry of iron into cells: a new role for the transferrin receptor in modulating iron release from transferrin // Ann Neurol. – 1992. – Vol. 32. – Suppl: S62–68.
300. Levy JE, Jin O, Fujiwara Y, et al. Transferrin receptor is necessary for development of erythrocytes and the nervous system // Nat Genet. – 1999. – Vol. 21. – P. 396–399.
301. Meldrum F, Heywood B, Mann S. Magnetoferritin: in vitro synthesis of a novel magnetic protein // Science. – 1992. – Vol. 257. – P. 522–523.
302. Ford GC, Harrison PM, Rice DW, et al. Ferritin: Design and Formation of an Iron–Storage Molecule. Philosophical Transactions of the Royal Society of London // Biological Sciences. – 1984. – Vol. 304. – P. 551–565.
303. Harrison PM, Arosio P. Ferritins: Molecular properties, iron storage function and cellular regulation // Biochimica Et Biophysica Acta–Bioenergetics. – 1996. – Vol. 1275. – P. 161–203.
304. Treffry A, Zhao Z, Quail MA, et al. Dinuclear center of ferritin: studies of iron binding and oxidation show differences in the two iron sites // Biochemistry. – 1997. – Vol. 36. – P. 432–441.
305. Frankel RB, Papaefthymiou GC, Watt GD. Variation of Superparamagnetic Properties with Iron Loading in Mammalian Ferritin // Hyperfine Interactions. – 1991. – Vol. 66. – P. 71–82.

306. Zhao G, Bou–Abdallah F, Arosio P, et al. Multiple pathways for mineral core formation in mammalian apoferritin. The role of hydrogen peroxide // Biochemistry. – 2003. – Vol. 42. – P. 3142–3150.
307. Arosio P, Levi S. Ferritin, iron homeostasis, and oxidative damage // Free Radic Biol Med. – 2002. – Vol. 33. – P. 457–463.
308. Valko M, Morris H, Cronin MT. Metals, toxicity and oxidative stress // Curr Med Chem. – 2005. – Vol. 12. – P. 1161–1208.
309. Munro HN, Linder MC. Ferritin: structure, biosynthesis, and role in iron metabolism // Physiol Rev. – 1978. – Vol. 58. – P. 317–396.
310. Theil EC. Ferritin: structure, gene regulation, and cellular function in animals, plants, and microorganisms // Annu Rev Biochem. – 1987. – Vol 56. – P. 289–315.
311. Ferreira C, Bucchini D, Martin ME, et al. Early embryonic lethality of H ferritin gene deletion in mice // J Biol Chem. – 2000. – Vol. 275. – P. 3021–3024.
312. Li JY, Paragas N, Ned RM, et al. Scara5 is a ferritin receptor mediating non–transferrin iron delivery // Dev Cell. – 2009. – Vol. 16. – P. 35–46.
313. Shayeghi M, Latunde–Dada GO, Oakhill JS, et al. Identification of an intestinal heme transporter // Cell. – 2005. – Vol. 122. – P. 789–801.
314. Rajagopal A, Rao AU, Amigo J, et al. Haem homeostasis is regulated by the conserved and concerted functions of HRG–1 proteins // Nature. – 2008. – Vol. 453. – P. 1127–1131.
315. Levi S, Corsi B, Bosisio M, et al. A human mitochondrial ferritin encoded by an intronless gene // J Biol Chem. – 2001. – Vol. 276. – P. 24437–24440.
316. Santambrogio P, Biasiotto G, Sanvito F, et l. Mitochondrial ferritin expression in adult mouse tissues // J Histochem Cytochem. – 2007. – Vol. 55. – P. 1129–1137.
317. Nie G, Sheftel AD, Kim SF, Ponka P. Overexpression of mitochondrial ferritin causes cytosolic iron depletion and changes cellular iron homeostasis // Blood. – 2005. – Vol. 105. – P. 2161–2167.
318. Corsi B, Cozzi A, Arosio P, et al. Human Mitochondrial Ferritin Expressed in HeLa Cells Incorporates Iron and Affects Cellular Iron Metabolism // J Biol Chem. – 2002. – Vol. 277. – P. 22430–22437.
319. Wish JB. Assessing Iron Status: Beyond Serum Ferritin and Transferrin Saturation // Clinical Journal of the American Society of Nephrology. – 2006. – Vol. 1. – P. S4–S8.
320. Weir MP, Sharp GA, Peters TJ. Electron microscopic studies of human haemosiderin and ferritin // Journal of Clinical Pathology. – 1985. – Vol. 38. – P. 915–918.
321. De Domenico I, Ward DM, Kaplan J. Specific iron chelators determine the route of ferritin degradation // Blood. – 2009. – Vol. 114. – P. 4546–4551.
322. Koorts AM, Viljoen M. Ferritin and ferritin isoforms I: Structure–function relationships, synthesis, degradation and secretion // Archives of Physiology and Biochemistry. – 2007. – Vol. 113. – P. 30–54.
323. Koorts AM, Viljoen M. Ferritin and ferritin isoforms II: Protection against uncontrolled cellular proliferation, oxidative damage and inflammatory processes // Archives of Physiology and Biochemistry. – 2007. – Vol. 113. – P. 55–64.
324. Schenck JF, Zimmerman EA. High–field magnetic resonance imaging of brain iron: birth of a biomarker? // NMR Biomed. – 2004. – Vol. 17. – P. 433–445.
325. Berg D, Youdim MB. Role of iron in neurodegenerative disorders // Top Magn Reson Imaging. – 2006. – Vol. 17. – P. 5–17.
326. Ropele S, Kilsdonk ID, Wattjes MP, et al. Determinants of iron accumulation in deep grey matter of multiple sclerosis patients // Multiple Sclerosis Journal. – 2014. – Vol. 20. – P. 1692–1698.
327. Khalil M, Langkammer C, Pichler A, et al. Dynamics of brain iron levels in multiple sclerosis: A longitudinal 3T MRI study // Neurology. – 2015. – Vol. 84. – P. 2396–2402.
328. Ghadery C, Pirpamer L, Hofer E, et al. R2* mapping for brain iron: associations with cognition in normal aging // Neurobiology of Aging. – 2015. – Vol. 36. – P. 925–932.

329. Aisen P. Transferrin, the transferrin receptor, and the uptake of iron by cells // Met Ions Biol Syst. – 1998. – Vol. 35. –P. 85–631.
330. Huebers HA, Finch CA. The physiology of transferrin and transferrin receptors // Physiol Rev. – 1987. – Vol. 67. – P. 520–582.
331. Bridges KR, Cudkowicz A. Effect of iron chelators on the transferrin receptor in K562 cells // J Biol Chem. – 1984. – Vol. 259. – P. 12970–12977.
332. Rao KK, Shapiro D, Mattia E, et al. Effects of alterations in cellular iron on biosynthesis of the transferrin receptor in K562 cells // Mol Cell Biol. – 1985. – Vol. 5. – P. 595–600.
333. Sotak CH, Sharer K, Koretsky AP. Manganese cell labeling of murine hepatocytes using manganese(III)–transferrin // Contrast Media Mol Imaging. – 2008. – Vol. 3. – P. 95–105.
334. Ono K, Fuma K, Tabata K, Sawada M. Ferritin reporter used for gene expression imaging by magnetic resonance // Biochem Biophys Res Commun. – 2009. – Vol. 388. – P. 589–594.
335. Kim HS, Cho HR, Choi SH, et al. In vivo imaging of tumor transduced with bimodal lentiviral vector encoding human ferritin and green fluorescent protein on a 1.5T clinical magnetic resonance scanner // Cancer Res. – 2010. – Vol. 70. – P. 7315–7324.
336. Cohen B, Ziv K, Plaks V, et al. MRI detection of transcriptional regulation of gene expression in transgenic mice // Nat Med. – 2007. – Vol. 13. – P. 498–503.
337. Ziv K, Meir G, Harmelin A, et al. Ferritin as a reporter gene for MRI: chronic liver over expression of H–ferritin during dietary iron supplementation and aging // NMR Biomed. – 2010. - Vol. 23. – P. 523–531.
338. Uchida M, Terashima M, Cunningham CH, et al. A human ferritin iron oxide nano–composite magnetic resonance contrast agent // Magn Reson Med. – 2008. – Vol. 60. – P. 1073–1081.
339. Terashima M, Uchida M, Kosuge H, et al. Human ferritin cages for imaging vascular macrophages // Biomaterials. – 2011. – Vol. 32. – P. 1430–1437.
340. Bulte JWM, Douglas T, Mann S, et al. Magnetoferritin: biomineralization as a novel molecular approach in the design of iron–oxide–based magnetic resonance contrast agents // Invest Radiol. – 1994. – Vol. 29. – P. S214–S216.
341. Bulte JWM, Douglas T, Mann S, et al. Initial assessment of magnetoferritin biokinetics and proton relaxation enhancement in rats // Acad Radiol. – 1995. – Vol. 2. – P. 871–878.
342. Iordanova B, Hitchens TK, Robison CS, Ahrens ET. Engineered Mitochondrial Ferritin as a Magnetic Resonance Imaging Reporter in Mouse Olfactory Epithelium // PLOS ONE. – 2013. – Vol. 8. – P. e72720.
343. Feng Y, Liu Q, Zhu J, Xie F, Li L. Efficiency of ferritin as an MRI reporter gene in NPC cells is enhanced by iron supplementation // J Biomed Biotechnol. – 2012. – Vol. 2012. – P. 434878.
344. Liu J, Cheng EC, Long RC, et al. Noninvasive monitoring of embryonic stem cells in vivo with MRI transgene reporter // Tissue Eng Part C Methods. – 2009. – Vol. 15. – P. 739–747.
345. Iordanova B, Robison CS, Ahrens ET. Design and characterization of a chimeric ferritin with enhanced iron loading and transverse NMR relaxation rate // J Biol Inorg Chem. – 2010. – Vol. 15. – P. 957–965.
346. Vande Velde G, Rangarajan JR, Toelen J, et al. Evaluation of the specificity and sensitivity of ferritin as an MRI reporter gene in the mouse brain using lentiviral and adeno–associated viral vectors // Gene Ther. – 2011. – Vol. 18. – P. 594–605.
347. Aung W, Hasegawa S, Koshikawa–Yano M, et al. Visualization of in vivo electroporation–mediated transgene expression in experimental tumors by optical and magnetic resonance imaging // Gene Ther. – 2009. – Vol. 16. – P. 830–839.
348. Blakemore R. Magnetotactic bacteria // Science. – 1975. – Vol. 190. – P. 377–379.
349. Bazylinski DA, Frankel RB. Magnetosome formation in prokaryotes // Nat Rev Microbiol. – 2004. – Vol. 2. – P. 217–230.
350. Goldhawk DE, Rohani R, Sengupta A, et al. Using the magnetosome to model effective gene–based contrast for magnetic resonance imaging // Wiley Interdiscip Rev Nanomed Nanobiotechnol. – 2012. – Vol. 4. – P. 378–388.

351. Nakamura C, Burgess JG, Sode K, Matsunaga T. An iron–regulated gene, magA, encoding an iron transport protein of Magnetospirillum sp. strain AMB–1 // J Biol Chem. – 1995. – Vol. 270. – P. 28392–28396.
352. Murat D, Quinlan A, Vali H, Komeili A. Comprehensive genetic dissection of the magnetosome gene island reveals the step–wise assembly of a prokaryotic organelle // Proceedings of the National Academy of Sciences. – 2010. – Vol. 107. – P. 5593–5598.
353. Uebe R, Henn V, Schuler D. The MagA protein of Magnetospirilla is not involved in bacterial magnetite biomineralization // J Bacteriol. – 2012. – Vol. 194. – P. 1018–1023.
354. Zurkiya O, Chan AW, Hu X. MagA is sufficient for producing magnetic nanoparticles in mammalian cells, making it an MRI reporter // Magn Reson Med. – 2008. – Vol. 59. – P. 1225–1231.
355. Goldhawk DE, Lemaire C, McCreary CR, et al. Magnetic resonance imaging of cells overexpressing MagA, an endogenous contrast agent for live cell imaging // Mol Imaging. – 2009. – Vol. 8. – P. 129–139.
356. Sengupta A, Quiaoit K, Thompson RT, et al. Biophysical features of MagA expression in mammalian cells: implications for MRI contrast // Front Microbiol. – 2014. – Vol. 5. – P. 29.
357. Zhang XY, Robledo BN, Harris SS, Hu XP. A bacterial gene, mms6, as a new reporter gene for magnetic resonance imaging of mammalian cells // Mol Imaging. – 2014. – Vol. 13. - doi: 10.2310/7290.2014.00046.
358. Radoul M, Lewin L, Cohen B, et al. Genetic manipulation of iron biomineralization enhances MR relaxivity in a ferritin–M6A chimeric complex // Scientific Reports. – 2016. – Vol. 6. – P. 26550.
359. Han J, Seaman WE, Di X, et al. Iron Uptake Mediated by Binding of H–Ferritin to the TIM–2 Receptor in Mouse Cells // PLOS ONE. – 2011. – Vol. 6. – P. e23800.
360. Elhami E, Dietz B, Xiang B, et al. Assessment of three techniques for delivering stem cells to the heart using PET and MR imaging // EJNMMI Research. – 2013. – Vol. 3. – N. 1. – P. 72.
361. Kang WJ, Kang HJ, Kim HS, et al. Tissue distribution of 18F–FDG–labeled peripheral hematopoietic stem cells after intracoronary administration in patients with myocardial infarction // J Nucl Med. – 2006. – Vol. 47. – N. 8. – P. 1295–1301.
362. Schachinger V, Aicher A, Döbert N, et al. Pilot trial on determinants of progenitor cell recruitment to the infarcted human myocardium // Circulation. – 2008. – Vol. 118. – P. 1425–1432.
363. van der Bogt KE, Sheikh AY, Schrepfer S, et al. Comparison of different adult stem cell types for treatment of myocardial ischemia // Circulation. – 2008. – Vol. 118. – P. S121–129.
364. Robey TE, Saiget MK, Reinecke H, Murry CE. Systems approaches to preventing transplanted cell death in cardiac repair // J Mol Cell Cardiol. – 2008. – Vol. 45. – N. 4. – P. 567–581.
365. Mitchell AJ, Sabondjian E, Blackwood KJ, et al. Comparison of the myocardial clearance of endothelial progenitor cells injected early versus late into reperfused or sustained occlusion myocardial infarction // Int J Cardiovasc Imaging. – 2013. – Vol. 29. – N. 2. – P. 497–504.
366. McGill LA, Ismail TF, Nielles–Vallespin S, et al. Reproducibility of in–vivo diffusion tensor cardiovascular magnetic resonance in hypertrophic cardiomyopathy // J Cardiovasc Magn Reson. - 2012. – Vol. 14. – P. 86.
367. Mekkaoui C, Huang S, Chen HH, et al. Fiber architecture in remodeled myocardium revealed with a quantitative diffusion CMR tractography framework and histological validation // J Cardiovasc Magn Reson. – 2012. – Vol. 14. – P. 70.
368. Shiba Y, Fernandes S, Zhu WZ, et al. Human ES–cell–derived cardiomyocytes electrically couple and suppress arrhythmias in injured hearts // Nature. – 2012. – Vol. 489. –P. 322–325.
369. Chong JJ, Yang X, Don CW, et al. Human embryonic–stem–cell–derived cardiomyocytes regenerate non–human primate hearts // Nature. – 2014. – Vol. 510. – N. 7504. – P. 273–277.
370. Power JM, Tonkin AM. Large animal models of heart failure // Aust N Z J Med. –1999. – Vol. 29. – N. 3. – P. 395–402.

371. McGreevy JW, Hakim CH, McIntosh MA, Duan D. Animal models of Duchenne muscular dystrophy: from basic mechanisms to gene therapy // Dis Model Mech. – 2015. – Vol. 8. – N. 3. - P. 195–213.
372. Ostergaard G, Hansen HN, Ottesen JL. Physiological, Hematological, and Clinical Chemistry Parameters, Including Conversion Factors. // In: Handbook of laboratory animal science, Volume I: Essential Principles and Practices. Boca Raton, FL, CRC Press. 3rd ed, 2010. – Vol. 1. – P. 667–707.
373. Milani–Nejad N, Janssen PM. Small and large animal models in cardiac contraction research: advantages and disadvantages // Pharmacol Ther. – 2014. – Vol. 141. – N. 3. – P. 235–49.
374. Epstein FH, Yang Z, Gilson WD, et al. MR Tagging early after myocardial infarction in mice demonstrates contractile dysfunction in adjacent and remote regions // Magn Res Med. – 2002. – Vol. 48. – P. 399–403.
375. Epstein FH, Yang Z, Roy RJ, et al. CMR Demonstrates Reduced Post–infarct left Ventricular Remodeling in Mice with iNOS Inhibition // J Cardiovasc Magn Res. – 2005. – Vol. 7. – P. 29–30.
376. Nagueh SF, Appleton CP, Gillebert TC, et al. Recommendations for the evaluation of left ventricular diastolic function by echocardiography // J Am Soc Echocardiogr. – 2009. – Vol. 22. – N. 2. – P. 107–133.
377. Bottomley PA, Hardy CJ, Weiss RG. Correcting human heart 31P NMR spectra for partial saturation. Evidence that saturation factors for PCr//ATP are homogeneous in normal and diseased states // J Mag Res. – 1991. – Vol. 95. – P. 341–355.
378. Silberstein L, Webster SG, Travis M, Blau HM. Developmental progression of myosin gene expression in cultured muscle cells // Cell. – 1986. – Vol. 46. – N. 7. – P. 1075–1081.
379. Thomson JA, Itskovitz–Eldor J, Shapiro SS, et al. Embryonic stem cell lines derived from human blastocysts // Science. – 1998. – Vol. 282. – P. 1145–1147.
380. Xu C, Inokuma MS, Denham J, et al. Feeder–free growth of undifferentiated human embryonic stem cells // Nat Biotechnol. – 2001. – Vol. 19. – N. 10. – P. 971–974.
381. Gold J. Efficient serum–free generation of cardiomyocytes from human embryonic stem cells in the absence of embryoid bodies // Circulation. – 2005. – Vol. 112. – P. 14.
382. Ren Y, Lee MY, Schliffke S, et al. Small molecule Wnt inhibitors enhance the efficiency of BMP–4–directed cardiac differentiation of human pluripotent stem cells // J Mol Cell Cardiol. – 2011. – Vol. 51. – N. 3. – P. 280–287.
383. Minami I, Yamada K, Otsuji TG, et al. A small molecule that promotes cardiac differentiation of human pluripotent stem cells under defined, cytokine– and xeno–free conditions // Cell Rep. – 2012. – Vol. 2. – N. 5. – P. 1448–1460.
384. Bialik S, Cryns VL, Drincic A, et al. The mitochondrial apoptotic pathway is activated by serum and glucose deprivation in cardiac myocytes // Circ Res. – 1999. – Vol. 85. – N. 5. – P. 403–414.
385. Malhotra R, Brosius FC. Glucose uptake and glycolysis reduce hypoxia–induced apoptosis in cultured neonatal rat cardiac myocytes // J Biol Chem. – 1999. – Vol. 274. – N. 18. – P. 12567–12575.
386. Shimizu S, Konishi A, Kodama T, Tsujimoto Y. BH4 domain of antiapoptotic Bcl–2 family members closes voltage–dependent anion channel and inhibits apoptotic mitochondrial changes and cell death // Proc Natl Acad Sci USA. – 2000. – Vol. 97. – P. 3100–3105.
387. Griffiths EJ, Halestrap AP. Protection by Cyclosporin A of ischemia//reperfusion–induced damage in isolated rat hearts // J Mol Cell Cardiol. – 1993. – Vol. 25. – P. 1461–1469.
388. Halestrap AP, Connern CP, Griffiths EJ, Kerr PM. Cyclosporin A binding to mitochondrial cyclophilin inhibits the permeability transition pore and protects hearts from ischaemia//reperfusion injury // Mol Cell Biochem. – 1997. – Vol. 174. – P. 167–172.
389. Baines CP, Kaiser RA, Purcell NH, et al. Loss of cyclophilin D reveals a critical role for mitochondrial permeability transition in cell death // Nature. – 2005. – Vol. 434. – P. 658–662.

390. Reiss K, Cheng W, Pierzchalski P, et al. Insulin–like growth factor–1 receptor and its ligand regulate the reentry of adult ventricular myocytes into the cell cycle // Exp Cell Res. – 1997. – Vol. 235. – P. 198–209.
391. Mehrhof FB, Müller FU, Bergmann MW, et al. In cardiomyocyte hypoxia, insulin–like growth factor–I–induced antiapoptotic signaling requires phosphatidylinositol–3–OH–kinase–dependent and mitogen–activated protein kinase–dependent activation of the transcription factor cAMP response element–binding protein // Circulation. – 2001. – Vol. 104. – P. 2088–2094.
392. Vanden Hoek T, Becker LB, Shao ZH, et al. Preconditioning in cardiomyocytes protects by attenuating oxidant stress at reperfusion // Circ Res. – 2000. – Vol. 86. – P. 541–548.
393. Akao M, Ohle, A, O'Rourke B, Marban E. Mitochondrial ATP–sensitive potassium channels inhibit apoptosis induced by oxidative stress in cardiac cells // Circ Res. – 2001. – Vol. 88. – P. 1267–1275.
394. Akao M, O'Rourke B, Kusuoka H, et al. Differential actions of cardioprotective agents on the mitochondrial death pathway // Circ Res. – 2003. – Vol. 92. – P. 195–202.
395. Weier HU, Lucas JN, Poggensee M, et al. Two–color hybridization with high complexity chromosome–specific probes and a degenerate alpha satellite probe DNA allows unambiguous discrimination between symmetrical and asymmetrical translocations // Chromosoma. – 1991. – Vol. 100. – P. 371–376.
396. Gilson WD, Kraitchman DL. Cardiac Magnetic Resonance Imaging in Small Rodents using Clinical 1.5T and 3.0T Scanners // Methods. – 2007. – Vol. 43. – N. 1. – P. 35–45.
397. Selvanayagam JB, Jerosch–Herold M, Porto I, et al. Resting myocardial blood flow is impaired in hibernating myocardium: a magnetic resonance study of quantitative perfusion assessment // Circulation. – 2005. – Vol. 112. – P. 3289–3296.
398. Cury RC, Cattani CA, Gabure LA, et al. Diagnostic performance of stress perfusion and delayed–enhancement MR imaging in patients with coronary artery disease // Radiology. – 2006. - Vol. 240. – P. 39–45.
399. Tsukiji M, Nguyen P, Narayan G, et al. Peri–infarct ischemia determined by cardiovascular magnetic resonance evaluation of myocardial viability and stress perfusion predicts future cardiovascular events in patients with severe ischemic cardiomyopathy // Journal of Cardiovascular Magnetic Resonance. – 2006. – Vol. 8. – P. 773–779.
400. Gerber BL, Raman SV, Nayak K, et al. Myocardial first–pass perfusion cardiovascular magnetic resonance: history, theory, and current state of the art // Journal of Cardiovascular Magnetic Resonance. – 2008. – Vol. 10. – P. 18.
401. Doesch C, Seeger A, Doering J, et al. Risk stratification by adenosine stress cardiac magnetic resonance in patients with coronary artery stenoses of intermediate angiographic severity // JACC: Cardiovascular Imaging. – 2009. – Vol. 2. – P. 424–433.
402. Korosoglou G, Elhmidi Y, Steen H, et al. Prognostic value of high–dose dobutamine stress magnetic resonance imaging in 1,493 consecutive patients: assessment of myocardial wall motion and perfusion // Journal of the American College of Cardiology. – 2010. – Vol. 56. – P. 1225–1234.
403. Bingham SE, Hachamovitch R. Incremental prognostic significance of combined cardiac magnetic resonance imaging, adenosine stress perfusion, delayed enhancement, and left ventricular function over preimaging information for the prediction of adverse events // Circulation. – 2011. – Vol. 123. – P. 1509–1518.
404. Diesbourg LD, Prato FS, Wisenberg G, et al. Quantification of myocardial blood flow and extracellular volumes using a bolus injection of Gd–DTPA: kinetic modeling in canine ischemic disease // Magn Reson Med. – 1992. – Vol. 23. – P. 239–253.
405. Kalman RE. A new approach to linear filtering and prediction problems // J Basic Eng. – 1960. – Vol. 82. – P. 35–45.
406. Hajnal JV, Saeed N, Oatridge A, et al. Detection of subtle brain changes using subvoxel registration and subtraction of serial MR images // J Comput Assist Tomogr. – 1995. – Vol. 19. – P. 677– 691.

407. Kerwin WS, Cai J, Yuan C. Noise and motion correction in dynamic contrast–enhanced MRI for analysis of atherosclerotic lesions // Magn Reson Med. – 2002. – Vol. 47. – P. 1211–1217.
408. Weiss RG, Kalil–Filho R, Herskowitz A, et al. Tricarboxylic acid cycle activity in post–ischemic rat hearts // Circulation. – 1993. – Vol. 87. – P. 270–282.
409. von Kienlin M, Rosch C, Le Fur Y, et al. Three–dimensional 31P magnetic resonance spectroscopic imaging of regional high–energy phosphate metabolism in injured rat heart // Magn Reson Med. – 1998. – Vol. 39. – N. 5. – P. 731–741.
410. Neubauer S, Horn M, Naumann A, et al. Impairment of energy metabolism in intact residual myocardium of rat hearts with chronic myocardial infarction // J Clin Invest. – 1995. – Vol. 95. – P. 1092–1100.
411. Neubauer S, Hu K, Horn M, et al. Functional and energetic consequences of chronic myocardial creatine depletion by b–guanidinopropionate in perfused hearts and in intact rats // J Mol Cell Cardiol. – 1999. – Vol. 31. – P. 1845–1855.
412. Omerovic E, Bollano E, Basetti M, et al. Bioenergetic, functional and morphological consequences of postinfarct cardiac remodeling in the rat // J Mol Cell Cardiol. – 1999. – Vol. 31. – N. 9. – P. 1685–1695.
413. Kinnaird T, Stabile E, Burnett MS, et al. Marrow–derived stromal cells express genes encoding a broad spectrum of arteriogenic cytokines and promote in vitro and in vivo arteriogenesis through paracrine mechanisms // Circ Res. – 2004. – Vol. 94. – P. 678–685.
414. Ebelt H, Jungblut M, Zhang Y, et al. Cellular cardiomyoplasty: improvement of left ventricular function correlates with the release of cardioactive cytokines // Stem Cells. – 2007. – Vol. 25. – P. 236–244.
415. Stevens KR, Kreutziger KL, Dupras SK, et al. Physiological function and transplantation of scaffold–free and vascularized human cardiac muscle tissue // Proc Natl Acad Sci USA. – 2009. – Vol. 106. – P. 16568–16573.
416. Desmouliere A, Redard M, Darby I, Gabbiani G. Apoptosis mediates the decrease in cellularity during the transition between granulation tissue and scar // Am J Pathol. – 1995. – Vol. 146. – P. 56–66.
417. Vaessen LM, Broekhuizen R, Rozing J, et al. T–cell development during ageing in congenitally athymic (nude) rats // Scand J Immunol. – 1986. – Vol. 24. – P. 223–235.
418. Rolstad B. The athymic nude rat: an animal experimental model to reveal novel aspects of innate immune responses? // Immunol Rev. – 2001. – Vol. 184. – P. 136–144.
419. Nussbaum J, Minami E, Laflamme MA, et al. Transplantation of undifferentiated murine embryonic stem cells in the heart: teratoma formation and immune response // Faseb J. – 2007. – Vol. 21. – N. 7. – P. 1345–1357.
420. Swijnenburg RJ, Tanaka M, Vogel H, et al. Embryonic stem cell immunogenicity increases upon differentiation after transplantation into ischemic myocardium // Circulation. – 2005. – Vol. 112. – P. I166–172.
421. Lee AS, Tang C, Rao MS, et al. Tumorigenicity as a clinical hurdle for pluripotent stem cell therapies // Nat Med. – 2013. – Vol. 19. – P. 998–1004.
422. Hodgkinson CP, Bareja A, Gomez JA, Dzau VJ. Emerging Concepts in Paracrine Mechanisms in Regenerative Cardiovascular Medicine and Biology // Circ Res. – 2016. – Vol. 118. – P. 95–107.
423. Liao SY, Tse HF, Chan YC, et al. Overexpression of Kir2.1 channel in embryonic stem cell–derived cardiomyocytes attenuates posttransplantation proarrhythmic risk in myocardial infarction // Heart Rhythm. – 2013. – Vol. 10. – P. 273–282.
424. Liao SY, Liu Y, Siu CW, et al. Proarrhythmic risk of embryonic stem cell–derived cardiomyocyte transplantation in infarcted myocardium // Heart Rhythm. – 2010. – Vol. 7. – P. 1852–1859.
425. Roell W, Lewalter T, Sasse P, et al. Engraftment of connexin 43–expressing cells prevents post–infarct arrhythmia // Nature. – 2007. – Vol. 450. – P. 819–824.
426. Shiba Y, Gomibuchi T, Seto T, et al. Allogeneic transplantation of iPS cell–derived cardiomyocytes regenerates primate hearts // Nature. – 2016. – Vol. 538. – P. 388–391.

427. Mielcarek M, Storb R, Georges GE, et al. Mesenchymal stromal cells fail to prevent acute graft–versus–host disease and graft rejection after dog leukocyte antigen–haploidentical bone marrow transplantation // Biol Blood Marrow Transplant. – 2011. – Vol. 17. – P. 214–225.
428. Iwata M, Madtes DK, Abrams K, et al. Late infusion of cloned marrow fibroblasts stimulates endogenous recovery from radiation–induced lung injury // PLoS One. – 2013. –Vol. 8. – P. e57179.
429. Weber KT. Cardiac interstitium in health and disease: the collagen fiber network // J Am Coll Cardiol. – 1989. – Vol. 13. – P. 1637–1652.
430. Nagueh SF, Appleton CP, Gillebert TC, et al. Recommendations for the evaluation of left ventricular diastolic function by echocardiography // J Am Soc Echocardiogr. – 2009. – Vol. 22. – N. 2. – P. 107–133.
431. Graves SS, Hogan W, Kuhr CS, et al. Stable trichimerism after marrow grafting from 2 DLA–identical canine donors and nonmyeloablative conditioning // Blood. – 2007. – Vol. 110. – P. 418–423.
432. Spindler M, Saupe KW, Christe ME, et al. Diastolic dysfunction and altered energetics in the βMHC403//+ mouse model of familial hypertrophic cardiomyopathy // J Clin Invest. – 1998. – Vol. 101. – P. 1775–1783.
433. Saupe KW, Spindler M, Hopkins JAC, et al. Kinetic, thermodynamic, and developmental consequences of deleting creatine kinase isoenzymes from the heart // J Biol Chem. – 2000. – Vol. 275. – P. 19742–19746.
434. Schaefer S, Schwartz GG, Steinman SK, et al. Metabolic response of the human heart to inotropic stimulation: in vivo phosphorus–31 studies of normal and cardiomyopathic myocardium // Magn Reson Med. – 1992. – Vol. 25. – P. 260–272.
435. Bache RJ, Zhang J, Murakami Y, et al. Myocardial oxygenation at high workstates in hearts with left ventricular hypertrophy // Cardiovasc Res. – 1999. – Vol. 42. – P. 616–626.
436. Territo PR, French SA, Balaban RS. Simulation of cardiac work transitions, in vitro: effects of simultaneous Ca2+ and ATPase additions on isolated porcine heart mitochondria // Cell Calcium. - 2001. – Vol. 30. – P. 19–27.
437. Wilson DF, Owen CS, Holian A. Control of mitochondrial respiration: a quantitative evaluation of the roles of cytochrome c and oxygen // Arch Biochem. Biophys. – 1977. – Vol. 182. – P. 749–762.
438. Jacobus WE, Moreadith RW, Vandegaer KM. Mitochondrial respiratory control. Evidence against the regulation of respiration by extramitochondrial phosphorylation potentials or by [ATP]//[ADP] ratios // J Biol Chem. – 1982. – Vol. 257. – P. 2397–2402.
439. Balaban RS, Kantor HL, Katz LA, Briggs RW. Relation between work and phosphate metabolites in the in vivo paced mammalian heart // Science. – 1986. – Vol. 232. – P. 1121–1123.
440. Gong G, Ugurbil K, Zhang J. Transmural metabolic heterogeneity at high cardiac work states // Am J Physiol. – 1999. – Vol. 277. – P. H236–H242.
441. Territo PR, French SA, Dunleavy MC, et al. Calcium activation of heart mitochondrial oxidative phosphorylation: rapid kinetics of mVO2, NADH, AND light scattering // J Biol Chem. – 2001. – Vol. 276. – N. 4. – P. 2586–2599.
442. Mitchell GF, Pfeffer MA. Left ventricular remodeling after myocardial infarction: progression toward heart failure // Heart Failure. – 1999. –Vol. 8. – P. 55–69.
443. Olivetti G, Capasso JM, Meggs LG, et al. Cellular basis of chronic ventricular remodeling after myocardial infarction in rats // Circ Res. – 1991. – Vol. 68. – P. 856–869.
444. Patten RD, Aronovitz MJ, Deras–Mejia L, et al. Ventricular remodeling in a mouse model of myocardial infarction // Am J Physiol. – 1998. – Vol. 274. – P. H1812–H1820.
445. Udelson JE, Patten RD, Konstam MA. New concepts in post–infarction ventricular remodeling // Rev Cardiovasc Med. – 2003. – Vol. 4. – P. S3–S12.
446. Murakami Y, Zhang J, Eijgelshoven MHJ, et al. Myocardial creatine kinase kinetics in hearts with postinfarction left ventricular remodeling // Am J Physiol Heart Circ Physiol. – 1999. – Vol. 276. – P. H892–H900.

447. Neubauer M, Remkes H, Strömer H, et al. Chronic phosphocreatine depletion by the creatine analogue ß–guanidinopropionate is associated with increased mortality and loss of ATP in rats after myocardial infarction // Circulation. – 2001. – Vol. 104. – P. 1844–1849.
448. Abadeh S, Case PC, Harrison R. Purification of xanthine oxidase from human heart // Biochem Soc Tran. – 1993. – Vol. 21. – N.2. – P. 99S.
449. Cappola TP, Kass DA, Nelson GS, et al. Allopurinol improves myocardial efficiency in patients with idiopathic dilated cardiomyopathy // Circulation. – 2001. – Vol. 104. – N. 20. – P. 2407–2411.
450. Ekelund UE, Harrison RW, Shokek O, et al. Intravenous allopurinol decreases myocardial oxygen consumption and increases mechanical efficiency in dogs with pacing–induced heart failure // Circ Res. – 1999. – Vol. 85. – P. 437–445.
451. Stull LB, Leppo MK, Gao WD, Marbán E. Chronic treatment with allopurinol boosts survival and cardiac contractility in murine postischemic cardiomyopathy // Circ Res. – 2004. – Vol. 95. – P. 1005–1011.
452. Engberding N, Spiekermann S, Schaefer A, et al. Allopurinol attenuates left ventricular remodeling and dysfunction after experimental myocardial infarction: a new action for an old drug? // Circulation. – 2004. – Vol. 110. –P. 2175–2179.
453. Nahrendorf M, Hiller KH, Hu K, et al. Cardiac magnetic resonance imaging in small animal models of human heart failure // Med Image Anal. – 2003. – Vol. 7. – N. 3. – P. 369–375.
454. Neubauer S, Horn M, Cramer M, et al. Myocardial phosphocreatine–to–ATP ratio is a predictor of mortality in patients with dilated cardiomyopathy // Circulation. – 1997. – Vol. 96. – P. 2190–2196.
455. Liao R, Jain M, Cui L, et al. Cardiac–specific overexpression of GLUT1 prevents the development of heart failure attributable to pressure overload in mice // Circulation. – 2002. –Vol. 106. – N. 16. – P. 2125–2131.
456. Chandler MP, Stanley WC, Morita H, et al. Short–term treatment with ranolazine improves mechanical efficiency in dogs with chronic heart failure // Circ Res. – 2002. – Vol. 91. – N. 4. –P. 278–280.
457. Hügel S, Horn M, Groot M, Remkes H. Effects of ACE inhibition and beta–receptor blockade on energy metabolism in rats postmyocardial infarction // Am J Physiol Heart Circ Physiol. – 1999. – Vol. 277. – P. H2167–H2175.
458. Shen W, Asai K, Uechi M, et al. Progressive loss of myocardial ATP due to a loss of total purines during the development of heart failure in dogs: a compensatory role for the parallel loss of creatine // Circulation. – 1999. – Vol. 100. – P. 2113–2118.
459. Jerosch–Herold M. Quantification of myocardial perfusion by cardiovascular magnetic resonance // Journal of Cardiovascular Magnetic Resonance. – 2010. – Vol. 12. – P. 57.
460. Patel PP, Koppenhafer SL, Scholz TD. Measurement of kinetic perfusion parameters of gadoteridol in intact myocardium: effects of ischemia/reperfusion and coronary vasodilation // Magn Reson Imag. – 1995. – Vol. 13. –P. 799–806.
461. Pack NA, Dibella EV, Wilson BD, McGann CJ. Quantitative myocardial distribution volume from dynamic contrast–enhanced MRI // Magnetic Resonance Imaging. – 2008. – Vol. 26. – P. 532–542.
462. Kelle S, Graf K, Dreysse S, et al. Evaluation of contrast wash–in and peak enhancement in adenosine first pass perfusion CMR in patients post bypass surgery // Journal of Cardiovascular Magnetic Resonance. – 2010. – Vol. 12. – P. 28.
463. Valentine BA, Cooper BJ, de Lahunta A, et al. Canine X–linked muscular dystrophy. An animal model of Duchenne muscular dystrophy: clinical studies // Journal of the Neurological Sciences. - 1988. – Vol. 88. – P. 69–81.
464. Kerwin WS, Oikawa M, Yuan C, et al. MR imaging of adventitial vasa vasorum in carotid atherosclerosis // Magn Reson Med. – 2008. – Vol. 59. – P. 507–514.
465. Tyler KL. Origins and early descriptions of "Duchenne muscular dystrophy" // Muscle & Nerve. - 2003. – Vol. 28. – P. 402–422.

466. Muntoni F, Torelli S, Ferlini A. Dystrophin and mutations: one gene, several proteins, multiple phenotypes // Lancet Neurology. – 2003. – Vol. 2. – P. 731–740.
467. Finsterer J, Stollberger C. The heart in human dystrophinopathies // Cardiology. – 2003. – Vol. 99. – P. 1–19.
468. Duan D. Challenges and opportunities in dystrophin–deficient cardiomyopathy gene therapy // Human Molecular Genetics. – 2006. – Vol. 15. – N. 2. – P. R253–R261.
469. Hoogerwaard EM, van der Wouw PA, Wilde AA, et al. Cardiac involvement in carriers of Duchenne and Becker muscular dystrophy // Neuromuscular Disorders. – 1999. – Vol. 9. – P. 347–351.
470. Silva MC, Meira ZM, Gurgel GJ, et al. Myocardial delayed enhancement by magnetic resonance imaging in patients with muscular dystrophy // Journal of the American College of Cardiology. – 2007. – Vol. 49. – P. 1874–1879.
471. Puchalski MD, Williams RV, Askovich B, et al. Late gadolinium enhancement: precursor to cardiomyopathy in Duchenne muscular dystrophy? // The International Journal of Cardiovascular Imaging. – 2009. – Vol. 25. – P. 57–63.
472. Bilchick KC, Salerno M, Plitt D, et al. Prevalence and distribution of regional scar in dysfunctional myocardial segments in Duchenne muscular dystrophy // Journal of Cardiovascular Magnetic Resonance. – 2011. – Vol. 13. – P. 20.
473. Perloff JK, Henze E, Schelbert HR. Alterations in regional myocardial metabolism, perfusion, and wall motion in Duchenne muscular dystrophy studied by radionuclide imaging // Circulation. - 1984. – Vol. 69. – P. 33–42.
474. Nishimura T, Yanagisawa A, Sakata H, et al. Thallium–201 single photon emission computed tomography (SPECT) in patients with duchenne's progressive muscular dystrophy: a histopathologic correlation study // Japanese Circulation Journal. – 2001. – Vol. 65. – P. 99–105.
475. Ahmad N, Welch I, Grange R, et al. Use of imaging biomarkers to assess perfusion and glucose metabolism in the skeletal muscle of dystrophic mice // BMC Musculoskeletal Disorders. – 2011. – Vol. 12. – P. 127.
476. Melacini P, Vianello A, Villanova C, et al. Cardiac and respiratory involvement in advanced stage Duchenne muscular dystrophy // Neuromuscular Disorders. – 1996. – Vol. 6. – P. 367–376.
477. Lanza GA, Dello RA, Giglio V, et al. Impairment of cardiac autonomic function in patients with Duchenne muscular dystrophy: relationship to myocardial and respiratory function // American Heart Journal. – 2001. – Vol. 141. – P. 808–812.
478. van Bockel EA, Lind JS, Zijlstra JG, et al. Cardiac assessment of patients with late stage Duchenne muscular dystrophy // Netherlands Heart Journal. – 2009. – Vol. 17. – P. 232–237.
479. Borrello JA, Chenevert TL, Aisen AM. Regional phase correction of inversion–recovery MR images // Magn Reson Med. – 1990. – Vol. 14. – N. 1. – P. 56–67.
480. Xiang QS. Inversion recovery image reconstruction with multiseed region–growing spin reversal // J Magn Reson Imaging. – 1996. – Vol. 6. – N. 5. – P. 775–778.
481. Wang J, Bornert P, Zhao H, et al. Simultaneous noncontrast angiography and intraplaque hemorrhage (SNAP) imaging for carotid atherosclerotic disease evaluation // Magn Reson Med. – 2013. – Vol. 69. – N. 2. – P. 337–334.
482. Wang J, Chen H, Maki JH, et al. Referenceless acquisition of phase–sensitive inversionrecovery with decisive reconstruction (RAPID) imaging // Magn Reson Med. – 2014. – Vol. 72. – N. 3. – P. 806–815.
483. Liu H, Wilson GJ, Balu N, et al. 3D true–phase polarity recovery with independent phase estimation using three–tier stacks based region growing (3D–TRIPS) // MAGMA. – 2018. –Vol. 31. – N. 1. – P. 87–99.
484. Kraitchman DL, Tatsumi M, Gilson WD, et al. Dynamic imaging of allogeneic mesenchymal stem cells trafficking to myocardial infarction // Circulation. – 2005. – Vol. 112. – N. 10. – P. 1451–1461.
485. Edelman RR, Chien D, Kim D. Fast selective black blood MR imaging // Radiology. – 1991. – Vol. 181. – P. 655–660.

486. Wang J, Yarnykh VL, Yuan C. Enhanced image quality in black–blood MRI using the improved motion–sensitized driven–equilibrium (iMSDE) sequence // J Magn Res Imaging. – 2010. – Vol. 31. – N. 5. – P. 1256–1263.
487. Wang J, Yarnykh VL, Hatsukami T, et al. Improved suppression of plaque–mimicking artifacts in black–blood carotid atherosclerosis imaging using a multislice motion–sensitized driven–equilibrium (MSDE) turbo spin–echo (TSE) sequence // Magn Reson Med. – 2007. – Vol. 58. –P. 973–981.
488. Iancu TC. Ferritin and hemosiderin in pathological tissues // Electron Microsc Rev. – 1992. – Vol. 5. – P. 209–229.
489. Miyazaki E, Kato J, Kobune M, et al. Denatured H ferritin subunit is a major constituent of haemosiderin in the liver of patients with iron overload // Gut. – 2002. – Vol. 50. – P. 413–419.
490. Loncar R, Flesche CW, Deussen A. Ischemia results in an enhanced ferritin content in relation to the degree of ischemia // Acta Physiol Scand. – 2004. – Vol. 180. – P. 21–28.
491. Rigol M, Solanes N, Roqué M, et al Hemosiderin deposits confounds tracking of iron–oxide–labeled stem cells: an experimental study // Transplant Proc. – 2008. – Vol. 40. – N. 10. – P. 3619–3622.
492. Jensen JH, Chandra R. Theory of nonexponential NMR signal decay in liver with iron overload or superparamagnetic iron oxide particles // Magn Reson Med. – 2002. – Vol. 47. – P. 1131–1138.
493. Wu EX, Kim D, Tosti CL, et al. Magnetic resonance assessment of iron overload by separate measurement of tissue ferritin and hemosiderin iron // Ann. N.Y. Acad. Sci. – 2010. – Vol. 1202. – P. 115–122.
494. Mills PH, Ahrens ET. Enhanced positive–contrast visualization of paramagnetic contrast agents using phase images // Magn Reson Med. – 2009. – Vol. 62. – P. 1349–1355.
495. Herynek V, Bulte JW, Douglas T, Brooks RA. Dynamic relaxometry: application to iron uptake by ferritin // J Biol Inorg Chem. – 2000. – Vol. 5. – N. 1. – P. 51–56.